# A trajectory equation for walking droplets: hydrodynamic pilot-wave theory

by

Anand Uttam Oza

A.B., Princeton University (2008)
MASt, University of Cambridge (2009)

Submitted to the Department of Mathematics
in partial fulfillment of the requirements for the degree of
Doctor of Philosophy
at the
MASSACHUSETTS INSTITUTE OF TECHNOLOGY
June 2014

© Anand Uttam Oza, MMXIV. All rights reserved.

The author hereby grants to MIT permission to reproduce and distribute publicly paper and electronic copies of this thesis document in whole or in part.

Author . . . . . . . . . . . . . . . . . . . . . . . . . . . . . . . . . . . . . . . . . . . . . . . . . . . . . . . .
Department of Mathematics
May 2, 2014

Certified by . . . . . . . . . . . . . . . . . . . . . . . . . . . . . . . . . . . . . . . . . . . . . . . . . . . .
John W. M. Bush
Professor of Applied Mathematics
Thesis Supervisor

Certified by . . . . . . . . . . . . . . . . . . . . . . . . . . . . . . . . . . . . . . . . . . . . . . . . . . . .
Rodolfo R. Rosales
Professor of Applied Mathematics
Thesis Supervisor

Accepted by . . . . . . . . . . . . . . . . . . . . . . . . . . . . . . . . . . . . . . . . . . . . . . . . . . . .
Michel Goemans
Chairman, Department Committee on Graduate Theses

# A trajectory equation for walking droplets: hydrodynamic pilot-wave theory

by

Anand Uttam Oza

Submitted to the Department of Mathematics
on May 2, 2014, in partial fulfillment of the
requirements for the degree of
Doctor of Philosophy

## Abstract

Yves Couder and coworkers have demonstrated that millimetric droplets walking on a vibrating fluid bath exhibit several features previously thought to be peculiar to the microscopic quantum realm, including single-particle diffraction, tunneling, quantized orbits, and wave-like statistics in a corral. We here develop an integro-differential trajectory equation for these walking droplets with a view to gaining insight into their subtle dynamics. The orbital quantization is rationalized by assessing the stability of the orbital solutions. The stability analysis also predicts the existence of wobbling orbital states reported in recent experiments, and the absence of stable orbits in the limit of large vibrational forcing. In this limit, the complex walker dynamics give rise to a coherent statistical behavior with wave-like features. We characterize the progression from quantized orbits to chaotic dynamics as the vibrational forcing is increased progressively. We then describe the dynamics of a weakly-accelerating walker in terms of its wave-induced added mass, which provides rationale for the anomalously large orbital radii observed in experiments.

Thesis Supervisor: John W. M. Bush
Title: Professor of Applied Mathematics

Thesis Supervisor: Rodolfo R. Rosales
Title: Professor of Applied Mathematics

# Acknowledgments

First and foremost, I would like to thank my advisers John Bush and Ruben Rosales for their support throughout my PhD. John introduced me to this research problem on the first day of his fluid mechanics course in the fall of 2009, and I was instantly hooked. What began as a course project eventually morphed into this thesis. The combination of John's deep physical intuition, collaborative spirit and enthusiasm for traveling (and stinky cheese) created an unusually exciting and rewarding academic experience. Ruben provided much of the mathematical backbone for this project, and has taught me how to use mathematical tools to gain physical insight into problems. I thank Ruben for his willingness to work alongside me, sometimes late into the night, in the pursuit of new ideas. This thesis is really the product of our combined efforts, and I hope it marks the beginning of a lasting collaboration.

I would also like to thank Yves Couder, whose original experiments provided the inspiration for this thesis. Even after studying this problem for five years, I still marvel at the physical insight it took to link the behavior of silicone oil droplets to quantum mechanical phenomena, and Yves' deep questions have guided much of this research program. I am grateful to his entire group for their hospitality during both of our trips to Paris. Special thanks go to Stéphane Perrard, Matthieu Labousse and Emmanuel Fort for many interesting discussions.

The work in this thesis would not have been possible without a number of experimentalists, most notably Dan Harris, who led the experimental effort at MIT. This research has benefited from the dynamic interplay between theory and experiment, and the two have worked in tandem throughout this project. Despite the difficulty of the experiments, Dan was able to verify many of our theoretical predictions and discover several new phenomena, all of which are highly sensitive to experimental error. I also thank Tristan Gilet for guiding me in the beginning, and for supervising me during my first (and last) week in the lab. Thanks also go to Jan Moláček, who preceded me, and Lucas Tambasco, to whom I will pass the torch, for a number of valuable discussions.

On a personal note, I would like to thank my family and friends for their support throughout my academic career. My parents have been a constant source of strength and love during my rather convoluted academic journey. I thank my sister Anuja for her constant friendship, and for reminding me how boring math really is. Special thanks go to my friends in Boston for providing laughter and companionship through good and bad times alike: Pat Ho, Jocelyn Drummond, William Davy, Saish Setty, Ashrit Kamireddi, George Tucker, Rosalie Bélanger-Rioux, Jan Moláček, Dan Harris and Lucas Tambasco.

A special mention goes to my wife Roshina Nandra, who went from my girlfriend to fiancée to wife during the course of this PhD. She has heard more about this research problem than anyone should have to, and has been a constant source of enthusiasm and encouragement. Much of the research in this thesis was done while visiting her in (the original) Cambridge, and I have benefited from both her academic insights and constant love. The academic life is not for the faint of heart, and she has selflessly given me the strength and support to pursue my passions.

Finally, I would like to thank the National Science Foundation and the Hertz Foundation for their generous financial support throughout my PhD.

# Contents

**1 Introduction** **27**

**2 Integro-differential trajectory equation for walking droplets** **33**

2.1 Introduction . . . . . . . . . . . . . . . . . . . . . . . . . . . . . . 33

2.2 Integro-differential equation of motion . . . . . . . . . . . . . . . . . 36

2.3 Bouncing to walking . . . . . . . . . . . . . . . . . . . . . . . . . . 42

2.3.1 Stuart-Landau equation for the walking velocity . . . . . . . . 44

2.4 Straight-line walking . . . . . . . . . . . . . . . . . . . . . . . . . . 46

2.4.1 Walking speed . . . . . . . . . . . . . . . . . . . . . . . . . . 47

2.4.2 Wave field . . . . . . . . . . . . . . . . . . . . . . . . . . . . 48

2.5 Stability analysis . . . . . . . . . . . . . . . . . . . . . . . . . . . . 49

2.5.1 Stability to perturbations in the direction of motion . . . . . . 51

2.5.2 Stability to lateral perturbations . . . . . . . . . . . . . . . . 54

2.6 Discussion . . . . . . . . . . . . . . . . . . . . . . . . . . . . . . . . 55

**3 Pilot-wave dynamics in a rotating frame** **59**

3.1 Introduction . . . . . . . . . . . . . . . . . . . . . . . . . . . . . . 59

3.2 Trajectory equation . . . . . . . . . . . . . . . . . . . . . . . . . . . 62

3.3 Orbital solutions . . . . . . . . . . . . . . . . . . . . . . . . . . . . 64

3.3.1 Low orbital memory $M_e^O \ll 1$ . . . . . . . . . . . . . . . . . . 68

3.3.2 Mid-memory $M_e^O = O(1)$: orbital quantization . . . . . . . . . 71

3.3.3 High orbital memory $M_e^O \gg 1$: an analog Zeeman effect . . . 72

3.3.4 Trapped states . . . . . . . . . . . . . . . . . . . . . . . . . . 76

3.4 Orbital stability . . . . . . . . . . . . . . . . . . . . . . . . . . . . . . 78

3.4.1 Origin of orbital quantization . . . . . . . . . . . . . . . . . . . . 82

3.5 Discussion . . . . . . . . . . . . . . . . . . . . . . . . . . . . . . . . 83

**4 Pilot-wave dynamics in a rotating frame: exotic orbits 87**

4.1 Introduction . . . . . . . . . . . . . . . . . . . . . . . . . . . . . . . 87

4.2 Trajectory equation and numerical method . . . . . . . . . . . . . . . 90

4.3 Wobbling orbits . . . . . . . . . . . . . . . . . . . . . . . . . . . . . 93

4.4 Drifting orbits . . . . . . . . . . . . . . . . . . . . . . . . . . . . . . 94

4.5 Wobble-and-leap dynamics . . . . . . . . . . . . . . . . . . . . . . . 99

4.6 Other periodic and quasiperiodic orbits . . . . . . . . . . . . . . . . 104

4.7 Chaotic pilot-wave dynamics . . . . . . . . . . . . . . . . . . . . . . 107

4.8 Discussion . . . . . . . . . . . . . . . . . . . . . . . . . . . . . . . . 109

**5 Orbital stability in hydrodynamic pilot-wave theory 113**

5.1 Introduction . . . . . . . . . . . . . . . . . . . . . . . . . . . . . . . 113

5.2 Integro-differential trajectory equation . . . . . . . . . . . . . . . . 114

5.3 Bouncing to orbiting . . . . . . . . . . . . . . . . . . . . . . . . . . 117

5.4 Orbital solutions . . . . . . . . . . . . . . . . . . . . . . . . . . . . 120

5.5 Linear stability problem for orbital solutions . . . . . . . . . . . . . 124

5.5.1 Rotational and translational invariance . . . . . . . . . . . . . 128

5.6 Stability properties of orbital solutions in various limiting cases . . . 129

5.6.1 Orbital stability in the small radius limit . . . . . . . . . . . . 129

5.6.2 Orbital stability in the large radius limit . . . . . . . . . . . . 132

5.6.3 Orbital stability in the low-memory limit . . . . . . . . . . . . 134

5.7 Numerical method for assessing orbital stability . . . . . . . . . . . 137

5.7.1 Proof that only finitely many zeros of $\tilde{F}(s; r_0)$ need consideration139

5.8 Results of stability analysis . . . . . . . . . . . . . . . . . . . . . . 143

5.8.1 Stability diagram . . . . . . . . . . . . . . . . . . . . . . . . . 145

5.8.2 Wobbling orbits . . . . . . . . . . . . . . . . . . . . . . . . . . 145

5.8.3 Chaotic dynamics at high memory . . . . . . . . . . . . . . . . 148

5.9 Discussion . . . . . . . . . . 150

**6 The wave-induced added mass of walking droplets 155**

6.1 Introduction . . . . . . . . . . 155

6.2 Pilot-wave hydrodynamics . . . . . . . . . . 156

6.2.1 The weak-acceleration limit . . . . . . . . . . 157

6.3 Response to a weak unidirectional force . . . . . . . . . . 159

6.4 Orbital motion . . . . . . . . . . 161

6.4.1 Walking in a rotating frame . . . . . . . . . . 162

6.4.2 Walking in a central force . . . . . . . . . . 163

6.5 Discussion . . . . . . . . . . 165

**7 Concluding remarks 167**

7.1 Future directions . . . . . . . . . . 170

**A Evaluation of integral terms in $F_1(s), F_2(s), G_1(s), G_2(s)$ 173**

**B Proof that $F_0(r_0) = r_0 \omega d_1 \frac{\mathrm{d}\Omega}{\mathrm{d}r_0}$ 175**

**C Asymptotic limit $\omega \ll 1$ 177**

**D Asymptotic limit $\omega \gg 1$ 179**

**E Proof that $\tilde{F}(s; r_0)$ is an entire function of $s$ 181**

**F Computation of the error terms in (5.76) 183**

# List of Figures

2-1 A walker, a millimetric droplet, self-propagates on a vibrating fluid bath through an interaction with its own wave field. (a) Oblique view. (b) Top view. . . . . . . . . . . . . . . . . . . . . . . . . . . . . 35

2-2 Plot of the walking speed $u$ (in mm/s) as a function of the nondimensional forcing acceleration $\gamma/g$. The dots represent experimental data from Moláček and Bush [46], and the curves are obtained from our model prediction (2.35) for a resonant walker using (a) $\nu = 20$ cS, $f = 80$ Hz, $\rho = 949$ kg m$^{-3}$, $\sigma = 20.6 \times 10^{-3}$ N m$^{-1}$, $\gamma_F = 4.3g$, $T_d = 1/54.9$ s, $R = 0.40$ mm, and (b) $\nu = 50$ cS, $f = 50$ Hz, $\rho = 960$ kg m$^{-3}$, $\sigma = 20.8 \times 10^{-3}$ N m$^{-1}$, $\gamma_F = 4.23g$, $T_d = 1/57.9$ s, $R = 0.39$ mm. The single free parameter in our stroboscopic model is the phase of impact, chosen here to be (a) $\sin\Phi = 0.3$ and (b) $\sin\Phi = 0.35$. Characteristic error bars are shown. . . . . . . . . . . . . . . . . . . . . 48

2-3 Simulated wave fields generated by (a) a stationary bouncer and (b-d) walkers for, respectively, (a) very low ($\gamma = 3.0g$), (b) low ($\gamma = 3.4g$), (c) medium ($\gamma = 3.8g$), and (d) high ($\gamma = 4.2g$) path-memory. The plots are generated using $\nu = 20$ cS, $f = 80$ Hz, $\rho = 949$ kg m$^{-3}$, $\sigma = 20.6 \times 10^{-3}$ N m$^{-1}$, $T_d = 1/54.9$ s, $R = 0.40$ mm, and $\sin\Phi = 0.3$. The walking and Faraday thresholds are $\gamma_W = 3.12g$ and $\gamma_F = 4.3g$, respectively. The wave amplitude is given in microns. Upper figures: Plot of the strobed wave field $h(\boldsymbol{x}, t)$ (2.15) accompanying the drop. The drop is located at the origin and moves to the right according to $\boldsymbol{x}_p = (ut, 0)$, where $u$ is determined by (2.35). Lower figures: Wave profiles $h(x, t)$ along the direction of motion of the walker. As the memory increases, the walker moves away from the crest towards a region with higher slope, thus moving faster. . . . . . . . . . . . . . . 50

2-4 Plot of the real part of the (nonzero) poles of $\mathcal{L}[x_1(t)] = X(s)$ as a function of $\beta$, for (a) $\kappa = 1$, (b) $\kappa = 1.5$, and (c) $\kappa = 5$, respectively. $X(s)$ is the Laplace transform of the perturbation $x_1$, $\beta$ the nondimensional memory force coefficient, and $\kappa$ the nondimensional mass of the drop (see table 2.1). The three plots are representative of the ranges $0 \leq \kappa \lesssim 1.3$, $1.3 \lesssim \kappa < 2$, and $\kappa > 2$, respectively. Note that merging of the curves indicates the existence of two complex conjugate poles with the same real part. . . . . . . . . . . . . . . . . . . . . . . . . 53

3-1 The predicted dependence of the orbital radius $r_0$ ((a) and (c)) and orbital frequency $\omega$ ((b) and (d)) on the bath's rotation rate $\Omega$ in the low memory regime. The dotted lines represent the standard prediction for inertial orbits, (a) $r_0 = u_0/2\Omega$, (b) $\omega = -2\Omega$. The solid curves are the theoretical predictions determined by solving (3.9) with experimental parameters corresponding to the data reported in Harris and Bush [38], who used a silicone oil of viscosity $\nu = 20.9$ cSt, density $\rho = 950$ kg/m$^3$, surface tension $\sigma = 0.0206$ N/m, and forcing frequency $f = 80$ Hz. There are no fitting parameters. For (a) and (b), $\gamma/\gamma_F = 0.822$, free walking speed $u_0 = 9.0$ mm/s and drop radius $R_D = 0.4$ mm. For (c) and (d), $\gamma/\gamma_F = 0.922$, $u_0 = 9.5$ mm/s and $R_D = 0.4$ mm. Note that both $r_0$ and $\omega$ vary continuously with the rotation rate $\Omega$. . . . 66

3-2 The predicted dependence of the orbital radius $r_0$ ((a) and (c)) and orbital frequency $\omega$ ((b) and (d)) on the bath's rotation rate $\Omega$ in the high memory regime. The curves are the theoretical predictions determined by solving (3.9) with the experimental parameters corresponding to the data reported in Harris and Bush [38], who used a silicone oil of viscosity $\nu = 20.9$ cSt, density $\rho = 950$ kg/m$^3$, surface tension $\sigma = 0.0206$ N/m, and forcing frequency $f = 80$ Hz. There are no fitting parameters. The blue portions of the curves are stable, while the red and green portions are unstable (see §3.4). For (a) and (b), $\gamma/\gamma_F = 0.954$, $R_D = 0.43$ mm and $u_0 = 12.0$ mm/s. For (c) and (d), $\gamma/\gamma_F = 0.971$, $R_D = 0.4$ mm and $u_0 = 10.9$ mm/s (■) and 11.7 mm/s (□). The theoretical curves in (c) and (d) are constructed using the average of the observed $u_0$ values. Note that both $r_0$ and $\omega$ are quantized. . . . 67

3-3 Plots of the wave field (3.6) accompanying a drop of viscosity $\nu = 20.9$ cSt, density $\rho = 950$ kg/m$^3$, surface tension $\sigma = 0.0206$ N/m, period $T_F = 0.025$ s, radius $R_D = 0.4$ mm, and phase $\sin\Phi = 0.16$. The amplitude of the wave field is in units of microns. The drop (black dot) orbits clockwise according to $\boldsymbol{x}_p(t) = (r_0 \cos\omega t, r_0 \sin\omega t)$, with orbital radius $r_0 = 0.95\lambda_F$ and orbital frequency $\omega$ defined by (3.9). The forcing accelerations are (a) $\gamma/\gamma_F = 0.822$, (b) $\gamma/\gamma_F = 0.922$, (c) $\gamma/\gamma_F = 0.954$, and (d) $\gamma/\gamma_F = 0.971$. The walking threshold in the absence of rotation is $\gamma_W/\gamma_F = 0.806$. Note that interference effects in the wave field become more pronounced with increased forcing and path memory. . . . . . . . . . . . . . . . . . . . . . . . . . . . 69

3-4 Schematic (top view) of the wave force acting on the walker in the low-memory regime. The walker orbits in a circle of radius $r_0$ with angular speed $u_0 = |r_0\omega|$ while bouncing with period $T_F$ on a fluid bath rotating with angular frequency $\Omega$. The force $\boldsymbol{F}$ acting on the drop at $\boldsymbol{x} = \boldsymbol{x}_p(t)$ is primarily due to the wave created by the prior bounce at $\boldsymbol{x} = \boldsymbol{x}_p(t - T_F)$, whose form is suggested by the circular wave crest. The radial component of the force is $|\boldsymbol{F}|\sin\theta$. The wave force thus causes the observed orbital radius $r_0 = au_0/2\Omega$ to be larger than the inertial orbital radius $r_c = u_0/2\Omega$. . . . . . . . . . . . . . . . 71

3-5 Orbital solutions in the high orbital memory regime $M_e^O \gg 1$. The curves are determined by solving (3.9) numerically for $\gamma/\gamma_F = 0.985$, assuming a drop of radius $R_D = 0.4$ mm, phase $\sin\Phi = 0.16$, and free walking speed $u_0 = 11.6$ mm/s. Both the red and green portions of the curves represent unstable solutions (see §3.4). (a) Orbital radii as a function of $\Omega$. (b) Orbital radii for which $\Omega > 0$. (c) Orbital frequencies $\omega$ as a function of $\Omega$. The analog Zeeman effect is apparent in panel (b), as the self-orbiting solutions of radius $r_0^*$ at $\Omega = 0$ split into two solutions as $\Omega$ is increased. The adjoining co-rotating orbital solutions ($\omega > 0$) have slightly larger orbital radii than their counter-rotating counterparts ($\omega < 0$), the difference $\Delta r_0$ being defined in (3.24). . . . 74

3-6 The critical rotation rate for trapping $\Omega_0$ as defined by (3.29) is plotted as a function of the nondimensional forcing acceleration $\gamma/\gamma_F$. The drop bounces in place for $|\Omega| > \Omega_0$ (Chapter 5, [49]). We assume a drop of radius $R_D = 0.4$ mm and phase $\sin\Phi = 0.16$, for which the walking threshold in the absence of rotation is $\gamma_W/\gamma_F = 0.806$. . . . . 78

3-7 Orbital stability diagram for a walker of radius $R_D = 0.4$ mm, phase $\sin\Phi = 0.16$, viscosity $\nu = 20.9$ cSt, and forcing frequency $f = 80$ Hz, determined by finding the eigenvalues of the linear stability problem (3.32). The stability of the circular orbit is governed by the eigenvalue with the largest real part, denoted by $s_*$. Stable orbits ($\Re(s_*) < 0$) are indicated in blue. Unstable orbits for which $s_*$ is complex ($\Re(s_*) > 0$, $\Im(s_*) \neq 0$) are colored in green, while those for which $s_*$ is on the positive real axis ($\Re(s_*) > 0$, $\Im(s_*) = 0$) are colored in red. The horizontal traverses A–C correspond to, respectively, the curves in figures 3-1(c), 3-2(a), and 3-2(c), the color coding being the same. We note that the phase $\sin\Phi$ and drop radius $R_D$ vary slightly between the traverses A–C but are assumed to be fixed in the orbital stability diagram. . . 84

4-1 Summary of the linear stability analysis for circular orbits presented in Chapter 3 [50], for a walker of radius 0.4 mm and phase $\sin\Phi = 0.2$ bouncing on a 20 cS silicone oil bath forced at 80 Hz. The dimensionless orbital radius $r_0/\lambda_F$ and vibrational acceleration $\gamma/\gamma_F$ uniquely specify the circular orbit. Blue indicates stable orbits, for which each eigenvalue has a negative real part. Green corresponds to unstable orbits with an oscillatory instability, for which the eigenvalues with the largest (positive) real part are complex conjugates. Red corresponds to unstable orbits for which the eigenvalue with the largest (positive) real part is purely real. We note that the experimental parameters used here are slightly different to those used to generate Figure 3-7. 89

4-2 Regime diagram delineating the dependence of the walker's trajectory on the initial orbital radius $r_0$ and vibrational forcing $\gamma$. The trajectory equation (4.2) is numerically simulated using circular orbit initial conditions, initial perturbation $\boldsymbol{\delta} = (0.02, 0)$, time step $\Delta t = 2^{-6}$ and $t_{max} = 1000$. The walker's trajectory is color-coded according to the legend. . . . . . . . . . . . . . . . . . . . . . . . . . . . . . 92

4-3 Panels (a) and (b): examples of $2\omega$- and $3\omega$-wobbling orbits at $n = 1$, respectively. The $2\omega$-wobbling orbit was obtained using initial orbital radius $r_0/\lambda_F = 0.85$ and vibrational forcing $\gamma/\gamma_F = 0.955$, and the $3\omega$-wobbling orbit using $r_0/\lambda_F = 0.94$ and $\gamma/\gamma_F = 0.9745$. The corresponding (unstable) circular orbit is indicated by the dashed line. Panels (c) and (d): plots of the corresponding orbital radius $\bar{r}(t)$ as a function of $t/T$, where $T$ is the orbital period. In the upper plots, note that the radius grows and then saturates, which is characteristic of a Hopf-type instability. The lower plots resolve the oscillations, showing that the wobbling frequency is $\approx 2\omega$ in (c) and $\approx 3\omega$ in (d). . . . . . 95

4-4 Numerical characterization of wobbling orbits (panels (a) and (c)), compared with experimental data from Harris and Bush [38] (panels (b) and (d)). Panels (a) and (b) show the dependence of the wobbling amplitude $A$ on the rotation rate $\Omega$ for various values of memory $\gamma/\gamma_F$. Panels (c) and (d) show the dependence of the wobbling frequency $\omega_{\text{wob}}$ on the rotation rate $\Omega$. The wobbling frequency is normalized by the orbital frequency $\omega$. The symbols correspond to different values of the memory $\gamma/\gamma_F$, as defined in the legend. . . . . . . . . . . . . . . . . . 96

4-5 (a) Numerical simulation of a drifting trajectory at $n = 1$, obtained using the initial orbital radius $r_0/\lambda_F = 0.8005$ and vibrational forcing $\gamma/\gamma_F = 0.959$. The trajectory (gray line) consists of a loop (dashed line) drifting along a larger circle (black solid line). (b) Plot of the orbital radius $\bar{r}(t)$ as a function of $t/T$, where $T = 4.3$ is the orbital period. (c) Plot of the orbital center $(\bar{x}_c, \bar{y}_c)$ as a function of $t/T$. Note that the center moves on a much slower timescale than the radius $\bar{r}$. (d) Numerical simulation of another drifting trajectory using $r_0/\lambda_F = 0.893$ and $\gamma/\gamma_F = 0.966$, for which the center does not move along a precise circle. (e) Experimentally observed [38] drifting trajectory similar to that in panel (d), obtained using $\gamma/\gamma_F = 0.978 \pm 0.003$ and rotation rate $\Omega = 1.72\ \text{s}^{-1}$. The trajectory is indicated by the dashed line, the motion of the center by the solid line. . . . . . . . . . . . . . 98

4-6 Numerical characterization of drifting orbits at $n = 1$. Top panels (a) and (d): the curve shows the theoretical orbital radius $r_0$ as a function of the nondimensional rotation rate $2\Omega\lambda_F/u_0$, calculated using (4.3). The blue segments indicate stable circular orbits, and the green unstable solutions due to an oscillatory instability. The trajectory equation (4.2) was numerically simulated within the green regions, and both wobbling and drifting orbits were found. The markers correspond to the mean orbital radius $\bar{r}$ of a wobbling orbit, and the error bars indicate the wobbling amplitude. The unmarked green regions correspond to drifting orbits, in which the orbital center $(\bar{x}_c, \bar{y}_c)$ drifts in a circle. The middle panels, (b) and (e), show the radius $R_{\text{drift}}$ of the orbital center, and the lower panels (c) and (f) the period of the orbital center $T_{\text{drift}}$ normalized by the orbital period $T$. Panels (a–c) correspond to a vibrational forcing $\gamma/\gamma_F = 0.957$ and (d–f) to $\gamma/\gamma_F = 0.958$. . . . . 100

4-7 Numerical simulations of drifting orbits, for various values of the vibrational forcing $\gamma/\gamma_F$ and initial orbital radius $r_0$. In panel (a), the gray curve corresponds to a trajectory with $r_0/\lambda_F = 0.7262$ and $\gamma/\gamma_F = 0.971$, which consists of a loop (dashed black curve) that drifts along a square epicycle (black curve). The plots along the top row of panel (b) show the orbital centers of some drifting orbits at $n = 0$. From left to right, the parameter values are: $(r_0/\lambda_F, \gamma/\gamma_F) = (0.7221,$ $0.973)$, (0.3635, 0.968), (0.7514, 0.971), (0.7870, 0.971) and (0.775, 0.971). The bottom row shows those corresponding to $n = 1$, with parameter values $(r_0/\lambda_F, \gamma/\gamma_F) =$ (0.8541, 0.9612), (0.8537, 0.9609), (0.8541, 0.96125), (0.8542, 0.9613) and (0.8537, 0.96085), which correspond to the same dimensionless rotation rate $\hat{\Omega} = 0.5734$. . . . . . . 101

4-8 Numerical simulation of a wobble-and-leap trajectory at $n = 1$, obtained using initial orbital radius $r_0/\lambda_F = 0.8029$ and vibrational forcing $\gamma/\gamma_F = 0.960$. Panel (a) shows the mean orbital radius $\bar{r}(t)$. Panel (b) shows the trajectory (dashed gray curve), resulting from the orbital center (solid black curve) jumping between the transiently stable points (black dots). The dashed black curves are circles of radius $r_0/\lambda_F$ centered on the stable points. Panels (c) and (d) show the coordinates $\bar{x}_c(t)$ and $\bar{y}_c(t)$ of the orbital center. Panel (e) shows a qualitatively similar trajectory observed in the experiments of Harris and Bush [38], obtained using $\gamma/\gamma_F = 0.978 \pm 0.003$ and rotation rate $\Omega = 1.76$ s$^{-1}$. The trajectory is indicated by the dashed line, the center by the solid line. . . . . . . . . . . . . . . . . . . . . . . . . . . . . . . . . . . 102

4-9 Numerical simulations of wobble-and-leap trajectories at $n = 0$, for various values of the initial radius $r_0/\lambda_F$ and vibrational forcing $\gamma/\gamma_F$. The plots show the paths of the orbital centers, nondimensionalized by the Faraday wavelength, $(\bar{x}_c(t), \bar{y}_c(t))/\lambda_F$. From top left to bottom right, the parameter values are: $(r_0/\lambda_F, \gamma/\gamma_F) =$ (0.376, 0.9665), (0.370, 0.966), (0.3769, 0.9665), (0.365, 0.966), (0.3654, 0.966), (0.3657, 0.966), (0.3659, 0.966), (0.3656, 0.966), (0.368, 0.966), (0.373, 0.9665), (0.372, 0.9665), (0.3763, 0.9665), (0.3775, 0.9665), (0.3647, 0.966), (0.370, 0.9665) and (0.370, 0.967). . . . . . . . . . . . . . . . . . . . . . 103

4-10 Numerical simulations of quasiperiodic trajectories observed for various values of the initial orbital radius $r_0/\lambda_F$ and vibrational forcing $\gamma/\gamma_F$. The plots show the trajectories nondimensionalized by the Faraday wavelength, $(x(t), y(t))/\lambda_F$. From top left to bottom right, the parameter values are: $(r_0/\lambda_F, \gamma/\gamma_F) =$ (1.4007, 0.97), (0.8924, 0.969), (0.8898, 0.966), (0.8778, 0.966), (0.8398, 0.961), (0.8249, 0.960), (0.3897, 0.976), (1.2348, 0.979) and (0.8417, 0.969). . . . . . . . . . . . . . . . . . . . . 105

4-11 Numerical simulation of a trajectory exhibiting a periodic oscillation between two orbital radii, obtained using initial radius $r_0/\lambda_F = 1.2691$ and vibrational forcing $\gamma/\gamma_F = 0.971$. Panel (a) shows the trajectory, which consists of the loop in panel (b) drifting along a circle. Panel (c) shows the loop radius $R(t)$ of the trajectory. The shaded portion corresponds to the trajectory in panel (b). The walker evidently oscillates periodically between the two unstable orbital solutions with radii $r_0/\lambda_F = 0.409$ and $r_0/\lambda_F = 0.869$, indicated by the horizontal lines. . 106

4-12 Numerical simulation of a chaotic trajectory in the high-memory regime, using time step $\Delta t = 2^{-8}$ and $t_{max} = 1000$. Panel (a) shows a portion of the trajectory, obtained using initial orbital radius $r_0/\lambda_F = 2.3775$ and vibrational forcing $\gamma/\gamma_F = 0.985$. Panel (b) shows the corresponding loop radius $R(t)$ over the same time interval, and panel (c) the histogram of the loop radius over the entire trajectory. The bin size is fixed at $0.02\lambda_F$. The vertical lines are located at the zeros of the Bessel function $J_0(k_F r)$. . . . . . . . . . . . . . . . . . . . . . . . . . . 108

4-13 Numerical simulations showing the dependence of the orbital statistics on the dimensionless rotation rate $2\Omega\lambda_F/u_0$, for three different values of the vibrational forcing $\gamma/\gamma_F$. Each simulation was performed from stationary initial conditions, using time step $\Delta t = 2^{-8}$ and $t_{max} = 1000$. In the top panels, each column is colored according to the prevalence of the corresponding loop radius $R(t)$, with red segments being the most prevalent radii. The bottom panels show three histograms corresponding to $\hat{\Omega} = 0.17$ (or $2\Omega\lambda_F/u_0 \approx 0.5$), indicated by the vertical lines in the top panels. The peaks of the histograms are centered at the zeros of the Bessel function $J_0(k_F r)$, indicated by the vertical lines. The bin size is fixed at $0.02\lambda_F$. . . . . . . . . . . . . . . . . . . . . . . . . . 109

4-14 Numerical simulations showing the dependence of the orbital statistics on the vibrational forcing $\gamma/\gamma_F$. The simulations were initiated with the circular orbit at $n = 4$ corresponding to the fixed dimensionless rotation rate $\hat{\Omega} = 0.1784$ (or $\Omega = 0.70\ \mathrm{s}^{-1}$), with time step $\Delta t = 2^{-8}$ and $t_{max} = 1000$. In panel (a), each column is colored according to the prevalence of the corresponding loop radius $R(t)$, with red segments being the most prevalent radii. Note that the brightest segments lie near the zeros of $J_0(k_F r)$. Panel (b) shows the corresponding experimental data from Harris and Bush [38], obtained for $\Omega = 0.79\ \mathrm{s}^{-1}$. . . . . . 110

5-1 Diagrams used in the numerical justification of Proposition 1. (a) The black curves show the cross sections $v_{r_0}(\omega) \equiv V(r_0, \omega)$, as defined by (5.22), for $r_0 = 0.5$, 1, 2, 3, 5 and 10. The black curve with the largest amplitude corresponds to $r_0 = 0.5$, and the amplitude monotonically decreases with $r_0$. The blue curve corresponds to $v_0(\omega) = \omega/2(1 + \omega^2)$. The dashed red lines correspond to $\omega/\beta$ for $\beta = 2$, 3 and 10. This picture suggests that $\omega = \omega(r_0)$, as defined by the intersection of the black and red curves, is a single-valued monotonically decreasing function of $r_0$. (b) Plot confirming convergence of the functions $v_{r_0}(\omega)$ to the function $V_\infty(r_0\omega)/r_0$, as defined in (5.24), in the limit $r_0 \gg 1$. The difference between the two clearly decreases like $r_0^{-3}$, as expected from the calculation in (5.24). . . . . . . . . . . . . . . . . . . . . . . . 122

5-2 (a) Partition of the $\tilde{s}$-plane used in §5.7.1, where $\tilde{s} = (s + 1)/|\omega|$. The black dots indicate the positions of the roots $\tilde{s} = \mathrm{i}n$ at $r_0 = 0$, where $n \in \mathbb{Z}$. The white regions surrounding these roots represent $C_n$, outside of which $\left|1 - \mathrm{e}^{-2\pi\tilde{s}}\right| > 1 - \mathrm{e}^{-2\pi/|\omega|}$. (b) Plot of $\mathcal{S}(\gamma)$ as a function of the forcing acceleration $\gamma/\gamma_F$, computed on the basis of (5.86). We show in §5.7.1 that the roots $s_n$ for $n > \lceil\mathcal{S}\rceil$ are confined within $C_n$ for all $r_0 < R_0(\gamma)$, which ensures that they do not generate an instability. . . 140

5-3 Plots of selected roots of $\tilde{F}(s;r_0)$ as a function of the orbital radius $r_0$, for fixed values of the forcing acceleration $\gamma/\gamma_F$. The left panels correspond to the real part of the roots, the right panel to the imaginary part. The first row shows the eigenvalue pair $s_0$ (solid) and $s_z$ (dashed) for $\gamma/\gamma_F = 0.956$. The second row shows $s_2(r_0)$ for $\gamma/\gamma_F = 0.970$, and the third $s_3(r_0)$ for $\gamma/\gamma_F = 0.975$. . . . . . . . . . . . . . . . . . . . . . 144

5-4 Orbital stability of circular orbit solutions to (5.9), plotted as a function of the dimensionless orbital radius $r_0/\lambda_F$ and forcing acceleration $\gamma/\gamma_F$. The results of §5.4 show that a point on this diagram uniquely specifies the circular orbit. For a given value of $r_0$ and $\gamma$, the roots of $\tilde{F}(s;r_0)$ are computed and ordered by their imaginary part, according to the scheme described in §5.8.1. We thus obtain a list of roots $q_1, q_2, \ldots$. We then select the root $q_i$ with the largest real part, and color the point on the stability diagram according to the index $i$. We use the color scheme $q_1$ = red, $q_2$ = light green, $q_3$ = yellow, $q_4$ = magenta, $q_5$ = cyan, $q_6$ = brown and $q_7$ = gray. . . . . . . . . . . . . . . . . . . . 146

5-5 Plots of the eigenvalues $s_2(r_0)$ (solid) and $s_3(r_0)$ (dashed) for $\gamma/\gamma_F = 0.981$. Panel (a) shows the trajectory of the two eigenvalues in the complex plane as $r_0$ is varied. Panels (b) and (c) show, respectively, the real and imaginary parts of the two roots, plotted for the same values of $r_0$. The imaginary parts are normalized by the orbital frequency $|\omega|$. Note that the imaginary part of $s_2$, which starts at $\Im(s_2(0)) = 2|\omega|$, rapidly changes to $\Im(s_2) \approx 3|\omega|$, and vice versa for $s_3$. . . . . . . . . 147

5-6 Plot of the wobbling frequency $\omega_{wob}$ normalized by the orbital frequency $\omega$ as a function of the dimensionless rotation rate $2\Omega\lambda_F/u_0$. The points indicate experimental data from Harris and Bush [38], corresponding to the four different values of the vibrational forcing $\gamma/\gamma_F$ and walking speed $u_0$: $\gamma/\gamma_F = 0.961 \pm 0.002$ and $u_0 = 12.0$ mm s$^{-1}$ (●); $\gamma/\gamma_F = 0.969 \pm 0.005$ and $u_0 = 12.3$ mm s$^{-1}$ (○); $\gamma/\gamma_F = 0.974 \pm 0.002$ and $u_0 = 12.3$ mm s$^{-1}$ (■); and $\gamma/\gamma_F = 0.978 \pm 0.003$ and $u_0 = 12.4$ mm s$^{-1}$ (□). The theoretical curve (dashed) plots the imaginary part of the unstable eigenvalue at the boundary of the green region in Figure 5-4, between $0.7 \leq r_0/\lambda_F \leq 0.9$. . . . . . . . . . . . . . . . . . . . . . . . . 149

5-7 (a) Histogram of the walker's loop radius $R(t)$, computed on the basis of numerical simulations of (5.9) for $\Omega = 0.70$ s$^{-1}$ and $\gamma/\gamma_F = 0.983$ (top panel) and $\gamma/\gamma_F = 0.985$ (bottom panel) (Chapter 4 [51]). The red vertical bars are located at the radii of the possible orbital solutions, as determined by (5.20). Their height is determined by $\tau \equiv 1/\Re(s_{max})$, $s_{max}$ being the eigenvalue of the appropriate orbital solution with the largest real part. The vertical bars and histograms have been normalized so that their maximum height is 1. (b) Orbital stability diagram color coded according to the size of $\Re(s_{max})$. Blue denotes stable orbits, for which $\Re(s_{max}) < 0$. The solid lines are located at the roots of $J_0(2\pi r)$, and the dashed lines at the roots of $J_1(2\pi r)$. Note that the orbital radii satisfying $J_1(r_0/\lambda_F) \approx 0$ are more unstable than those satisfying $J_0(r_0/\lambda_F) \approx 0$, which explains why the latter are more prominent in panel (a). . . . . . . . . . . . . . . . . . . . . . . . . . . . . . . . . 151

6-1 Dependence of the hydrodynamic boost factor $\gamma_B$ on the walker speed $u_0$ and forcing acceleration $\gamma/\gamma_F$. . . . . . . . . . . . . . . . . . . . 159

6-2 Walker's trajectory under the influence of a weak unidirectional force, computed on the basis of (6.18). The left panel shows the evolution of the walking direction $\theta(T)$. The right panel shows the walker's trajectory $(x(T), y(T))$. Calculations were based on values of $\gamma/\gamma_F = 0.9$, $\epsilon = 0.1$ and $f(T) = 1$, for which the timescale of turning $T_\theta \approx 2.4$. The walker starts with $\theta(0) = \pi/2$ and rapidly turns toward the direction of the applied force, $\theta = 0$, over the timescale $T_\theta$. . . . . . . 161

6-3 The observed dependence of the orbital radius $r_0$ and frequency $\omega$ on the rotation rate $\Omega$ for a droplet walking at speed $u_0$ in a rotating frame in the low-memory regime ($u_0 = 9.0$ mm s$^{-1}$, $\gamma/\gamma_F = 0.82$). The experimental data are those reported by Harris and Bush [38]. The dashed lines indicate the standard solutions for inertial orbits, $r_0 = R_c \equiv u_0/2\Omega$ and $\omega = \omega_c \equiv -2\Omega$. The solid lines correspond to the predictions of (6.22), which incorporate the walker's wave-induced added mass. . . . . . . . . . . . . . . . . . . . . . . . . . . . 163

6-4 The observed dependence of the orbital radius $r_0$ and frequency $\omega$ on the spring constant $k$ for a droplet walking at speed $u_0$ under a spring force $\boldsymbol{F} = -k\boldsymbol{x}$ in the low-memory regime ($u_0 = 12.2$ mm s$^{-1}$, $\gamma/\gamma_F = 0.9$). The experimental data are from Perrard et al. [52]. The dashed lines indicate the standard solutions $r_0 = R_h \equiv u_0/\sqrt{k/m}$ and $\omega = \omega_h \equiv \sqrt{k/m}$. The solid lines correspond to the predictions of (6.23), which incorporate the walker's wave-induced added mass. . . 165

# List of Tables

2.1 The variables appearing in the trajectory equations (2.16) and (2.18). 42

3.1 The variables appearing in the trajectory equations (3.7) and (3.8). . 65

# Chapter 1

# Introduction

The complex interaction between fluids and macroscopic objects is the source of a number of fascinating physical phenomena. For instance, a flag flapping in the wind exhibits many interesting behaviors and constitutes a highly nonlinear dynamical system, as the flag both perturbs and responds to the external flow [57]. Some insects are able to propel themselves across a fluid surface by virtue of the vortices they generate [40]. The motivation for this thesis is a remarkable set of experiments conducted by Yves Couder and his group, who showed that the interaction between bouncing droplets and their self-generated waves can give rise to a complex dynamics reminiscent of phenomena at the quantum scale.

In their experiments, Couder and his coworkers placed a droplet of silicone oil on the surface of a vertically vibrating bath of the same fluid [17, 54, 18]. Provided the forcing acceleration of the bath is sufficiently large, the droplet may propel itself across the fluid surface while bouncing vertically [54, 46]. The walking droplet, or walker, is propelled because it lands on the sloping surface of its own wave field. While the waves eventually decay due to the influence of fluid viscosity, they may persist for hundreds of bounces. The walker's trajectory is thus determined by the waves generated in its past. Experiments conducted over the past eight years have revealed that the resulting "path memory" is responsible for the complex walker dynamics and their quantum-like behavior [29]. Multiple walkers may interact with each other through their wave fields and thus exhibit interesting coherent behavior

[26, 28, 55, 30].

In a landmark experiment, Couder and Fort [15, 16] showed that a single walker may be deflected by a gap between two submerged barriers, the statistics of the deflection angle resembling the single-slit diffraction pattern of photons [60] and electrons [20]. They also demonstrated a walker may tunnel across regions of relatively low fluid depth in which walking is forbidden, thus exhibiting an analogue of quantum tunneling [27]. More recently, experiments conducted at MIT revealed that the chaotic dynamics of a walker placed in a confined geometry exhibits a coherent statistical behavior reflecting the cavity's dominant eigenmode [39], the system thus being reminiscent of electrons in a quantum corral [19].

Fort et al. [32] and Harris and Bush [38] demonstrated that the circular orbits of walkers in a rotating frame may be quantized in radius, thus exhibiting a hydrodynamic analogue of an electron's Landau levels from quantum mechanics. Similarly, Perrard et al. [52] demonstrated that the orbits of walkers in a harmonic potential are doubly quantized in both mean radius and angular momentum. In both systems, in the limit of large vibrational forcing, the walker dynamics becomes chaotic but exhibits a coherent wave-like statistics. An experimental study of the walker dynamics in a rotating frame showed that, when the walker dynamics becomes chaotic, its statistical behavior reflects the persistent influence of the quantized circular orbits [38].

These experiments represent the first macroscopic realization of a pilot-wave system of the form proposed by Louis de Broglie as a realist model of quantum mechanics [1, 21, 22]. He posited that a quantum particle is propelled by a guiding pilot wave generated by the particle's internal vibration. While such a physical picture provides a rational explanation for a number of quantum oddities, including single-particle diffraction [2, p. 112], the physical origin of the pilot wave was left unspecified, and self-consistent equations of motion for both particle and pilot wave were not developed. In 1952, David Bohm proposed an alternate pilot-wave theory [4, 5], in which particles are guided by a pilot-wave but do not generate it. Since the guiding wave is postulated to be a solution to Schrödinger's equation, Bohmian mechanics is mathematically equivalent to standard quantum theory. However, it was criticized as being overly complicated, as the underlying pilot-wave and particle trajectories could not be observed directly.

The pilot-wave description was eventually superseded by the Copenhagen Interpretation as the standard view, which denied the existence of well-defined trajectories for quantum particles and instead propounded the idea of an intrinsically probabilistic universe. There has since been a proliferation of competing quantum interpretations, from the Many Worlds Interpretation to the Transactional Interpretation, few of which attempt to restore realism and determinism to quantum theory [10]. The scientific community has recently given considerable attention to the bouncing droplet system, as it could provide inspiration for a deterministic quantum theory [35, 9, 10].

Investigations of the bouncing droplet system have been largely experimental. While theoretical models for the walker dynamics have developed, they have contained a number of free parameters and so have been unable to quantitatively reproduce experimental data [54, 32, 58]. The first comprehensive model of the system was developed by Moláček and Bush [45, 46], who performed a detailed analysis of the bouncing dynamics and underlying wave field. In this thesis, we build upon their work in order to develop and analyze an integro-differential trajectory equation for the drop's horizontal motion. We show that the model can be treated analytically in some cases and efficiently simulated in others. Our work has allowed us to rationalize certain observed features of the walker system, and has led to a number of predictions that have since been confirmed in laboratory experiments. The trajectory equation requires two constants: the drag coefficient on the drop, and the amplitude of the standing wave generated by a single drop impact, both of which were derived by Moláček and Bush [46].

This thesis is motivated by the following three questions:

- How can we develop an analytically tractable description of the walking droplets?
- How does orbital quantization arise in a rotating frame?
- How does wave-like statistical behavior emerge in the limit of large vibrational

forcing?

In Chapter 2, we present the results of a theoretical investigation of droplets bouncing on a vertically vibrating fluid bath. An integro-differential equation describing the horizontal motion of the drop is developed by approximating the drop as a continuous moving source of standing waves. Our model indicates that, as the forcing acceleration is increased, the bouncing state destabilizes into steady horizontal motion along a straight line, a walking state, via a supercritical pitchfork bifurcation. Predictions for the dependence of the walking threshold and drop speed on the system parameters compare favorably with experimental data. By considering the stability of the walking state, we show that the drop is stable to perturbations in the direction of motion and neutrally stable to lateral perturbations. Chapter 2 appears as published in: A trajectory equation for walking droplets: hydrodynamic pilot-wave theory, Oza, A. U., Rosales, R. R. and Bush, J. W. M., *Journal of Fluid Mechanics*, **737**, 552–570 (2013) [48].

In Chapter 3, we present the results of a theoretical investigation of droplets walking on a rotating vibrating fluid bath. The droplet's trajectory is described in terms of a similar integro-differential equation that incorporates the influence of its propulsive wave force. Predictions for the dependence of the orbital radius on the bath's rotation rate compare favorably with experimental data and capture the progression from continuous to quantized orbits as the vibrational acceleration is increased. The orbital quantization is rationalized by assessing the stability of the orbital solutions, and may be understood as resulting directly from the dynamic constraint imposed on the drop by its monochromatic guiding wave. The stability analysis also predicts the existence of wobbling orbital states reported in recent experiments, and the absence of stable orbits in the limit of large vibrational forcing. Chapter 3 appears as published in: Pilot-wave dynamics in a rotating frame: on the emergence of orbital quantization, Oza, A. U., Harris, D. M., Rosales, R. R. and Bush, J. W. M., *Journal of Fluid Mechanics*, **744**, 404–429 (2014) [50].

In Chapter 4, we present the results of a numerical investigation of droplets walking on a rotating vibrating fluid bath. The integro-differential trajectory equation is simulated numerically in various parameter regimes. As the forcing acceleration is progressively increased, stable circular orbits give way to wobbling orbits, which are succeeded in turn by instabilities of the orbital center characterized by steady drifting then discrete leaping. In the limit of large vibrational forcing, the walker's trajectory becomes chaotic, but its statistical behavior reflects the influence of the unstable orbital solutions. The study results in a complete regime diagram that summarizes the dependence of the walker's behavior on the system parameters. Our predictions compare favorably to the experimental observations of Harris and Bush [38]. Chapter 4 is currently under view at *Physics of Fluids*: Pilot-wave dynamics in a rotating frame: exotic orbits, Oza, A. U., Wind-Willassen, Ø., Harris, D. M., Rosales, R.R. and Bush, J. W. M. [51].

In Chapter 5, we present a mathematical treatment of the walker dynamics in a rotating frame. We show that, above a critical value of the forcing acceleration and below a critical value of the rotation rate, the bouncing state may destabilize into a circular orbital solution. We explore the mathematical properties of orbital solutions to the trajectory equation, and assess their stability by recasting the trajectory equation as an initial value problem. We demonstrate that circular orbits are stable in the asymptotic limits of low forcing acceleration, and both small and large orbital radius. We then construct a numerical method for assessing orbital stability outside of these asymptotic regimes, which involves finding the roots of an analytic function. We conclude by presenting a stability diagram for orbital solutions and comparing our results with the experimental data reported by Harris and Bush [38]. The results of the mathematical framework presented in this chapter were used in Chapter 3 to gain physical insight into the walker's orbital dynamics. Chapter 5 is to be submitted as: Orbital stability in hydrodynamic pilot-wave theory, Oza, A. U., Bush, J. W. M. and Rosales, R. R., *SIAM Journal on Applied Mathematics* [49].

In Chapter 6, we examine the dependence of the walker mass and momentum on its velocity. Doing so indicates that, if the walker accelerates slowly relative to the wave decay rate, its dynamics may be described in terms of the mechanics of a particle with a speed-dependent mass and a nonlinear drag force that drives it towards a fixed speed. Drawing an analogy with relativistic mechanics, we define a hydrodynamic boost factor for these walking droplets. This perspective provides new rationale for the anomalous orbital radii reported in recent studies. Chapter 6 appears as submitted: The wave-induced added mass of walking droplets, Bush, J. W. M., Oza, A. U. and Moláček, J., *Journal of Fluid Mechanics* [11].

In Chapter 7, we conclude the study of our integro-differential equation of motion. We discuss the advantages and shortcomings of our model, and propose future research directions.

# Chapter 2

# Integro-differential trajectory equation for walking droplets

## 2.1 Introduction

In this chapter, we develop an integro-differential trajectory equation for the walking droplets with a view to gaining insight into their subtle dynamics. We consider a fluid bath vibrating vertically with acceleration $\gamma \cos \omega t$, where $\omega = 2\pi f$. When $\gamma$ is increased beyond $\gamma_F$, the fluid surface goes unstable to a standing field of Faraday waves. The critical acceleration $\gamma_F$, the Faraday threshold, depends on the fluid viscosity, depth, and surface tension. At the onset of instability, subharmonic waves with frequency $\omega/2$ emerge; at higher $\gamma$, higher harmonics of frequency $n\omega/2$ (for integer $n$) can arise. This system was first examined by Faraday [31], and has since been explored by many others [24, 43, 47]. A theoretical description of Faraday waves was developed for inviscid fluids by Benjamin and Ursell [3] and extended to the case of viscous fluids by Kumar [41]. In this thesis, we will only consider the regime $\gamma < \gamma_F$, for which the flat interface would be stable if not for the presence of a drop.

---

This chapter appears as published in: A trajectory equation for walking droplets: hydrodynamic pilot-wave theory, Oza, A. U., Rosales, R. R. and Bush, J. W. M, *Journal of Fluid Mechanics*, **737**, 552–570 (2013) [48].

Walker [62] demonstrated that droplets can be made to bounce indefinitely at frequency $\omega$ on the surface of a vertically vibrating bath of the same fluid. When $\gamma < \gamma_B$, $\gamma_B$ being the bouncing threshold, the drop simply coalesces with the fluid bath; however, for $\gamma > \gamma_B$, coalescence is precluded by the sustenance of an air layer between the drop and bath for the duration of the drop impact [17]. The first theoretical examinations of the bouncing process are presented by Couder et al. [17], Gilet et al. [33, 34] and Terwagne et al. [61], and built upon by Moláček and Bush [45]. In summary, the drop bounces provided its contact time is less than the time required for the air layer between the drop and bath to drain to a critical thickness of approximately 50 nm, at which coalescence is initiated. Moláček and Bush [45] developed a complete theoretical description of the bouncing drop dynamics that provides rationale for all reported periodic and chaotic bouncing states [65].

Protière et al. [54] demonstrate that, as $\gamma$ is increased beyond $\gamma_B$, the drop undergoes a sequence of bifurcations. First, the drop undergoes a period-doubling transition, after which it bounces at frequency $\omega/2$. Its bouncing frequency is then commensurate with the frequency of the least stable Faraday mode, which is thus locally excited through the resonant interaction between drop and bath. For $\gamma > \gamma_W > \gamma_B$, $\gamma_W$ being the walking threshold, the waves generated by the drop destabilize the bouncing state. If the drop is perturbed in some direction, it lands on a sloping interface and so receives a horizontal force on impact that propels it forward. In certain parameter regimes delineated by Protière et al. [54] and Eddi et al. [25] and rationalized by Moláček and Bush [46], the resulting walking state is quite robust: the drop can walk steadily and stably at a uniform horizontal velocity while bouncing vertically at frequency $\omega/2$. Images of a walking drop and its associated wave field are shown in figure 2-1.

The coupled vertical and horizontal dynamics of a walking drop were considered by Moláček and Bush [46], who elucidated the walker's rich and complex behavior. For example, the walker may switch between various vertical bouncing modes that coexist for identical system parameters, or walk in an irregular fashion while bouncing chaotically [65]. The authors also highlight the importance of the walker's phase

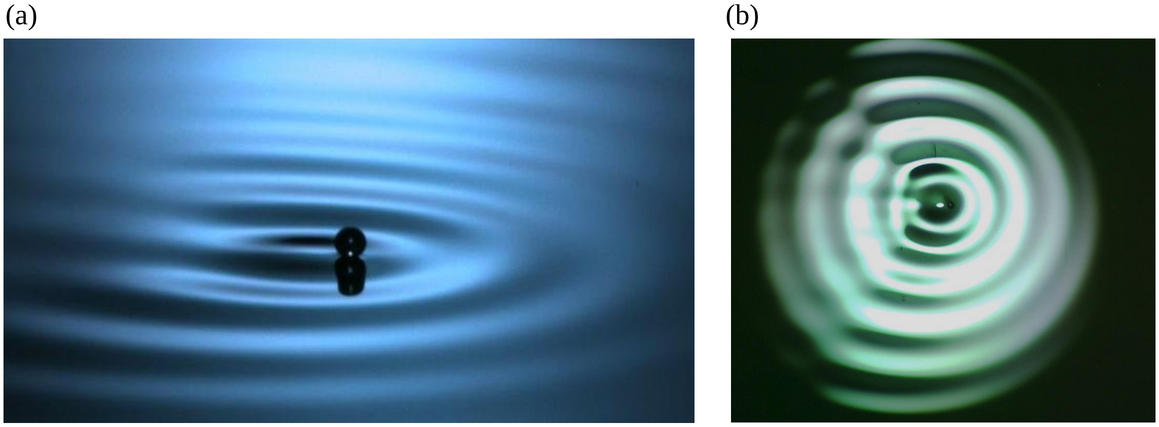

Figure 2-1: A walker, a millimetric droplet, self-propagates on a vibrating fluid bath through an interaction with its own wave field. (a) Oblique view. (b) Top view.

with respect to the bath. The amplitude of the waves generated by the drop has a complicated dependence on system parameters through the walker's phase, owing to the coupling between the horizontal and vertical motion. For the sake of simplicity, we here consider the special case of "resonant walkers," for which the drop is in a period-doubled bouncing mode, so its vertical motion is precisely synchronized with the underlying wave. We thus neglect the coupling between the horizontal and vertical motion and average over the vertical motion, which allows us to construct and study a trajectory equation for the walker's horizontal motion.

As the propulsive wave force on the walking drop depends on the location of its prior impacts, and so on the walker's past, Fort et al. [32] and Eddi et al. [29] introduced the concept of path-memory. The quantum mechanical features arise only in the high path-memory regime, close to the Faraday threshold, where the waves generated by the walker decay slowly in time and so strongly affect the drop's dynamics [15, 32, 39]. In this regime, the drop's trajectory is most strongly influenced by its history, which is effectively stored in the wave field. The goal of the current study is to provide insight into these experiments by developing a trajectory equation for the walkers that illustrates the influence of path-memory on their dynamics.

Protière et al. [54] postulate the following trajectory equation for the horizontal position $x_p$ of the drop, in the absence of barriers and external forces:

$$m\ddot{x}_p + D\dot{x}_p \;=\; F^b \sin\left(\frac{2\pi\dot{x}_p}{V_F}\right), \tag{2.1}$$

where $m$ is the drop mass, $F^b$ the effective force due to bouncing on an inclined surface, $D$ the viscous damping coefficient, and $V_F$ the phase velocity of the Faraday waves. Equation (2.1) is derived by time-averaging the horizontal force on the drop over a single bouncing period, and it correctly predicts a supercritical pitchfork bifurcation to a walking state; however, we will see that it only includes the effect of a single previous bounce on the drop's trajectory. A similar approach was taken by Shirokoff [58] in his theoretical description of walkers in confined geometries. Both papers attempt to model the path-memory through the coefficient $F^b$. We here develop an improved trajectory equation that explicitly models the system's path-memory by incorporating the drop's entire history.

In §2.2, we derive an integro-differential equation of motion for the drop by adopting the results presented by Moláček and Bush [46]. The equation indicates that the bouncing state destabilizes at a critical acceleration $\gamma$ into straight-line walking, as shown in §2.3. We present an exact formula for the walking speed and compare it to experimental data in §2.4, where we also explore the dependence of the guiding wave field on the walking speed. The stability of the walking solution is analyzed in §2.5. Future directions and applications of the model are discussed in §2.6.

## 2.2 Integro-differential equation of motion

Consider a drop of mass $m$ and radius $R$ in the presence of a gravitational acceleration $g$ walking on the surface of a vertically vibrating fluid bath of surface tension $\sigma$, density $\rho$, dynamic viscosity $\mu$, kinematic viscosity $\nu$, and mean depth $H$. Let $\boldsymbol{x}_p(t) = (x_p(t), y_p(t))$ denote the horizontal position of the drop at time $t$. We assume that the drop is a resonant walker in the period-doubled regime, so the vertical motion is periodic with period $T_F = 4\pi/\omega$. The force balance in the horizontal direction yields the equation of motion

$$m\ddot{\boldsymbol{x}}_p + D\dot{\boldsymbol{x}}_p = -\overline{F(t)\boldsymbol{\nabla}\mathcal{H}(\boldsymbol{x}_p, t)}, \tag{2.2}$$

where all terms represent time-averages over the bouncing period $T_F$, and $F(t)$ is the vertical force on the drop [46]. The drop moves in response to both propulsive and drag forces. The propulsive force is the wave force imparted by the sloping bath surface during impact. We express the total fluid depth as $H + \mathcal{H}(\boldsymbol{x}, t)$, where we assume the perturbation height $\mathcal{H}(\boldsymbol{x}, t) \ll H$ to be small. The horizontal component of the propulsive force may then be approximated by $-F(t)\boldsymbol{\nabla}\mathcal{H}(\boldsymbol{x}_p, t)$. The drop motion is opposed by a drag force $-D\dot{\boldsymbol{x}}_p$, where the time-averaged drag coefficient $D$ can be written in terms of the system parameters as [46]

$$D \;=\; Cmg\sqrt{\frac{\rho R}{\sigma}} + 6\pi\mu_a R\left(1 + \frac{\pi\rho_a g R}{6\mu_a\omega}\right), \tag{2.3}$$

where $\mu_a = 1.84 \times 10^{-5}$ kg m$^{-1}$ s$^{-1}$ and $\rho_a = 1.2$ kg m$^{-3}$ are the dynamic viscosity and density of air, and $C$ is the nondimensional drag coefficient. In (2.3), the first term arises from the transfer of momentum from the drop to the bath during impact, and the second from the aerodynamic drag exerted on the droplet during flight. We note that $C$ actually depends weakly on the system parameters, and $0.17 \le C \le 0.33$ over the parameter range of interest for walkers [46]. For our purposes, it suffices to treat $C = 0.17$ as a constant, a value consistent with the experimental data for $\nu = 20$ cS, $f = 80$ Hz and $\nu = 50$ cS, $f = 50$ Hz [46].

To determine an expression for the interface deflection $\mathcal{H}(\boldsymbol{x}, t)$, we first consider the interface deflection $h_n(\boldsymbol{x}, t)$ generated by the single bounce of a drop at time $t_n$ and position $\boldsymbol{x}_p(t_n)$. We assume the fluid container to be sufficiently large that we may neglect the influence of boundaries. When the drop hits the surface, it emits a traveling transient wave that is typically an order of magnitude faster than the walker [29]. We neglect this wave in our model because it does not interact with the drop on subsequent bounces. In the wake of the transient wave, a field of standing waves persists on the interface. Eddi et al. [29] numerically model this standing wave field as

$$h_n(\boldsymbol{x}, t) = \sum_{m=1}^{\infty} a_m(t - t_n) J_0 \left( k_m \left| \boldsymbol{x} - \boldsymbol{x}_p(t_n) \right| \right), \tag{2.4}$$

where $J_0$ is a Bessel function of the first kind, the wavenumbers $k_m$ satisfy the relation $J_0(k_m r_0) = 0$, and $r_0$ is a numerical cutoff parameter. The time-dependence is prescribed by the functions $a_m(t)$, which satisfy the equation

$$\ddot{a}_m + 2\nu_{phen} k_m^2 \dot{a}_m + a_m \left( g - \gamma \cos \omega t + \frac{\sigma k_m^2}{\rho} \right) k_m \tanh k_m H = 0, \tag{2.5}$$

where $\nu_{phen} \gtrsim \nu$ is the phenomenological kinematic viscosity of the fluid, chosen to match the observed Faraday threshold.

Rather than summing over infinitely many modes, we here make some simplifying assumptions that make the model more tractable. Since $\gamma < \gamma_F$, the fluid surface is stable, so all disturbances decay in time. The slowest decaying mode is the subharmonic Faraday wave with temporal decay time $T_F M_e$, where $M_e$ is the nondimensional memory parameter

$$M_e = M_e(\gamma) \equiv \frac{T_d}{T_F \left(1 - \gamma/\gamma_F\right)} \tag{2.6}$$

[29], and $T_d$ is the temporal decay time in the absence of forcing [46]. In the short-path-memory limit, just above the walking threshold $M_e \gtrsim M_e(\gamma_W)$, the standing waves generated by the drop decay relatively quickly, so the droplet motion depends only on its recent past. In the long-path-memory limit, close to the Faraday threshold $M_e \gg M_e(\gamma_W)$, the standing waves are long-lived, so the walker is more strongly influenced by its history. Both $T_d$ and $\gamma_F$ can be calculated numerically for different fluids and forcing frequencies [41, 46].

The Faraday wave oscillates in time with frequency $\omega/2$, and its dominant wavenumber $k_F$ can be calculated numerically [41, 46] or approximated as the solution to the standard water-wave dispersion relation:

$$\left(\frac{\omega}{2}\right)^2 = \left(gk + \frac{\sigma k^3}{\rho}\right)\tanh kH. \tag{2.7}$$

In the experiments, the Faraday wavenumber is typically $k_F \approx 1.25\text{mm}^{-1}$, which corresponds to a Faraday wavelength of $\lambda_F \approx 5\text{mm}$. Fort et al. [32] approximate the Faraday wave generated by a single bounce as

$$h_n(\boldsymbol{x}, t) = \frac{A}{|\boldsymbol{x} - \boldsymbol{x}_p(t_n)|}\cos\left(k_F|\boldsymbol{x} - \boldsymbol{x}_p(t_n)| + \phi\right)\mathrm{e}^{-|\boldsymbol{x}-\boldsymbol{x}_p(t_n)|/\delta}\mathrm{e}^{-(t-t_n)/(T_F M_e)}, \tag{2.8}$$

where the parameters $A$ and $\delta$ are determined experimentally, and $\phi$ is a free parameter. While this model allows them to reproduce many of the experimental results and provides an adequate description in the far field $k_F|\boldsymbol{x} - \boldsymbol{x}_p(t_n)| \gg 1$, it contains a troubling singularity at $\boldsymbol{x} = \boldsymbol{x}_p(t_n)$, and the phase-shifted cosine does not accurately describe the spatial dependence of the Faraday wave near the drop.

Following Moláček and Bush [46], we approximate the wave as a radial Bessel function of the first kind $J_0$ with a single dominant wavenumber $k_F$. This gives the interface height after a single bounce at time $t = t_n$:

$$h_n(\boldsymbol{x}, t) = \tilde{A} J_0(k_F|\boldsymbol{x} - \boldsymbol{x}_p(t_n)|)\mathrm{e}^{-(t-t_n)/(T_F M_e)}\cos\frac{\omega(t - t_n)}{2} H(t - t_n) \tag{2.9}$$

where $H(t)$ is the Heaviside step function. The amplitude $\tilde{A}$ can be expressed in terms of the system parameters as

$$\tilde{A} = \sqrt{\frac{2}{\pi}}\frac{k_F R}{3k_F^2 R^2 + \mathcal{B}o}\frac{R k_F^2 \nu_{\text{eff}}^{1/2}}{\sigma\sqrt{T_F}} m g T_F \sin\frac{\Phi}{2}, \quad \mathcal{B}o = \frac{\rho g R^2}{\sigma}, \quad \nu_{\text{eff}} = \nu D_\mu \tag{2.10}$$

where $\mathcal{B}o$ is the Bond number, $\nu_{\text{eff}}$ is the effective kinematic viscosity, and $\Phi$ is the mean phase of the wave during the contact time [46]. The coefficient $D_\mu$ is defined as [53, 46]

$$D_\mu = -\frac{r_1 + r_2}{2ar_1r_2}, \quad \text{where} \quad a = \frac{\mathcal{O}h(Rk_F)^{3/2}}{\left[\mathcal{B}o + (Rk_F)^2\right]^{1/2}}, \quad \mathcal{O}h = \frac{\mu}{\sqrt{\rho\sigma R}}, \tag{2.11}$$

and $r_1$ and $r_2$ are the roots with largest real part of the polynomial

$$p(x;a) = x^4 + 8ax^3 + (2 + 24a^2)x^2 + a(8 + 16a^2)x + 1 + 8a^2. \tag{2.12}$$

We note that the formula for the interface height (2.9) with amplitude $\tilde{A}$ is an approximation to that given by Moláček and Bush [46]. Here we neglect the $t^{-1/2}$ temporal decay of the waves, as the decay rate is dominated by the exponential $\mathrm{e}^{-(t-t_n)/(T_F M_e)}$. The algebraic factor $t^{-1/2}$ is only valid for $t > T_F$ and makes the governing equation analytically intractable; thus, for the sake of simplicity we replace it by the constant $T_F^{-1/2}$. In addition, we neglect the possibility of multiple vertical bouncing modes for a single forcing acceleration $\gamma$ [46, 65]. For a particular bouncing mode, the impact phase $\Phi$ depends in general on $\mu$, $R$, and $\gamma$; however, it depends only weakly on $\gamma$ in the high-memory limit of interest, so we treat it as a constant for a given drop.

We assume the surface waves to be linear, so that we can apply the superposition principle. Thus, the interface height $\mathcal{H}(\boldsymbol{x}, t)$ may be expressed as the sum of the individual waves $h_n(\boldsymbol{x}, t)$ generated by previous bounces at prior times $t_n = nT_F$:

$$\mathcal{H}(\boldsymbol{x}, t) = \sum_n h_n(\boldsymbol{x}, t) = \sum_{n=-\infty}^{\lfloor t/T_F \rfloor} \tilde{A} J_0(k_F|\boldsymbol{x} - \boldsymbol{x}_p(nT_F)|)\mathrm{e}^{-(t-nT_F)/(T_F M_e)} \cos\frac{\omega t}{2}. \tag{2.13}$$

As shown in Moláček and Bush [46], since the drop's bouncing period $T_F$ is equal to the period of the surface waves, we may replace $\overline{F(t)\boldsymbol{\nabla}\mathcal{H}(\boldsymbol{x}_p, t)}$ by $mg\boldsymbol{\nabla}h(\boldsymbol{x}_p, t)$, where

$$h(\boldsymbol{x}, t) = \sum_{n=-\infty}^{\lfloor t/T_F \rfloor} A J_0(k_F|\boldsymbol{x} - \boldsymbol{x}_p(nT_F)|)\mathrm{e}^{-(t-nT_F)/(T_F M_e)}, \quad A = \tilde{A}\cos\frac{\Phi}{2}. \tag{2.14}$$

We call this the *stroboscopic approximation* since, by averaging over the vertical dynamics, we eliminate consideration of the drop's vertical motion. The drop motion is thus effectively "strobed" at the bouncing frequency.

Substituting (2.14) into (2.2) yields a delay-differential equation of motion for the drop, which is quite difficult to study analytically. We thus approximate the sum in (2.14) by the integral:

$$h(\boldsymbol{x},t) = \frac{AC_f}{T_F}\int_{-\infty}^{t} J_0(k_F|\boldsymbol{x}-\boldsymbol{x}_p(s)|)\mathrm{e}^{-(t-s)/(T_F M_e)}\,\mathrm{d}s, \tag{2.15}$$

where $C_f = \frac{1}{M_e\left(\mathrm{e}^{1/M_e}-1\right)}$. This approximation is valid provided the timescale of horizontal motion $T_H = \frac{\lambda_F}{|\dot{\boldsymbol{x}}_p|}$ is much greater than the timescale $T_F$ of vertical motion, that is, $T_F \ll T_H$, as is the case for walkers. The resonant walker is thus approximated as a continuous moving source of standing waves, and is viewed as sweeping across the fluid interface. We make the additional approximation that $C_f = 1$, since walkers typically arise when $M_e \gg 1$.

Substituting (2.15) into (2.2), we obtain an integro-differential equation of motion:

$$m\ddot{\boldsymbol{x}}_p + D\dot{\boldsymbol{x}}_p = \frac{F}{T_F}\int_{-\infty}^{t} \frac{J_1(k_F|\boldsymbol{x}_p(t)-\boldsymbol{x}_p(s)|)}{|\boldsymbol{x}_p(t)-\boldsymbol{x}_p(s)|}(\boldsymbol{x}_p(t)-\boldsymbol{x}_p(s))\mathrm{e}^{-(t-s)/(T_F M_e)}\,\mathrm{d}s, \tag{2.16}$$

where $F = mgAk_F$. Note that the equation of motion at time $t$ depends on the drop's entire trajectory prior to that time, on its path memory as stored in the wave field. Nevertheless, the dominant contribution of the integral comes from its recent past, specifically $t - s \sim O(T_F M_e)$. The drop is thus influenced by more of its history as stored in its wavefield $h(\boldsymbol{x},t)$ as its path-memory $M_e$ increases. The term on the right-hand side of (2.16) is thus referred to alternatively as the *wave force* or *memory force*.

The trajectory equation (2.16) is markedly different from that developed by Protière et al. [54], equation (2.1), which assumes that $h(x,t) = A\cos(k_F(x-x_p(t)))$. By using $V_F = \frac{\omega/2}{k_F}$ and $\dot{x}_p(t)T_F \approx x_p(t) - x_p(t-T_F)$ for $T_F \ll 1$, one can obtain from (2.1) the delay-differential equation

$$m\ddot{x}_p + D\dot{x}_p = F^b \sin\left(k_F(x_p(t) - x_p(t-T_F))\right). \tag{2.17}$$

Unlike (2.16), which incorporates the drop's entire history, the model (2.17) only includes the influence of a single prior impact. It can thus be valid only in the short-

| **Dimensional variables** | **Definition** |
|---|---|
| $\boldsymbol{x}_p$ | drop position |
| $m$ | drop mass |
| $D$ | drag coefficient |
| $g$ | gravitational acceleration |
| $\mathcal{H}(\boldsymbol{x}, t)$ | interface deflection |
| $T_F$ | Faraday period |
| $\tilde{A}$ | amplitude of single surface wave |
| $k_F$ | Faraday wavenumber |
| $T_d$ | decay time of waves without forcing |
| $\gamma$ | forcing acceleration |
| $\gamma_F$ | Faraday instability threshold |
| $F = mgAk_F$ | memory force coefficient |
| **Nondimensional variables** | |
| $M_e = \frac{T_d}{T_F(1-\gamma/\gamma_F)}$ | memory |
| $\kappa = \frac{m}{DT_F M_e}$ | nondimensional mass |
| $\beta = \frac{F k_F T_F M_e^2}{D}$ | nondimensional memory force coefficient |

Table 2.1: The variables appearing in the trajectory equations (2.16) and (2.18).

path-memory limit for walkers just beyond the walking threshold $M_e \gtrsim M_e(\gamma_W)$, and is incapable of capturing the drop dynamics at large $M_e$.

The variables appearing in (2.16) are listed in table 2.1. Note that the model has no free parameters: formulae for $D$ and $F$ are derived by Moláček and Bush [46], and $T_d$ and $\gamma_F$ can be determined numerically [41, 46]. We proceed by demonstrating that the trajectory equation (2.16) captures certain key aspects of the walker dynamics.

## 2.3 Bouncing to walking

Note that $\boldsymbol{x}_p \equiv$ constant is a solution to equation (2.16) that represents a stationary bouncing state. In this section, we will study the stability of this bouncing state, and demonstrate that increasing $M_e$ causes it to destabilize into a walking state, in which the drop moves along a straight line at constant horizontal velocity.

We first nondimensionalize (2.16). We choose $\lambda_F$ and $T_F M_e$ as our natural length- and timescales, respectively, and so nondimensionalize via $\boldsymbol{x}' = k_F \boldsymbol{x}$ and

$t' = t/(T_F M_e)$. Substituting into (2.16) and dropping primes, we deduce the nondimensional equation of motion:

$$\kappa \ddot{\boldsymbol{x}}_p + \dot{\boldsymbol{x}}_p = \beta \int_{-\infty}^{t} \frac{J_1(|\boldsymbol{x}_p(t) - \boldsymbol{x}_p(s)|)}{|\boldsymbol{x}_p(t) - \boldsymbol{x}_p(s)|} (\boldsymbol{x}_p(t) - \boldsymbol{x}_p(s)) \mathrm{e}^{-(t-s)} \, \mathrm{d}s, \tag{2.18}$$

where $\kappa = m/DT_F M_e$ and $\beta = F k_F T_F M_e^2/D$ represent, respectively, the nondimensional mass and memory force coefficient.

We now examine the stability of the bouncing solution $\boldsymbol{x}_p \equiv$ constant. By linearizing (2.18) around this solution, $\boldsymbol{x}_p = \text{constant} + \delta\boldsymbol{x}$, we deduce

$$\kappa \delta\ddot{\boldsymbol{x}} + \delta\dot{\boldsymbol{x}} = \frac{\beta}{2} \int_{-\infty}^{t} [\delta\boldsymbol{x}(t) - \delta\boldsymbol{x}(s)] \mathrm{e}^{-(t-s)} \, \mathrm{d}s, \tag{2.19}$$

where we have used the fact that $J_1'(0) = 1/2$. This equation can be expressed as a system of ordinary differential equations by introducing the variable

$$\delta\boldsymbol{X}(t) = \int_{-\infty}^{t} \delta\boldsymbol{x}(s) \mathrm{e}^{-(t-s)} \, \mathrm{d}s. \tag{2.20}$$

Solutions to (2.19) thus form a subset of solutions to the system of equations

$$\kappa \ddot{\boldsymbol{x}} + \dot{\boldsymbol{x}} = \frac{\beta}{2}(\boldsymbol{x} - \boldsymbol{X}), \quad \dot{\boldsymbol{X}} = \boldsymbol{x} - \boldsymbol{X}. \tag{2.21}$$

Since the $x$- and $y$-directions are uncoupled in this equation, we can simply consider the $x$-direction, the calculation for the $y$-direction being identical. Letting $\dot{x} = u$, we obtain the system

$$\frac{\mathrm{d}}{\mathrm{d}t} \begin{bmatrix} x \\ u \\ X \end{bmatrix} = \begin{bmatrix} 0 & 1 & 0 \\ \frac{\beta}{2\kappa} & -\frac{1}{\kappa} & -\frac{\beta}{2\kappa} \\ 1 & 0 & -1 \end{bmatrix} \begin{bmatrix} x \\ u \\ X \end{bmatrix}. \tag{2.22}$$

The characteristic polynomial $p(s)$ of this matrix is

$$p(s) = -s \left[ s^2 + \left(1 + \frac{1}{\kappa}\right) s + \frac{1}{\kappa}\left(1 - \frac{\beta}{2}\right) \right]. \tag{2.23}$$

The $s = 0$ solution simply indicates that the bouncing state is invariant under translation, so we neglect it. Since $\kappa > 0$, the stability of the bouncing state is controlled by the constant term in $p(s)$. Specifically, the bouncing state is stable for $\beta < 2$ and unstable for $\beta > 2$. In terms of the dimensional variables, the bouncing state is stable for forcing accelerations $\gamma < \gamma_W$, where

$$\gamma_W = \gamma_F \left( 1 - \sqrt{\frac{F k_F T_d^2}{2 D T_F}} \right) \tag{2.24}$$

defines the walking threshold. Note that $\gamma_W$ increases with the drop drag coefficient $D$ but decreases with the memory force coefficient $F$. Note also that the memory force increases with $\gamma$, as indicated by the definition of the memory parameter $M_e$ (2.6). The bouncing state is thus stabilized by the drag force $-D\dot{\boldsymbol{x}}_p$ (which opposes the drop's motion) and destabilized by the memory force. Once the latter is sufficiently large to overcome the former, the bouncing solution is destabilized, and the drop begins to walk. As we will see in the next section, for $\gamma \gtrsim \gamma_W$ the drop begins to walk at a constant velocity.

### 2.3.1 Stuart-Landau equation for the walking velocity

The experiments of Protière et al. [54] demonstrate that, in a parameter regime delineated by Moláček and Bush [46], there is a supercritical pitchfork bifurcation at $\gamma = \gamma_W$ (corresponding to $\beta = 2$), where the bouncing state destabilizes into straight-line walking. We proceed by demonstrating that this behavior is captured by our integro-differential equation of motion, by analyzing the drop motion near the bifurcation. Assume that $\gamma$ is slightly above the walking threshold, so $\beta = 2 + \alpha\epsilon^2$ for $0 < \epsilon \ll 1$ and $\alpha > 0$. Near the bifurcation, we can write an asymptotic expansion for $\boldsymbol{x}_p(t)$:

$$\boldsymbol{x}_p(t) = \frac{1}{\epsilon}\boldsymbol{a}(T) + \epsilon^3 \boldsymbol{x}_1(t, T) + O(\epsilon^5), \tag{2.25}$$

where $T = \epsilon^2 t$ is the slow time scale. In what follows, we use the notation $\dot{f} = \frac{\partial f}{\partial t}$, $f' = \frac{\partial f}{\partial T}$. We substitute this expansion into the nondimensional equation of motion (2.18) and extract the leading order terms. Due to the exponential term, the dominant contribution in the integral comes from the region $t - s = O(1)$. Note that

$$\boldsymbol{x}_p(t) - \boldsymbol{x}_p(s) \;=\; \epsilon \boldsymbol{a}'(T)(t-s) + \epsilon^3\left(-\frac{1}{2}\boldsymbol{a}''(T)(t-s)^2 + \boldsymbol{x}_1(t,T) - \boldsymbol{x}_1(s,S)\right) + O(\epsilon^5), \tag{2.26}$$

where $S = \epsilon^2 s$, which gives

$$\begin{aligned} |\boldsymbol{x}_p(t) - \boldsymbol{x}_p(s)|^2 \;=\;& \epsilon^2 |\boldsymbol{a}'(T)|^2 (t-s)^2 + \epsilon^4\left[-(\boldsymbol{a}'(T)\cdot\boldsymbol{a}''(T))(t-s)^3\right. \\ &\left. + 2(t-s)\boldsymbol{a}'(T)\cdot(\boldsymbol{x}_1(t,T) - \boldsymbol{x}_1(s,S))\right] + O(\epsilon^6). \end{aligned} \tag{2.27}$$

Therefore

$$\frac{J_1(|\boldsymbol{x}_p(t) - \boldsymbol{x}_p(s)|)}{|\boldsymbol{x}_p(t) - \boldsymbol{x}_p(s)|} = \frac{1}{2} - \frac{\epsilon^2}{16}|\boldsymbol{a}'(T)|^2(t-s)^2 + O(\epsilon^4), \tag{2.28}$$

where we use the fact that $J_1^{(3)}(0) = -3/8$. The leading order terms in the integral are thus

$$\begin{aligned} &\int_{-\infty}^{t} \frac{J_1(|\boldsymbol{x}_p(t) - \boldsymbol{x}_p(s)|)}{|\boldsymbol{x}_p(t) - \boldsymbol{x}_p(s)|}\left(\boldsymbol{x}_p(t) - \boldsymbol{x}_p(s)\right)\mathrm{e}^{-(t-s)}\,\mathrm{d}s = \frac{\epsilon}{2}\int_{-\infty}^{t} \boldsymbol{a}'(T)(t-s)\mathrm{e}^{-(t-s)}\,\mathrm{d}s \\ &+\frac{\epsilon^3}{2}\int_{-\infty}^{t}\left[-\frac{1}{2}\boldsymbol{a}''(t-s)^2 - \frac{1}{8}\boldsymbol{a}'(T)|\boldsymbol{a}'(T)|^2(t-s)^3 + (\boldsymbol{x}_1(t,T) - \boldsymbol{x}_1(s,S))\right]\mathrm{e}^{-(t-s)}\,\mathrm{d}s + O(\epsilon^5). \end{aligned} \tag{2.29}$$

By changing variables $t - s = z$, we can evaluate some of these integrals. Then using $\beta = 2 + \alpha\epsilon^2$, the equation of motion (2.18) reduces, at leading order, to

$$\kappa\ddot{\boldsymbol{x}}_1 + \dot{\boldsymbol{x}}_1 - \boldsymbol{x}_1 + \int_{-\infty}^{t} \boldsymbol{x}_1(s,S)\mathrm{e}^{-(t-s)}\,\mathrm{d}s = \frac{\alpha}{2}\boldsymbol{a}' - (1+\kappa)\boldsymbol{a}'' - \frac{3}{4}\boldsymbol{a}'|\boldsymbol{a}'|^2. \tag{2.30}$$

Introducing the variable $\boldsymbol{X}_1 = \int_{-\infty}^{t} \boldsymbol{x}_1(s,S)\mathrm{e}^{-(t-s)}\,\mathrm{d}s$, (2.30) can be written in the form

$$\frac{\partial}{\partial t}\left(\kappa\dot{\boldsymbol{x}}_1 + \boldsymbol{x}_1 - \boldsymbol{X}_1\right) \;=\; \frac{\alpha}{2}\boldsymbol{a}' - (1+\kappa)\boldsymbol{a}'' - \frac{3}{4}\boldsymbol{a}'|\boldsymbol{a}'|^2. \tag{2.31}$$

In order for the expansion (2.25) to be consistent, $\boldsymbol{x}_1$ should be a bounded function of $t$, which implies that the right side of (2.31) must vanish. This yields an evolution equation for the leading-order velocity $\boldsymbol{a}'$:

$$\boldsymbol{a}'' = \frac{1}{2(1+\kappa)}\boldsymbol{a}'\left(\alpha - \frac{3}{2}|\boldsymbol{a}'|^2\right). \tag{2.32}$$

This is a Stuart-Landau equation [59] for the velocity $\boldsymbol{a}'$. We write $\boldsymbol{a}' = u(T)(\cos\theta(T), \sin\theta(T))$, where $u(T)$ is the speed of the drop and $\theta(T)$ determines its direction, so that (2.32) becomes

$$u' = \frac{1}{2(1+\kappa)}u\left(\alpha - \frac{3}{2}u^2\right), \quad \theta' = 0. \tag{2.33}$$

We thus confirm that the speed $u$ undergoes a supercritical pitchfork bifurcation when $\beta = 2$. For $\beta < 2$, only the bouncing state $u = 0$ is stable; for $\beta \gtrsim 2$, the walking solution is stable and has speed $u \approx \sqrt{2\alpha/3}$. The equation $\theta' = 0$ implies that, as expected, the drop walks in a straight line in an arbitrary direction: since the wave field produced at each bounce is rotationally symmetric, there is no preferred direction of motion at the onset of instability. Therefore, in the experiment, the initial direction of motion is presumably governed by random or imposed perturbations.

## 2.4 Straight-line walking

The drop's bouncing state becomes unstable for $\gamma > \gamma_W$, beyond which it walks in a straight line at constant speed. We proceed by deriving a formula for the walking speed of the resonant walker, and showing that the resonant walking state is stable for all $\gamma_W < \gamma < \gamma_F$.

### 2.4.1 Walking speed

To find a formula for the walking speed $u$, we substitute the solution $\boldsymbol{x}_p = (ut, 0)$ into (2.18):

$$u = \beta \int_0^\infty J_1(uz)\mathrm{e}^{-z}\,\mathrm{d}z.$$

The integral can be evaluated exactly, yielding

$$u = \frac{\beta}{u}\left(1 - \frac{1}{\sqrt{1+u^2}}\right) \quad \Rightarrow \quad u = \frac{1}{\sqrt{2}}\left(-1 + 2\beta - \sqrt{1+4\beta}\right)^{1/2}. \tag{2.34}$$

Note that this solution is real-valued only for $\beta > 2$, in accord with the stability analysis of the bouncing state presented in §2.3. In terms of dimensional variables, the walking speed $u$ has the form

$$u = \frac{1}{k_F T_d}\left(1 - \frac{\gamma}{\gamma_F}\right)\left\{\frac{1}{4}\left[-1 + \sqrt{1 + 8\left(\frac{\gamma_F - \gamma_W}{\gamma_F - \gamma}\right)^2}\,\right]^2 - 1\right\}^{1/2}. \tag{2.35}$$

Figure 2-2 shows a comparison between the experimental dependence of the walking speed $u$ on the forcing acceleration $\gamma$, as reported by Moláček and Bush [46], and that predicted by (2.35). The equation for the resonant walking speed adequately describes the experimental data, provided that the impact phase $\Phi$ is judiciously chosen. Note that the impact phases chosen in figure 2-2 are roughly consistent with those reported in Moláček and Bush [46]; however, they are also known to depend weakly on $\gamma$ [46].

It follows from (2.35) that $u$ is a monotonically increasing function of $\gamma$. As $\gamma$ increases, so does the propulsive memory force and the drop speed. Moreover, one can show that in the infinite memory limit $M_e \to \infty$ (or $\gamma \to \gamma_F$), the walking speed remains bounded, and assumes the value

$$\lim_{\gamma \to \gamma_F} u = \frac{\sqrt{2}}{k_F T_d}\left(1 - \frac{\gamma_W}{\gamma_F}\right) = \sqrt{\frac{F}{D k_F T_F}} = \sqrt{\frac{mgA}{D T_F}}. \tag{2.36}$$

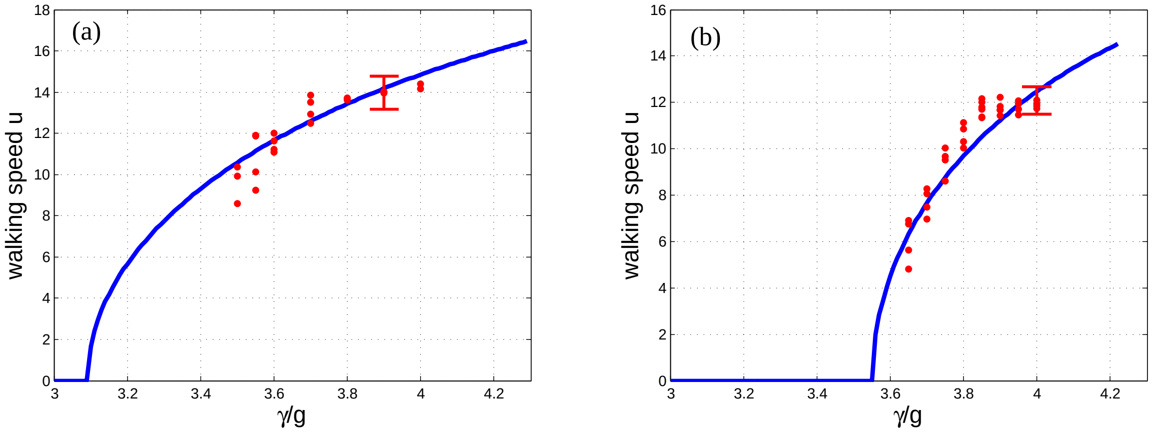

Figure 2-2: Plot of the walking speed $u$ (in mm/s) as a function of the nondimensional forcing acceleration $\gamma/g$. The dots represent experimental data from Moláček and Bush [46], and the curves are obtained from our model prediction (2.35) for a resonant walker using (a) $\nu = 20$ cS, $f = 80$ Hz, $\rho = 949$ kg m$^{-3}$, $\sigma = 20.6 \times 10^{-3}$ N m$^{-1}$, $\gamma_F = 4.3g$, $T_d = 1/54.9$ s, $R = 0.40$ mm, and (b) $\nu = 50$ cS, $f = 50$ Hz, $\rho = 960$ kg m$^{-3}$, $\sigma = 20.8 \times 10^{-3}$ N m$^{-1}$, $\gamma_F = 4.23g$, $T_d = 1/57.9$ s, $R = 0.39$ mm. The single free parameter in our stroboscopic model is the phase of impact, chosen here to be (a) $\sin\Phi = 0.3$ and (b) $\sin\Phi = 0.35$. Characteristic error bars are shown.

In reality, the amplitude $A$ depends on $\gamma$ through the phase $\Phi$, so $u$ does not necessarily increase with $\gamma$. Moreoever, Moláček and Bush [46] demonstrate that the walking speed curves such as those in figure 2-2 may have discontinuities resulting from the drop switching between different walking modes as $\gamma$ increases, an effect that could not be captured with our resonant walker model.

### 2.4.2 Wave field

Plots of the strobed wave field (2.15) generated by a walker moving according to $\boldsymbol{x}_p = (ut, 0)$ are shown in figure 2-3 for low, medium, and high memory. The plots are shown in the drop's reference frame, with the drop at the origin and moving to the right. Note that, as the memory increases, the interference effects of the standing waves become more pronounced. The computed wave fields are qualitatively similar to those reported by Eddi et al. [29]. Profiles of the wave fields along the drop's direction of motion are also shown. Note that the drop is effectively surfing on the crest of its guiding wave. If $\gamma < \gamma_W$, the drop bounces in place ($u = 0$) on the crest of the wave. As the memory increases, the drop slides further down the wave in the direction of increasing gradient, and so moves faster. The horizontal force $-mg\boldsymbol{\nabla} h(\boldsymbol{x}_p, t)$ imparted by the inclined surface precisely balances the drag $-D\dot{\boldsymbol{x}}_p$, allowing the drop to move at a constant speed.

## 2.5 Stability analysis

Steady rectilinear walking is observed in the laboratory for a substantial range of parameter space [54, 46], indicating that the walking state is relatively robust. We proceed by showing that the walking solution $\boldsymbol{x}_p = (ut, 0)$ is stable to perturbations in the direction of motion, and neutrally stable to transverse perturbations. To this end, we consider the dimensionless equation

$$\kappa\ddot{\boldsymbol{x}}_p + \dot{\boldsymbol{x}}_p = \beta \int_{-\infty}^{t} \frac{J_1(|\boldsymbol{x}_p(t) - \boldsymbol{x}_p(s)|)}{|\boldsymbol{x}_p(t) - \boldsymbol{x}_p(s)|}(\boldsymbol{x}_p(t) - \boldsymbol{x}_p(s))\mathrm{e}^{-(t-s)}\,\mathrm{d}s + \epsilon\boldsymbol{\delta}(t), \qquad (2.37)$$

where $\boldsymbol{\delta}(t) = (\delta_x(t), \delta_y(t))$ is the Dirac delta function and $0 < \epsilon \ll 1$. The delta function represents a small perturbation to the drop at time $t = 0$, the response to which we examine in what follows.

We write the drop trajectory as $\boldsymbol{x}_p(t) = \boldsymbol{x}_0(t) + \epsilon\boldsymbol{x}_1(t)H(t)$ where $\boldsymbol{x}_0(t) = (ut, 0)$ is the walking solution defined by (2.34) and $\boldsymbol{x}_1(t) = (x_1(t), y_1(t))$ is the perturbation. We impose the conditions $\boldsymbol{x}_1(0) = (0, 0)$ and $\dot{\boldsymbol{x}}_1(0) = (1/\kappa, 1/\kappa)$ to ensure that $\boldsymbol{x}_p$ is a solution of (2.37). We substitute this solution into (2.37) and retain only the $O(\epsilon)$ terms:

$$\begin{aligned} \kappa\ddot{x}_1 + \dot{x}_1 &= \beta \int_{-\infty}^{t} J_1'(u(t-s))(x_1(t) - x_1(s)H(s))\mathrm{e}^{-(t-s)}\,ds \\ \kappa\ddot{y}_1 + \dot{y}_1 &= \beta \int_{-\infty}^{t} \frac{J_1(u(t-s))}{u(t-s)}(y_1(t) - y_1(s)H(s))\mathrm{e}^{-(t-s)}\,ds. \end{aligned} \qquad (2.38)$$

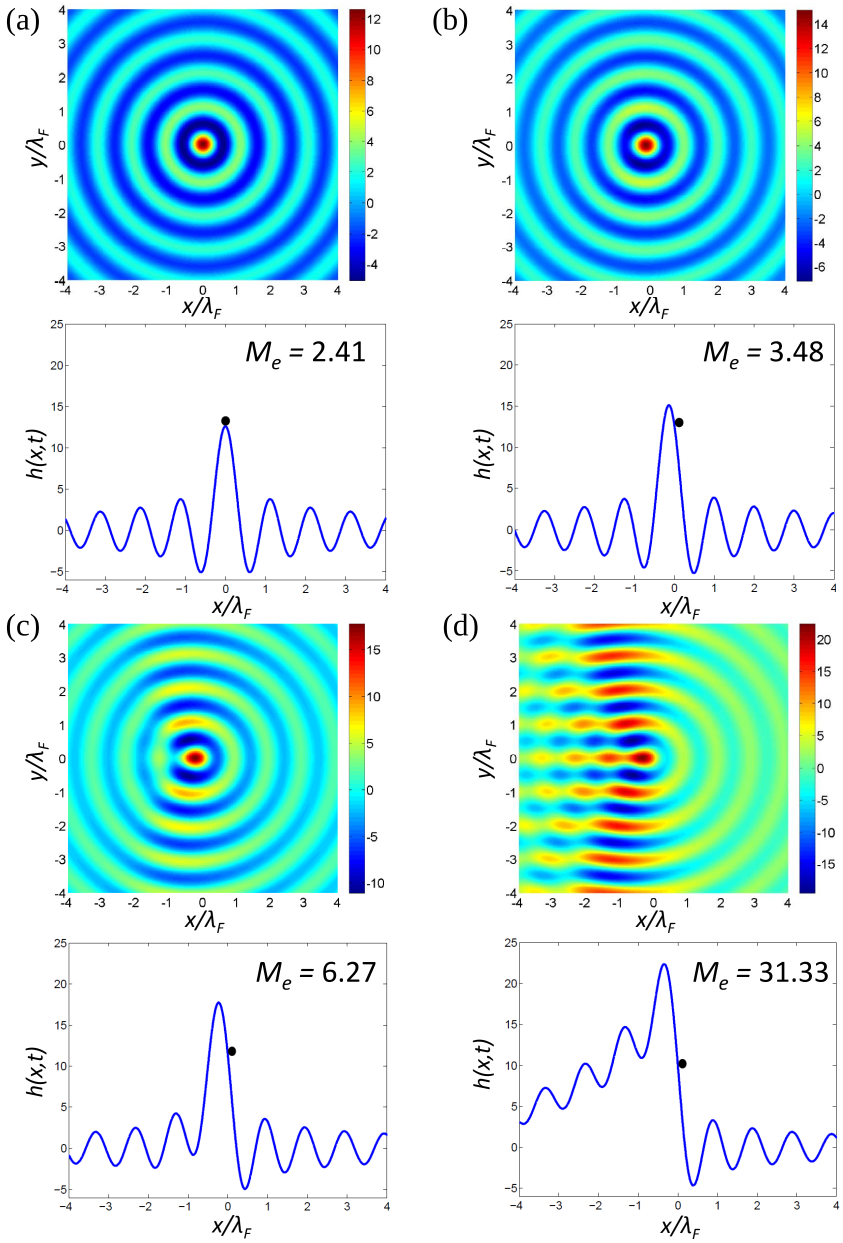

Figure 2-3: Simulated wave fields generated by (a) a stationary bouncer and (b-d) walkers for, respectively, (a) very low ($\gamma = 3.0g$), (b) low ($\gamma = 3.4g$), (c) medium ($\gamma = 3.8g$), and (d) high ($\gamma = 4.2g$) path-memory. The plots are generated using $\nu = 20$ cS, $f = 80$ Hz, $\rho = 949$ kg m$^{-3}$, $\sigma = 20.6 \times 10^{-3}$ N m$^{-1}$, $T_d = 1/54.9$ s, $R = 0.40$ mm, and $\sin\Phi = 0.3$. The walking and Faraday thresholds are $\gamma_W = 3.12g$ and $\gamma_F = 4.3g$, respectively. The wave amplitude is given in microns. Upper figures: Plot of the strobed wave field $h(\boldsymbol{x}, t)$ (2.15) accompanying the drop. The drop is located at the origin and moves to the right according to $\boldsymbol{x}_p = (ut, 0)$, where $u$ is determined by (2.35). Lower figures: Wave profiles $h(x, t)$ along the direction of motion of the walker. As the memory increases, the walker moves away from the crest towards a region with higher slope, thus moving faster.

Note that these equations can be written in the form

$$\begin{aligned}\kappa \ddot{x}_1 + \dot{x}_1 &= \beta\left[x_1 \int_0^\infty J_1'(uz)\mathrm{e}^{-z}\,\mathrm{d}z - x_1 * \left(J_1'(ut)\mathrm{e}^{-t}\right)\right]\\ \kappa \ddot{y}_1 + \dot{y}_1 &= \beta\left[y_1 \int_0^\infty \frac{J_1(uz)}{uz}\mathrm{e}^{-z}\,\mathrm{d}z - y_1 * \left(\frac{J_1(ut)}{ut}\mathrm{e}^{-t}\right)\right].\end{aligned} \tag{2.39}$$

where $f * g$ denotes the convolution of the functions $f$ and $g$. This form of the linearized equations of motion makes them particularly amenable to stability analysis, since we can now take the Laplace transform of both sides of the equations. Doing so yields algebraic equations for $X(s) = \mathcal{L}[x_1(t)]$ and $Y(s) = \mathcal{L}[y_1(t)]$, which can be readily solved. The poles of $X(s)$ and $Y(s)$ are the eigenvalues of their respective linear problems (2.39). If the poles lie in the left- or right-half of the complex plane, the walking solution $\boldsymbol{x}(t) = (ut, 0)$ is respectively stable or unstable to perturbations in the corresponding direction.

### 2.5.1 Stability to perturbations in the direction of motion

We first consider the equation for $x_1$, the perturbation along the walking direction. We take the Laplace transform of the equation and use the facts that $x_1(0) = 0$ and $\dot{x}_1(0) = 1/\kappa$, in order to deduce an equation for $X(s)$:

$$(\kappa s^2 + s)X(s) - 1 = \beta X(s)\int_0^\infty J_1'(uz)\mathrm{e}^{-z}\,\mathrm{d}z - \beta\mathcal{L}\left[J_1'(ut)\mathrm{e}^{-t}\right]X(s).$$

We now use the facts that

$$\begin{aligned}\int_0^\infty J_1'(uz)\mathrm{e}^{-z}\,\mathrm{d}z &= \frac{1}{2\sqrt{u^2+1}}\left(1 - \frac{u^2}{\left(1+\sqrt{u^2+1}\right)^2}\right) = \frac{1}{\beta}, \quad \text{and}\\ \mathcal{L}\left[J_1'(ut)\mathrm{e}^{-t}\right] &= \frac{1}{2\sqrt{u^2+(s+1)^2}}\left(1 - \frac{u^2}{\left(s+1+\sqrt{u^2+(s+1)^2}\right)^2}\right)\end{aligned}$$

in order to obtain

$$X(s) = \frac{1}{\kappa s^2 + s - 1 + \frac{\beta}{2\sqrt{u^2+(s+1)^2}}\left(1 - \frac{u^2}{\left(s+1+\sqrt{u^2+(s+1)^2}\right)^2}\right)}. \tag{2.40}$$

Note that the appropriate branch for the square root is defined by $\sqrt{u^2+(s+1)^2} > 0$ for $s = 0$, with branch cuts $s = -1 \pm \mathrm{i}\xi$ for $\xi \geq u$. For simplicity, we write $X(s)$ in terms of the variable $\tilde{s} = s + 1$. After some algebra, we can rewrite (2.40) as

$$X(s) = \frac{\sqrt{u^2+\tilde{s}^2}\left(\tilde{s} + \sqrt{u^2+\tilde{s}^2}\right)}{\kappa(\tilde{s}-1)^2(u^2+\tilde{s}^2) + \beta\tilde{s} + (\tilde{s}-2)(u^2+\tilde{s}^2) + \left[\tilde{s}(\tilde{s}-2) + \kappa\tilde{s}(\tilde{s}-1)^2\right]\sqrt{u^2+\tilde{s}^2}}.$$

The poles of $X(s)$ are the zeros of its denominator, which solve the equation

$$[\tilde{s}(\tilde{s}-2) + \kappa\tilde{s}(\tilde{s}-1)^2]\sqrt{u^2+\tilde{s}^2} = (2-\tilde{s})(\tilde{s}^2+u^2) - \beta\tilde{s} - \kappa(\tilde{s}-1)^2(\tilde{s}^2+u^2). \tag{2.41}$$

Squaring both sides of this equation and some further algebra yields

$$[u^2(\tilde{s}-2+\kappa(\tilde{s}-1)^2)^2 + 2\beta\tilde{s}(\tilde{s}-2+\kappa(\tilde{s}-1)^2)](\tilde{s}^2+u^2) = -\beta^2\tilde{s}^2. \tag{2.42}$$

Note that the poles of $X(s)$ are a subset of the solutions to this equation, since squaring both sides may introduce spurious solutions; that is, some solutions of (2.42) may not solve (2.41). Therefore, the poles of $X(s)$ are a subset of the roots of the sixth-degree polynomial $p_x(\tilde{s}) = \sum_{k=0}^{6} c_k \tilde{s}^k$, with coefficients

$$\begin{aligned}
c_0 &= 4u^4\left(1 - \kappa + \frac{\kappa^2}{4}\right), \quad c_1 = -u^2\left[4\beta + 4u^2 + \kappa(-2\beta - 10u^2 + 4\kappa u^2)\right] \\
c_2 &= \beta^2 + 4u^2 + 2\beta u^2 + u^4 + \kappa\left(-4u^2 - 4\beta u^2 - 8u^4 + \kappa u^2 + 6\kappa u^4\right) \\
c_3 &= -\left[4\beta + 4u^2 + \kappa\left(-2\beta - 10u^2 - 2\beta u^2 - 2u^4 + 4\kappa u^2 + 4\kappa u^4\right)\right] \\
c_4 &= u^2 + 2\beta + \kappa\left(-4\beta - 8u^2 + 6\kappa u^2 + \kappa u^4\right) \\
c_5 &= \kappa(2\beta + 2u^2 - 4\kappa u^2), \quad c_6 = \kappa^2 u^2.
\end{aligned} \tag{2.43}$$

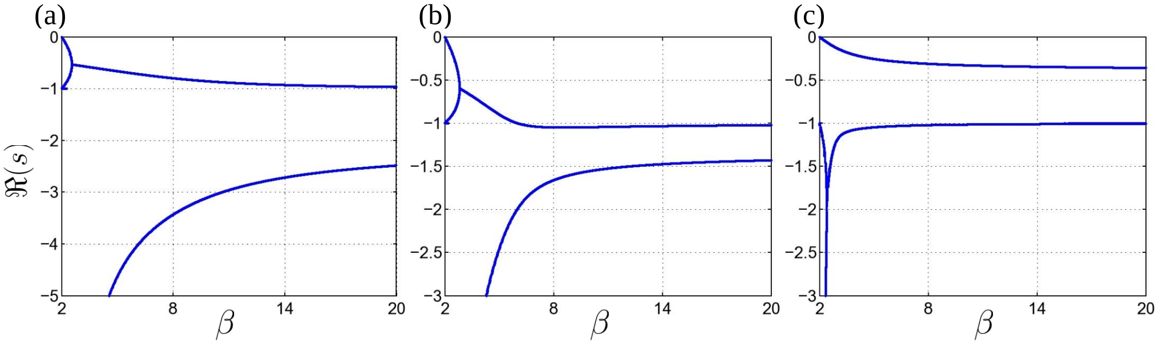

Figure 2-4: Plot of the real part of the (nonzero) poles of $\mathcal{L}[x_1(t)] = X(s)$ as a function of $\beta$, for (a) $\kappa = 1$, (b) $\kappa = 1.5$, and (c) $\kappa = 5$, respectively. $X(s)$ is the Laplace transform of the perturbation $x_1$, $\beta$ the nondimensional memory force coefficient, and $\kappa$ the nondimensional mass of the drop (see table 2.1). The three plots are representative of the ranges $0 \leq \kappa \lesssim 1.3$, $1.3 \lesssim \kappa < 2$, and $\kappa > 2$, respectively. Note that merging of the curves indicates the existence of two complex conjugate poles with the same real part.

It can be verified that $p_x(1) = 0$, so $X(s)$ has a pole at the origin $s = 0$. This reflects the fact that the equation of motion (2.18) is invariant under translation in the $x$-direction; that is, if $\boldsymbol{x}_p(t)$ is a solution to (2.18), so is $\boldsymbol{x}_p(t) + (\tilde{x}, 0)$, where $\tilde{x}$ is a constant. Since $\mathcal{L}[\tilde{x}] = \tilde{x}/s$, the translational invariance of the solution implies that $X(s)$ has a pole at $s = 0$ (or $\tilde{s} = 1$). Therefore, the nontrivial poles of $X(s)$ are a subset of the roots of the fifth-degree polynomial $q_x(\tilde{s}) = \sum_{k=0}^{5} d_k \tilde{s}^k$, where $p_x(\tilde{s}) = (\tilde{s} - 1)q_x(\tilde{s})$. The coefficients of $q_x(\tilde{s})$ are related to the coefficients of $p_x(\tilde{s})$ by the formula $d_i = -\sum_{k=0}^{i} c_k$.

We find the roots of $q_x(\tilde{s})$ numerically with Matlab for a range of parameters $\beta$ and $\kappa$, and only select the roots that are actually poles of $X(s)$, that is, solutions of (2.41). The real parts of the roots are plotted in figure 2-4 for a range of parameters $\kappa$ and $\beta > 2$. Note that the poles of $X(s)$ always have negative real part, indicating that the walking solution $\boldsymbol{x}_p(t) = (ut, 0)$ is stable to perturbations along the direction of motion. That is, if the drop is infinitesimally perturbed along its walking direction, it will converge exponentially quickly to a solution of the form $\boldsymbol{x}_p(t) = (ut + \epsilon\tilde{x}, 0)$. It will thus continue to walk along the same line at the same constant speed.

### 2.5.2 Stability to lateral perturbations

We now show that the walking drop with trajectory $\boldsymbol{x}_p(t) = (ut, 0)$ is neutrally stable to perturbations in the $y$-direction, that is, perpendicular to its direction of motion. Taking the Laplace transform of the $y_1$-equation in (2.39) and using the fact that $y_1(0) = 0$ and $\dot{y}_1(0) = 1/\kappa$ yields an algebraic equation for $Y(s) = \mathcal{L}[y_1(t)]$:

$$(\kappa s^2 + s)Y(s) - 1 = \beta Y(s) \int_0^\infty \frac{J_1(uz)}{uz} \mathrm{e}^{-z}\, \mathrm{d}z - \beta \mathcal{L}\left[\frac{J_1(ut)}{ut}\mathrm{e}^{-t}\right] Y(s). \qquad (2.44)$$

We now use the facts that

$$\begin{aligned} \int_0^\infty \frac{J_1(uz)}{uz}\mathrm{e}^{-z}\, \mathrm{d}z &= \frac{1}{u^2}\left(-1 + \sqrt{1+u^2}\right) = \frac{1}{\beta}\sqrt{1+u^2}, \quad \text{and} \\ \mathcal{L}\left[\frac{J_1(ut)}{ut}\mathrm{e}^{-t}\right] &= \frac{1}{u}\left(-\frac{s+1}{u} + \sqrt{1 + \left(\frac{s+1}{u}\right)^2}\right), \end{aligned}$$

to deduce the solution

$$Y(s) = \frac{1}{\kappa s^2 + s - \sqrt{1+u^2} + \frac{\beta}{u^2}\left(-(s+1) + \sqrt{u^2 + (s+1)^2}\right)}, \qquad (2.45)$$

where the square root has the same meaning as before. Using (2.34) for the walking speed $u$ allows us to rewrite $Y(s)$ as

$$Y(s) = \frac{-1 + 2\beta - \beta^*}{\kappa s^2 \left(-1 + 2\beta - \beta^*\right) - s\left(1 + \beta^*\right) + \beta\left(1 - \beta^*\right) + \beta\sqrt{\left(-1+\beta^*\right)^2 + 4s(s+2)}},$$

where $\beta^* = \sqrt{1 + 4\beta}$. As previously, the poles of $Y(s)$ are the zeros of its denominator, which are solutions to

$$\beta\sqrt{\left(-1+\beta^*\right)^2 + 4s(s+2)} = \beta\left(\beta^* - 1\right) + s\left(1+\beta^*\right) - \kappa s^2\left(-1 + 2\beta - \beta^*\right). \quad (2.46)$$

Squaring both sides of this equation and subsequent algebra yields

$$s^2(1+2\beta+\beta^*) = \kappa^2 s^4 \left(-1+2\beta-\beta^*\right) - 2\kappa s^3 \left(1+\beta^*\right) - 2\kappa s^2 \beta \left(-1+\beta^*\right). \quad (2.47)$$

Therefore, the poles of $Y(s)$ are a subset of the roots of the polynomial $p_Y(s) = s^2(c_0 + c_1 s + c_2 s^2)$, with coefficients

$$\begin{aligned} c_0 &= -\left[2\kappa\beta\left(-1+\beta^*\right) + 1 + 2\beta + \beta^*\right] \\ c_1 &= -2\kappa\left(1+\beta^*\right), \quad c_2 = \kappa^2\left(-1+2\beta-\beta^*\right). \end{aligned} \quad (2.48)$$

Note that $p_Y(s)$ has a double zero at the origin $s = 0$, as well as the two roots of $c_0+c_1s+c_2s^2$. However, one can show numerically that these roots do not solve (2.46), and hence they are not poles of $Y(s)$. As a result, $Y(s)$ has only a double pole at the origin, so the drop is neutrally stable with respect to perturbations perpendicular to the direction of motion.

Since the equation of motion (2.18) is invariant under translation in the $y$-direction, we expect a pole at the origin. The double pole, which arises from the rotational invariance of the problem, indicates that the perturbation $y_1$ grows linearly in time, rather than exponentially. Physically, this indicates that the drop can change direction when perturbed perpendicular to its walking direction. Note that the waves emitted by the drop have radial symmetry, and that the drop is effectively surfing on the central crest of its pilot wave field (figure 2-3). Hence, there is no force to stabilize the drop to lateral perturbations, so its direction of motion can be readily altered. However, once so perturbed, it will simply walk at a constant speed in the new direction.

## 2.6 Discussion

We have developed and analyzed an integro-differential trajectory equation to describe the horizontal motion of a droplet walking in resonance on a vibrating fluid bath. The equation was developed by approximating the resonant walker as a continuous moving source of standing waves. The resulting theoretical model makes predictions that are consistent with many of the experimental results reported by Protière et al. [54] and Moláček and Bush [46]. Specifically, it predicts that the bouncing state becomes unstable at a critical value of the memory parameter $M_e$ consistent with that observed experimentally. By deriving a Stuart-Landau equation for the motion of the drop near this critical value, we have shown that the bouncing state destabilizes into straight-line walking $\boldsymbol{x}_p = (ut, 0)$ via a supercritical pitchfork bifurcation. The trajectory equation also yields an analytical expression (2.35) for the dependence of the walking speed $u$ on the forcing acceleration $\gamma$ that compares favorably with the experimental results reported by Moláček and Bush [46].

We have also analyzed the stability of the resonant walking state. By demonstrating that the walker is stable to perturbations in the direction of motion, we have provided new rationale for the robustness of the resonant walking state. By demonstrating that the walker is neutrally stable to perturbations perpendicular to the direction of motion, we provide evidence that the dynamics may be chaotic in more complicated geometries. In the presence of boundaries, the walkers are easily diverted; indeed, steady rectilinear walking is rarely observed in confined geometries [39], as the wave field is complicated by reflections from the boundaries. The drop trajectory is then extremely sensitive to its initial conditions, which may result in chaotic dynamics. Rationalizing how the coherent statistical behavior [15, 39] emerges from the underlying complex nonlinear dynamics is a subject of ongoing research.

It is worth stressing that the stroboscopic approximation assumes *a priori* that the droplet and accompanying wave are in a state of perfect resonance. While this resonance assumption greatly simplifies the mathematical analysis, the model does not consider the detailed coupling between the horizontal and vertical drop motion, an important aspect of the dynamics that one expects to have significant bearing on the stability characteristics of the walkers. In particular, the model fails to capture the experimental observations that the walking state is sometimes unstable for sufficiently small or large drops [46, 65], that large drops can undergo a subcritical transition to walking [54], and that the walking speed of some drops is a non-monotonic or even discontinuous function of the forcing acceleration, owing to the switching between two resonant bouncing modes [46].

Another limitation of the trajectory equation (2.18) is that it only applies in free space; that is, the fluid bath must be large compared to the damping length of the Faraday and transient wavefields, so that the boundaries and reflected waves can be safely neglected. Specifically, the Bessel-function approximation (2.9) for the standing wave field generated by a single bounce will no longer be valid if the drop is near a submerged barrier or the container boundary. As many of the interesting quantum analogues such as tunneling [27], diffraction and interference [15] occur in the presence of submerged barriers, the incorporation of boundary effects into the pilot-wave model developed herein will be the subject of future work.

While analyzing the stability of resonant straight-line walking is informative, the real value of the trajectory equation will be in elucidating certain aspects of the walkers' quantum-like behavior. In Chapter 3, we will show that our trajectory equation can be simply extended to include a Coriolis force, allowing us to elucidate the orbital quantization reported by Fort et al. [32] and to predict qualitatively new phenomena [38, 50]. Our model can incorporate central force fields in a similar fashion, thus allowing us to analyze the hydrodynamic analogue of the quantum harmonic oscillator, which is currently being explored in the laboratory of Yves Couder [52].

# Chapter 3

# Pilot-wave dynamics in a rotating frame

## 3.1 Introduction

In this chapter, we consider the behavior of walkers on a circular bath of radius $R_b$ rotating with angular frequency $\mathbf{\Omega} = \Omega\hat{\boldsymbol{z}}$ about its centerline, the physical system first considered by Fort et al. [32]. The centrifugal force on the bath will induce a parabolic deformation of the fluid interface of the form

$$h_0(r) = H - \frac{\Omega^2 R_b^2}{4g} + \frac{\Omega^2}{2g} r^2, \tag{3.1}$$

where $H$ is the depth of the fluid at rest and $r$ the radial distance from the rotation axis. Classically, a ball rolling with speed $u_0$ on a rotating frictionless parabolic table of height $h_0(r)$ will execute an inertial orbit of radius $r_c$, in which the radially outwards centripetal force $mu_0^2/r_c$ is balanced by the inward Coriolis force $2m\Omega u_0$, so $r_c = u_0/2\Omega$. Fort et al. [32] found that walkers on a rotating bath likewise execute

---

This chapter appears as published in: Pilot-wave dynamics in a rotating frame: on the emergence of orbital quantization, Oza, A. U., Harris, D. M., Rosales, R. R. and Bush, J. W. M., *Journal of Fluid Mechanics*, **744**, 404–429 (2014) [50].

circular orbits, and characterized the dependence of the orbital radii on the rotation rate $\Omega$. In the low-memory limit, the walker's orbital radii decrease monotonically and continuously with $\Omega$ according to the formula $r_0 = au_0/2\Omega$, where $1.2 \leq a \leq 1.5$ is a fitting parameter. One contribution of this study will be to deduce a formula for the factor $a$ and rationalize the difference between $r_0$ and $r_c$ on physical grounds.

At high memory, Fort et al. [32] demonstrated that the behavior is markedly different: the orbital radius $r_0$ no longer varies continuously with $\Omega$, and the orbital radii become quantized. The authors also report orbital degeneracy and hysteresis, in that two different orbital radii may be observed for the same rotation rate $\Omega$, depending on whether $\Omega$ is approached from above or below. They suggest that the wave force on the drop in the high-memory regime reduces to that of a single diametrically opposed image source, proposing the governing equation

$$\frac{mu_0^2}{r_0} = \frac{2m\Omega u_0}{a} + K\cos\left(2k_F r_0\right), \tag{3.2}$$

where $K$ is a constant. The range of validity of this approximation will be made clear in §3.3.3.

As the Coriolis force $-2m\boldsymbol{\Omega} \times \dot{\boldsymbol{x}}_p$ on the walker in a rotating container is similar in form to the Lorentz force $-q\boldsymbol{B} \times \dot{\boldsymbol{x}}_p$ on an electron in a uniform magnetic field $\boldsymbol{B} = B\hat{\boldsymbol{z}}$ [64], Fort et al. [32] propose a correspondence between the quantized orbits of walkers and Landau levels. They observe that in the high-memory regime, the quantized orbital radii approximately satisfy the relation

$$\frac{r_0}{\lambda_F} = \frac{b^2}{a}\left(n + \frac{1}{2}\right), \quad \text{for integer } n \geq 0, \tag{3.3}$$

where the pre-factors $a \approx 1.5$ and $b \approx 0.89$ were deduced empirically. This is similar in form to the quantized Larmor radii $r_{\mathrm{L}}$ of an electron in a uniform magnetic field

$$\frac{r_{\mathrm{L}}}{\lambda_{\mathrm{dB}}} = \frac{1}{\pi}\left(n + \frac{1}{2}\right), \tag{3.4}$$

where $\lambda_{\mathrm{dB}}$ is the de Broglie wavelength. In §3.3.3, we shall demonstrate that the quantized orbital radii in the high-memory regime are better approximated in terms of the zeros of the Bessel function $J_0(k_F r_0)$.

Eddi et al. [30] examined two identical walkers orbiting each other in a rotating frame. The authors observe that the orbital radii of co-rotating orbits (orbits that rotate in the same sense as the fluid bath) increase with the rotation rate, while those of counter-rotating orbits decrease. The difference $\Delta r$ depends linearly on the rotation rate $\Omega$, which suggests an analogy with the Zeeman effect from quantum mechanics [14]. An analogous level-splitting phenomenon will be explored here for the case of single walkers moving on circular orbits.

Harris and Bush [38] present the results of a comprehensive experimental study of walkers in a rotating frame, in which they observed a number of effects not reported by Fort et al. [32]. In particular, they find that orbital quantization only exists for a finite range of memory $M_e$. As $M_e$ is progressively increased, the circular orbits destabilize into wobbling states, and subsequently into more complex trajectories. In the high-memory limit, the drop's trajectory becomes irregular, its radius of curvature oscillating erratically between those of accessible but unstable circular orbits. The histogram describing the trajectory's local radius of curvature thus takes a wavelike form, with peaks on the radii of the unstable orbital solutions. While the drop's trajectory is chaotic, the influence of the unstable orbital solutions is thus reflected in a wavelike statistical behavior.

The goal of the current study is to use the approach developed in Chapter 2 [48] to examine the influence of rotation on the orbital motion of drops in a rotating frame. We here introduce the orbital memory parameter $M_e^O = T_F M_e / T_O$, where $T_O \approx 2\pi r_0/u_0$ is the walker's orbital period. In the high orbital memory regime $M_e^O \gg 1$, the drop completes an orbit before the local Faraday waves have decayed, thus interacting with its own wake. Its trajectory is thus strongly influenced by its history, as is stored in the wave field. We here rationalize the emergence of quantized orbits by assessing the linear stability of circular orbits. Moreover, we rationalize the observations of Harris and Bush [38] that the circular orbits generally become unstable in the high-memory limit.

In §3.2, we derive an integro-differential equation of motion for a drop in a rotating frame by adapting the model in Chapter 2 [48]. In §3.3, we study the dependence of the orbital radius on the rotation rate in various memory regimes, showing that the theoretical predictions compare favorably to recent experimental data [38]. The stability of the orbital solutions is analyzed in §3.4, which allows us to rationalize the emergence of quantized orbits in the intermediate memory regime, and their disappearance at high memory. Future directions are discussed in §3.5.

## 3.2 Trajectory equation

Consider a drop of mass $m$ and radius $R_D$ walking on the surface of a fluid bath vibrating with vertical acceleration $\gamma \cos(2\pi f t)$. Let $\boldsymbol{x}_p(t) = (x_p(t), y_p(t))$ denote the horizontal position of the drop at time $t$. We assume the drop to be in a resonant state, so that its vertical motion is periodic with period $T_F = 2/f$. The horizontal force balance, time-averaged over the bouncing period, yields the equation of motion (Chapter 2 [48])

$$m\ddot{\boldsymbol{x}}_p + D\dot{\boldsymbol{x}}_p = -mg\boldsymbol{\nabla} h(\boldsymbol{x}_p, t), \tag{3.5}$$

where the wave field generated by the walker is given by

$$h(\boldsymbol{x}, t) = \frac{A}{T_F}\int_{-\infty}^{t} J_0\left(k_F\left|\boldsymbol{x} - \boldsymbol{x}_p(s)\right|\right) \mathrm{e}^{-(t-s)/(T_F M_e)}\, \mathrm{d}s. \tag{3.6}$$

The drop experiences a propulsive wave force $-mg\boldsymbol{\nabla} h(\boldsymbol{x}_p, t)$ and a time-averaged drag force $-D\dot{\boldsymbol{x}}_p$, where formulae for the amplitude $A$ and time-averaged drag coefficient $D$ are given in Table 3.1 [46]. The Faraday wavenumber $k_F$ is well approximated by (2.7), as the effect of the rotation on the dispersion relation is negligible in the regime of interest, $\Omega \ll f$.

If the container is forced below the walking threshold, the drop simply bounces in place, as the bouncing solution $\boldsymbol{x}_p \equiv$ constant is stable for $\gamma < \gamma_W$ (Chapter 2 [48]). When forced above the walking threshold ($\gamma > \gamma_W$), the bouncing solution destabilizes into a stable walking solution $\boldsymbol{x}_p(t) = u_0 t(\cos\theta, \sin\theta)$, where the arbitrary angle $\theta$ determines the walking direction. The balance between the wave and drag forces determines the speed $u_0$. Formulae for $\gamma_W$ and $u_0$ in terms of experimental parameters are provided in table 3.1 (Chapter 2 [48]).

In a container rotating about its vertical centerline with angular frequency $\boldsymbol{\Omega} = \Omega\hat{\boldsymbol{z}}$, there are three additional physical effects. The drop experiences a Coriolis force $-2m\boldsymbol{\Omega} \times \dot{\boldsymbol{x}}_p$ and centrifugal force $-m\boldsymbol{\Omega} \times (\boldsymbol{\Omega} \times \boldsymbol{x}_p)$, fictitious forces arising when Newton's laws are written in the rotating frame. It also experiences an additional time-averaged propulsive force $-\overline{F(t)\boldsymbol{\nabla} h_0(\boldsymbol{x}_p)}$ resulting from the parabolic deformation of the fluid interface, where $h_0(\boldsymbol{x})$ is given by (3.1) and $F(t)$ is the instantaneous vertical force acting on the drop. Since the drop's vertical motion is periodic, the average vertical force must equal the drop's weight, so $\overline{F(t)} = mg$ [46]. As the timescale of the drop's horizontal motion is much larger than the bouncing period, we may approximate $\overline{F(t)\boldsymbol{\nabla} h_0(\boldsymbol{x}_p)}$ as $m\Omega^2\boldsymbol{x}_p$, which precisely cancels the centrifugal force. We thus obtain the integro-differential equation of motion

$$\begin{aligned} m\ddot{\boldsymbol{x}}_p + D\dot{\boldsymbol{x}}_p \quad = \quad & \frac{F}{T_F}\int_{-\infty}^{t} \frac{J_1\left(k_F\left|\boldsymbol{x}_p(t) - \boldsymbol{x}_p(s)\right|\right)}{\left|\boldsymbol{x}_p(t) - \boldsymbol{x}_p(s)\right|}(\boldsymbol{x}_p(t) - \boldsymbol{x}_p(s))\mathrm{e}^{-(t-s)/(T_F M_e)}\,\mathrm{d}s \\ & -2m\boldsymbol{\Omega} \times \dot{\boldsymbol{x}}_p \end{aligned} \qquad (3.7)$$

where $F = mgAk_F$. We note that this equation simply corresponds to the pilot-wave trajectory equation (3.6) augmented by the Coriolis force.

We now nondimensionalize (3.7) by introducing the dimensionless variables $\hat{\boldsymbol{x}} = k_F\boldsymbol{x}$ and $\hat{t} = t/(T_F M_e)$. Using primes to denote differentiation with respect to $\hat{t}$, the nondimensional equation of motion becomes

$$\kappa\hat{\boldsymbol{x}}_p'' + \hat{\boldsymbol{x}}_p' = \beta\int_{-\infty}^{\hat{t}} \frac{J_1(|\hat{\boldsymbol{x}}_p(\hat{t}) - \hat{\boldsymbol{x}}_p(\hat{s})|)}{|\hat{\boldsymbol{x}}_p(\hat{t}) - \hat{\boldsymbol{x}}_p(\hat{s})|}(\hat{\boldsymbol{x}}_p(\hat{t}) - \hat{\boldsymbol{x}}_p(\hat{s}))\mathrm{e}^{-(\hat{t}-\hat{s})}\,\mathrm{d}\hat{s} - \hat{\boldsymbol{\Omega}} \times \hat{\boldsymbol{x}}_p', \qquad (3.8)$$

where $\kappa = m/DT_F M_e$, $\beta = Fk_F T_F M_e^2/D$ and $\hat{\boldsymbol{\Omega}} = 2m\boldsymbol{\Omega}/D$ represent, respectively, the nondimensional mass, wave force coefficient, and rotation rate. The variables appearing in (3.7) and (3.8) are listed in Table 3.1. Note that the model has no free parameters: formulae for $D$ and $A$ are derived by Moláček and Bush [46], and $T_d$ and $\gamma_F$ can be determined numerically [41, 46]. We proceed by examining the extent to which (3.7) describes the trajectory of a drop walking in a rotating frame.

## 3.3 Orbital solutions

We seek orbital solutions with constant radius $\hat{r}_0$ and orbital frequency $\hat{\omega}$, and so substitute $\hat{\boldsymbol{x}}_p = (\hat{r}_0 \cos\hat{\omega}\hat{t}, \hat{r}_0 \sin\hat{\omega}\hat{t})$ into (3.8). The integro-differential equation thus reduces to a system of algebraic equations that define $\hat{r}_0$ and $\hat{\omega}$ in terms of $M_e$ and $\hat{\Omega}$:

$$\begin{aligned} -\kappa\hat{r}_0\hat{\omega}^2 &= \beta\int_0^\infty J_1\left(2\hat{r}_0\sin\frac{\hat{\omega}z}{2}\right)\sin\frac{\hat{\omega}z}{2}\mathrm{e}^{-z}\,\mathrm{d}z + \hat{\Omega}\hat{r}_0\hat{\omega} \\ \hat{r}_0\hat{\omega} &= \beta\int_0^\infty J_1\left(2\hat{r}_0\sin\frac{\hat{\omega}z}{2}\right)\cos\frac{\hat{\omega}z}{2}\mathrm{e}^{-z}\,\mathrm{d}z. \end{aligned} \tag{3.9}$$

The predictions of (3.9) for the dependence of $r_0$ and $\omega$ on $\gamma/\gamma_F$ and $\Omega$ are compared with the experimental data of Harris and Bush [38] in figures 3-1 and 3-2. The theoretical predictions are generated as follows. The drop radius $R_D$ determines the drag coefficient $D$ (Table 3.1). The dimensionless forcing acceleration $\gamma/\gamma_F$ and the decay time $T_d \approx 0.0174$ s for 20.9 cSt oil [46] determine the memory parameter $M_e$ through (2.6). Using the formulae in Table 3.1, the experimentally observed free walking speed $u_0$ is used to determine the wave amplitude $A$, which in turn determines the phase $\Phi$. The values of $\sin\Phi$ so obtained are within 30% of those reported in Moláček and Bush [46]. Given the values of $D$, $A$, and $M_e$, the non-dimensional parameters $\kappa$, $\beta$, and $\Omega$ are determined through the definitions in Table 3.1. The algebraic equations (3.9) are then solved numerically, yielding the orbital radius $r_0$ and frequency $\omega$ as functions of $\hat{\Omega}$. In figures 3-1 and 3-2, stable orbital solutions are indicated in blue, while unstable ones are indicated in red and green. The rationale for the stability of the orbital solutions, and so the distinction between the blue, red and green regions, will be described in §3.4.

The wave fields $h(\boldsymbol{x}, t)$ accompanying the orbiting drop, as computed on the basis

| **Dimensional variables** | **Definition** |
|---|---|
| $\boldsymbol{x}_p$ | drop position |
| $m$ | drop mass |
| $R_D$ | drop radius |
| $\nu$ | fluid kinematic viscosity |
| $\nu_{\text{eff}}$ | effective kinematic viscosity [46] |
| $\sigma$ | fluid surface tension |
| $\rho$ | fluid density |
| $\mu_a$ | air dynamic viscosity |
| $\rho_a$ | air density |
| $f$ | forcing frequency |
| $\gamma$ | forcing acceleration |
| $\gamma_F$ | Faraday instability threshold |
| $g$ | gravitational acceleration |
| $T_F = 2/f$ | Faraday period |
| $T_d$ | decay time of waves without forcing |
| $\lambda_F$ | Faraday wavelength |
| $k_F = 2\pi/\lambda_F$ | Faraday wavenumber |
| $\Phi$ | mean phase during contact |
| $D = 0.17mg\sqrt{\frac{\rho R_D}{\sigma}} + 6\pi\mu_a R_D\left(1 + \frac{\rho_a g R_D}{12\mu_a f}\right)$ | drag coefficient |
| $A = \frac{1}{\sqrt{2\pi}}\frac{k_F R_D}{3k_F^2 R_D^2 + \mathcal{B}o}\frac{R_D k_F^2 \nu_{\text{eff}}^{1/2}}{\sigma\sqrt{T_F}} mgT_F \sin\Phi$ | amplitude of single surface wave |
| $F = mgAk_F$ | wave force coefficient |
| $\gamma_W = \gamma_F\left(1 - \sqrt{\frac{Fk_F T_d^2}{2DT_F}}\right)$ | walking threshold |
| $u_0 = \frac{1}{k_F T_d}\left(1 - \frac{\gamma}{\gamma_F}\right)\left\{\frac{1}{4}\left[-1 + \sqrt{1 + 8\left(\frac{\gamma_F - \gamma_W}{\gamma_F - \gamma}\right)^2}\right]^2 - 1\right\}^{1/2}$ | walking speed |
| $\boldsymbol{\Omega} = \Omega\hat{\boldsymbol{z}}$ | angular frequency of fluid bath |
| $r_0$ | orbital radius |
| $\omega$ | orbital frequency |
| **Nondimensional variables** | |
| $\mathcal{B}o = \frac{\rho g R_D^2}{\sigma}$ | Bond number |
| $M_e = \frac{T_d}{T_F(1-\gamma/\gamma_F)}$ | memory |
| $\kappa = \frac{m}{DT_F M_e}$ | mass |
| $\beta = \frac{Fk_F T_F M_e^2}{D}$ | wave force coefficient |
| $\hat{\boldsymbol{\Omega}} = \frac{2m\boldsymbol{\Omega}}{D}$ | bath angular frequency |
| $\hat{r}_0 = k_F r_0$ | orbital radius |
| $\hat{\omega} = \omega T_F M_e$ | orbital frequency |
| $M_e^O = \frac{\hat{\omega}}{2\pi}$ | orbital memory |

Table 3.1: The variables appearing in the trajectory equations (3.7) and (3.8).

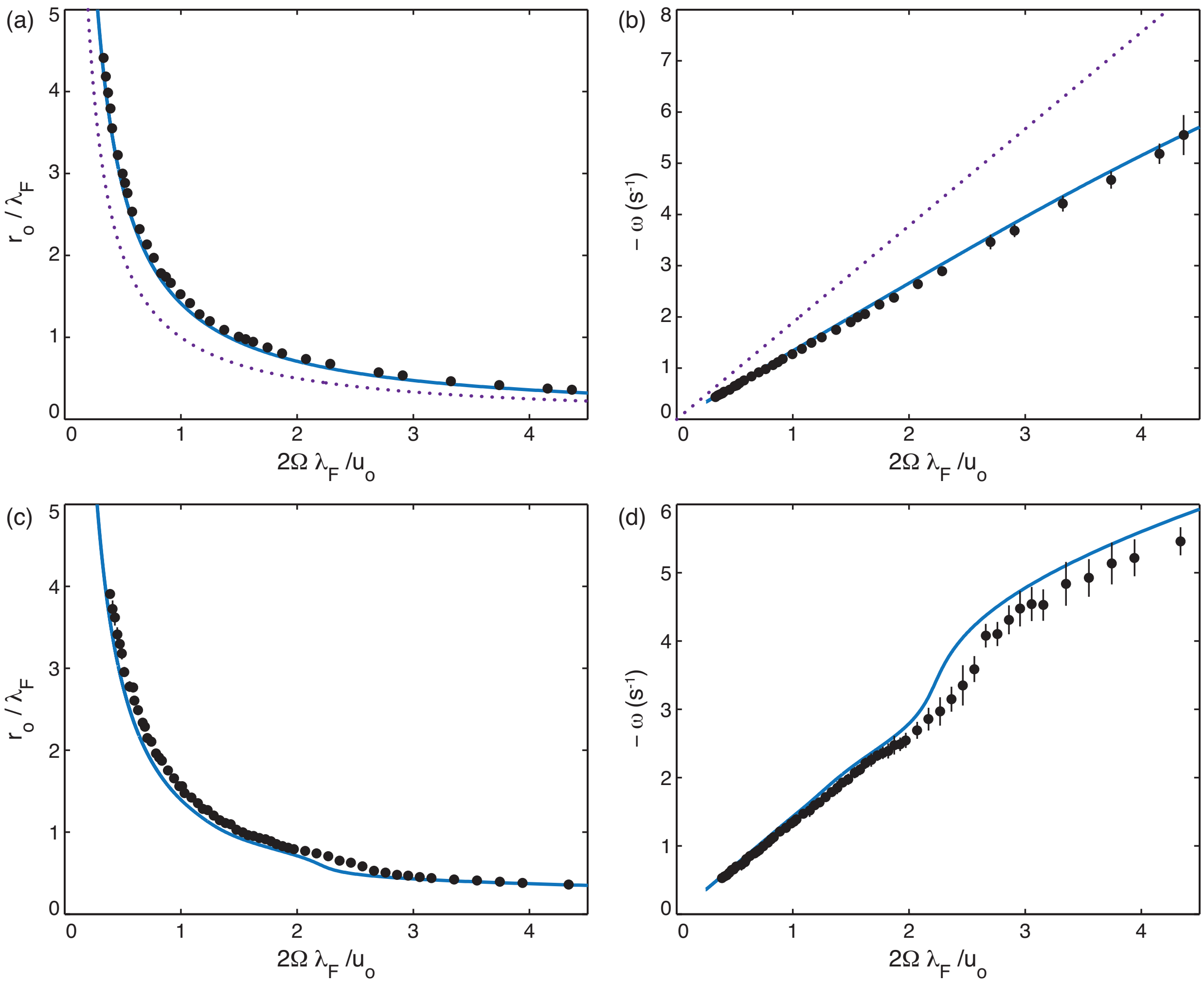

Figure 3-1: The predicted dependence of the orbital radius $r_0$ ((a) and (c)) and orbital frequency $\omega$ ((b) and (d)) on the bath's rotation rate $\Omega$ in the low memory regime. The dotted lines represent the standard prediction for inertial orbits, (a) $r_0 = u_0/2\Omega$, (b) $\omega = -2\Omega$. The solid curves are the theoretical predictions determined by solving (3.9) with experimental parameters corresponding to the data reported in Harris and Bush [38], who used a silicone oil of viscosity $\nu = 20.9$ cSt, density $\rho = 950$ kg/m$^3$, surface tension $\sigma = 0.0206$ N/m, and forcing frequency $f = 80$ Hz. There are no fitting parameters. For (a) and (b), $\gamma/\gamma_F = 0.822$, free walking speed $u_0 = 9.0$ mm/s and drop radius $R_D = 0.4$ mm. For (c) and (d), $\gamma/\gamma_F = 0.922$, $u_0 = 9.5$ mm/s and $R_D = 0.4$ mm. Note that both $r_0$ and $\omega$ vary continuously with the rotation rate $\Omega$.

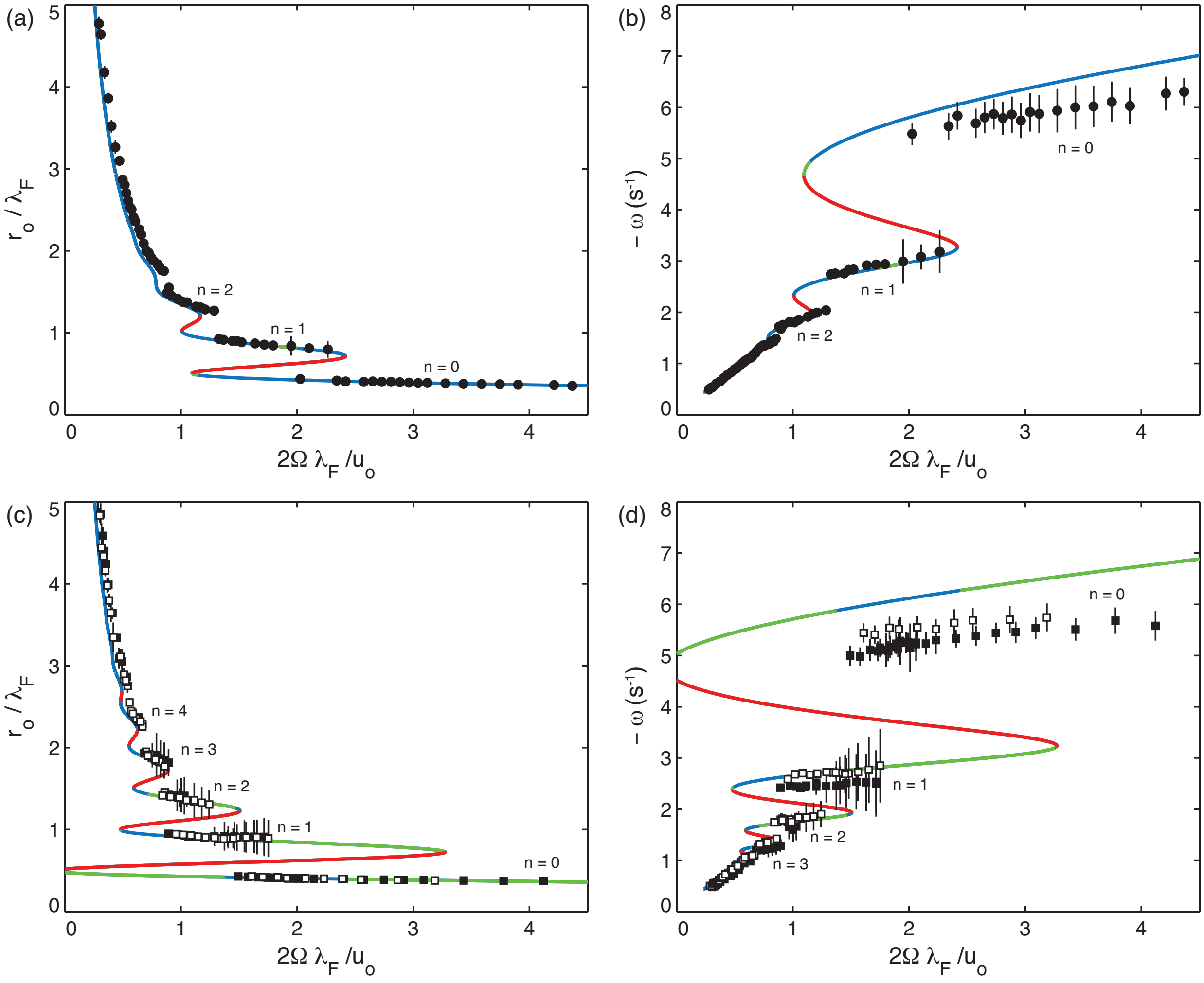

Figure 3-2: The predicted dependence of the orbital radius $r_0$ ((a) and (c)) and orbital frequency $\omega$ ((b) and (d)) on the bath's rotation rate $\Omega$ in the high memory regime. The curves are the theoretical predictions determined by solving (3.9) with the experimental parameters corresponding to the data reported in Harris and Bush [38], who used a silicone oil of viscosity $\nu = 20.9$ cSt, density $\rho = 950$ kg/m$^3$, surface tension $\sigma = 0.0206$ N/m, and forcing frequency $f = 80$ Hz. There are no fitting parameters. The blue portions of the curves are stable, while the red and green portions are unstable (see §3.4). For (a) and (b), $\gamma/\gamma_F = 0.954$, $R_D = 0.43$ mm and $u_0 = 12.0$ mm/s. For (c) and (d), $\gamma/\gamma_F = 0.971$, $R_D = 0.4$ mm and $u_0 = 10.9$ mm/s (■) and 11.7 mm/s (□). The theoretical curves in (c) and (d) are constructed using the average of the observed $u_0$ values. Note that both $r_0$ and $\omega$ are quantized.

of (3.6), are shown in figure 3-3. Note that interference effects in the wave field become more pronounced as the memory increases. We proceed by investigating the properties of these orbital solutions.

### 3.3.1 Low orbital memory $M_e^O \ll 1$

We first consider the low orbital memory regime $M_e^O \ll 1$, in which the drop's orbital period is much less than the decay time of the Faraday waves; consequently, the drop does not interact with its own wake. Since the dimensionless orbital frequency is $\hat{\omega} = \omega T_F M_e = 2\pi M_e^O$, we note that $M_e^O \ll 1$ is equivalent to $|\hat{\omega}| \ll 1$. In this limit, the defining equations (3.9) for the orbital radius and orbital frequency yield, to leading order in $\hat{\omega}$,

$$\begin{aligned} -\kappa\hat{r}_0\hat{\omega}^2 - \hat{\Omega}\hat{r}_0\hat{\omega} &= \beta\left[\frac{\hat{\omega}}{2}\int_0^\infty zJ_1(\hat{r}_0\hat{\omega}z)\mathrm{e}^{-z}\,\mathrm{d}z + O(\hat{\omega}^3)\right], \\ \hat{r}_0\hat{\omega} &= \beta\left[\int_0^\infty J_1(\hat{r}_0\hat{\omega}z)\mathrm{e}^{-z}\,\mathrm{d}z + O(\hat{\omega}^2)\right]. \end{aligned} \tag{3.10}$$

As discussed in Appendix C, this approximation is valid even for arbitrarily large $\hat{r}_0$. Both integrals in (3.10) can be evaluated exactly, yielding

$$-\kappa\hat{r}_0\hat{\omega}^2 - \hat{\Omega}\hat{r}_0\hat{\omega} = \frac{\beta\hat{r}_0\hat{\omega}^2}{2\left(1+(\hat{r}_0\hat{\omega})^2\right)^{3/2}}, \quad \hat{r}_0\hat{\omega} = \frac{\beta}{\hat{r}_0\hat{\omega}}\left(1 - \frac{1}{\sqrt{1+(\hat{r}_0\hat{\omega})^2}}\right). \tag{3.11}$$

The second equation allows us to solve for the orbital walking speed $\hat{u} \equiv |\hat{r}_0\hat{\omega}|$:

$$\hat{u} \equiv |\hat{r}_0\hat{\omega}| = \frac{1}{\sqrt{2}}\left(-1 + 2\beta - \sqrt{1+4\beta}\right)^{1/2}. \tag{3.12}$$

This is the same as the formula for the free speed $\hat{u}_0$ of a walker on a *non-rotating* bath (Chapter 2 [48]), the non-dimensional equivalent of that given in Table 3.1. Substituting (3.12) into the first equation of (3.11) yields a formula for the orbital

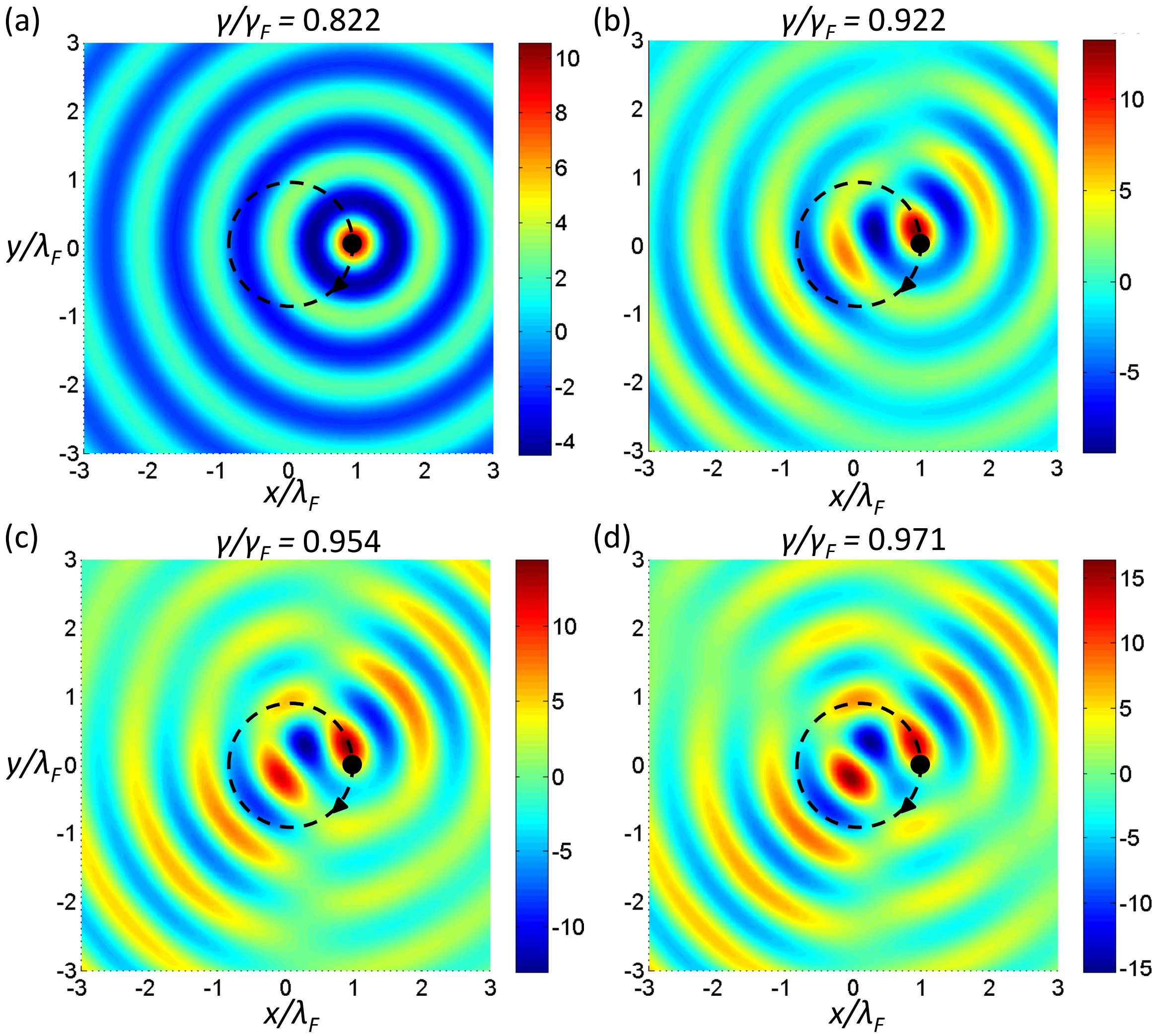

Figure 3-3: Plots of the wave field (3.6) accompanying a drop of viscosity $\nu = 20.9$ cSt, density $\rho = 950$ kg/m$^3$, surface tension $\sigma = 0.0206$ N/m, period $T_F = 0.025$ s, radius $R_D = 0.4$ mm, and phase $\sin\Phi = 0.16$. The amplitude of the wave field is in units of microns. The drop (black dot) orbits clockwise according to $\boldsymbol{x}_p(t) = (r_0 \cos\omega t, r_0 \sin\omega t)$, with orbital radius $r_0 = 0.95\lambda_F$ and orbital frequency $\omega$ defined by (3.9). The forcing accelerations are (a) $\gamma/\gamma_F = 0.822$, (b) $\gamma/\gamma_F = 0.922$, (c) $\gamma/\gamma_F = 0.954$, and (d) $\gamma/\gamma_F = 0.971$. The walking threshold in the absence of rotation is $\gamma_W/\gamma_F = 0.806$. Note that interference effects in the wave field become more pronounced with increased forcing and path memory.

frequency $\hat{\omega}$:

$$\hat{\omega} = -\hat{\Omega}\left(\kappa + \frac{\beta}{2\left(1+\hat{u}_0^2\right)^{3/2}}\right)^{-1} = -\hat{\Omega}\left(\kappa + \frac{4\beta}{\left(-1+\sqrt{1+4\beta}\right)^3}\right)^{-1} \tag{3.13}$$

since $\sqrt{1+\hat{u}_0^2} = \frac{1}{2}\left(-1+\sqrt{1+4\beta}\right)$. The solutions (3.12) and (3.13) are compatible with the initial assumption $|\hat{\omega}| \ll 1$ provided that $|\hat{\Omega}| \ll \kappa + 4\beta/\left(-1+\sqrt{1+4\beta}\right)^3$.

In dimensional units, the orbital frequency $\omega$ and radius $r_0$ are given by

$$\omega = -\frac{2\Omega}{a}, \quad r_0 = \frac{au_0}{2\Omega}, \tag{3.14}$$

where

$$a = 1 + \frac{4\beta}{\kappa\left(-1+\sqrt{1+4\beta}\right)^3} = 1 + \frac{4FM_e^3T_F^2k_F}{m\left(-1+\sqrt{1+\frac{4FM_e^2T_Fk_F}{D}}\right)^3}. \tag{3.15}$$

Over the parameter regime explored in the experiments of Harris and Bush [38], $a$ was measured to be 1.51, and calculated using (3.15) to be 1.41. Both results are consistent with the empirical deduction of $a = 1.2 - 1.5$ reported by Fort et al. [32]. Plots of the drop's orbital radius and orbital frequency as a function of $\Omega$ in the low-memory regime are shown in figure 3-1(a) and (b), and adequately collapse the data presented in Harris and Bush [38]. In figure 3-1(c) and (d), we begin to see some deviation from the low-memory result (3.14) for the orbits of smallest radius, as these orbits have the longest orbital memory.

The a-factor, and the associated increase of the orbital radius relative to inertial orbits, may be understood in terms of the geometry of the wave force. Figure 3-4 shows that the force $\boldsymbol{F}$ on the drop due to the wave generated during its prior impact has a component $|\boldsymbol{F}|\sin\theta = |\boldsymbol{F}|\,u_0T_F/2r_0$ that points radially outwards. In the low orbital memory regime, the drop's trajectory is primarily influenced by the waves generated by a few prior impacts, all of which make contributions pointing radially outwards. The pre-factor $a$ can thus be understood as originating from the dynamic influence of the walker's guiding wavefield. Alternatively, the anomalously large radius

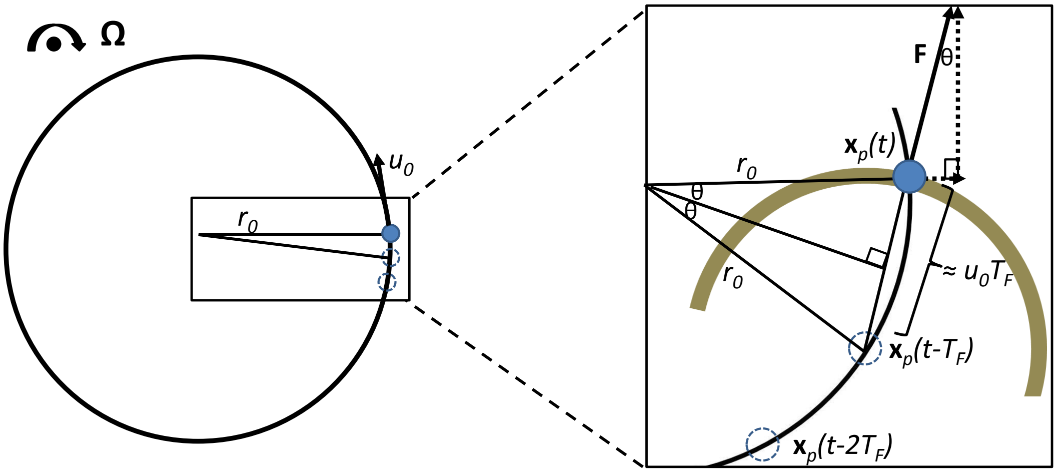

Figure 3-4: Schematic (top view) of the wave force acting on the walker in the low-memory regime. The walker orbits in a circle of radius $r_0$ with angular speed $u_0 = |r_0\omega|$ while bouncing with period $T_F$ on a fluid bath rotating with angular frequency $\Omega$. The force $\boldsymbol{F}$ acting on the drop at $\boldsymbol{x} = \boldsymbol{x}_p(t)$ is primarily due to the wave created by the prior bounce at $\boldsymbol{x} = \boldsymbol{x}_p(t - T_F)$, whose form is suggested by the circular wave crest. The radial component of the force is $|\boldsymbol{F}|\sin\theta$. The wave force thus causes the observed orbital radius $r_0 = au_0/2\Omega$ to be larger than the inertial orbital radius $r_c = u_0/2\Omega$.

of the walker's orbit may be understood as resulting from an increased effective mass $\tilde{m}$ associated with its wave field, as (3.11) may be expressed in dimensional form as

$$\frac{\tilde{m}u_0^2}{r_0} = 2m\Omega u_0, \quad \text{where } \frac{\tilde{m}}{m} = a. \tag{3.16}$$

### 3.3.2 Mid-memory $M_e^O = O(1)$: orbital quantization

In the low-orbital-memory regime $M_e^O \ll 1$, the drop's orbital radius $r_0$ is a monotonically decreasing function of the rotation rate $\Omega$, as shown in figure 3-1. Solving the algebraic equations (3.9) numerically indicates that such is no longer the case in the mid-orbital-memory regime $M_e^O = O(1)$, which arises at higher forcing acceleration $\gamma/\gamma_F$. The solution curve first develops an inflection point and then two turning points. More turning points appear with increasing memory $M_e$, as shown in figures

3-2(a) and 3-2(c). In §3.4, we will show that the regions of the solution curves with positive slope represent unstable orbital solutions. The unstable regions of the solution curve represent forbidden orbital radii. This demonstrates the origins of orbital quantization: the set of observable orbital radii is discrete and discontinuous. This system represents a classical analogue of the quantized Landau levels of an electron in a uniform magnetic field [32]. Here, however, the walker's orbital quantization can be rationalized in terms of its pilot-wave dynamics.

We follow the convention of [32] for numbering the orbits, the smallest being denoted by $n = 0$. At certain rotation rates, orbital degeneracy arises: multiple orbits of different radii may exist for a fixed rotation rate. The orbital degeneracy becomes even more pronounced at high memory, as we observe the coexistence of up to three possible radii for a single rotation rate. Even at the highest path memory considered, as the orbits become larger in radius, they cease to be quantized, and the data essentially follows the low-memory curve. This might be anticipated on the grounds that, for sufficiently large radii, the drop is in the low orbital memory regime $M_e^O \ll 1$: its orbital period $T_O \approx 2\pi r_0/u_0$ is much longer than the decay time $T_F M_e$ of its wave field.

The equations in (3.9) adequately capture the observed dependence of the orbital radius $r_0$ and frequency $\omega$ on $\Omega$ and $M_e$. Note that, in figures 3-2(b) and 3-2(d), the largest discrepancy between theory and experiment occurs in frequencies $\omega$ of the innermost orbital $n = 0$, for which $r_0/\lambda_F < 0.5$. Such a discrepancy might be accounted for through a variation of the bouncing phase $\sin\Phi$ for the smallest orbits.

### 3.3.3 High orbital memory $M_e^O \gg 1$: an analog Zeeman effect

The set of orbital solutions has qualitatively different behavior in the high orbital-memory limit $M_e^O \gg 1$, or equivalently $|\hat{\omega}| \gg 1$. Let $\Omega$ be the rotation rate of the container, in which the drop orbits with radius $r_0$ and orbital frequency $\omega$. If the container rotates in the opposite direction (with angular frequency $-\Omega$), the drop will clearly orbit with the same radius $r_0$ but opposite orbital frequency $-\omega$. Thus, the solution curves for the orbital radii in figures 3-1 and 3-2 should be symmetric about the vertical axis, with an additional curve corresponding to solutions with identical radii for $\Omega < 0$. As the memory $M_e$ increases, the solution curves approach the $r_0$-axis and, in the high memory limit, eventually cross, as shown in figure 3-5(a). Our pilot-wave model thus predicts the possibility of a *self-orbiting solution* with some radius $r_0^*$ that exists even in the absence of rotation, at $\Omega = 0$. For such solutions, which might be interpreted as "hydrodynamic spin states", the waves generated by the walker are sufficient to compensate for the absent Coriolis force, balancing the radial inertial force and so sustaining the walker's circular motion.

Note that the self-orbiting solutions (arising at $\Omega = 0$) come in pairs, corresponding to positive and negative angular frequencies $\pm\omega^*$ (figure 3-5c). As shown in figure 3-5(b), the introduction of a finite rotation $\Omega > 0$ causes these two degenerate solutions to split, one with radius $r_0 \gtrsim r_0^*$ and the other with $r_0 \lesssim r_0^*$. To see this explicitly, we seek solutions to (3.9) with high orbital-memory $|\hat{\omega}| \gg 1$, which only arise in the high-path-memory regime $M_e \gg 1$. Specifically, we take $\beta \gg 1$, $\kappa = O\left(\beta^{-1/2}\right)$, $\hat{\omega} = O\left(\beta^{1/2}\right)$, $\hat{\Omega} = O(1)$, and $\hat{r}_0 = O(1)$. We first use integration by parts to rewrite the second equation in (3.9) in the form:

$$\hat{r}_0\hat{\omega} = \frac{\beta}{\hat{r}_0\hat{\omega}}\left[1 - \int_0^\infty J_0\left(2\hat{r}_0 \sin\frac{\hat{\omega}z}{2}\right)\mathrm{e}^{-z}\,\mathrm{d}z\right]. \tag{3.17}$$

From the argument in Appendix D, it follows that

$$\begin{aligned}\int_0^\infty J_1\left(2\hat{r}_0 \sin\frac{\hat{\omega}z}{2}\right)\sin\frac{\hat{\omega}z}{2}\mathrm{e}^{-z}\,\mathrm{d}z &= \frac{1}{2\pi}\int_0^{2\pi} J_1\left(2\hat{r}_0\sin x\right)\sin x\,\mathrm{d}x + O\left(\hat{\omega}^{-2}\right),\\ \int_0^\infty J_0\left(2\hat{r}_0 \sin\frac{\hat{\omega}z}{2}\right)\mathrm{e}^{-z}\,\mathrm{d}z &= \frac{1}{2\pi}\int_0^{2\pi} J_0\left(2\hat{r}_0\sin x\right)\,\mathrm{d}x + O\left(\hat{\omega}^{-2}\right).\end{aligned} \tag{3.18}$$

We simplify these integrals by using the identity [63, p. 151]

$$\int_0^{\pi/2} J_{p-q}\left(a\cos x\right)\cos(p+q)x\,\mathrm{d}x = \frac{\pi}{2}(-1)^q J_p(a/2)J_q(a/2), \quad p, q \text{ integers} \tag{3.19}$$

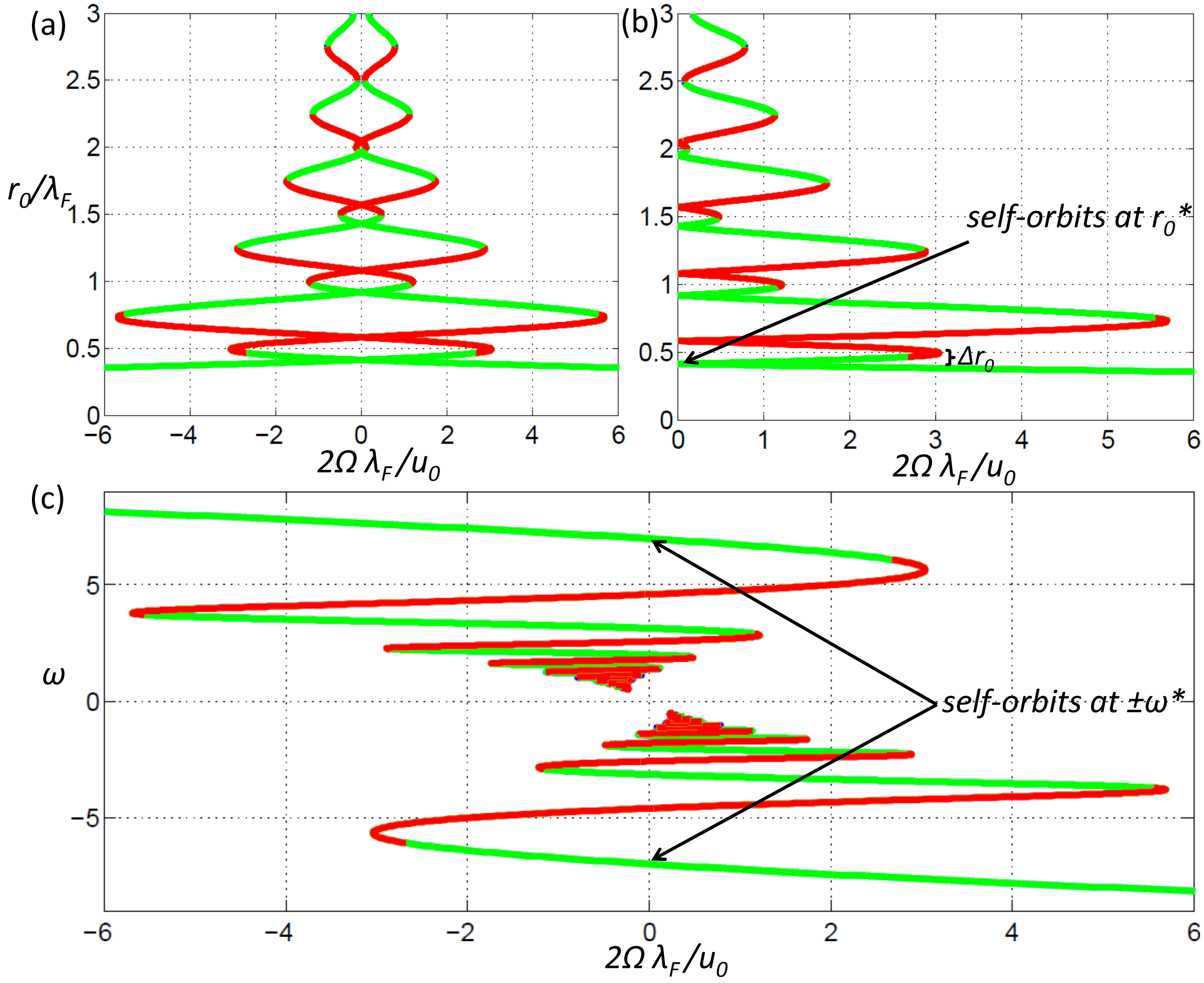

Figure 3-5: Orbital solutions in the high orbital memory regime $M_e^O \gg 1$. The curves are determined by solving (3.9) numerically for $\gamma/\gamma_F = 0.985$, assuming a drop of radius $R_D = 0.4$ mm, phase $\sin\Phi = 0.16$, and free walking speed $u_0 = 11.6$ mm/s. Both the red and green portions of the curves represent unstable solutions (see §3.4). (a) Orbital radii as a function of $\Omega$. (b) Orbital radii for which $\Omega > 0$. (c) Orbital frequencies $\omega$ as a function of $\Omega$. The analog Zeeman effect is apparent in panel (b), as the self-orbiting solutions of radius $r_0^*$ at $\Omega = 0$ split into two solutions as $\Omega$ is increased. The adjoining co-rotating orbital solutions ($\omega > 0$) have slightly larger orbital radii than their counter-rotating counterparts ($\omega < 0$), the difference $\Delta r_0$ being defined in (3.24).

which implies that

$$\begin{aligned}\int_0^{\pi/2} J_1(a\cos x)\cos x\,\mathrm{d}x &= \frac{\pi}{2}J_0(a/2)J_1(a/2), \quad (p=1,q=0)\\ \int_0^{\pi/2} J_0(a\cos x)\cos x\,\mathrm{d}x &= \frac{\pi}{2}J_0^2(a/2) \quad (p=0,q=0). \qquad (3.20)\end{aligned}$$

Letting $x \to x+\pi/2$, we find that

$$\frac{1}{2\pi}\int_0^{2\pi} J_1(a\sin x)\sin x\,\mathrm{d}x = J_0(a/2)J_1(a/2), \quad \frac{1}{2\pi}\int_0^{2\pi} J_0(a\sin x)\,\mathrm{d}x = J_0^2(a/2), \qquad (3.21)$$

and thus obtain the high-orbital-memory limit of (3.9):

$$\begin{aligned}-\kappa\hat{r}_0\hat{\omega}^2 &= \beta\left[J_0(\hat{r}_0)J_1(\hat{r}_0)+O\left(\hat{\omega}^{-2}\right)\right]+\hat{\Omega}\hat{r}_0\hat{\omega}\\ \hat{r}_0\hat{\omega} &= \frac{\beta}{\hat{r}_0\hat{\omega}}\left[1-J_0(\hat{r}_0)^2+O\left(\hat{\omega}^{-2}\right)\right]. \qquad (3.22)\end{aligned}$$

Let $\hat{r}_0^*$ be a zero of either $J_0(r)$ or $J_1(r)$. To leading order in $\beta$, the orbital radius $\hat{r}_0$ and frequency $\hat{\omega}$ are

$$\begin{aligned}\hat{r}_0 &= \hat{r}_0^*+\frac{\kappa\hat{r}_0^*\hat{\omega}^{*2}}{\beta}\left(1+\frac{\hat{\Omega}}{\kappa\hat{\omega}^*}\right)\cdot\begin{cases} J_1(\hat{r}_0^*)^{-2}, & \text{if } J_0(\hat{r}_0^*)=0\\ -\left[J_0(\hat{r}_0^*)J_1'(\hat{r}_0^*)\right]^{-1}, & \text{if } J_1(\hat{r}_0^*)=0.\end{cases}+O\left(\beta^{-1}\right),\\ \hat{\omega}^* &= \left(\frac{\beta\left(1-J_0(\hat{r}_0^*)^2\right)}{\hat{r}_0^{*2}}\right)^{1/2}+O\left(1\right). \qquad (3.23)\end{aligned}$$

The radii $\hat{r}_0$ satisfying $J_1(\hat{r}_0)\approx 0$ correspond to solutions in the red portions of the curve and are never observed experimentally, as is evident in figure 3-2(c), so we instead consider the solutions with $J_0(\hat{r}_0)\approx 0$. We note that these solutions, though also unstable, do leave an imprint on the walker's statistics in the high-memory limit ([38], Chapter 4 [51]). Taking $\hat{\Omega}>0$, we see from (3.23) that co-rotating solutions ($\hat{\omega}>0$) have slightly larger radii than the counter-rotating solutions ($\hat{\omega}<0$). In terms of dimensional variables, the difference in radius $\Delta r_0$ is prescribed by

$$\frac{\Delta r_0}{\lambda_F}=\frac{2mr_0^*\left|\omega^*\right|}{FM_e\pi J_1(k_F r_0^*)^2}\Omega, \quad \text{where } r_0^* \text{ is defined by } J_0(k_F r_0^*)=0. \qquad (3.24)$$

Thus, the magnitude of the splitting is proportional to the rotation rate $\Omega$. Building upon the correspondence proposed by Fort et al. [32] between inertial orbits and Landau levels, we see that this orbital splitting represents a hydrodynamic analogue of the Zeeman effect, in which an electron's degenerate energy level splits in the presence of a uniform magnetic field. For weak fields, the size of the split is proportional to the strength of the magnetic field. We note that this splitting is similar in form to that reported by Eddi et al. [30] for orbiting pairs of walkers in a rotating frame, but would apply to single orbiting walkers were such hydrodynamic spin states stable.

We observe from (3.23) that, in the high-orbital-memory regime, the physically significant orbital radii may be approximated by the zeros of the Bessel function $J_0(k_F r)$. We note that the approximation (3.3) proposed in Fort et al. [32] is consistent with this result for large $r_0$. Indeed, using the approximation $J_\alpha(x) \approx \sqrt{2/\pi x}\cos(x - \alpha\pi/2 - \pi/4)$ for $x \gg |\alpha^2 - 1/4|$, the radial equation in (3.22) for counter-rotating solutions ($\omega < 0$) can be expressed as

$$\frac{mu^2}{r_0} \approx 2m\Omega u + \frac{FM_e}{\pi k_F r_0}\cos(2k_F r_0), \quad \text{where } u = r_0|\omega|. \tag{3.25}$$

This is similar in form to the high-memory governing equation (3.2) proposed in [32], which was derived using purely geometrical arguments. Both equations indicate that most of the sources on the circle cancel out, and that the droplet essentially orbits in the wave field created by a virtual droplet of mass $\tilde{m} = mM_e/\pi k_F r_0$ on the opposite side of the circle. However, we expect (3.25) to be valid only for sufficiently large orbital radii $r_0$, for which the large-argument approximation for $J_\alpha(x)$ may be safely applied.

### 3.3.4 Trapped states

We now consider orbits of small radius, specifically $r_0 \ll \lambda_F/2$. In the limit of $r_0 \to 0$, the non-dimensional equations (3.9) reduce to

$$-\kappa\hat{\omega}_0^2 - \hat{\Omega}_0\hat{\omega}_0 = \beta\int_0^\infty \sin^2\frac{\hat{\omega}_0 z}{2}\mathrm{e}^{-z}\,\mathrm{d}z, \quad \hat{\omega}_0 = \frac{\beta}{2}\int_0^\infty \sin\hat{\omega}_0 z\,\mathrm{e}^{-z}\,\mathrm{d}z \tag{3.26}$$

where $\hat{\omega}_0, \hat{\Omega}_0$ are the values corresponding to the $\hat{r}_0 = 0$ solution. The integrals can be evaluated explicitly, which yields the system of equations

$$\kappa \hat{\omega}_0^2 + \hat{\Omega}_0 \hat{\omega}_0 = -\frac{\beta \hat{\omega}_0^2}{2\left(1+\hat{\omega}_0^2\right)}, \quad \hat{\omega}_0 = \frac{\beta \hat{\omega}_0}{2\left(1+\hat{\omega}_0^2\right)} \tag{3.27}$$

with solutions

$$\hat{\omega}_0 = \pm\sqrt{\frac{\beta}{2} - 1}, \quad \hat{\Omega}_0 = -\hat{\omega}_0 \left(1+\kappa\right). \tag{3.28}$$

We call these solutions *trapped states*, as they have infinitesimal radius but finite orbital frequency. In terms of dimensional variables, the angular frequencies $\omega_0$ and $\Omega_0$ corresponding to these trapped states are

$$\omega_0 = \frac{1}{T_F M_e}\sqrt{\frac{F k_F T_F M_e^2}{2D} - 1}, \quad \Omega_0 = \frac{D}{2m}\sqrt{\frac{F k_F T_F M_e^2}{2D} - 1}\left(1 + \frac{m}{D M_e T_F}\right). \tag{3.29}$$

It is shown in Chapter 5 [49] that the bouncing state $\boldsymbol{x}_p \equiv$ constant is stable for $|\Omega| > \Omega_0$. That is, even above the walking threshold ($\gamma > \gamma_W$), the drop will simply bounce in place if the rotation rate is sufficiently high ($|\Omega| > \Omega_0$). The stability of the bouncing state is determined by the balance between the destabilizing wave force and the stabilizing effects of the drag force (which opposes the drop's motion) and the Coriolis force (which radially confines the drop).

Figure 3-6 shows that the critical rotation rate required for trapping, $\Omega_0$, is an increasing function of the forcing acceleration $\gamma$, and diverges as $\gamma \to \gamma_F$. Experimental validation of the curve presented in figure 3-6 was impractical owing to the significant deflection of the free surface at high $\Omega$, which caused the Faraday threshold to be spatially nonuniform. Thus, the prediction (3.29) for the critical rotation rate $\Omega_0$ could not be tested reliably with our experimental arrangement.

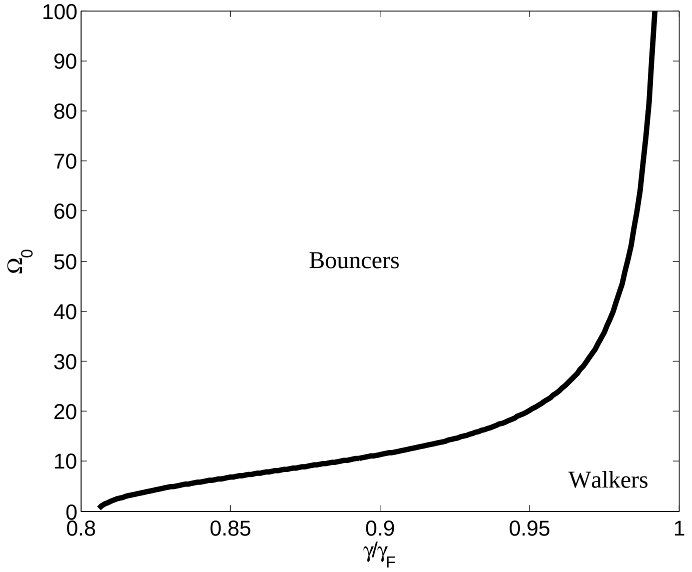

Figure 3-6: The critical rotation rate for trapping $\Omega_0$ as defined by (3.29) is plotted as a function of the nondimensional forcing acceleration $\gamma/\gamma_F$. The drop bounces in place for $|\Omega| > \Omega_0$ (Chapter 5, [49]). We assume a drop of radius $R_D = 0.4$ mm and phase $\sin\Phi = 0.16$, for which the walking threshold in the absence of rotation is $\gamma_W/\gamma_F = 0.806$.

## 3.4 Orbital stability

In order to rationalize the observed orbital quantization, we proceed by analyzing the stability of the orbital solutions found in §3.3. A more precise approach for doing so will be given in §5.5. We write $\boldsymbol{x}_p(t) = (r(t)\cos\theta(t), r(t)\sin\theta(t))$ and express the nondimensional equation of motion (3.8) in polar coordinates, all of the variables here being nondimensional. We thus obtain

$$\begin{aligned}
\kappa\left(\ddot{r} - r\dot{\theta}^2\right) + \dot{r} &= \beta\int_{-\infty}^{t} \frac{J_1(|\boldsymbol{x}_p(t) - \boldsymbol{x}_p(s)|)}{|\boldsymbol{x}_p(t) - \boldsymbol{x}_p(s)|}\left[r(t) - r(s)\cos\left(\theta(t) - \theta(s)\right)\right]\mathrm{e}^{-(t-s)}\,\mathrm{d}s \\
&\quad + \Omega r\dot{\theta} + \epsilon c_r \delta(t) \\
\kappa\left(2\dot{r}\dot{\theta} + r\ddot{\theta}\right) + r\dot{\theta} &= \beta\int_{-\infty}^{t} \frac{J_1(|\boldsymbol{x}_p(t) - \boldsymbol{x}_p(s)|)}{|\boldsymbol{x}_p(t) - \boldsymbol{x}_p(s)|} r(s)\sin\left(\theta(t) - \theta(s)\right)\mathrm{e}^{-(t-s)}\,\mathrm{d}s \\
&\quad - \Omega\dot{r} + \epsilon r_0 c_\theta \delta(t), \qquad (3.30)
\end{aligned}$$

where

$$|\boldsymbol{x}_p(t) - \boldsymbol{x}_p(s)|^2 \;=\; r(t)^2 + r(s)^2 - 2r(t)r(s)\cos\left(\theta(t) - \theta(s)\right), \tag{3.31}$$

and $\delta_r(t), \delta_\theta(t)$ are Dirac delta functions, $c_r, c_\theta$ are $O(1)$ constants, and $0 < \epsilon \ll 1$. The delta functions represent a small perturbation to the drop at time $t = 0$, the response to which we examine in what follows.

We linearize (3.30) about an orbital solution of radius $r_0$ and frequency $\omega$, where $r_0$ and $\omega$ are defined by (3.9). The drop's trajectory is thus written as $r(t) = r_0 + \epsilon r_1(t)H(t)$ and $\theta(t) = \omega t + \epsilon\theta_1(t)H(t)$, where $r_1(t)$ and $\theta_1(t)$ are the radial and angular perturbations to the orbital solution, respectively, and $H(t)$ is the Heaviside step function. We impose the conditions $r_1(0) = \theta_1(0) = 0$ and $\dot{r}_1(0) = \frac{c_r}{\kappa}$, $\dot{\theta}_1(0) = \frac{c_\theta}{\kappa}$ in order to ensure that $\boldsymbol{x}_p(t)$ is a solution of (3.30). We substitute these expressions into (3.30) and retain only the $O(\epsilon)$ terms to find

$$\begin{aligned}
&\kappa\left(\ddot{r}_1 - \omega^2 r_1 - 2r_0\omega\dot{\theta}_1\right) + \dot{r}_1 = \omega\Omega r_1 + \Omega r_0\dot{\theta}_1 + \frac{\beta}{2}\left\{\mathcal{I}\left[\left(f(t) + g(t)\right)\sin\omega t\right] r_0\theta_1(t)\right.\\
&\left.-r_0\left[\left(f(t) + g(t)\right)\sin\omega t\right] * \theta_1(t)\right\} + \beta\left\{\mathcal{I}\left[f(t)\cos^2\frac{\omega t}{2} + g(t)\sin^2\frac{\omega t}{2}\right] r_1(t)\right.\\
&\left.+\left(g(t)\sin^2\frac{\omega t}{2} - f(t)\cos^2\frac{\omega t}{2}\right) * r_1(t)\right\}\\
&\kappa\left(2\omega\dot{r}_1 + r_0\ddot{\theta}_1\right) + \omega r_1 + r_0\dot{\theta}_1 = -\Omega\dot{r}_1 + \frac{\beta}{2}\left\{\mathcal{I}\left[\left(g(t) - f(t)\right)\sin\omega t\right] r_1(t)\right.\\
&\left.+\left[\left(f(t) + g(t)\right)\sin\omega t\right] * r_1(t)\right\} + \beta\left\{\mathcal{I}\left[g(t)\cos^2\frac{\omega t}{2} - f(t)\sin^2\frac{\omega t}{2}\right] r_0\theta_1(t)\right.\\
&\left.+r_0\left(f(t)\sin^2\frac{\omega t}{2} - g(t)\cos^2\frac{\omega t}{2}\right) * \theta_1(t)\right\}
\end{aligned} \tag{3.32}$$

where

$$\begin{aligned}
f(z) &= \frac{J_1\left(2r_0\sin\frac{\omega z}{2}\right)}{2r_0\sin\frac{\omega z}{2}}\mathrm{e}^{-z}, \quad g(z) = J_1'\left(2r_0\sin\frac{\omega z}{2}\right)\mathrm{e}^{-z},\\
\mathcal{I}[f] &= \int_0^\infty f(z)\,\mathrm{d}z, \quad \text{and } f * g(t) = \int_0^t f(z)g(t-z)\,\mathrm{d}z.
\end{aligned} \tag{3.33}$$

Written in this form, the linearized equations are particularly amenable to analysis, as we can now take their Laplace transform and deduce algebraic equations for $R(s) = \mathcal{L}[r_1]$ and $\Theta(s) = \mathcal{L}[\theta_1]$. Using the initial conditions $r_1(0) = \theta_1(0) = 0$ and $\dot{r}_1(0) = \frac{c_r}{\kappa}$, $\dot{\theta}_1(0) = \frac{c_\theta}{\kappa}$, we obtain

$$\begin{aligned}
\left[\kappa s^2 + s - \kappa\omega^2 - \Omega\omega - \beta F_1(s)\right] R - \left[2\kappa\omega s + \Omega\omega s + \beta F_2(s)\right] r_0\Theta &= c_r \\
\left[2\omega\kappa s + \omega + \Omega s - \beta G_1(s)\right] R + \left[\kappa s^2 + s - \beta G_2(s)\right] r_0\Theta &= r_0 c_\theta, \quad (3.34)
\end{aligned}$$

where

$$\begin{aligned}
F_1(s) &= \mathcal{I}\left[f(t)\cos^2\frac{\omega t}{2} + g(t)\sin^2\frac{\omega t}{2}\right] + \mathcal{L}\left[g(t)\sin^2\frac{\omega t}{2} - f(t)\cos^2\frac{\omega t}{2}\right] \\
F_2(s) &= \frac{1}{2}\left\{\mathcal{I}\left[(f(t)+g(t))\sin\omega t\right] - \mathcal{L}\left[(f(t)+g(t))\sin\omega t\right]\right\} \\
G_1(s) &= \frac{1}{2}\left\{\mathcal{I}\left[(g(t)-f(t))\sin\omega t\right] + \mathcal{L}\left[(f(t)+g(t))\sin\omega t\right]\right\} \\
G_2(s) &= \mathcal{I}\left[g(t)\cos^2\frac{\omega t}{2} - f(t)\sin^2\frac{\omega t}{2}\right] + \mathcal{L}\left[f(t)\sin^2\frac{\omega t}{2} - g(t)\cos^2\frac{\omega t}{2}\right]. \quad (3.35)
\end{aligned}$$

As shown in Appendix A, some of the integrals above can be done in closed form, so (3.34) can be expressed as

$$\begin{bmatrix} A(s) & -B(s) \\ C(s) & D(s) \end{bmatrix} \begin{bmatrix} R(s) \\ r_0\Theta(s) \end{bmatrix} = \begin{bmatrix} c_r \\ r_0 c_\theta \end{bmatrix} \quad (3.36)$$

where

$$\begin{aligned}
A(s) &= \kappa s^2 + s - \kappa\omega^2 - \Omega\omega - \beta\left(\mathcal{I}\left[f(t)\cos^2\frac{\omega t}{2} + g(t)\sin^2\frac{\omega t}{2}\right]\right. \\
&\quad \left. + \mathcal{L}\left[g(t)\sin^2\frac{\omega t}{2} - f(t)\cos^2\frac{\omega t}{2}\right]\right) \\
B(s) &= (2\omega\kappa + \Omega)\, s - (\kappa\omega + \Omega) - \frac{\beta}{2}\mathcal{L}\left[(f(t)+g(t))\sin\omega t\right] \\
C(s) &= (2\omega\kappa + \Omega)\, s + 2\omega + \kappa\omega + \Omega - \frac{\beta}{2}\mathcal{L}\left[(f(t)+g(t))\sin\omega t\right] \\
D(s) &= \kappa s^2 + s - 1 - \beta\mathcal{L}\left[f(t)\sin^2\frac{\omega t}{2} - g(t)\cos^2\frac{\omega t}{2}\right]. \quad (3.37)
\end{aligned}$$

The solution to (3.36) is

$$\begin{aligned} R(s) &= \frac{c_r D(s) + r_0 c_\theta B(s)}{A(s)D(s) + B(s)C(s)} \\ \Theta(s) &= \frac{-c_r C(s) + r_0 c_\theta A(s)}{r_0 \left(A(s)D(s) + B(s)C(s)\right)}. \end{aligned} \tag{3.38}$$

The poles of $R(s)$ and $\Theta(s)$ are the eigenvalues of the linear problem (3.32). If all of the poles lie in the left-half complex plane, the orbital solution $\boldsymbol{x}_p(t) = (r_0 \cos \omega t, r_0 \sin \omega t)$ is linearly stable. An instability occurs if any pole is in the right-half complex plane.

It is shown in Chapter 5 [49] that a necessary and sufficient condition for either $R(s)$ or $\Theta(s)$ to have a pole at $s = s^*$ is $\tilde{F}(s^*; r_0) = 0$, where

$$\tilde{F}(s; r_0) = \left(1 - \mathrm{e}^{2\pi(s+1)/|\omega|}\right) F(s; r_0), \quad F(s; r_0) = A(s)D(s) + B(s)C(s). \tag{3.39}$$

Thus, assessing the stability of an orbital solution with radius $r_0$ amounts to finding the real parts of the zeros of the function $\tilde{F}(s; r_0)$. Note that we parametrize the orbital solutions in terms of the radius $r_0$ instead of the nondimensional rotation rate $\Omega$, since $\omega$ and $\Omega$ are single-valued functions of $r_0$. That is, the radius $r_0$ uniquely determines the drop's orbital frequency $\omega$ and the bath rotation rate $\Omega$, but multiple radii $r_0$ could exist for a given value of $\Omega$, as predicted by (3.9) and seen in experiments (figure 3-2; Harris and Bush [38]; Fort et al. [32]).

It is shown in Chapter 5 [49] that $\tilde{F}(s; r_0)$ has trivial zeros at $s = 0$ and $s = \pm\mathrm{i}\omega$, which reflect, respectively, the rotational and translational invariance of the orbital solution. Note that $\tilde{F}(s; r_0)$ is a complicated function of $s$, so it is difficult to determine its nontrivial zeros in closed form. In Chapter 5 [49], we instead expand $\tilde{F}(s; r_0)$ in various limits for which we can approximate its zeros and thus assess the stability of the orbital solutions in the appropriate parameter regimes. We show that orbits of small radius $r_0 \ll 1$ are stable, which confirms that the bouncing state destabilizes into an orbital state with radius $r_0 \sim |\Omega_0 - \Omega|^{1/2}$ for $\Omega \lesssim \Omega_0$. We also show that the stability problem for orbits of large radius $r_0 \gg \sqrt{\beta}$ reduces to that for steady rectilinear walking; this is apparent on physical grounds, as such orbits have small curvature and so can be approximated locally by a straight line. Since steady rectilinear walking is stable (Chapter 2 [48]), we expect that such large orbits will be likewise, which is consistent with our inference that such orbits are not quantized (figures 3-1 and 3-2).

### 3.4.1 Origin of orbital quantization

We here demonstrate that the orbital solutions for which $\frac{\mathrm{d}\Omega}{\mathrm{d}r_0} > 0$ are unstable. This explains why the upward sloping branches of the solution curves in figure 3-2(a) and (c) are never seen experimentally, a feature that is ultimately responsible for the orbital quantization.

We proceed by proving the following:

**Theorem 1** *Orbital solutions for which* $\frac{\mathrm{d}\Omega}{\mathrm{d}r_0} > 0$ *are linearly unstable, with an instability corresponding to a real and positive eigenvalue.*

**Proof:** Let $F(s;r_0) = F_0(r_0)s + F_1(r_0)s^2 + O(s^3)$. We show in Appendix B that $F_0(r_0) = r_0\omega d_1\frac{\mathrm{d}\Omega}{\mathrm{d}r_0}$, where $d_1 = 1 + \beta\mathcal{I}\left[\left(f(t)\sin^2\frac{\omega t}{2} - g(t)\cos^2\frac{\omega t}{2}\right)t\right]$. Since $F(s;r_0) \sim \kappa^2 s^4$ as $s \to \infty$, it follows that $F(s;r_0)$ has at least one positive real root if $F_0(r_0) < 0$. Since $d_1 > 0$ (see Proposition 2 in Chapter 5) and $\omega < 0$, $F_0(r_0)$ has the opposite sign as $\frac{\mathrm{d}\Omega}{\mathrm{d}r_0}$. It follows that $F(s;r_0)$ has at least one real positive root if $\frac{\mathrm{d}\Omega}{\mathrm{d}r_0} > 0$.

Figure 3-7 summarizes the stability characteristics of the circular orbits. For a given value of the dimensionless forcing acceleration $\gamma/\gamma_F$, the stability of an orbital solution of radius $r_0$ is assessed by finding the zeros of $\tilde{F}(s;r_0)$, using the method detailed in Chapter 5 [49]. The perturbations $r_1(t)$ and $\theta_1(t)$ to the orbital solution will behave like $\mathrm{e}^{s_* t}$, where $s_*$ is the zero of $\tilde{F}(s;r_0)$ with the largest real part. The points colored in blue signify stable orbits, for which all of the zeros lie in the left-half of the complex plane ($\Re(s_*) < 0$). The points colored in red and green signify unstable orbits ($\Re(s_*) > 0$). Unstable orbits for which $s_*$ has a nonzero imaginary component ($\Re(s_*) > 0$, $\Im(s_*) \neq 0$) are colored green, while those for which $s_*$ is on the positive real axis ($\Re(s_*) > 0$, $\Im(s_*) = 0$) are colored red.

We find that orbits for which $\frac{\mathrm{d}\Omega}{\mathrm{d}r_0} > 0$, proven to be unstable in Theorem 1, are contained within the red regions of figure 3-7. We note that the converse of Theorem 1 is not necessarily true: orbital solutions for which $\frac{\mathrm{d}\Omega}{\mathrm{d}r_0} < 0$ are not necessarily stable, as indicated by the green regions in figure 3-2(a) and (c). While orbital solutions are observed within these green regions, their relatively large error bars reflect a periodic fluctuation in the measured radius of curvature, corresponding to a wobbling orbit [38]. We may thus surmise that the oscillatory instability is stabilized by a nonlinear mechanism beyond the scope of our linear stability analysis.

Figure 3-7 indicates that all circular orbits are stable for $\gamma/\gamma_F < 0.930$. Above this critical value, an unstable (red) solution branch arises for $r_0 \approx 0.6\lambda_F$, corresponding roughly to the first positive zero of $J_1(k_F r)$. Along horizontal traverse B, there are two unstable branches, which correspond to the red portions of the curve in figure 3-2(a). As $\gamma/\gamma_F$ is progressively increased, more unstable red tongues arise, for increasing orbital radius. The orbital solutions have blue, red, and green branches along traverse C ($\gamma/\gamma_F = 0.971$), corresponding to the curve presented in figure 3-2(c). We note that wobbling orbits have been observed inside the green regions [38]. Moreover, there is experimental and numerical evidence of more complex periodic and quasiperiodic orbits within the green regions as the memory is further increased ([38], Chapter 4 [51]). The lateral extent of the unstable regions increases with increasing memory; consequently, virtually all of the orbital solutions become unstable in the high-memory limit $\gamma \to \gamma_F$. It is in this limit that a wave-like statistical behavior emerges from a chaotic pilot-wave dynamics ([38], Chapter 4 [51]).

## 3.5 Discussion

We have developed and analyzed an integro-differential trajectory equation that describes the pilot-wave dynamics of a walker in a rotating frame. The theoretical predictions for the walker's orbital radius $r_0$ and frequency $\omega$ agree well with the experimental results of Harris and Bush [38]. Specifically, our model allows us to rationalize the emergence of quantized orbits and wobbling states as the memory is

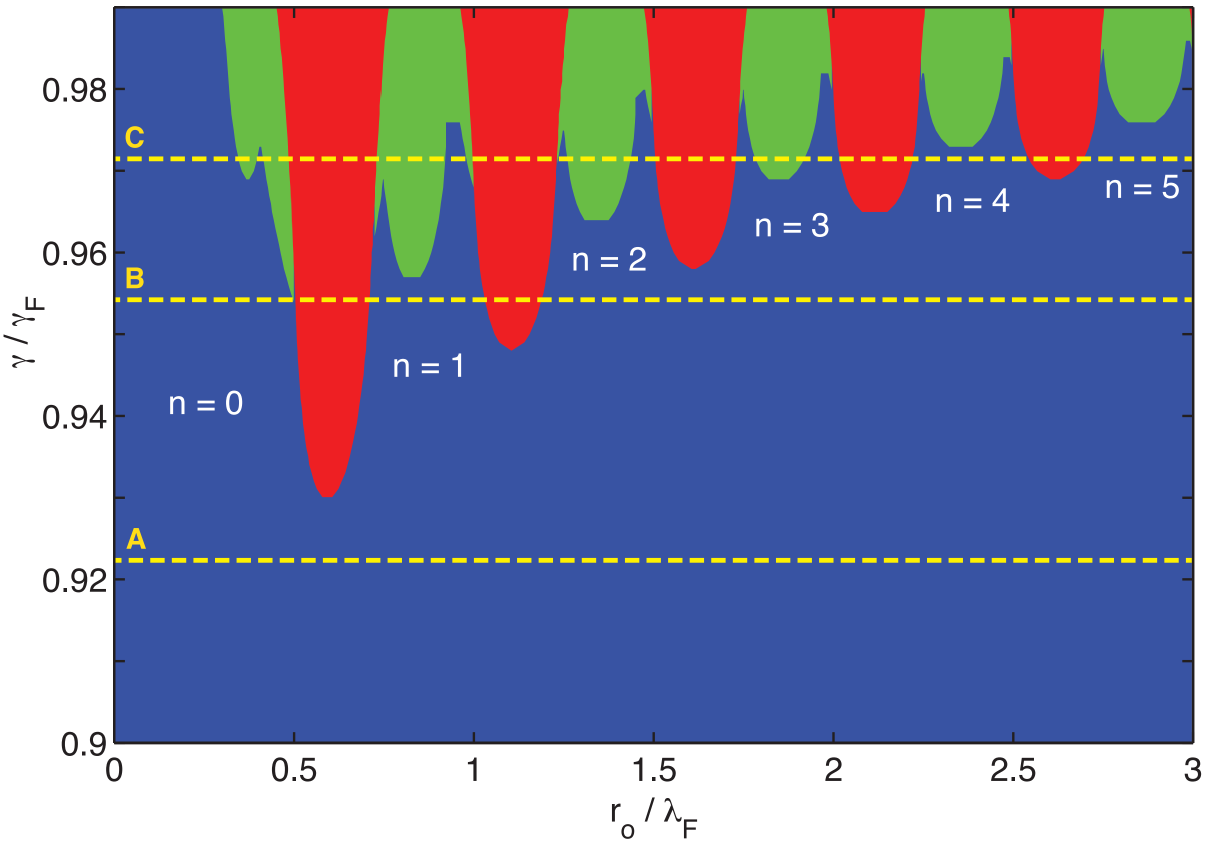

Figure 3-7: Orbital stability diagram for a walker of radius $R_D = 0.4$ mm, phase $\sin\Phi = 0.16$, viscosity $\nu = 20.9$ cSt, and forcing frequency $f = 80$ Hz, determined by finding the eigenvalues of the linear stability problem (3.32). The stability of the circular orbit is governed by the eigenvalue with the largest real part, denoted by $s_*$. Stable orbits ($\Re(s_*) < 0$) are indicated in blue. Unstable orbits for which $s_*$ is complex ($\Re(s_*) > 0$, $\Im(s_*) \neq 0$) are colored in green, while those for which $s_*$ is on the positive real axis ($\Re(s_*) > 0$, $\Im(s_*) = 0$) are colored in red. The horizontal traverses A–C correspond to, respectively, the curves in figures 3-1(c), 3-2(a), and 3-2(c), the color coding being the same. We note that the phase $\sin\Phi$ and drop radius $R_D$ vary slightly between the traverses A–C but are assumed to be fixed in the orbital stability diagram.

increased progressively, as well as the relative absence of stable orbits in the high-memory limit. The theory also predicts the existence of trapped states, which are orbital solutions of small radius $r_0 \sim |\Omega_0 - \Omega|^{1/2}$ that arise for $\Omega \lesssim \Omega_0$.

In the low orbital memory regime, the walker is found to execute circular orbits of radius $r_0 = au_0/2\Omega$, where $a$ is defined in terms of experimental parameters in (3.15). The factor $a$ originates from the small radial component of the wave force, and can be interpreted in terms of an added mass associated with the walker's pilot-wave field. In the mid-memory regime, the orbital radii are found to be quantized. The orbital quantization has been rationalized by analyzing the stability of the orbital solutions. Orbits on the portions of the solution curves in figure 3-2(a) and (c) with positive slope are found to be unstable.

As the memory is increased further, the theory predicts the existence of self-orbiting solutions, even at $\Omega = 0$, wherein the wave force balances the centripetal force. Such self-orbiting states might represent a hydrodynamic analogue of a quantum spin state. Indeed, the self-orbiting solution is reminiscent of the Kerr-Newman model of the electron, in which the electron is modeled as a charged particle orbiting in its own wave field [8]. These hydrodynamic 'spin states' have not yet been observed in experiments, and are unstable according to linear stability theory; nevertheless, it is conceivable that they could be stabilized by nonlinear effects, a possibility to be explored elsewhere. When subjected to rotation, the solutions that co-rotate with the bath would have slightly larger orbital radii than their counter-rotating counterparts, an effect reminiscent of Zeeman splitting in quantum mechanics.

In the future, we will analyze the transition from simple orbital to chaotic dynamics in greater detail. There is evidence that Hopf-like bifurcations of the orbital solutions lead to wobbling orbits, as reported in §3.4, which will be examined in Chapter 4 [51]. Higher-order instabilities may give rise to precessing orbits, intermittent wobbling, and complex quasiperiodic orbits, all of which have been observed either in our experiments [38] or numerical simulations (Chapter 4 [51]). We will also analyze the statistical behavior of the walker's motion, characterizing the emergence of wave-like statistics in the high-memory limit ([38], Chapter 4 [51]).

A similar approach will be applied to analyzing walkers moving in a central force field, a configuration currently being examined experimentally by Couder and coworkers [52]. The integro-differential equation of motion has adequately captured the observed behavior of a walker in a rotating frame; moreover, it has allowed us to make predictions that have been confirmed experimentally. Having benchmarked our pilot-wave model against experimental data in this configuration, our hope is that we may now apply it to systems that are not necessarily accessible in the laboratory.

# Chapter 4

# Pilot-wave dynamics in a rotating frame: exotic orbits

## 4.1 Introduction

In this chapter, we continue our study of the walker dynamics in a rotating frame. In Chapter 3, the observed orbital quantization [32, 38] was rationalized theoretically through a linear stability analysis of circular orbits [50, 49], the results of which are summarized in Fig. 4-1. Each point on the diagram corresponds to a particular orbital radius $r_0$ and vibrational forcing $\gamma$. Orbits indicated in red are unstable so were not observed experimentally. Stable orbits, indicated in blue, thus become quantized at high memory. These quantized orbits are labeled by $n$, $n = 0$ being the smallest, and larger $n$ corresponding to larger orbits. Other orbits, indicated in green, destabilize via an oscillatory mechanism, which can give rise to wobbling orbits in the laboratory [38]. The analysis also predicts the relative absence of stable circular orbits in the high-memory limit, $\gamma \to \gamma_F$. Note, however, that the linear stability analysis can only assess the stability of the circular orbits and cannot provide insight into the dynamics

---

This chapter is currently under view at *Physics of Fluids*: Pilot-wave dynamics in a rotating frame: exotic orbits, Oza, A. U., Wind-Willassen, Ø., Harris, D. M., Rosales, R.R. and Bush, J. W. M. [51].

arising within the unstable regions. Such nonlinear dynamics is the subject of this chapter.

Harris and Bush [38] conducted a comprehensive experimental study of this system, which revealed a number of new phenomena. At high memory, in addition to quantized orbits, the authors report the existence of wobbling orbits, marked by a periodic fluctuation in the orbital radius. They also observe drifting orbits, in which the orbital center of a wobbling orbit traverses a nearly circular path. At higher values of memory, they report wobble-and-leap dynamics, in which the trajectory of the orbital center is characterized by a slow drift punctuated by short bursts of rapid motion. At the highest memory considered, they report that the walker's trajectory becomes erratic, presumably chaotic. Nevertheless, the histogram of its radius of curvature has a coherent multimodal structure, with peaks arising at the radii of the unstable quantized circular orbits.

Through numerical simulation of a single walker in a rotating frame, we characterize its behavior as a function of the forcing acceleration $\gamma$ and rotation rate $\Omega$. In addition to reproducing many of the experimental results of Harris and Bush [38], we report a number of new states marked by complex periodic and quasiperiodic trajectories. Our study culminates in a complete regime diagram indicating the dependence of the walker's behavior on the system parameters. We note that many of the phenomena described herein were predicted by the numerical simulations and subsequently observed in the laboratory experiments of Harris and Bush [38].

In §4.2 we review the hydrodynamic trajectory equation for walking drops in a rotating frame and explain the numerical method used to simulate the walker dynamics. We describe wobbling orbits in §4.3, drifting orbits in §4.4 and wobble-and-leap dynamics in §4.5. Other complex periodic and quasiperiodic trajectories are described in §4.6, and the statistical behavior of chaotic trajectories is discussed in §4.7. Future directions are discussed in §4.8.

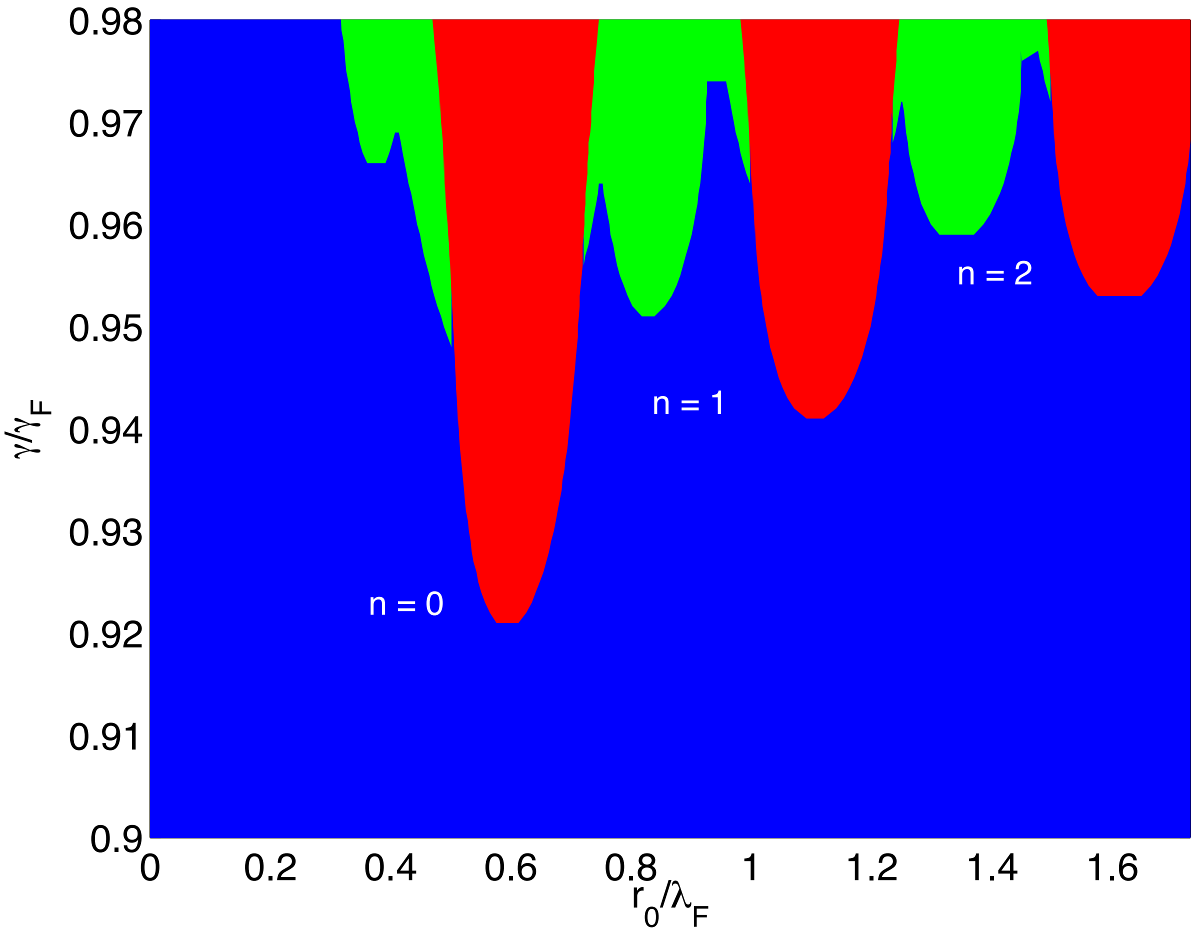

Figure 4-1: Summary of the linear stability analysis for circular orbits presented in Chapter 3 [50], for a walker of radius 0.4 mm and phase $\sin\Phi = 0.2$ bouncing on a 20 cS silicone oil bath forced at 80 Hz. The dimensionless orbital radius $r_0/\lambda_F$ and vibrational acceleration $\gamma/\gamma_F$ uniquely specify the circular orbit. Blue indicates stable orbits, for which each eigenvalue has a negative real part. Green corresponds to unstable orbits with an oscillatory instability, for which the eigenvalues with the largest (positive) real part are complex conjugates. Red corresponds to unstable orbits for which the eigenvalue with the largest (positive) real part is purely real. We note that the experimental parameters used here are slightly different to those used to generate Figure 3-7.

## 4.2 Trajectory equation and numerical method

We first review the trajectory equation for a resonant walker in a rotating frame, the complete derivation of which is presented in Chapter 3 [50]. Let $\boldsymbol{x}(t) = (x(t), y(t))$ denote the horizontal position of the walker at time $t$. The horizontal force balance on the walker, time-averaged over the bouncing period, yields the following integro-differential equation of motion (Chapter 3 [50]):

$$m\ddot{\boldsymbol{x}} + D\dot{\boldsymbol{x}} = \frac{F}{T_F}\int_{-\infty}^{t} \frac{J_1\left(k_F\left|\boldsymbol{x}(t)-\boldsymbol{x}(s)\right|\right)}{\left|\boldsymbol{x}(t)-\boldsymbol{x}(s)\right|}\left(\boldsymbol{x}(t)-\boldsymbol{x}(s)\right)\mathrm{e}^{-(t-s)/(T_F M_e)}\,\mathrm{d}s - 2m\boldsymbol{\Omega}\times\dot{\boldsymbol{x}}. \tag{4.1}$$

The simulations in this study were performed using the fluid parameters approximately corresponding to the silicone oil used in the experiments of Harris and Bush [38], with $\rho = 949$ kg/m$^3$, $\nu = 20$ cS, $\sigma = 0.206$ N/m, $H = 4$ mm, $f = 80$ Hz, $R_D = 0.4$ mm and $\sin\Phi = 0.2$, for which $m = 2.5441\times10^{-4}$ g, $D = 1.997\times10^{-3}$ g/s, $k_F = 1.3224$ mm$^{-1}$, $A = 3.4864\times10^{-3}$ mm and $T_d = 1.8215\times10^{-2}$ s ([46]; Table 3.1).

We non-dimensionalize (4.1) by introducing dimensionless variables $\hat{\boldsymbol{x}} = k_F\boldsymbol{x}$, $\hat{t} = t/T_F M_e$ and $\hat{\boldsymbol{\Omega}} = 2m\boldsymbol{\Omega}/D$. Using primes to denote differentiation with respect to $\hat{t}$, the trajectory equation becomes

$$\kappa\hat{\boldsymbol{x}}'' + \hat{\boldsymbol{x}}' = \beta\int_{-\infty}^{\hat{t}} \frac{J_1\left(\left|\hat{\boldsymbol{x}}(\hat{t})-\hat{\boldsymbol{x}}(\hat{s})\right|\right)}{\left|\hat{\boldsymbol{x}}(\hat{t})-\hat{\boldsymbol{x}}(\hat{s})\right|}\left(\hat{\boldsymbol{x}}(\hat{t})-\hat{\boldsymbol{x}}(\hat{s})\right)\mathrm{e}^{-(\hat{t}-\hat{s})}\,\mathrm{d}\hat{s} - \hat{\boldsymbol{\Omega}}\times\hat{\boldsymbol{x}}' \tag{4.2}$$

where $\kappa = m/DT_F M_e$ and $\beta = Fk_F T_F M_e^2/D$. For the experimental parameters listed above, $\kappa$ and $\beta$ are related to the forcing acceleration $\gamma$ through the formulae $\kappa = 6.994(1-\gamma/\gamma_F)$ and $\beta = 0.10112/(1-\gamma/\gamma_F)^2$.

We proceed by outlining the procedure used to numerically simulate the walker's trajectory. We assume the walker to be in a circular orbit prior to the initial time $t = 0$, that is, $\hat{\boldsymbol{x}}(t) = \hat{\boldsymbol{x}}_O(t) = (\hat{r}_0\cos\hat{\omega}\hat{t}, \hat{r}_0\sin\hat{\omega}\hat{t})$ for $t < 0$, where $\hat{r}_0$ and $\hat{\omega}$ are defined in terms of $M_e$ and $\hat{\Omega}$ through the following equations (Chapter 3 [50]):

$$\begin{aligned} -\kappa\hat{r}_0\hat{\omega}^2 &= \beta\int_0^\infty J_1\left(2\hat{r}_0\sin\frac{\hat{\omega}z}{2}\right)\sin\frac{\hat{\omega}z}{2}\mathrm{e}^{-z}\,\mathrm{d}z+\hat{\Omega}\hat{r}_0\hat{\omega} \\ \hat{r}_0\hat{\omega} &= \beta\int_0^\infty J_1\left(2\hat{r}_0\sin\frac{\hat{\omega}z}{2}\right)\cos\frac{\hat{\omega}z}{2}\mathrm{e}^{-z}\,\mathrm{d}z. \end{aligned} \tag{4.3}$$

The walker's trajectory is evolved in time using the fourth-order Adams-Bashforth linear multistep method [12]. Dropping the hats, the numerical scheme may be written as

$$\begin{aligned} \boldsymbol{x}_{n+1} &= \boldsymbol{x}_n+\Delta t\sum_{m=0}^{3}c_m\boldsymbol{u}_{n-m} \\ \boldsymbol{u}_{n+1} &= \boldsymbol{u}_n+\frac{\Delta t}{\kappa}\sum_{m=0}^{3}c_m\Big[-\boldsymbol{u}_{n-m}-\boldsymbol{\Omega}\times\boldsymbol{u}_{n-m}+\beta f_0(\boldsymbol{x}_{n-m})\mathrm{e}^{-t_{n-m}} \\ &\quad+\beta\int_0^{t_{n-m}}\frac{J_1\left(|\boldsymbol{x}_{n-m}-\boldsymbol{x}(s)|\right)}{|\boldsymbol{x}_{n-m}-\boldsymbol{x}(s)|}\left(\boldsymbol{x}_{n-m}-\boldsymbol{x}(s)\right)\mathrm{e}^{-(t_{n-m}-s)}\,\mathrm{d}s\Big] \\ f_0(\boldsymbol{x}) &= \int_{-\infty}^{0}\frac{J_1\left(|\boldsymbol{x}-\boldsymbol{x}_O(s)|\right)}{|\boldsymbol{x}-\boldsymbol{x}_O(s)|}\left(\boldsymbol{x}-\boldsymbol{x}_O(s)\right)\mathrm{e}^{s}\,\mathrm{d}s, \end{aligned} \tag{4.4}$$

where $\Delta t$ is the time step, $t_n = n\Delta t$, $\boldsymbol{x}_n = \boldsymbol{x}(t_n)$ and $\boldsymbol{u}_n = \boldsymbol{u}(t_n)$. The coefficients are [12] $c_0 = 55/24$, $c_1 = -59/24$, $c_2 = 37/24$ and $c_3 = -3/8$. The integral in (4.4) is computed using Simpson's rule, and $f_0(\boldsymbol{x})$ using an adaptive Gauss-Kronrod quadrature routine built into MATLAB. The first four time steps ($n = 0, 1, 2, 3$) employ the assumption that $\boldsymbol{x} = \boldsymbol{x}_O$ for $t < 0$, so $\boldsymbol{x}_j = \boldsymbol{x}_O(t_j)$ and $\boldsymbol{u}_j = \dot{\boldsymbol{x}}_O(t_j)$ for $j < 0$. Unless otherwise stated, the simulations in this study were performed with a fixed time step $\Delta t = 2^{-6}$ and initial perturbation $\boldsymbol{\delta} = (0.02, 0)$, so that $\boldsymbol{x}_0 = \boldsymbol{x}_O(0)+\boldsymbol{\delta}$. The trajectory was evolved beyond $t_{max} = 1000$, typically a sufficiently large value to capture its asymptotic behavior.

We proceed by characterizing the dependence of the walker's trajectory on its initial orbital radius $r_0$ and forcing acceleration $\gamma/\gamma_F$, with a resolution $\Delta\left(\gamma/\gamma_F\right) = 0.001$. The resulting dynamics is classified in Fig. 4-2, where each color corresponds to a different type of trajectory. Once again, blue denotes regions in which the circular orbit is stable. Red denotes jumping orbits, for which the initial circular orbit

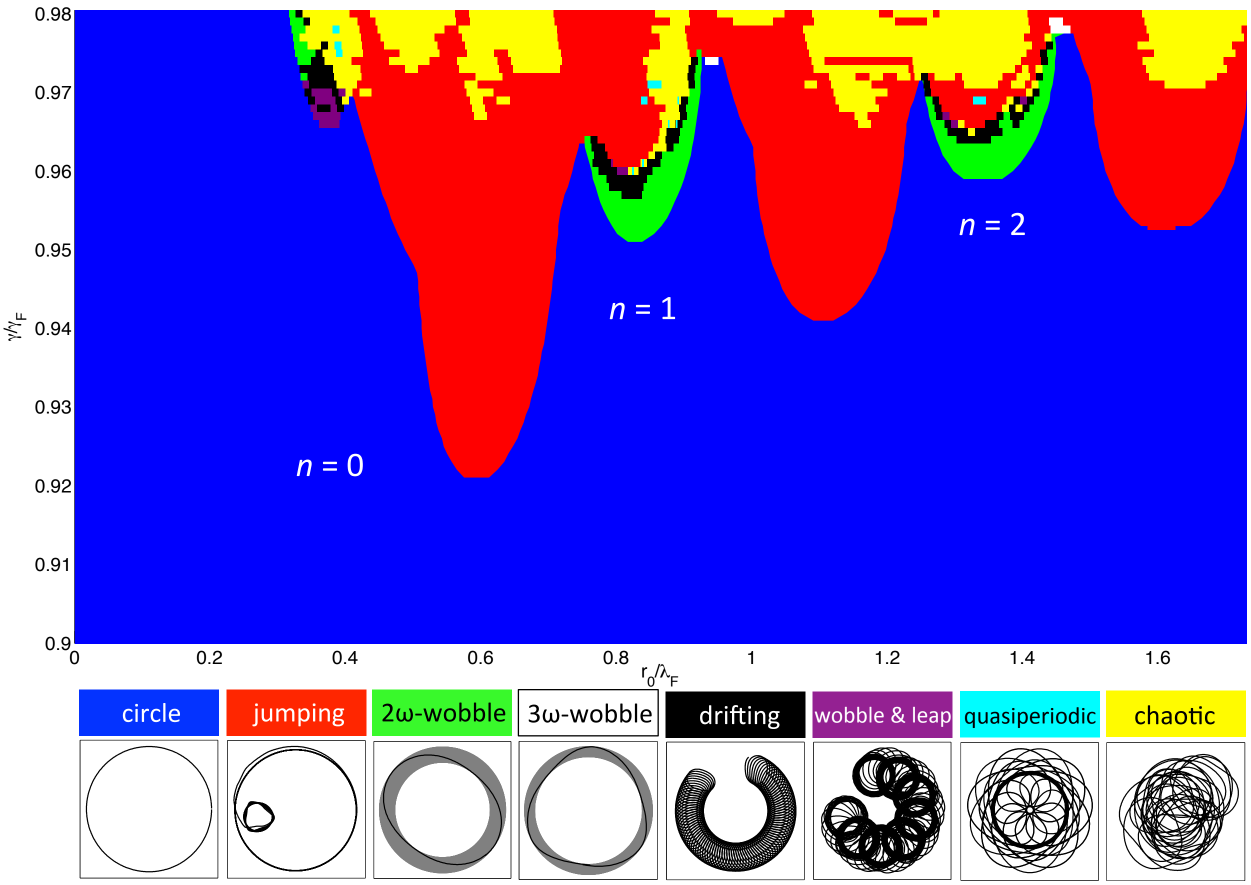

Figure 4-2: Regime diagram delineating the dependence of the walker's trajectory on the initial orbital radius $r_0$ and vibrational forcing $\gamma$. The trajectory equation (4.2) is numerically simulated using circular orbit initial conditions, initial perturbation $\boldsymbol{\delta} = (0.02, 0)$, time step $\Delta t = 2^{-6}$ and $t_{max} = 1000$. The walker's trajectory is color-coded according to the legend.

destabilizes into a different circular orbit, or into a quasiperiodic orbit with a significantly different mean radius. Green and white denote $2\omega$- and $3\omega$-wobbling orbits, which are respectively characterized by a radial oscillation with approximately twice and thrice the orbital frequency. Black denotes drifting orbits, and purple denotes wobble-and-leap orbits. The orbits in light blue correspond to other complex periodic or quasiperiodic orbits. The yellow regions denote erratic or chaotic trajectories for which there is no discernible periodic pattern.

For the initial orbital radii explored, $0 < r_0/\lambda_F < 1.73$, all circular orbits are stable for $\gamma/\gamma_F \leq 0.921$, and only jumping or erratic orbits are present for $\gamma/\gamma_F > 0.98$ and $r_0/\lambda_F > 0.32$. In the following sections, we detail the various trajectories observed.

## 4.3 Wobbling orbits

We here report two different types of wobbling orbits found in our numerical explorations. The existence of $2\omega$-wobbling orbits, indicated by the green regions in Fig. 4-2, was suggested theoretically by the linear stability analysis of circular orbits in Chapter 3 [50] and have been reported in laboratory experiments [38]. Fig. 4-3(a) shows a typical wobbling orbit at $n = 1$, which has a slightly oblong shape. Let $\bar{\boldsymbol{x}}_c$ be the stationary orbital center, defined as the mean value of $\boldsymbol{x}(t)$ over the entire trajectory. The orbital radius $\bar{r}(t) = |\boldsymbol{x}(t) - \bar{\boldsymbol{x}}_c|$ is plotted in Fig. 4-3(b). The top panel shows that the circular orbit solution with constant radius $r_0/\lambda_F = 0.85$ becomes unstable in an oscillatory fashion, and that the radial oscillations saturate after a finite time, which is characteristic of a Hopf-type instability. A small portion of the time trace of $\bar{r}(t)$, displayed in the lower panel, confirms that the wobbling frequency is roughly twice the orbital frequency, as $\bar{r}(t)$ completes approximately two cycles per orbital period. The orbital period $T$ is obtained by taking the Fourier transform of the trajectory $\boldsymbol{x}(t)$ and identifying the dominant frequency.

An example of a roughly triangular $3\omega$-wobbling orbit, indicated by the white regions in Fig. 4-2, is shown in Fig. 4-3(c). The lower panel of Fig. 4-3(d) shows that the wobbling frequency of $\bar{r}(t)$ is roughly thrice the orbital frequency. These $3\omega$-wobbling orbits have not yet been found in laboratory experiments, presumably because they arise only in a minuscule region of parameter space.

We further characterize the $2\omega$-wobbling orbits by comparing their wobbling amplitudes and frequencies to those observed in the laboratory experiments of Harris and Bush [38]. The wobbling frequency $\omega_{\mathrm{wob}}$ is obtained by taking the Fourier transform of the signal $\bar{r}(t)$ and identifying the largest peak. The wobbling amplitude $A$ is then defined as

$$A = \sqrt{2}\left[\frac{1}{T_{\mathrm{wob}}}\int_{T_{\mathrm{wob}}} \left(\bar{r}(t) - \bar{r}_a\right)^2 \,\mathrm{d}t\right]^{1/2}, \quad \text{where } \bar{r}_a = \frac{1}{T_{\mathrm{wob}}}\int_{T_{\mathrm{wob}}} \bar{r}(t)\,\mathrm{d}t \tag{4.5}$$

is the mean orbital radius and $T_{\mathrm{wob}} = 2\pi/\omega_{\mathrm{wob}}$ the wobbling period. Fig. 4-4(a) shows the dependence of the wobbling amplitude $A$ on the rotation rate $\Omega$ for various values of the forcing acceleration $\gamma/\gamma_F$. The lateral extent of the wobbling region increases with memory, which is consistent with the fact that increasing memory destabilizes the circular orbits. The breaks in the curves correspond to regions in which wobbling orbits are absent, a feature that will be discussed in §4.4.

We note a number of features that are consistent with the corresponding experimental observations of Harris and Bush [38], as are reproduced in Fig. 4-4(b). The qualitative shape of the experimental curve at $\gamma/\gamma_F = 0.961$ is similar to the numerically generated curves at the lowest memory, $\gamma/\gamma_F = 0.952$ to 0.956. At higher values of memory, the experimental curves ($\gamma/\gamma_F \geq 0.969$) and numerical curves ($\gamma/\gamma_F \geq 0.965$) end abruptly, indicating that the wobbling amplitude does not decrease smoothly to zero with increasing rotation rate. The onset of wobbling occurs for lower values of $\Omega$ as memory is increased, and the wobbling amplitude increases with memory for a fixed value of $\Omega$. Note that the wobbling amplitudes obtained in the numerical simulations are roughly consistent with experiment. However, the data points do not coincide precisely, presumably because the system is highly sensitive to small deviations in drop size and fluid viscosity. Nevertheless, it is clear that our model results capture the essential dynamical features of the observed wobbling orbits.

The dependence of the wobbling frequency $\omega_{\text{wob}}$ on the rotation rate $\Omega$ is shown in Fig. 4-4(c), which is qualitatively consistent with the experimental data [38] reproduced in Fig. 4-4(d). Note that the wobbling frequencies for a wide range of memory values lie near a single curve, an effect that can be rationalized through the linear stability analysis of circular orbits (Chapter 5 [49]). The wobbling frequency typically decreases slowly with rotation rate while remaining close to the value $2\omega$.

## 4.4 Drifting orbits

At higher values of memory, wobbling orbits destabilize, their orbital centers drifting in a regular fashion on a timescale long relative to the orbital period. Drifting orbits

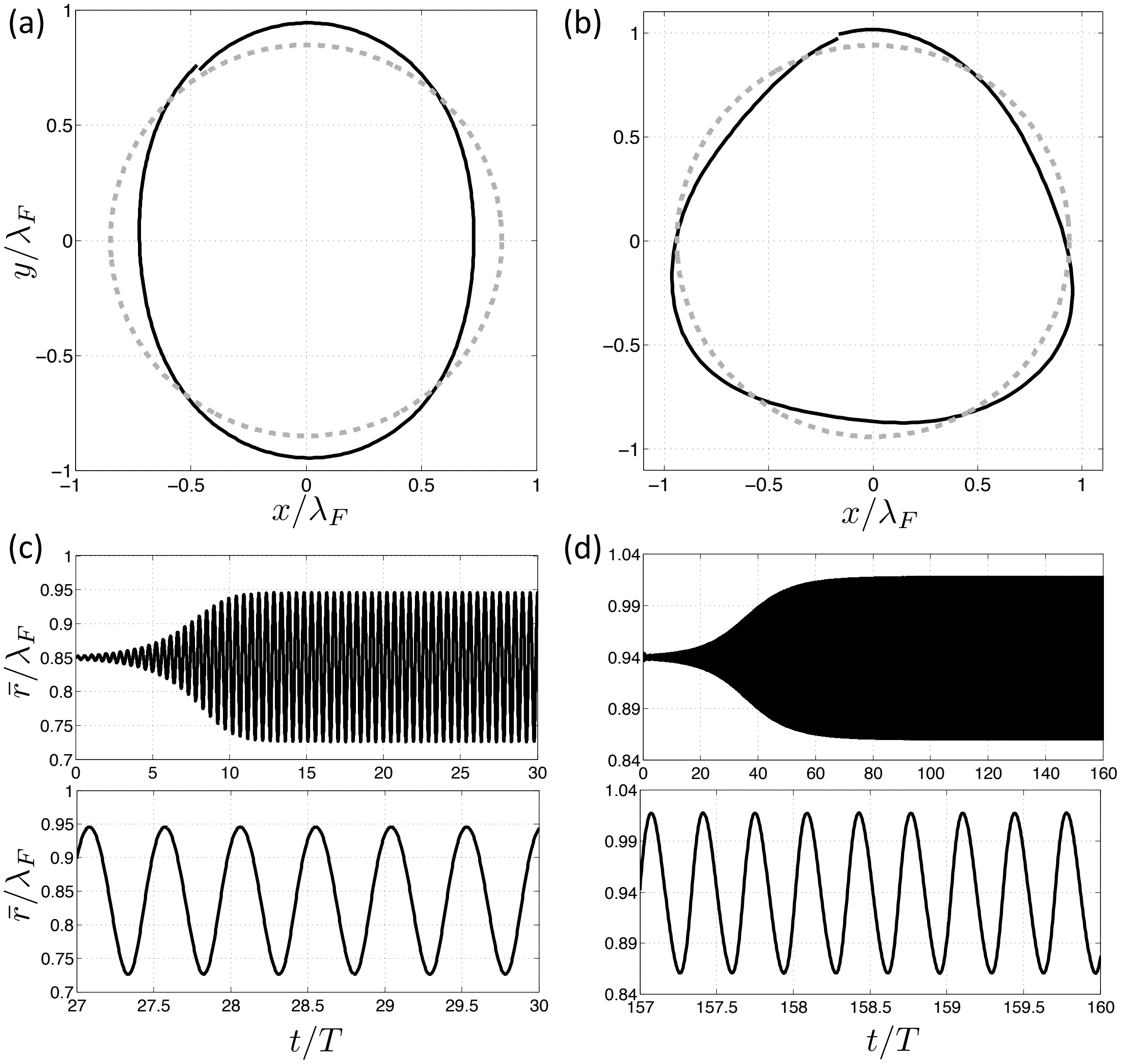

Figure 4-3: Panels (a) and (b): examples of $2\omega$- and $3\omega$-wobbling orbits at $n = 1$, respectively. The $2\omega$-wobbling orbit was obtained using initial orbital radius $r_0/\lambda_F = 0.85$ and vibrational forcing $\gamma/\gamma_F = 0.955$, and the $3\omega$-wobbling orbit using $r_0/\lambda_F = 0.94$ and $\gamma/\gamma_F = 0.9745$. The corresponding (unstable) circular orbit is indicated by the dashed line. Panels (c) and (d): plots of the corresponding orbital radius $\bar{r}(t)$ as a function of $t/T$, where $T$ is the orbital period. In the upper plots, note that the radius grows and then saturates, which is characteristic of a Hopf-type instability. The lower plots resolve the oscillations, showing that the wobbling frequency is $\approx 2\omega$ in (c) and $\approx 3\omega$ in (d).

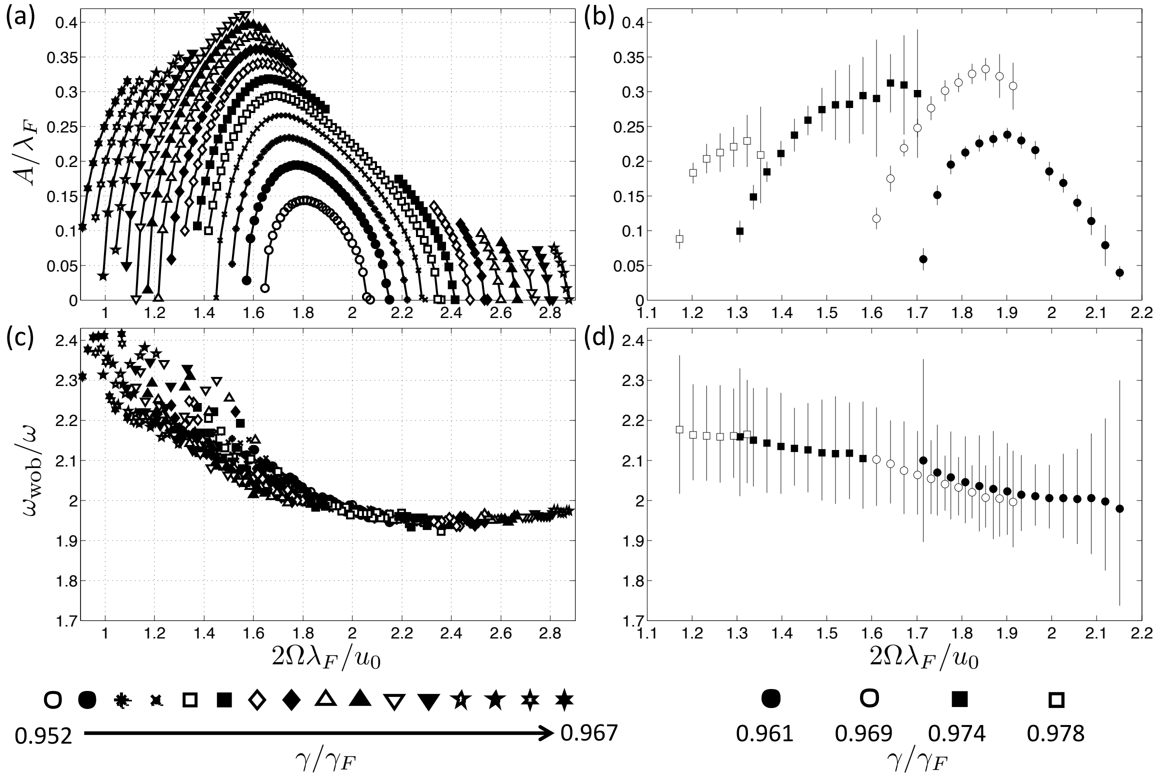

Figure 4-4: Numerical characterization of wobbling orbits (panels (a) and (c)), compared with experimental data from Harris and Bush [38] (panels (b) and (d)). Panels (a) and (b) show the dependence of the wobbling amplitude $A$ on the rotation rate $\Omega$ for various values of memory $\gamma/\gamma_F$. Panels (c) and (d) show the dependence of the wobbling frequency $\omega_{\mathrm{wob}}$ on the rotation rate $\Omega$. The wobbling frequency is normalized by the orbital frequency $\omega$. The symbols correspond to different values of the memory $\gamma/\gamma_F$, as defined in the legend.

are denoted by the black regions in Fig. 4-2. We define the orbital center $\bar{\boldsymbol{x}}_c(t)$ of a drifting orbit as the average value of $\boldsymbol{x}(t)$ over an orbital period $T$,

$$\bar{\boldsymbol{x}}_c(t) = \frac{1}{T}\int_t^{t+T} \boldsymbol{x}(s)\,\mathrm{d}s. \tag{4.6}$$

An example of a drifting orbit is shown in Fig. 4-5. The time trace of the orbital radius $\bar{r}(t) = |\boldsymbol{x}(t) - \bar{\boldsymbol{x}}_c(t)|$ suggests that the drifting orbit arises from the period-doubling bifurcation of a wobbling orbit, a phenomenon to be detailed elsewhere. Note that the period of the orbital center is much larger than the orbital period $T$, this slow oscillation being characteristic of drifting orbits. Fig. 4-5(d) shows another example of a drifting orbit, alongside its experimental counterpart as reported by Harris and Bush [38] (Fig. 4-5(e)).

In Fig. 4-6(a) and (d), we illustrate the relationship between circular, wobbling, and drifting orbits at the second orbital, $n = 1$, for two particular values of memory, $\gamma/\gamma_F = 0.957$ and 0.958. Stable circular orbits are indicated by the blue curve, and unstable ones by the green curve. The mean radii $\bar{r}_a$ of the wobbling orbits, which lie on the green curve, are marked by the data points, the error bars reflecting the wobbling amplitude $A$. The wobbling orbits destabilize into drifting orbits in the open green regions of the two curves, which is reflected by the breaks in the corresponding wobbling amplitude curves in Fig. 4-4(a). For these values of memory, the orbital center $\bar{\boldsymbol{x}}_c(t)$ of a drifting orbit is found to traverse a circular path of radius $R_{\text{drift}}$ over a period $T_{\text{drift}}$. Fig. 4-6(b) and 4-6(e) show that the drift radius $R_{\text{drift}}$ depends continuously on the rotation rate $\Omega$ for these two values of memory. Unlike the wobbling frequency (Fig. 4-4(c)), the drift period $T_{\text{drift}}$ exhibits a strong dependence on the rotation rate, as shown in Fig. 4-6(c) and 4-6(f). The large values of $T_{\text{drift}}/T$ indicate that drifting orbits evolve over a very slow timescale relative to the orbital period, making experimental exploration of the curves in Fig. 4-6 impractical. For higher values of memory, $\gamma/\gamma_F \geq 0.959$, the orbital centers $\bar{\boldsymbol{x}}_c(t)$ of some drifting orbits follow irregular noncircular paths, indicating that simple drifting orbits may destabilize into more complex trajectories. We expect qualitatively similar behavior

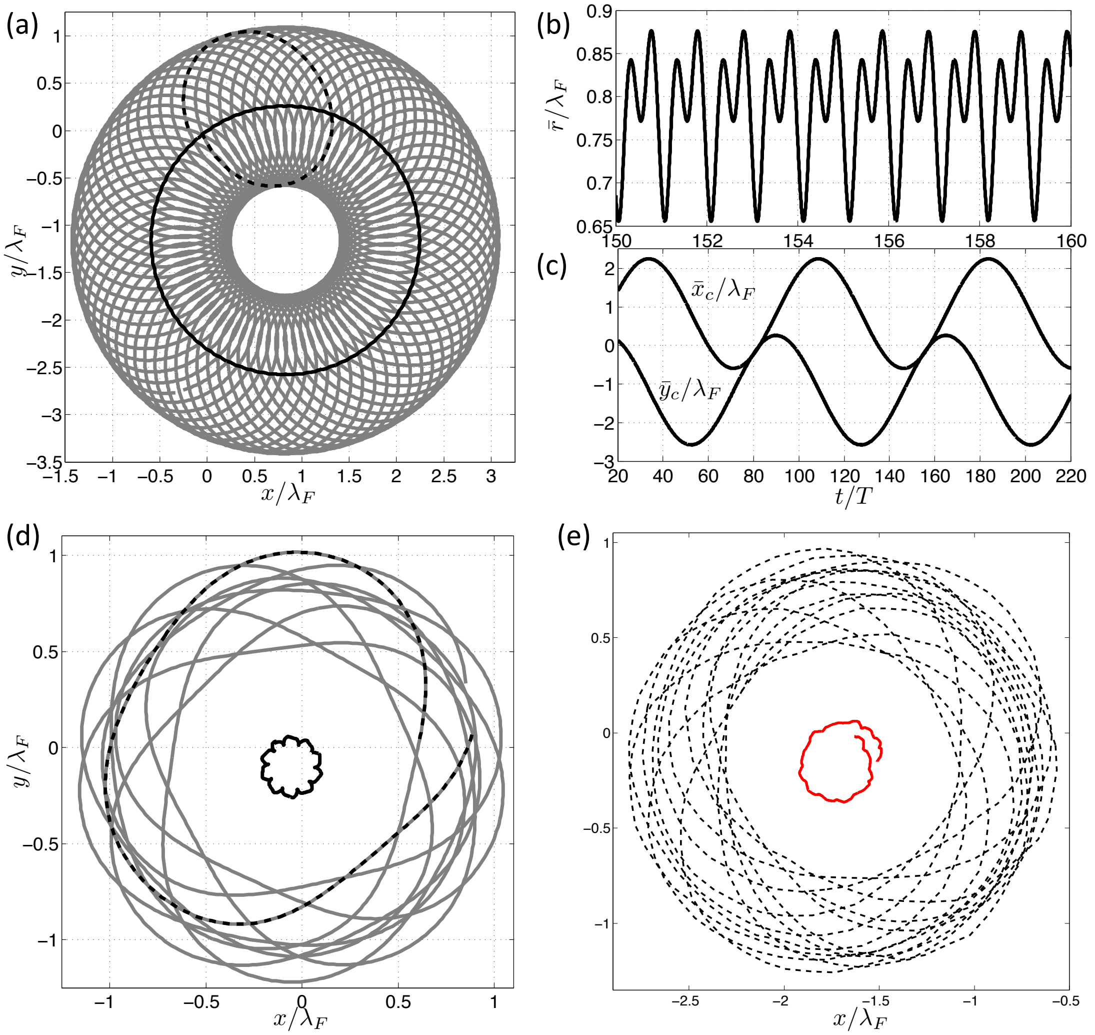

Figure 4-5: (a) Numerical simulation of a drifting trajectory at $n = 1$, obtained using the initial orbital radius $r_0/\lambda_F = 0.8005$ and vibrational forcing $\gamma/\gamma_F = 0.959$. The trajectory (gray line) consists of a loop (dashed line) drifting along a larger circle (black solid line). (b) Plot of the orbital radius $\bar{r}(t)$ as a function of $t/T$, where $T = 4.3$ is the orbital period. (c) Plot of the orbital center $(\bar{x}_c, \bar{y}_c)$ as a function of $t/T$. Note that the center moves on a much slower timescale than the radius $\bar{r}$. (d) Numerical simulation of another drifting trajectory using $r_0/\lambda_F = 0.893$ and $\gamma/\gamma_F = 0.966$, for which the center does not move along a precise circle. (e) Experimentally observed [38] drifting trajectory similar to that in panel (d), obtained using $\gamma/\gamma_F = 0.978 \pm 0.003$ and rotation rate $\Omega = 1.72\ \mathrm{s}^{-1}$. The trajectory is indicated by the dashed line, the motion of the center by the solid line.

to arise at the higher orbital levels, $n > 1$.

An example of a drifting orbit at the innermost orbital level, $n = 0$, is shown in Fig. 4-7(a). Such orbits were found in the black portions of the $n = 0$ region in Fig. 4-2. The walker's trajectory (gray curve) consists of a loop (dashed black curve) periodically drifting along a square epicycle (black curve). As the rotation rate $\Omega$ and memory are slightly varied, the orbital center $\bar{\boldsymbol{x}}_c(t)$ is found to drift along a variety of epicycloidal paths, as shown in the top row of Fig. 4-7(b). The orbital center associated with an $n = 1$ orbit may traverse a star-shaped path, as shown in the bottom row of Fig. 4-7(b). However, such regular drifting orbits arise in a relatively narrow range of parameter space, outside of which the orbital centers drift with a relatively incoherent pattern.

## 4.5 Wobble-and-leap dynamics

The purple regions in Fig. 4-2 denote wobble-and-leap trajectories, which are characterized by a sequence of alternating wobbling and leaping phases [38]. During the wobbling phase, the orbital radius grows in an oscillatory fashion, while the orbital center remains stationary. The orbital center then rapidly jumps to a new location, after which the process begins anew.

Wobble-and-leap trajectories at $n = 1$ appear to arise from the instability of the drifting orbits in response to increased memory. A numerical example of such a trajectory is given in Fig. 4-8. The orbital center $\bar{\boldsymbol{x}}_c(t)$ (panels (c) and (d)) remains relatively stationary while the oscillations in the orbital radius $\bar{r}(t)$ grow (panel (a)). This wobbling phase persists for roughly five orbital periods, before it is interrupted by the rapid shift of the orbital center $\bar{\boldsymbol{x}}_c(t)$ to a new location. The extended trajectory $\boldsymbol{x}(t)$ is indicated by the dashed gray curve in panel (b), and the orbital center $\bar{\boldsymbol{x}}_c(t)$ by the solid black curve. The walker essentially jumps between various wobbling orbits, which are marked by circles (dashed black curves) centered at the transiently stable orbital centers (black dots). We note that the average leap distance is $(0.342 \pm 0.038)\lambda_F$, quite close to the first zero of $J_0(k_F r)$ at $0.383\lambda_F$, which roughly corresponds

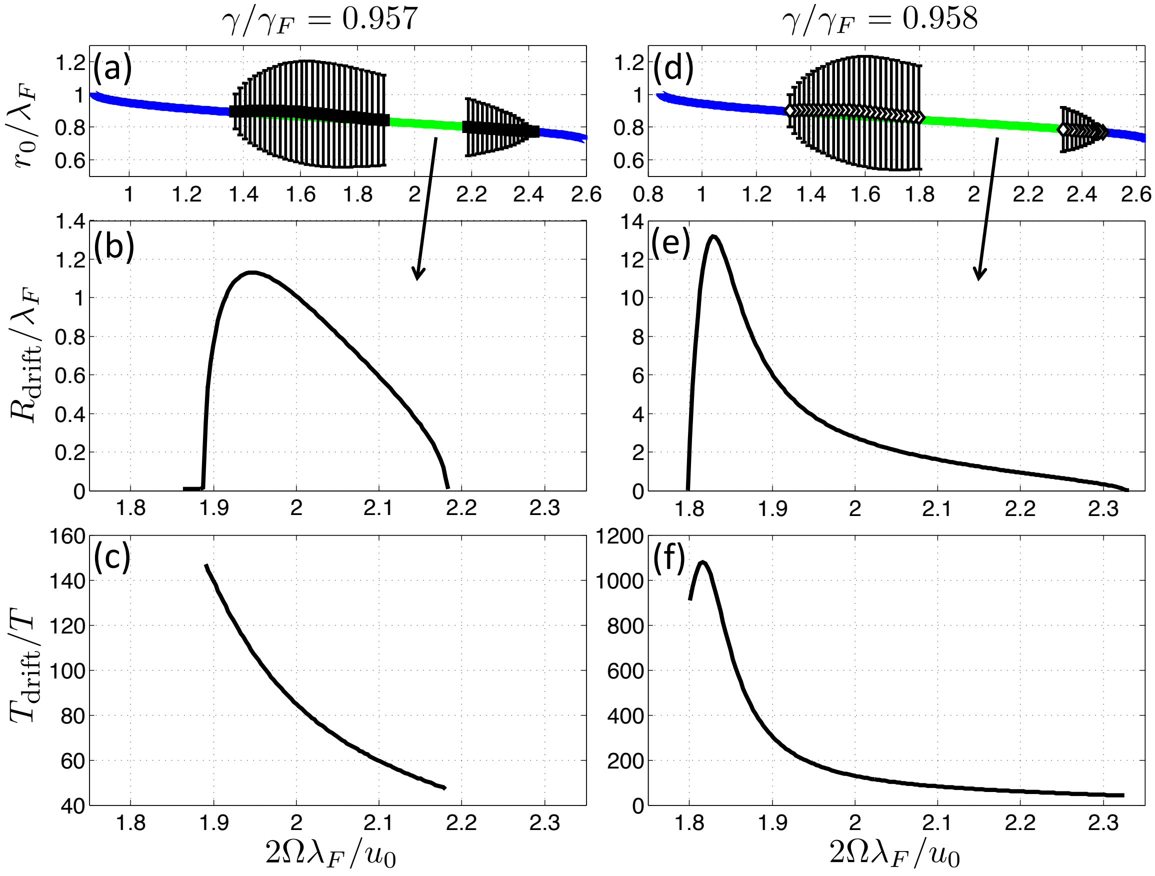

Figure 4-6: Numerical characterization of drifting orbits at $n = 1$. Top panels (a) and (d): the curve shows the theoretical orbital radius $r_0$ as a function of the nondimensional rotation rate $2\Omega\lambda_F/u_0$, calculated using (4.3). The blue segments indicate stable circular orbits, and the green unstable solutions due to an oscillatory instability. The trajectory equation (4.2) was numerically simulated within the green regions, and both wobbling and drifting orbits were found. The markers correspond to the mean orbital radius $\bar{r}$ of a wobbling orbit, and the error bars indicate the wobbling amplitude. The unmarked green regions correspond to drifting orbits, in which the orbital center $(\bar{x}_c, \bar{y}_c)$ drifts in a circle. The middle panels, (b) and (e), show the radius $R_{\text{drift}}$ of the orbital center, and the lower panels (c) and (f) the period of the orbital center $T_{\text{drift}}$ normalized by the orbital period $T$. Panels (a–c) correspond to a vibrational forcing $\gamma/\gamma_F = 0.957$ and (d–f) to $\gamma/\gamma_F = 0.958$.

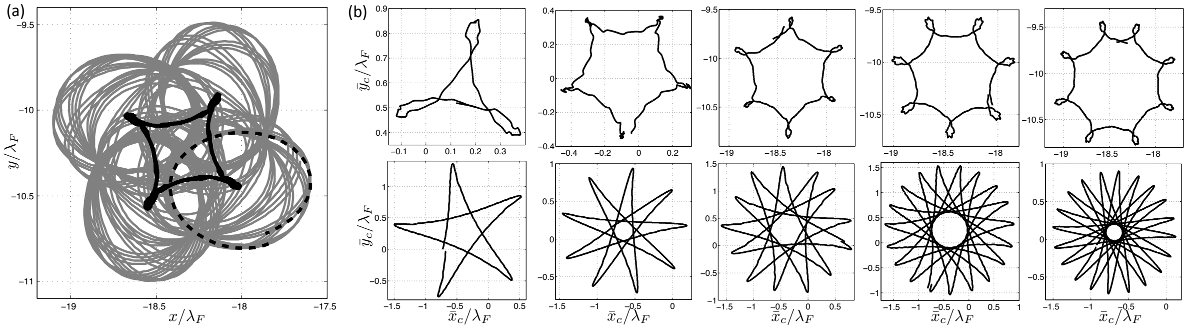

Figure 4-7: Numerical simulations of drifting orbits, for various values of the vibrational forcing $\gamma/\gamma_F$ and initial orbital radius $r_0$. In panel (a), the gray curve corresponds to a trajectory with $r_0/\lambda_F = 0.7262$ and $\gamma/\gamma_F = 0.971$, which consists of a loop (dashed black curve) that drifts along a square epicycle (black curve). The plots along the top row of panel (b) show the orbital centers of some drifting orbits at $n = 0$. From left to right, the parameter values are: $(r_0/\lambda_F, \gamma/\gamma_F) = (0.7221, 0.973)$, (0.3635, 0.968), (0.7514, 0.971), (0.7870, 0.971) and (0.775, 0.971). The bottom row shows those corresponding to $n = 1$, with parameter values $(r_0/\lambda_F, \gamma/\gamma_F) = (0.8541, 0.9612)$, (0.8537, 0.9609), (0.8541, 0.96125), (0.8542, 0.9613) and (0.8537, 0.96085), which correspond to the same dimensionless rotation rate $\hat{\Omega} = 0.5734$.

to the radius of a circular orbit at $n = 0$. A similar phenomenon was observed in the experiments of Harris and Bush [38], who reported a qualitatively similar trajectory (panel (e)).

While we did not find any wobble-and-leap trajectories at $n = 1$ for which the orbital center $\bar{\boldsymbol{x}}_c(t)$ followed a nearly periodic path, many were found at $n = 0$. Several such trajectories are shown in Fig. 4-9, which were found by varying the initial orbital radius $r_0$ and forcing acceleration $\gamma/\gamma_F$ over the narrow parameter range denoted by the purple portion of the $n = 0$ region in Fig. 4-2. The figure shows the orbital centers $\bar{\boldsymbol{x}}_c(t)$, the darker portions denoting the transiently stable orbital centers. Such trajectories are characterized by an extended wobbling phase which typically lasts more than twenty orbital periods. As is evident from Fig. 4-2, circular orbits generally destabilize into wobble-and-leap trajectories for $n = 0$, rather than into wobbling orbits as they do for $n = 1$ and $n = 2$.

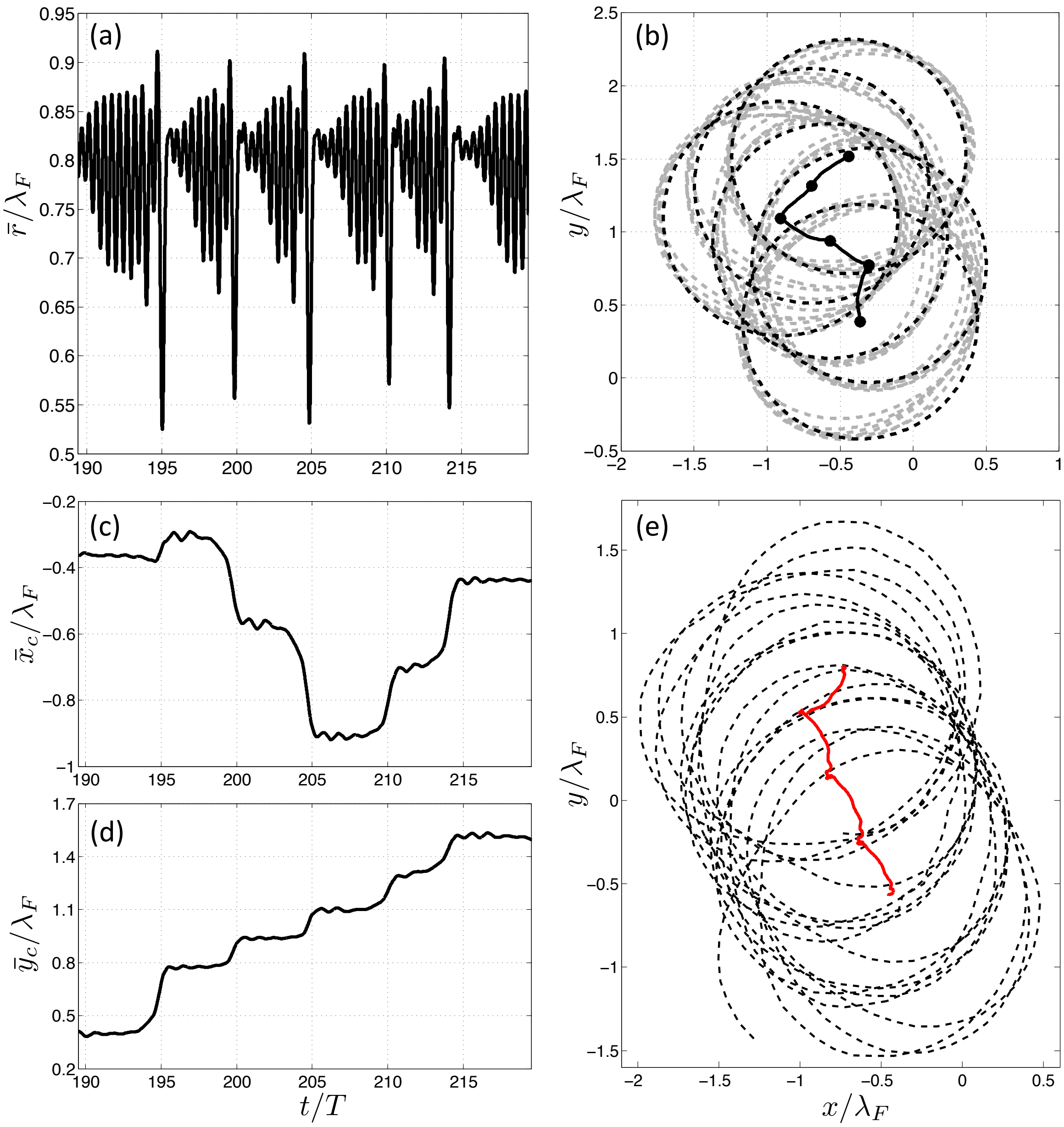

Figure 4-8: Numerical simulation of a wobble-and-leap trajectory at $n = 1$, obtained using initial orbital radius $r_0/\lambda_F = 0.8029$ and vibrational forcing $\gamma/\gamma_F = 0.960$. Panel (a) shows the mean orbital radius $\bar{r}(t)$. Panel (b) shows the trajectory (dashed gray curve), resulting from the orbital center (solid black curve) jumping between the transiently stable points (black dots). The dashed black curves are circles of radius $r_0/\lambda_F$ centered on the stable points. Panels (c) and (d) show the coordinates $\bar{x}_c(t)$ and $\bar{y}_c(t)$ of the orbital center. Panel (e) shows a qualitatively similar trajectory observed in the experiments of Harris and Bush [38], obtained using $\gamma/\gamma_F = 0.978 \pm 0.003$ and rotation rate $\Omega = 1.76$ s$^{-1}$. The trajectory is indicated by the dashed line, the center by the solid line.

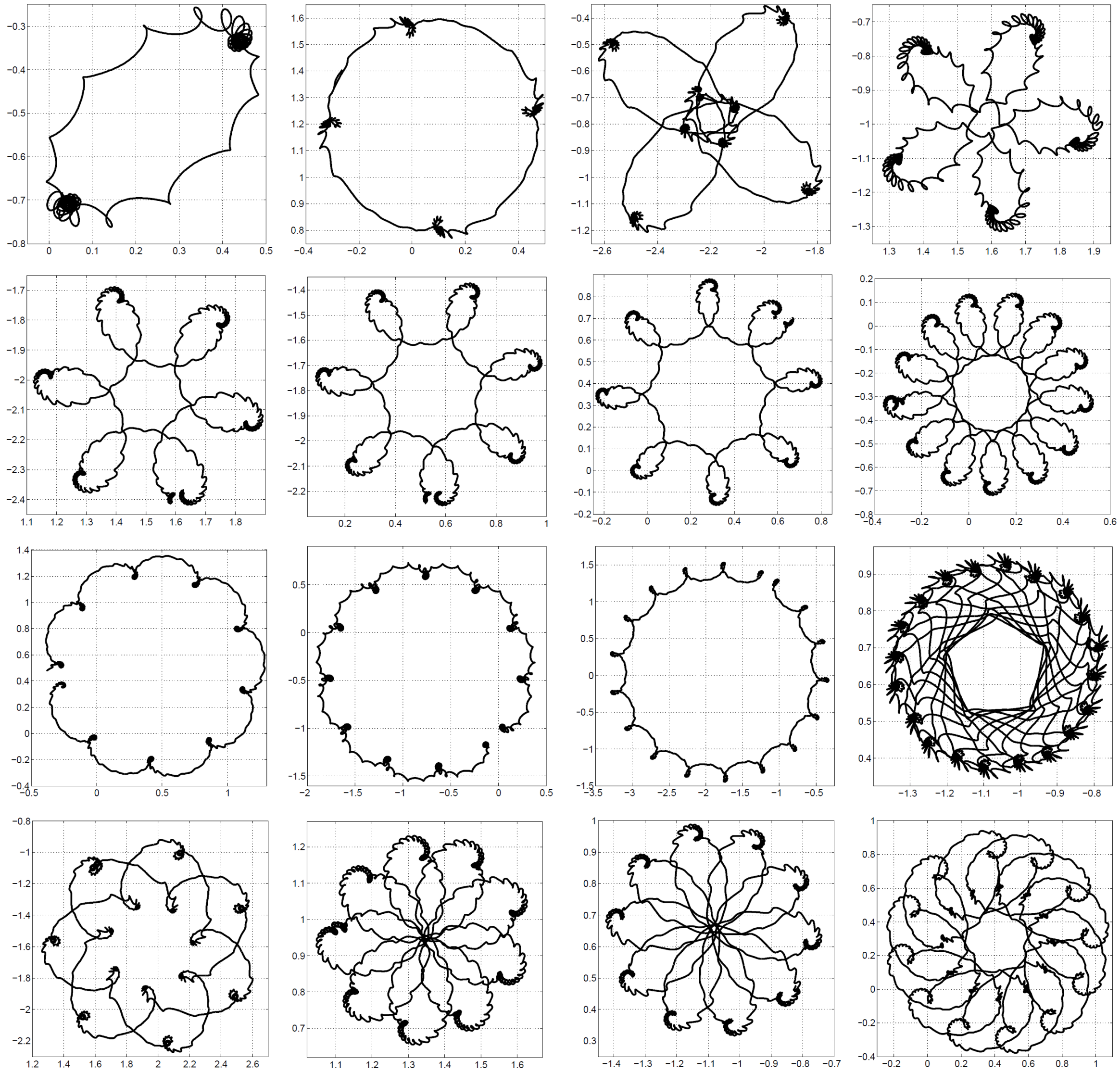

Figure 4-9: Numerical simulations of wobble-and-leap trajectories at $n = 0$, for various values of the initial radius $r_0/\lambda_F$ and vibrational forcing $\gamma/\gamma_F$. The plots show the paths of the orbital centers, nondimensionalized by the Faraday wavelength, $(\bar{x}_c(t), \bar{y}_c(t))/\lambda_F$. From top left to bottom right, the parameter values are: $(r_0/\lambda_F, \gamma/\gamma_F)$ = (0.376, 0.9665), (0.370, 0.966), (0.3769, 0.9665), (0.365, 0.966), (0.3654, 0.966), (0.3657, 0.966), (0.3659, 0.966), (0.3656, 0.966), (0.368, 0.966), (0.373, 0.9665), (0.372, 0.9665), (0.3763, 0.9665), (0.3775, 0.9665), (0.3647, 0.966), (0.370, 0.9665) and (0.370, 0.967).

## 4.6 Other periodic and quasiperiodic orbits

As the memory is increased progressively, the walker's trajectory becomes more complex. An assortment of other periodic or quasiperiodic trajectories is shown in Fig. 4-10. These trajectories, colored light blue in Fig. 4-2, have not yet been observed in laboratory experiments, presumably because they arise in such a limited region of parameter space. Many of them represent periodic windows in an otherwise chaotic regime.

A closer look at the trajectory shown in Fig. 4-11(a) reveals that it may be decomposed into the repeated loop shown in Fig. 4-11(b), which traverses a larger circle. The loop itself can be viewed as a combination of a larger loop (solid curve) and smaller loop (dashed curve). To quantify this, the loop radius $R(t)$ of the trajectory was computed using a modified osculating circle method with angle $\alpha = \pi/2$, which is described in the appendix of Harris and Bush [38]. The time trace of $R(t)$ is shown in Fig. 4-11(c), the gray portion corresponding to the loop in panel (b). It is evident that the loop radius executes persistent periodic oscillations between levels.

To elucidate the origin of this dynamics, we note that a number of unstable circular orbit solutions exist at this value of $\Omega$ and $\gamma/\gamma_F$, two of which have the radii indicated by the horizontal lines in Fig. 4-11(c). The complex trajectory in panel (a) appears to result from the walker jumping periodically between these unstable solutions. Based on the analogy between the Coriolis force on a walker and Lorentz force on an electron [32], we note that this trajectory is reminiscent of a Rabi oscillation, a quantum mechanical phenomenon in which an electron periodically jumps between two energy states in the presence of a oscillating magnetic field [14]. The possibility of forcing such an oscillation in this pilot-wave system by varying the rotation rate $\Omega$ will be pursued elsewhere.

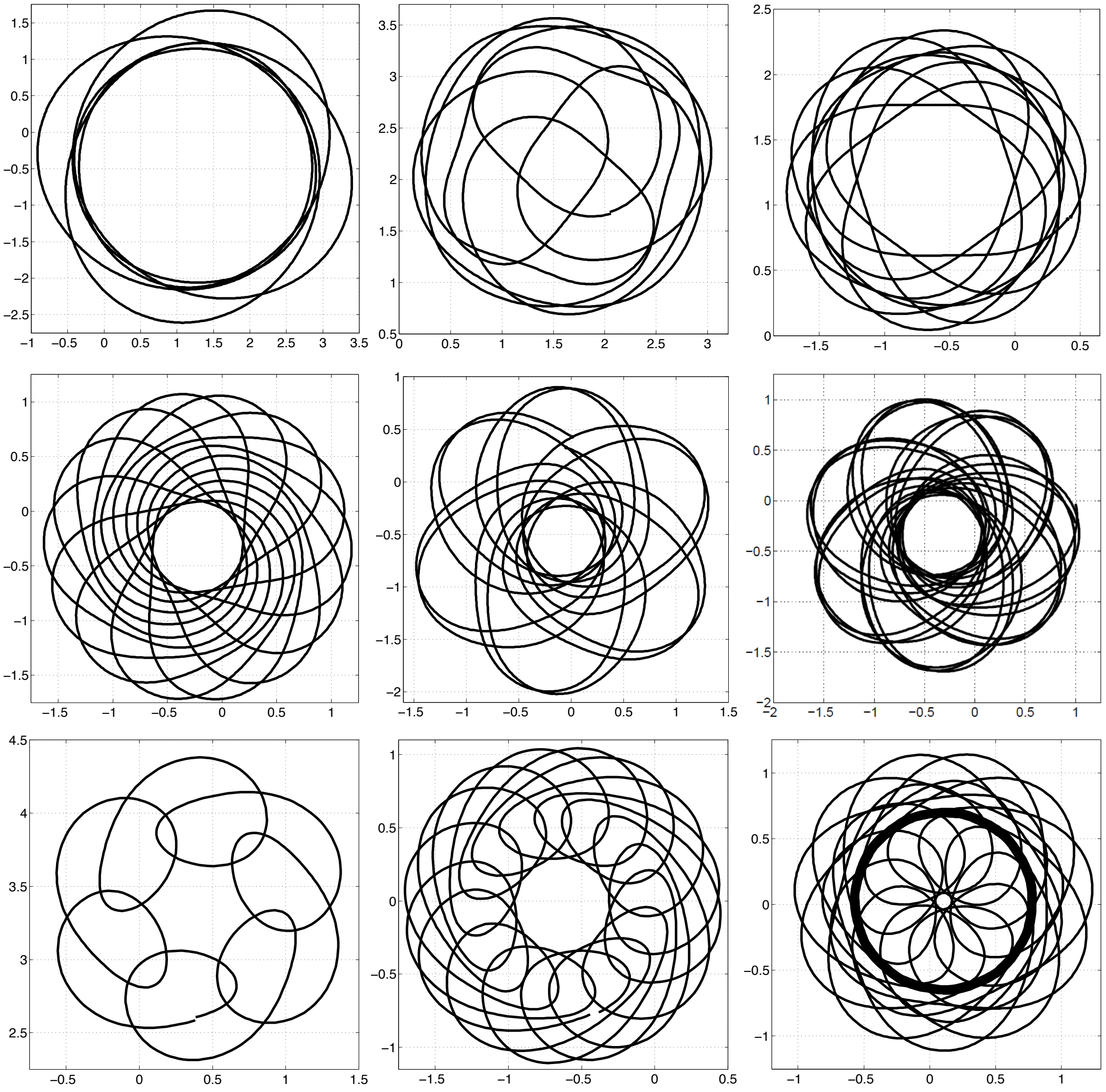

Figure 4-10: Numerical simulations of quasiperiodic trajectories observed for various values of the initial orbital radius $r_0/\lambda_F$ and vibrational forcing $\gamma/\gamma_F$. The plots show the trajectories nondimensionalized by the Faraday wavelength, $(x(t), y(t))/\lambda_F$. From top left to bottom right, the parameter values are: $(r_0/\lambda_F, \gamma/\gamma_F) = (1.4007, 0.97)$, (0.8924, 0.969), (0.8898, 0.966), (0.8778, 0.966), (0.8398, 0.961), (0.8249, 0.960), (0.3897, 0.976), (1.2348, 0.979) and (0.8417, 0.969).

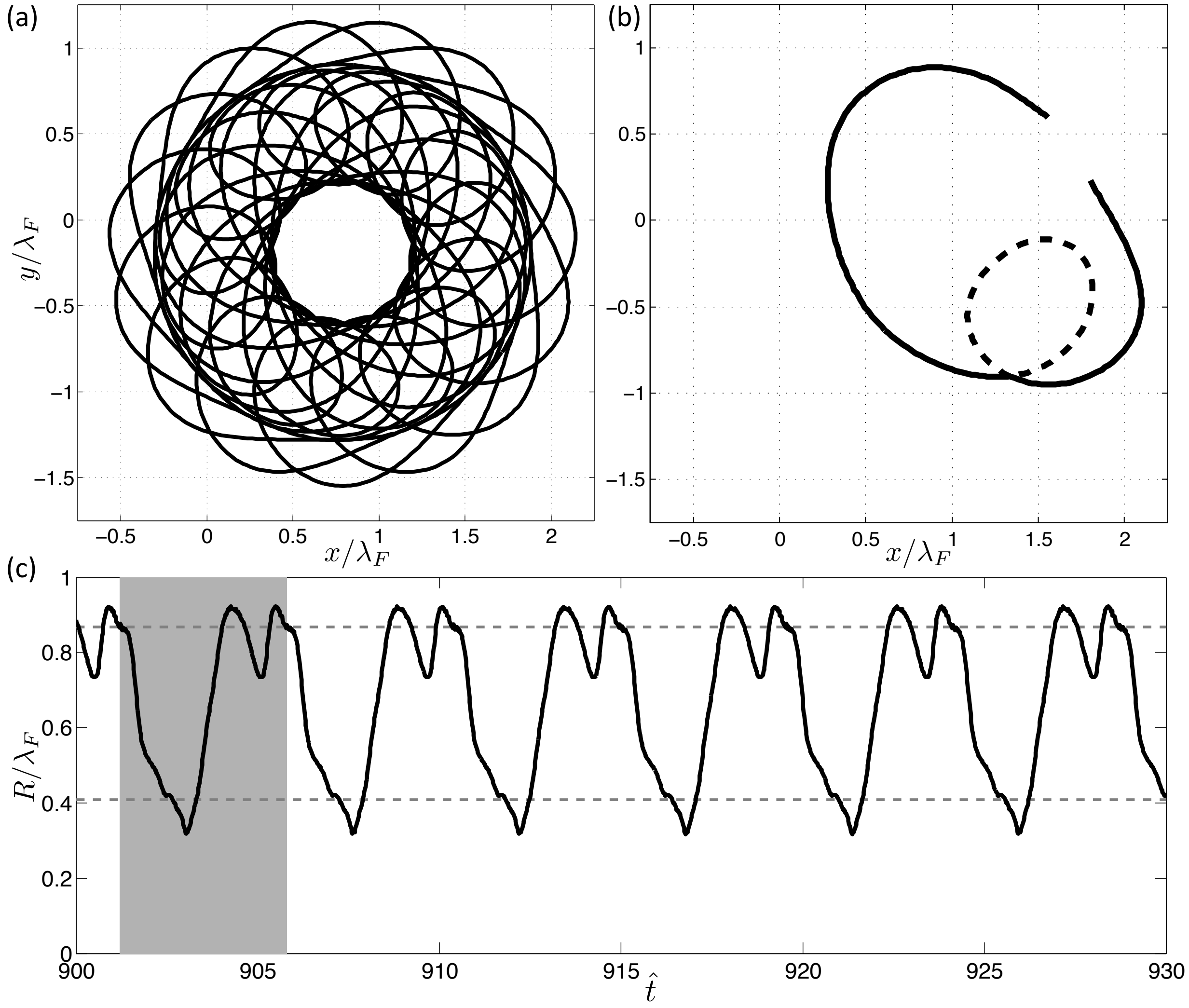

Figure 4-11: Numerical simulation of a trajectory exhibiting a periodic oscillation between two orbital radii, obtained using initial radius $r_0/\lambda_F = 1.2691$ and vibrational forcing $\gamma/\gamma_F = 0.971$. Panel (a) shows the trajectory, which consists of the loop in panel (b) drifting along a circle. Panel (c) shows the loop radius $R(t)$ of the trajectory. The shaded portion corresponds to the trajectory in panel (b). The walker evidently oscillates periodically between the two unstable orbital solutions with radii $r_0/\lambda_F = 0.409$ and $r_0/\lambda_F = 0.869$, indicated by the horizontal lines.

## 4.7 Chaotic pilot-wave dynamics

As the forcing acceleration $\gamma$ approaches the Faraday instability threshold $\gamma_F$, the trajectories become increasingly complex and chaotic, as indicated by the yellow regions in Fig. 4-2. An example of such a trajectory is shown in Fig. 4-12(a). To analyze such a complex trajectory, we compute its local loop radius $R(t)$ using a modified osculating circle method [38] with angle $\alpha = \pi/2$. The time trace of the loop radius is shown in panel (b), and the corresponding histogram in panel (c). The zeros of the Bessel function $J_0(k_F r)$, indicated by the dashed vertical lines, approximate well the maxima of the histogram, indicating that the chaotically evolving walker prefers to make loops roughly quantized on half the Faraday wavelength. It was previously shown (Chapter 3 [50]) that, in the high-memory regime, $\gamma/\gamma_F \to 1$, the orbital radii defined by (4.3) may be approximated by the zeros of $J_0(k_F r)$ and $J_1(k_F r)$. While all such orbital solutions are unstable, the former are less unstable than the latter (Chapter 5 [49]), as indicated by the eigenvalues of the linear stability problem. The footprint of these unstable circular orbits is thus present in the multimodal statistics of the walker's loop radius $R(t)$, an effect demonstrated in the laboratory experiments of Harris and Bush [38].

The walker's precise statistical behavior depends on the memory and rotation rate, as shown in Fig. 4-13 and Fig. 4-14. The top panels in Fig. 4-13 show the dependence of the statistics of $R(t)$ on the rotation rate $\Omega$ for three different values of forcing acceleration $\gamma/\gamma_F$. The vertical slices of the plots at $2\Omega\lambda_F/u_0 = 0.6$ correspond to the histograms in the lower panels, the color indicating the frequency count of a particular loop radius. Note that, for fixed forcing acceleration $\gamma/\gamma_F$, increasing the rotation rate shifts the histogram towards smaller loop radii, as expected.

Fig. 4-14 shows the dependence of the walker statistics on the memory, for a fixed value of the rotation rate. For a given value of $\gamma/\gamma_F$, the simulations were initiated with the circular orbit at $n = 4$. As in Fig. 4-13, each vertical column of Fig. 4-14(a) represents a histogram of $R(t)$. At low values of memory, a single circular orbit solution is accessible, as is indicated by the horizontal line. As the memory is

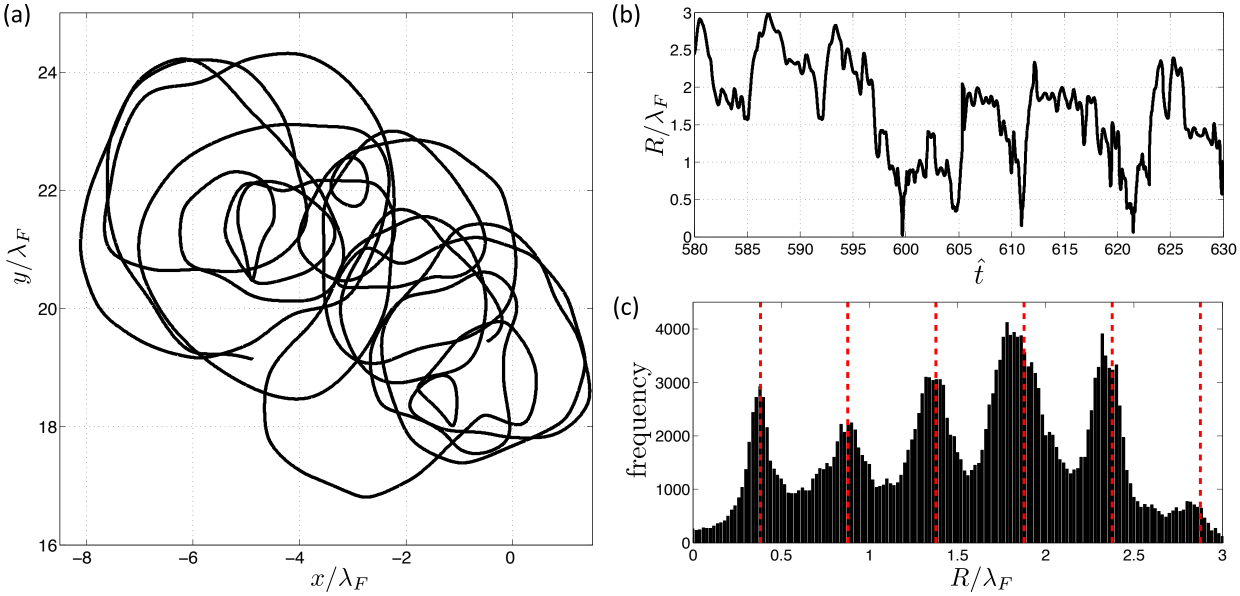

Figure 4-12: Numerical simulation of a chaotic trajectory in the high-memory regime, using time step $\Delta t = 2^{-8}$ and $t_{max} = 1000$. Panel (a) shows a portion of the trajectory, obtained using initial orbital radius $r_0/\lambda_F = 2.3775$ and vibrational forcing $\gamma/\gamma_F = 0.985$. Panel (b) shows the corresponding loop radius $R(t)$ over the same time interval, and panel (c) the histogram of the loop radius over the entire trajectory. The bin size is fixed at $0.02\lambda_F$. The vertical lines are located at the zeros of the Bessel function $J_0\left(k_F r\right)$.

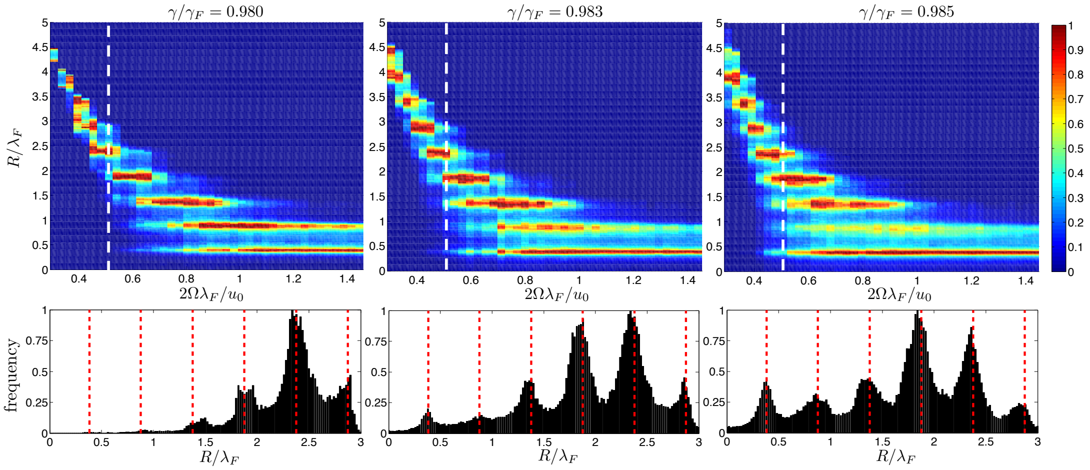

Figure 4-13: Numerical simulations showing the dependence of the orbital statistics on the dimensionless rotation rate $2\Omega\lambda_F/u_0$, for three different values of the vibrational forcing $\gamma/\gamma_F$. Each simulation was performed from stationary initial conditions, using time step $\Delta t = 2^{-8}$ and $t_{max} = 1000$. In the top panels, each column is colored according to the prevalence of the corresponding loop radius $R(t)$, with red segments being the most prevalent radii. The bottom panels show three histograms corresponding to $\hat{\Omega} = 0.17$ (or $2\Omega\lambda_F/u_0 \approx 0.5$), indicated by the vertical lines in the top panels. The peaks of the histograms are centered at the zeros of the Bessel function $J_0(k_F r)$, indicated by the vertical lines. The bin size is fixed at $0.02\lambda_F$.

progressively increased ($\gamma/\gamma_F \geq 0.97$), more orbital solutions become accessible. The orbital solutions then destabilize into wobbling orbits, then chaotic trajectories, as indicated by the broadening of the histograms. While all of the orbital solutions are unstable at high memory (Chapter 5 [49]), the sharp red bands in Fig. 4-14(a) reflect their persistent influence on the walker statistics.

## 4.8 Discussion

We have numerically simulated an integro-differential trajectory equation for the horizontal motion of a walker in a rotating frame. The results may be summarized in a regime diagram (Fig. 4-2), which delineates the dependence of the walker's trajectory on system parameters. Our numerical results rationalize the destabilization of circular orbits into wobbling orbits, drifting orbits, and wobble-and-leap orbits, all of which were found in the laboratory experiments of Harris and Bush [38]. Indeed,

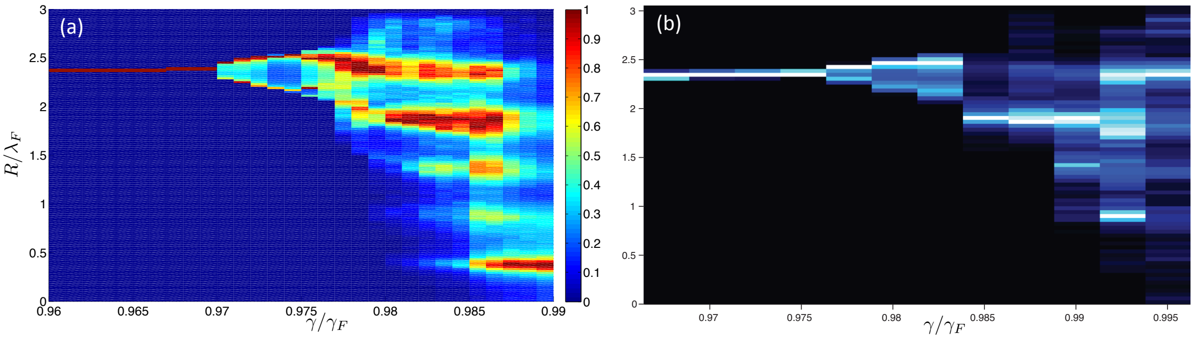

Figure 4-14: Numerical simulations showing the dependence of the orbital statistics on the vibrational forcing $\gamma/\gamma_F$. The simulations were initiated with the circular orbit at $n = 4$ corresponding to the fixed dimensionless rotation rate $\hat{\Omega} = 0.1784$ (or $\Omega = 0.70\ \text{s}^{-1}$), with time step $\Delta t = 2^{-8}$ and $t_{max} = 1000$. In panel (a), each column is colored according to the prevalence of the corresponding loop radius $R(t)$, with red segments being the most prevalent radii. Note that the brightest segments lie near the zeros of $J_0(k_F r)$. Panel (b) shows the corresponding experimental data from Harris and Bush [38], obtained for $\Omega = 0.79\ \text{s}^{-1}$.

many of these exotic trajectories were predicted by the numerical simulations and subsequently observed experimentally.

For $2\omega$-wobbling orbits, the wobbling amplitudes and frequencies obtained in the numerical simulations are consistent those reported in experiments [38]. Our simulations predict the existence of $3\omega$-wobbling orbits, which are expected to arise in a small region of parameter space. We have demonstrated that drifting orbits arise from the instability of $2\omega$-wobbling orbits. The orbital centers of drifting and wobble-and-leap orbits traverse a variety of periodic and quasiperiodic paths, revealing a rich nonlinear dynamics whose form depends strongly on both the bath rotation rate $\Omega$ and vibrational forcing $\gamma/\gamma_F$.

While the walker's trajectory becomes chaotic in the high-memory limit, $\gamma/\gamma_F \to 1$, its loop radius has a multimodal statistical behavior with peaks at the zeros of the Bessel function $J_0(k_F r)$, an effect observed in the experiments of Harris and Bush [38]. In this regime, the radii of circular orbits may be approximated by the zeros of $J_0(k_F r)$ and $J_1(k_F r)$ (Chapter 3 [50]). Linear stability analysis shows that these solutions are unstable, the former being less unstable than the latter (Chapter 5 [49]). The walker thus jumps intermittently between the least unstable orbital solutions, whose influence is apparent in the coherent multimodal statistics.

The relatively small discrepancies between the laboratory experiments of Harris and Bush [38] and the numerical results reported herein most likely arise from our neglect of the walker's vertical dynamics, as the trajectory equation (4.1) is obtained by time-averaging the forces on the walker over the bouncing period. We also assume the phase $\sin \Phi$ to be constant, while it is known to depend weakly on the vibrational forcing $\gamma/\gamma_F$ and fluid viscosity [46]. Nevertheless, the satisfactory agreement between the experiments and model predictions suggests that the essential features of the walker's pilot-wave dynamics are captured by the trajectory equation (4.1).

In their experimental study of walker dynamics in a harmonic potential, Perrard et al. [52] also report complex orbits, including lemniscates and trefoils centered at the origin. They interpret these complex orbits in terms of a double quantization in mean radius and angular momentum of the observed trajectories. In our system, while quantization of the angular momentum in the circular orbits was clearly evident, no such double-quantization was apparent. Specifically, we find that the mean radius and angular momentum of drifting orbits depends continuously rather than discretely on the rotation rate $\Omega$, as suggested by Fig. 4-6. We note, however, that the walker dynamics in these two systems is qualitatively different, as the orbital center is not imposed in the rotating system. While we observe erratic trajectories at high memory, one can imagine that quantized drifting orbits might arise for a different choice of fluid parameters, or in a more general pilot-wave setting.

Having benchmarked our model against the experimental results of Harris and Bush [38], we may now turn our attention to pilot-wave systems with different external forces and geometries. In future work, we plan to numerically characterize the dynamics of a walker in a harmonic potential, a system currently being studied in the laboratory of Yves Couder [52]. A similar approach will also enable us to study pilot-wave systems that are not accessible in the laboratory. It is our hope that such an investigation into the rich nonlinear pilot-wave dynamics of walkers will yield further insight into their quantum-like behavior.

# Chapter 5

# Orbital stability in hydrodynamic pilot-wave theory

## 5.1 Introduction

In this chapter, we present a complete framework for assessing the stability of circular orbit solutions to the integro-differential trajectory equation

$$m\ddot{\boldsymbol{x}} + D\dot{\boldsymbol{x}} = \frac{F}{T_F}\int_{-\infty}^{t} J_1\left(k\left|\boldsymbol{x}(t)-\boldsymbol{x}(s)\right|\right)\frac{\boldsymbol{x}(t)-\boldsymbol{x}(s)}{\left|\boldsymbol{x}(t)-\boldsymbol{x}(s)\right|}\mathrm{e}^{-(t-s)/T_M}\,\mathrm{d}s - 2m\boldsymbol{\Omega}\times\dot{\boldsymbol{x}}. \quad (5.1)$$

This equation was proposed in Chapter 3 as a model for droplets walking on the surface of a vertically vibrating fluid bath rotating about its centerline with angular frequency $\boldsymbol{\Omega} = \Omega\hat{\boldsymbol{z}}$. The methodology presented herein was used in Chapter 3 [50] to rationalize the experimental observations reported by Fort et al. [32] and Harris and Bush [38]. This study culminates in a stability diagram that delineates the stability characteristics of circular orbits as a function of their radii and the forcing acceleration. This chapter provides the mathematical foundation for the stability analysis in Chapter 3, and provides some insight into the numerical results presented

---

This chapter is to be submitted as: Orbital stability in hydrodynamic pilot-wave theory, Oza, A. U., Bush, J. W. M. and Rosales, R. R., *SIAM Journal on Applied Mathematics* [49].

in Chapter 4.

The chapter is organized as follows. In §5.2, we give a simplified derivation of the integro-differential equation of motion based on a few generic assumptions about the physical system. In §5.3, we demonstrate that the bouncing solution $\boldsymbol{x}$ = constant becomes unstable via a Hopf bifurcation above a critical value of the forcing acceleration $\gamma$, and below a critical value of the rotation rate $\Omega$. The properties of orbital solutions to (5.1) are discussed in §5.4. In §5.5, we demonstrate using Laplace transforms that the eigenvalues of the linear stability problem for orbital solutions are the roots of a function $F(s)$. We show in §5.5.1 that $F$ has three trivial roots that correspond to the invariance of (5.1) under translation and rotation. In §5.6, we perform asymptotic expansions of $F(s)$ in various limiting cases, showing that orbits of small radius (§5.6.1), large radius (§5.6.2), and weak forcing acceleration (§5.6.3) are stable.

Outside of these asymptotic regimes, we must find the roots of $F$ numerically, and we present a systematic method for doing so in §5.7. While $F(s)$ has infinitely many roots, we show in §5.7.1 that, for a fixed value of $\gamma$, only finitely many of them can generate an instability, thus ensuring the tractability of our numerical method. We present the results of the linear stability analysis in §5.8, culminating in a diagram that delineates the dependence of the stability characteristics on the orbital radius and forcing acceleration $\gamma$ (§5.8.1). In §5.8.2, we discuss the properties of wobbling orbits, which were predicted by the linear stability theory and subsequently observed in laboratory experiments [38]. In §5.8.3, we discuss the extent to which the walker's chaotic dynamics, as observed in laboratory experiments [38] and numerical simulations (Chapter 4 [51]), can be understood through the linear stability analysis. We summarize our results and discuss future directions in §5.9.

## 5.2 Integro-differential trajectory equation

We here summarize the derivation of the trajectory equation for the horizontal motion of a walker in the absence of boundaries, the complete derivation having been presented elsewhere ([46], Chapter 2 [48]). We restrict our attention to the regime $\gamma_{PDB} < \gamma < \gamma_F$, in which the walker is in a period-doubled bouncing state, and the fluid surface would remain flat if not for the presence of the walker.

Let $\boldsymbol{x}_p(t) = (x_p(t), y_p(t))$ denote the horizontal position of a walker of mass $m$ bouncing with period $T_F = 2/f$ in the presence of an external force $\boldsymbol{F}_{ext}$. The force balance in the horizontal direction yields the trajectory equation

$$m\ddot{\boldsymbol{x}}_p + D\dot{\boldsymbol{x}}_p = -F\boldsymbol{\nabla}h(\boldsymbol{x}_p, t) + \boldsymbol{F}_{ext}, \tag{5.2}$$

where all terms denote time-averages over the bouncing period. The walker moves in response to three forces: the external force, a drag force $-D\dot{\boldsymbol{x}}_p$, and a propulsive force $-F\boldsymbol{\nabla}h(\boldsymbol{x}_p, t)$ proportional to the local gradient of the fluid surface. The interface height is given by the expression (Chapter 2 [48])

$$h(\boldsymbol{x}, t) = \frac{1}{k_F T_F}\int_{-\infty}^{t} J_0\left(k_F\left|\boldsymbol{x} - \boldsymbol{x}_p(s)\right|\right)\mathrm{e}^{-(t-s)/T_M}\,\mathrm{d}s, \tag{5.3}$$

where $k_F$ is the Faraday wavenumber. The temporal decay time $T_M$ is related to the forcing acceleration $\gamma$ by the formula [29, 46]

$$T_M(\gamma) = \frac{T_d}{1 - \gamma/\gamma_F}, \tag{5.4}$$

where $T_d$ is the decay time of the waves in the absence of forcing, $\gamma = 0$. We thus obtain the integro-differential trajectory equation (Chapter 2 [48])

$$m\ddot{\boldsymbol{x}}_p + D\dot{\boldsymbol{x}}_p = \frac{F}{T_F}\int_{-\infty}^{t} J_1\left(k_F\left|\boldsymbol{x}_p(t) - \boldsymbol{x}_p(s)\right|\right)\frac{\boldsymbol{x}_p(t) - \boldsymbol{x}_p(s)}{\left|\boldsymbol{x}_p(t) - \boldsymbol{x}_p(s)\right|}\mathrm{e}^{-(t-s)/T_M}\,\mathrm{d}s + \boldsymbol{F}_{ext}. \tag{5.5}$$

Formulae for the constants $D$, $F$, $k_F$ and $T_d$ in terms of the fluid parameters are given by Moláček and Bush [46] and in Chapter 2 [48]. We note that they are independent of the forcing acceleration, which appears in (5.5) through the decay time $T_M$.

A derivation of (5.3) was presented in Chapter 2 [48], based on the detailed analysis of the wave field by Moláček and Bush [46]. However, we may give a simplified derivation based on the following generic assumptions:

1. The system is linear and invariant under rotation and translation in two dimensions.
2. The system is forced periodically with frequency $\omega$ by a rotationally symmetric source.
3. All disturbances generated by the source decay in time. However, there is a single dominant mode with a minimal decay rate, and it has the same frequency $\omega$ as the forcing.

We first determine the height of the interface $h_n(\boldsymbol{x}, t)$ in response to a single impact at time $t_n = nT_F$ and position $\boldsymbol{x}_n = \boldsymbol{x}_p(t_n)$. Linearity and translation invariance imply that the disturbances have the form $\exp\left(i\boldsymbol{k} \cdot (\boldsymbol{x} - \boldsymbol{x}_n) - \lambda(t - t_n)\right)$, where $\lambda = F(k)$ for $k = |\boldsymbol{k}|$ due to rotational invariance. We only retain the contribution from the dominant mode with the minimal decay rate $\nu^*$, where $F(k^*) = \nu^* + i\omega$. The dominant mode thus has the form

$$\exp\left(ik^* \left|\boldsymbol{x} - \boldsymbol{x}_n\right| \cos\theta\right) \exp\left(-\left(\nu^* + i\omega\right)\left(t - t_n\right)\right), \tag{5.6}$$

$\theta$ being the angle between $\boldsymbol{k}$ and $(\boldsymbol{x} - \boldsymbol{x}_n)$. Since the system is invariant under rotation, we may integrate over $\theta$ and obtain the mode profile

$$J_0\left(k^* \left|\boldsymbol{x} - \boldsymbol{x}_n\right|\right) \exp\left(-\left(\nu^* + i\omega\right)\left(t - t_n\right)\right). \tag{5.7}$$

The source is assumed to be in resonance with this mode and thus is not affected by the temporal oscillation, so the effective interface height from a single impact is $h_n(\boldsymbol{x}, t) \propto J_0\left(k^* \left|\boldsymbol{x} - \boldsymbol{x}_n\right|\right) \mathrm{e}^{-\nu^*(t - t_n)}$. Assuming that the disturbances are small, the full interface height $h(\boldsymbol{x}, t)$ is simply the linear superposition of the contributions from prior impacts $h_n(\boldsymbol{x}, t)$. Since the walker's horizontal dynamics occurs over a timescale long relative to the bouncing period, $T_F \ll \left(k^* |\dot{\boldsymbol{x}}_p|\right)^{-1}$, we may replace the sum over discrete impacts by the integral (5.3) (Chapter 2 [48]).

In the context of the experiment under consideration, the fluid bath is forced periodically with acceleration $\gamma \cos(2\pi f t)$, so Assumption #3 is satisfied through the mechanism of parametric resonance [3, 41]. Below the Faraday instability threshold, $\gamma < \gamma_F$, the dominant mode has wavelength $k^* = k_F$, where the Faraday wavenumber $k_F$ may be approximated by the solution to the standard water-wave dispersion relation [41]. The temporal evolution of the mode is governed by a Mathieu equation with a viscous correction term [41, 29, 46]. It can be shown using Floquet theory that the mode has frequency $\omega = f/2$ and decay rate $\nu^* = 1/T_M$, where $T_M$ is given by (5.4) [41, 46].

Motivated by the laboratory experiments in [32, 38], we here consider the dynamics of a droplet walking on a fluid bath rotating about its centerline with angular frequency $\underline{\boldsymbol{\Omega}} = \underline{\Omega}\hat{\boldsymbol{z}}$. As shown in Chapter 3 [50], the appropriate trajectory equation is obtained by augmenting (5.5) with a Coriolis force term:

$$\begin{aligned} m\ddot{\boldsymbol{x}}_p + D\dot{\boldsymbol{x}}_p \quad &= \quad \frac{F}{T_F}\int_{-\infty}^{t} J_1\left(k_F\left|\boldsymbol{x}_p(t)-\boldsymbol{x}_p(s)\right|\right)\frac{\boldsymbol{x}_p(t)-\boldsymbol{x}_p(s)}{\left|\boldsymbol{x}_p(t)-\boldsymbol{x}_p(s)\right|}\mathrm{e}^{-(t-s)/T_M}\,\mathrm{d}s \\ &\quad\; -2m\underline{\boldsymbol{\Omega}}\times\dot{\boldsymbol{x}}_p. \qquad (5.8) \end{aligned}$$

We proceed by studying the stability properties of bouncing and orbiting solutions to this trajectory equation.

## 5.3 Bouncing to orbiting

We non-dimensionalize the trajectory equation (5.8) via $\boldsymbol{x} \to k_F\boldsymbol{x}$ and $t \to t/T_M$, and thus obtain the dimensionless equation

$$\kappa\ddot{\boldsymbol{x}}_p + \dot{\boldsymbol{x}}_p = \beta\int_{-\infty}^{t} J_1\left(\left|\boldsymbol{x}_p(t)-\boldsymbol{x}_p(s)\right|\right)\frac{\boldsymbol{x}_p(t)-\boldsymbol{x}_p(s)}{\left|\boldsymbol{x}_p(t)-\boldsymbol{x}_p(s)\right|}\mathrm{e}^{-(t-s)}\,\mathrm{d}s - \boldsymbol{\Omega}\times\dot{\boldsymbol{x}}_p, \quad (5.9)$$

where $\kappa = m/DT_M$, $\beta = Fk_FT_M^2/DT_F$ and $\boldsymbol{\Omega} = 2m\underline{\boldsymbol{\Omega}}/D$. We note that both $\kappa$ and $\beta$ depend on the forcing acceleration $\gamma$ through (5.4), while $\kappa^2\beta$ is a constant that depends only on the fluid properties (viscosity, drop size, etc.).

We first demonstrate that the bouncing solution $\boldsymbol{x}_p \equiv$ constant is stable provided the rotation rate exceeds a critical value, $|\Omega| > \Omega_0$. We proceed by linearizing (5.9) around this solution, $\boldsymbol{x}_p =$ constant $+ \epsilon \boldsymbol{x}_1(t)$, and deduce

$$\kappa \ddot{\boldsymbol{x}}_1 + \dot{\boldsymbol{x}}_1 = \frac{\beta}{2} \int_{-\infty}^{t} [\boldsymbol{x}_1(t) - \boldsymbol{x}_1(s)] \mathrm{e}^{-(t-s)} \, \mathrm{d}s - \boldsymbol{\Omega} \times \dot{\boldsymbol{x}}_1, \tag{5.10}$$

where we have used the fact that $J_1'(0) = 1/2$. This equation can be expressed as a system of ordinary differential equations by introducing the variable

$$\boldsymbol{X}_1(t) = \int_{-\infty}^{t} \boldsymbol{x}_1(s) \mathrm{e}^{-(t-s)} \, \mathrm{d}s. \tag{5.11}$$

Solutions to (5.10) are thus a subset of solutions to the system of equations

$$\kappa \ddot{\boldsymbol{x}} + \dot{\boldsymbol{x}} = \frac{\beta}{2}(\boldsymbol{x} - \boldsymbol{X}) - \boldsymbol{\Omega} \times \dot{\boldsymbol{x}}, \quad \dot{\boldsymbol{X}} = \boldsymbol{x} - \boldsymbol{X}. \tag{5.12}$$

Letting $\dot{x} = u$ and $\dot{y} = v$, we obtain the system

$$\frac{\mathrm{d}}{\mathrm{d}t} \begin{bmatrix} x \\ u \\ X \\ y \\ v \\ Y \end{bmatrix} = \begin{bmatrix} 0 & 1 & 0 & 0 & 0 & 0 \\ \frac{\beta}{2\kappa} & -\frac{1}{\kappa} & -\frac{\beta}{2\kappa} & 0 & \frac{\Omega}{\kappa} & 0 \\ 1 & 0 & -1 & 0 & 0 & 0 \\ 0 & 0 & 0 & 0 & 1 & 0 \\ 0 & -\frac{\Omega}{\kappa} & 0 & \frac{\beta}{2\kappa} & -\frac{1}{\kappa} & -\frac{\beta}{2\kappa} \\ 0 & 0 & 0 & 1 & 0 & -1 \end{bmatrix} \begin{bmatrix} x \\ u \\ X \\ y \\ v \\ Y \end{bmatrix}, \tag{5.13}$$

which has the characteristic polynomial

$$p(s) = s^2 \left\{ \left[ \frac{\beta}{2\kappa} - (1+s)\left(\frac{1}{\kappa} + s\right) \right]^2 + \frac{\Omega^2}{\kappa^2}(1+s)^2 \right\}. \tag{5.14}$$

The $s = 0$ solutions simply indicate that the bouncing state is invariant under translation and rotation, so we neglect them. The four remaining roots can be written as

$s_{\pm_1}^{\pm_2} = a_{\pm_1} + \mathrm{i}b_{\pm_2}$, with real part

$$\begin{aligned}
\Re\left[s_{\pm_1}^{\pm_2}\right] &= a_{\pm_1} = \frac{1}{2}\left(-f \pm g\right), \quad \text{where } f = 1 + \frac{1}{\kappa}, \quad g^2 = h_1 + h_2, \\
h_1 &= \frac{1}{2}\left[\left(1 + \frac{1}{\kappa}\right)^2 - 4\left(\frac{\Omega^2}{4\kappa^2} + \frac{1}{\kappa} - \frac{\beta}{2\kappa}\right)\right], \quad \text{and} \\
h_2^2 &= \frac{1}{4}\left[\frac{4\Omega^2}{\kappa^2}\left(1 - \frac{1}{\kappa}\right)^2 + \left[-\frac{\Omega^2}{\kappa^2} + \frac{2\beta}{\kappa} + \left(1 - \frac{1}{\kappa}\right)^2\right]^2\right].
\end{aligned} \tag{5.15}$$

Note that $a_{-1} < 0$ since $f, g > 0$, so the stability of the bouncing state is controlled by the sign of $a_{+1}$, which may be written as

$$\operatorname{sgn}\left(a_{+1}\right) = -\operatorname{sgn}\left(f^2 - h_1 - h_2\right) = \begin{cases} -\operatorname{sgn}\left[\left(f^2 - h_1\right)^2 - h_2^2\right], & f^2 - h_1 > 0 \\ +1, & f^2 - h_1 < 0. \end{cases} \tag{5.16}$$

For a fixed value of $\kappa$, let $\mathcal{P}_1 = \{(\beta, \Omega) : \left(f^2 - h_1\right)^2 - h_2^2 < 0\,,\, f^2 - h_1 > 0\}$ and $\mathcal{P}_2 = \{(\beta, \Omega) : f^2 - h_1 < 0\}$, so that the bouncing state is unstable for $(\beta, \Omega) \in \mathcal{P}_1 \cup \mathcal{P}_2$. Note that

$$\begin{aligned}
\left(f^2 - h_1\right)^2 - h_2^2 &= \frac{4}{\kappa^3}\left[\Omega^2 - \left(\frac{\beta}{2} - 1\right)(1 + \kappa)^2\right], \\
f^2 - h_1 &= \frac{1}{2\kappa^2}\left[(1 + \kappa)^2 + \Omega^2 - 4\kappa\left(\frac{\beta}{2} - 1\right)\right].
\end{aligned} \tag{5.17}$$

The boundaries of $\mathcal{P}_1$ and $\mathcal{P}_2$ are thus defined by the curves $\Omega^2 = p_1(\beta)$ and $\Omega^2 = p_2(\beta)$, where $p_1(\beta) = (\beta/2 - 1)(1 + \kappa)^2$ and $p_2(\beta) = 4\kappa(\beta/2 - 1) - (1 + \kappa)^2$. The curves do not intersect since $p_1(\beta) - p_2(\beta) = \frac{1}{2}\left[\beta(-1 + \kappa)^2 + 8\kappa\right] > 0$, so the stability boundary is determined by the curve $\Omega^2 = p_1(\beta)$. We thus deduce that the bouncing state is unstable for $\beta > 2$ and $|\Omega| < \Omega_0 \equiv (1 + \kappa)\sqrt{\beta/2 - 1}$, and stable otherwise. For $\beta > 2$ and $\Omega = \Omega_0$, the nontrivial roots of $p(s)$ are

$$s = \pm\mathrm{i}\sqrt{\frac{\beta}{2} - 1}, \quad s = \frac{1}{\kappa}\left(-(1 + \kappa) \pm \mathrm{i}\sqrt{\frac{\beta}{2} - 1}\right). \tag{5.18}$$

The presence of imaginary eigenvalues at $|\Omega| = \Omega_0$ suggests that the bouncing solution destabilizes into a periodic solution via a Hopf bifurcation. We will prove in §5.6.1 that this solution is stable.

This analysis bears some resemblance to the theoretical treatment of walker dynamics in the absence of an external force ($\boldsymbol{F}_{ext} = 0$), which was presented in Chapter 2 [48]. The bouncing state $\boldsymbol{x}_p = \text{constant}$ was shown to be stable for $\beta < 2$ and unstable otherwise, indicating that $\beta = 2$ corresponds to the walking threshold $\gamma = \gamma_W$. The bouncing state was also shown to destabilize into a steady rectilinear walking solution for $\beta \gtrsim 2$ via a supercritical pitchfork bifurcation. For $\beta > 2$, the trajectory equation admits the steady rectilinear walking solution $\boldsymbol{x}_p(t) = u_0 t(\cos\theta, \sin\theta)$, where

$$u_0 = \frac{1}{\sqrt{2}}\left(-1 + 2\beta - \sqrt{1+4\beta}\right)^{1/2} \tag{5.19}$$

is the walking speed and $\theta$ the walking direction. The predicted dependence of the walking speed $u_0$ on the forcing acceleration $\gamma$ agrees well with experimental observations (Chapter 2 [48]). It was also shown that the walking state is stable to perturbations in the direction of motion and neutrally stable to lateral perturbations, indicating that the walker may change its direction if so perturbed.

## 5.4 Orbital solutions

The analysis in §5.3 suggests that the bouncing state destabilizes into a limit cycle via a Hopf bifurcation at $|\Omega| = \Omega_0$ so we seek periodic solutions to (5.20). Substituting $\boldsymbol{x}_p(t) = r_0(\cos\omega t, \sin\omega t)$ into (5.20), we obtain a system of algebraic equations that determines the orbital radius $r_0$ and frequency $\omega$ in terms of the parameters $\Omega, \kappa$ and $\beta$:

$$\begin{aligned} -\kappa r_0\omega^2 &= \beta\int_0^\infty J_1\left(2r_0\sin\frac{\omega z}{2}\right)\sin\frac{\omega z}{2}\mathrm{e}^{-z}\,\mathrm{d}z + \Omega r_0\omega \\ r_0\omega &= \beta\int_0^\infty J_1\left(2r_0\sin\frac{\omega z}{2}\right)\cos\frac{\omega z}{2}\mathrm{e}^{-z}\,\mathrm{d}z. \end{aligned} \tag{5.20}$$

Figures 3-1 and 3-2 show the predicted dependence of the orbital radius $r_0$ on the rotation rate $\Omega$ for different values of the forcing acceleration $\gamma$, compared with experimental data [38]. Stable orbital solutions are indicated in blue, while unstable ones are indicated in red and green. We note that these equations are symmetric under the change $(\omega, \Omega) \to (-\omega, -\Omega)$, the plots in Figures 3-1 and 3-2 corresponding to the regime $\Omega \geq 0$ and $\omega < 0$.

For the remainder of this chapter, we take $\omega > 0$ without loss of generality, unless otherwise stated. We now present a numerical justification for the following two statements, which will be used throughout the chapter.

**Proposition 1** *The second equation in (5.20) defines $\omega$ as a single-valued and infinitely differentiable function of both $r_0$ and $\beta$ for $r_0 \geq 0$ and $\beta > 2$. The function $\omega$ decreases monotonically with $r_0$ and increases with $\beta$.*

**Proposition 2** *The equations in (5.20) define $\Omega$ as a single-valued and infinitely differentiable function of both $r_0$ and $\beta$ for $r_0 \geq 0$ and $\beta > 2$, with $\Omega \geq -\omega(1+\kappa)$.*

Beginning with Proposition 1, we write (5.20) in the form

$$\frac{\Omega + \omega(1+\kappa)}{\beta} = \frac{\omega}{\beta} - U(r_0, \omega), \quad \frac{\omega}{\beta} = V(r_0, \omega), \tag{5.21}$$

where

$$\begin{aligned} U(r_0, \omega) &= \frac{1}{r_0 \omega} \int_0^\infty J_1\left(2r_0 \sin\frac{\omega z}{2}\right) \sin\frac{\omega z}{2} \mathrm{e}^{-z}\, \mathrm{d}z \\ V(r_0, \omega) &= \frac{1}{r_0} \int_0^\infty J_1\left(2r_0 \sin\frac{\omega z}{2}\right) \cos\frac{\omega z}{2} \mathrm{e}^{-z}\, \mathrm{d}z. \end{aligned} \tag{5.22}$$

Figure 5-1(a) shows numerical plots of the cross sections $v_{r_0}(\omega) \equiv V(r_0, \omega)$ for various values of $r_0$, starting with $V(0, \omega) = \omega/2(1+\omega^2)$. The plots suggest that each cross section $v_{r_0}(\omega)$ has a unique maximum $\omega_m(r_0)$, and that $v_{r_0}(\omega)$ is concave for $\omega < \omega_m$. The orbital frequency $\omega(r_0, \beta)$ is defined by the intersection of the curves $v_{r_0}(\omega)$ with $\omega/\beta$, indicated by the dashed lines. Note that the absence of an intersection for $\beta < 2$, due to the fact that $V(r_0, \omega) \sim \omega/2$ as $\omega \to 0$, indicates that orbital solutions

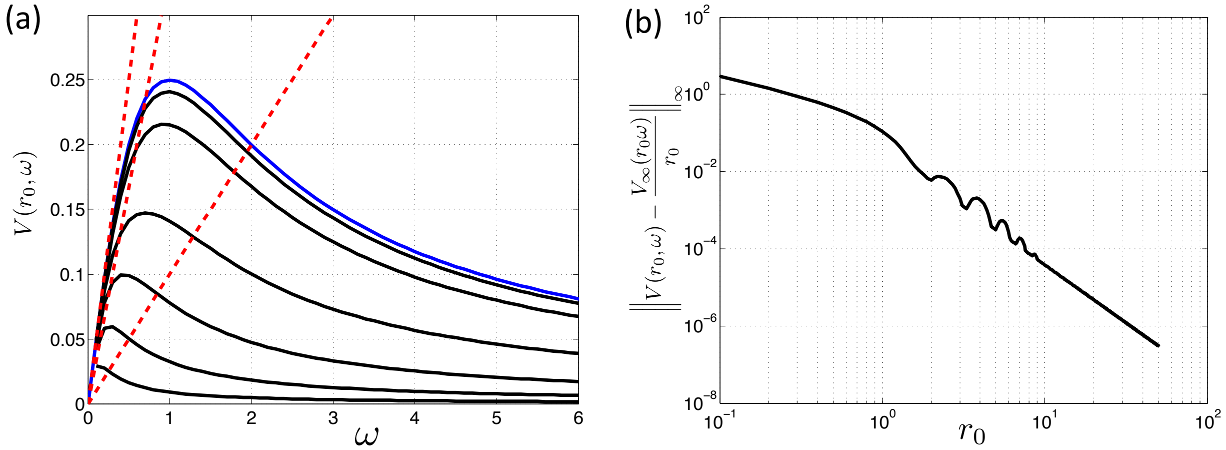

Figure 5-1: Diagrams used in the numerical justification of Proposition 1. (a) The black curves show the cross sections $v_{r_0}(\omega) \equiv V(r_0,\omega)$, as defined by (5.22), for $r_0 = 0.5$, 1, 2, 3, 5 and 10. The black curve with the largest amplitude corresponds to $r_0 = 0.5$, and the amplitude monotonically decreases with $r_0$. The blue curve corresponds to $v_0(\omega) = \omega/2(1+\omega^2)$. The dashed red lines correspond to $\omega/\beta$ for $\beta =$ 2, 3 and 10. This picture suggests that $\omega = \omega(r_0)$, as defined by the intersection of the black and red curves, is a single-valued monotonically decreasing function of $r_0$. (b) Plot confirming convergence of the functions $v_{r_0}(\omega)$ to the function $V_\infty(r_0\omega)/r_0$, as defined in (5.24), in the limit $r_0 \gg 1$. The difference between the two clearly decreases like $r_0^{-3}$, as expected from the calculation in (5.24).

only exist above the walking threshold, $\beta \geq 2$. The figure suggests that each of the cross sections $v_{r_0}(\omega)$ has a unique intersection $\omega^*(r_0,\beta)$ with the line $\omega/\beta$, and that $\partial_\omega V(r_0,\omega^*(r_0,\beta)) < 1/\beta$.

We now consider the differentiability of $\omega$ with respect to $r_0$ and $\beta$. Differentiating (5.21) with respect to both, we obtain

$$\frac{\mathrm{d}\omega}{\mathrm{d}r_0} = \frac{\beta\partial_{r_0}V}{1-\beta\partial_\omega V} \quad \text{and} \quad \frac{\mathrm{d}\omega}{\mathrm{d}\beta} = \frac{\beta V}{1-\beta\partial_\omega V}, \tag{5.23}$$

which implies that both derivatives exist for all $r_0$ and $\beta \geq 2$. Since $V$ is infinitely differentiable in both $r_0$ and $\omega$, we conclude that $\omega$ is an infinitely differentiable function of $r_0$ and $\beta$. Figure 5-1 suggests that $\partial_{r_0}V \leq 0$ and $V \geq 0$, implying that $\mathrm{d}\omega/\mathrm{d}r_0 \leq 0$ and $\mathrm{d}\omega/\mathrm{d}\beta \geq 0$, as desired.

Such a numerical argument can be made for finite values of $r_0$ and $\omega$, so we proceed by examining the behavior of $V(r_0,\omega)$ in the limits $r_0 \to \infty$ and $\omega \to \infty$. Starting with the former, we note that $|V| \leq c/r_0$, $c \approx 0.6$ being the maximum value of $J_1(x)$, which implies that solutions to (5.21) satisfy $\omega < \beta c/r_0$. Using the argument presented in Appendix C, we deduce that

$$\begin{aligned} V(r_0, \omega < \beta c/r_0) &= \frac{1}{r_0} \int_0^\infty J_1(r_0 \omega z)\, \mathrm{e}^{-z}\, \mathrm{d}z + O(r_0^{-2}) \\ &= \frac{V_\infty(r_0\omega)}{r_0} + O(r_0^{-3}), \quad V_\infty(x) = \frac{1}{x}\left(1 - \frac{1}{\sqrt{1+x^2}}\right). \end{aligned} \tag{5.24}$$

Since $V_\infty$ has a unique maximum $x^*$ and is concave in the region $0 \leq x \leq x^*$, we surmise that $\omega$ is a single-valued function of $r_0$ for arbitrarily large values of $r_0$. Figure 5-1 confirms that the numerically computed curves $v_{r_0}(\omega)$ indeed approach the asymptotic solution $V_\infty(r_0\omega)/r_0$ as $r_0 \to \infty$. For the limit $\omega \to \infty$, we use the argument in Appendix D to obtain the asymptotic expression

$$\begin{aligned} V(r_0, \omega) &= \frac{1}{r_0^2 \omega}\left[1 - \int_0^\infty J_0\left(2r_0 \sin\frac{\omega z}{2}\right) \mathrm{e}^{-z}\, \mathrm{d}z\right] \\ &= \frac{1}{r_0^2 \omega}\left[1 - \frac{1}{2\pi}\int_0^{2\pi} J_0\left(2r_0 \sin\frac{z}{2}\right) \mathrm{d}z + O(\omega^{-2})\right] \\ &= \frac{1}{\omega}\left[V^\infty(r_0) + O(\omega^{-2})\right], \quad \text{where} \quad V^\infty(r_0) = \frac{1 - J_0(r_0)^2}{r_0^2}. \end{aligned} \tag{5.25}$$

The integral above follows from an identity in Watson [63, p. 151]. This confirms that $V(r_0, \omega) \sim 1/\omega$ as $\omega \to \infty$, so we need only plot the curves $v_{r_0}(\omega)$ for finite $\omega$.

Proposition 2 may be justified through a similar argument. The differentiability of $\Omega(r_0, \beta)$ follows from that of $\omega(r_0, \beta)$, and the fact that $U(r_0, \omega)$ is infinitely differentiable in both $r_0$ and $\omega$. For finite values of $r_0$ and $\omega$, numerical plots of the cross sections $u_{r_0}(\omega) \equiv U(r_0, \omega)$ show that $v_{r_0}(\omega) \geq u_{r_0}(\omega)$, with equality at $r_0 = 0$ and $\omega = 0$, which suggests that $\Omega \geq -\omega(1 + \kappa)$. To ensure that this remains valid for large values of $r_0$, we observe that

$$\begin{aligned} U(r_0, \omega < \beta c/r_0) &= \frac{1}{r_0 \omega^2} \int_0^\infty J_1(r_0 z) \frac{z}{2} \mathrm{e}^{-z/\omega}\, \mathrm{d}z + O(r_0^{-4}) \\ &= \frac{1}{r_0} U_\infty(r_0\omega) + O(r_0^{-4}), \quad U_\infty(x) = \frac{x}{2\left(1+x^2\right)^{3/2}}, \end{aligned} \tag{5.26}$$

which follows from Appendix C. For large values of $\omega$, we may use Appendix D to show that

$$\begin{aligned} U(r_0,\omega) &= \frac{1}{r_0\omega^2\left(1-\mathrm{e}^{-2\pi/\omega}\right)}\int_0^{2\pi} J_1\left(2r_0\sin\frac{z}{2}\right)\sin\frac{z}{2}\mathrm{e}^{-z/w}\,\mathrm{d}z \\ &= \frac{1}{\omega}\left[U^{\infty}(r_0)+O(\omega^{-2})\right], \quad \text{where} \quad U^{\infty}(r_0)=\frac{J_0(r_0)J_1(r_0)}{r_0}. \end{aligned} \tag{5.27}$$

The integral above follows from an identity in Watson [63, p. 151]. Note that $V_\infty \geq U_\infty$ and $V^\infty \geq U^\infty$, with equality at $\omega = 0$ and $r_0 = 0$, respectively. We confirm that the numerical plots of $u_{r_0}(\omega)$ indeed converge to the asymptotic solutions above for large $r_0$ and $\omega$, which justifies Proposition 2.

We thus parametrize the orbital solutions by the radius $r_0$ instead of the rotation rate $\Omega$, since $\omega$ and $\Omega$ are single-valued functions of $r_0$. That is, the radius $r_0$ uniquely determines the drop's angular frequency $\omega$ and the bath rotation rate $\Omega$, but multiple radii $r_0$ could exist for a given value of $\Omega$, as is evident from Figures 3-2(a) and (c).

## 5.5 Linear stability problem for orbital solutions

We now analyze the stability of the orbital solutions found in §5.4, making precise the approach used in §3.4. To this end, we first write the integro-differential trajectory equation (5.9) as the following initial value problem:

$$\kappa\ddot{\boldsymbol{x}}_p+\dot{\boldsymbol{x}}_p = -\beta\,\boldsymbol{\nabla}\varphi(\boldsymbol{x},t)\big|_{\boldsymbol{x}=\boldsymbol{x}_p}-\boldsymbol{\Omega}\times\dot{\boldsymbol{x}}_p \tag{5.28a}$$

$$\varphi_t+\varphi = J_0\left(|\boldsymbol{x}-\boldsymbol{x}_p(t)|\right) \tag{5.28b}$$

where

$$\varphi(\boldsymbol{x},0)=\int_{-\infty}^{0} J_0\left(|\boldsymbol{x}-\boldsymbol{x}_p(s)|\right)\mathrm{e}^{s}\,\mathrm{d}s, \tag{5.29}$$

and $\boldsymbol{x}_p(t)$ is prescribed for $t<0$.

The orbital solution $\boldsymbol{x}_p(t)=\boldsymbol{x}_c(t)\equiv r_0(\cos\omega t,\sin\omega t)$, as defined by (5.20), takes a particularly simple form in polar coordinates. Writing $\boldsymbol{x} = r(\cos\theta, \sin\theta)$ and $\boldsymbol{x}_p(t) = r_p(t)(\cos\theta_p(t), \sin\theta_p(t))$, (5.28) assumes the form

$$\begin{aligned} \kappa\left(\ddot{r}_p - r_p\dot{\theta}_p^2\right) + \dot{r}_p - \Omega r_p\dot{\theta}_p &= -\beta \left.\frac{\partial\varphi}{\partial r}\right|_{\boldsymbol{x}=\boldsymbol{x}_p} && (5.30\text{a}) \\ \kappa\left(2\dot{r}_p\dot{\theta}_p + r_p\ddot{\theta}_p\right) + r_p\dot{\theta}_p + \Omega\dot{r}_p &= -\frac{\beta}{r_p}\left.\frac{\partial\varphi}{\partial\theta}\right|_{\boldsymbol{x}=\boldsymbol{x}_p} && (5.30\text{b}) \\ \varphi_t + \varphi &= J_0\left(|\boldsymbol{x} - \boldsymbol{x}_p(t)|\right), && (5.30\text{c}) \end{aligned}$$

where $|\boldsymbol{x} - \boldsymbol{x}_p(t)| = \left[r^2 + r_p^2 - 2rr_p\cos(\theta - \theta_p)\right]^{1/2}$. The solution to (5.30) corresponding to a circular orbit may be written as

$$r_p(t) = r_0, \quad \theta_p(t) = \omega t, \quad \text{and} \quad \varphi(\boldsymbol{x}, t) = \varphi_c(\boldsymbol{x}, t) \equiv \int_{-\infty}^{t} J_0\left(|\boldsymbol{x} - \boldsymbol{x}_c(s)|\right) \mathrm{e}^{-(t-s)}\,\mathrm{d}s.$$

To assess the linear stability of this solution, we substitute $r_p(t) = r_0 + \epsilon r_1(t)$, $\theta_p(t) = \omega t + \epsilon\theta_1(t)$ and $\varphi(\boldsymbol{x}, t) = \varphi_c(\boldsymbol{x}, t) + \epsilon\varphi_1(\boldsymbol{x}, t)$ into (5.30), where $0 < \epsilon \ll 1$. We thus obtain the linearized equations

$$\begin{aligned} &\kappa\left(\ddot{r}_1 - \omega^2 r_1 - 2r_0\omega\dot{\theta}_1\right) + \dot{r}_1 - \omega\Omega r_1 - \Omega r_0\dot{\theta}_1 = -\beta\left.\frac{\partial\varphi_1}{\partial r}\right|_{\substack{r=r_0 \\ \theta=\omega t}} && (5.31\text{a}) \\ &-\beta\left.\left[\frac{\partial^2\varphi_c}{\partial r^2}r_1 + \frac{\partial^2\varphi_c}{\partial r\partial\theta}\theta_1\right]\right|_{\substack{r=r_0 \\ \theta=\omega t}} \\ &\kappa\left(2\omega\dot{r}_1 + r_0\ddot{\theta}_1\right) + \omega r_1 + r_0\dot{\theta}_1 + \Omega\dot{r}_1 = -\frac{\beta}{r_0}\left.\frac{\partial\varphi_1}{\partial\theta}\right|_{\substack{r=r_0 \\ \theta=\omega t}} && (5.31\text{b}) \\ &-\frac{\beta}{r_0}\left.\left[\left(\frac{\partial^2\varphi_c}{\partial r\partial\theta} - \frac{1}{r_0}\frac{\partial\varphi_c}{\partial\theta}\right)r_1 + \frac{\partial^2\varphi_c}{\partial\theta^2}\theta_1\right]\right|_{\substack{r=r_0 \\ \theta=\omega t}} \\ &\dot{\varphi}_1 + \varphi_1 = \frac{J_0'\left(|\boldsymbol{x} - \boldsymbol{x}_c(t)|\right)}{|\boldsymbol{x} - \boldsymbol{x}_c(t)|}\left[-rr_1\cos(\theta - \omega t) + r_0\left(r_1 - r\theta_1\sin(\theta - \omega t)\right)\right]. && (5.31\text{c}) \end{aligned}$$

We proceed by computing the derivatives of $\varphi_c$ and evaluating them at $r = r_0$ and $\theta = \omega t$. We find that they are all time-independent, so (5.31a) and (5.31b) may be written as

$$\begin{aligned}
&\kappa\left(\ddot{r}_1 - \omega^2 r_1 - 2r_0\omega\dot{\theta}_1\right) + \dot{r}_1 - \omega\Omega r_1 - \Omega r_0\dot{\theta}_1 = -\beta\left.\frac{\partial\varphi_1}{\partial r}\right|_{\substack{r=r_0\\ \theta=\omega t}} && \text{(5.32a)}\\
&+\beta\left(\mathcal{I}\left[f(t)\cos^2\frac{\omega t}{2} + g(t)\sin^2\frac{\omega t}{2}\right] r_1 + \frac{1}{2}\mathcal{I}\left[(f(t)+g(t))\sin\omega t\right]\right) r_0\theta_1\\
&\kappa\left(2\omega\dot{r}_1 + r_0\ddot{\theta}_1\right) + \omega r_1 + r_0\dot{\theta}_1 + \Omega\dot{r}_1 = -\frac{\beta}{r_0}\left.\frac{\partial\varphi_1}{\partial\theta}\right|_{\substack{r=r_0\\ \theta=\omega t}} && \text{(5.32b)}\\
&+\beta\left(\frac{1}{2}\mathcal{I}\left[(g(t)-f(t))\sin\omega t\right] r_1 + \mathcal{I}\left[g(t)\cos^2\frac{\omega t}{2} - f(t)\sin^2\frac{\omega t}{2}\right] r_0\theta_1\right),
\end{aligned}$$

where

$$f(t) = \frac{J_1\left(2r_0\sin\frac{\omega t}{2}\right)}{2r_0\sin\frac{\omega t}{2}}\mathrm{e}^{-t}, \quad g(t) = J_1'\left(2r_0\sin\frac{\omega t}{2}\right)\mathrm{e}^{-t}, \quad \mathcal{I}[f] = \int_0^\infty f(t)\,\mathrm{d}t.$$

We may simplify the integrals above by using the identities listed in Appendix A.

The initial condition (5.29) implies that $\varphi_1(\boldsymbol{x},0)=0$, so (5.31c) may be integrated to obtain

$$\varphi_1(\boldsymbol{x},t) = \int_0^t \frac{J_0'\left(|\boldsymbol{x}-\boldsymbol{x}_c(s)|\right)}{|\boldsymbol{x}-\boldsymbol{x}_c(s)|}\left[-r r_1(s)\cos(\theta-\omega s) + r_0\left(r_1(s) - r\theta_1(s)\sin(\theta-\omega s)\right)\right]\mathrm{e}^{-(t-s)}\,\mathrm{d}s.$$

Differentiating $\varphi_1$ with respect to $r$ and $\theta$ and evaluating the derivatives at $r=r_0$ and $\theta=\omega t$, we obtain

$$\begin{aligned}
\left.\frac{\partial\varphi_1}{\partial r}\right|_{\substack{r=r_0\\ \theta=\omega t}} &= \left[f(t)\cos^2\frac{\omega t}{2} - g(t)\sin^2\frac{\omega t}{2}\right] * r_1(t) + \frac{r_0}{2}\left(f(t)+g(t)\right)\sin\omega t * \theta_1(t),\\
\frac{1}{r_0}\left.\frac{\partial\varphi_1}{\partial\theta}\right|_{\substack{r=r_0\\ \theta=\omega t}} &= -\frac{1}{2}\left[f(t)+g(t)\right]\sin\omega t * r_1(t) + r_0\left[g(t)\cos^2\frac{\omega t}{2} - f(t)\sin^2\frac{\omega t}{2}\right] * \theta_1(t),
\end{aligned}$$

where $f*g(t) = \int_0^t f(s)g(t-s)\,\mathrm{d}s$ denotes the convolution of the functions $f$ and $g$. Using these identities, we deduce that the linear stability problem (5.32) is equivalent to that obtained in §3.4.

Written in this form, the linear equations (5.31) are amenable to analysis by Laplace transform. Defining $R(s) = \mathcal{L}[r_1(t)]$ and $\Theta(s) = \mathcal{L}[\theta_1(t)]$) and taking the

Laplace transform of both sides of (5.32a) and (5.32b), we obtain

$$\begin{bmatrix} A(s) & -B(s) \\ C(s) & D(s) \end{bmatrix} \begin{bmatrix} R(s) \\ r_0\Theta(s) \end{bmatrix} = \begin{bmatrix} a(s) \\ b(s) \end{bmatrix}, \tag{5.33}$$

where

$$\begin{aligned} A(s) &= \kappa s^2 + s - \kappa\omega^2 - \Omega\omega - \beta\mathcal{I}\left[f(t)\cos^2\frac{\omega t}{2} + g(t)\sin^2\frac{\omega t}{2}\right] \\ &\quad -\beta\mathcal{L}\left[g(t)\sin^2\frac{\omega t}{2} - f(t)\cos^2\frac{\omega t}{2}\right] \\ B(s) &= (2\omega\kappa + \Omega)\,s - (\kappa\omega + \Omega) - \frac{\beta}{2}\mathcal{L}\left[(f(t) + g(t))\sin\omega t\right] \\ C(s) &= (2\omega\kappa + \Omega)\,s + 2\omega + \kappa\omega + \Omega - \frac{\beta}{2}\mathcal{L}\left[(f(t) + g(t))\sin\omega t\right] \\ D(s) &= \kappa s^2 + s - 1 - \beta\mathcal{L}\left[f(t)\sin^2\frac{\omega t}{2} - g(t)\cos^2\frac{\omega t}{2}\right] \end{aligned} \tag{5.34}$$

and

$$\begin{aligned} a(s) &= (\kappa s + 1)\,r_1(0) + \kappa\dot{r}_1(0) - (2\kappa\omega + \Omega)r_0\theta_1(0) \\ b(s) &= (2\omega\kappa + \Omega)\,r_1(0) + (\kappa s + 1)r_0\theta_1(0) + \kappa r_0\dot{\theta}_1(0). \end{aligned} \tag{5.35}$$

The solution to (5.33) is

$$\begin{aligned} R(s) &= \frac{a(s)D(s) + b(s)B(s)}{A(s)D(s) + B(s)C(s)} \\ \Theta(s) &= \frac{-a(s)C(s) + b(s)A(s)}{r_0\left(A(s)D(s) + B(s)C(s)\right)}. \end{aligned} \tag{5.36}$$

The poles of $R(s)$ and $\Theta(s)$ correspond to the eigenvalues of the linear problem (5.31a)–(5.31c). If the poles lie in the left- or right-half complex plane, the orbital solution $\boldsymbol{x}_c(t) = r_0(\cos\omega t, \sin\omega t)$ is respectively stable or unstable to perturbations. Note that the region of convergence for the Laplace transforms in (5.34) is $\Re(s) > -1$, so the functions defined by (5.34) are analytic in this region. Therefore, the orbital solution $\boldsymbol{x}_c(t)$ is unstable if and only if the function $F(s; r_0) = A(s)D(s) + B(s)C(s)$

has a root in the region $\Re(s) > 0$.

### 5.5.1 Rotational and translational invariance

We proceed by showing that $F(s; r_0)$ has roots at $s = \pm \mathrm{i}\omega$ and $s = 0$, which arise due to the invariance of (5.9) under translation and rotation. We first evaluate the functions defined by (5.34) at $s = \mathrm{i}\omega$, the calculation for $s = -\mathrm{i}\omega$ being identical. Splitting the functions into their real and imaginary parts by writing them in the form $G(\mathrm{i}\omega) = G_r + \mathrm{i}G_i$, we obtain

$$
\begin{aligned}
A_r &= -2\kappa\omega^2 - \Omega\omega - \frac{\beta}{2}\left(\mathcal{I}[f(t)\sin^2\omega t] + \mathcal{I}[g(t)\sin^2\omega t]\right)\\
A_i &= \omega - \beta\left(\mathcal{I}\left[f(t)\sin\omega t\cos^2\frac{\omega t}{2}\right] - \mathcal{I}\left[g(t)\sin\omega t\sin^2\frac{\omega t}{2}\right]\right)\\
B_r &= \beta\left(\mathcal{I}\left[f(t)\sin\omega t\sin^2\frac{\omega t}{2}\right] + \mathcal{I}\left[g(t)\sin\omega t\sin^2\frac{\omega t}{2}\right]\right)\\
C_r &= \omega - \beta\left(-\mathcal{I}\left[f(t)\sin\omega t\sin^2\frac{\omega t}{2}\right] + \mathcal{I}\left[g(t)\sin\omega t\cos^2\frac{\omega t}{2}\right]\right)\\
C_i &= (2\omega\kappa + \Omega)\omega + \frac{\beta}{2}\left(\mathcal{I}[f(t)\sin^2\omega t] + \mathcal{I}[g(t)\sin^2\omega t]\right)\\
D_r &= -\kappa\omega^2 - \beta\left(-2\mathcal{I}\left[f(t)\sin^4\frac{\omega t}{2}\right] + \frac{1}{2}\mathcal{I}[g(t)\sin^2\omega t]\right),
\end{aligned}
\tag{5.37}
$$

where $B_i = -A_r$ and $D_i = C_r$. Using Appendix A, we find that $A_i = B_r$ and $C_i = -D_r$, so $A(\mathrm{i}\omega) = \mathrm{i}B(\mathrm{i}\omega)$ and $C(\mathrm{i}\omega) = -\mathrm{i}D(\mathrm{i}\omega)$. It follows that $F(\mathrm{i}\omega; r_0) = A(\mathrm{i}\omega)D(\mathrm{i}\omega) + B(\mathrm{i}\omega)C(\mathrm{i}\omega) = 0$, as desired. The identities in Appendix A also imply that $B(0) = D(0) = 0$, so $F(s; r_0)$ has a root at $s = 0$ for all values of $r_0$.

We now show that these roots are linked to the rotational and translational invariance of (5.9). Indeed, note that an orbital solution with radius $r_0$ and angular frequency $\omega$ can be written as $\boldsymbol{x}_p(t) = (x_0 + \cos(\omega t + T_0), y_0 + \sin(\omega t + T_0))$, where $(x_0, y_0)$ is an arbitrary translation and $T_0$ an arbitrary phase shift. By linearizing $\boldsymbol{x} = r(t)(\cos\theta(t), \sin\theta(t))$ around the orbital solution $r(t) = r_0, \theta(t) = \omega t$, we observe that perturbations $(\delta x, \delta y)$ in Cartesian coordinates are related to perturbations

$(\delta r, \delta\theta)$ in polar coordinates by the formulae

$$\delta x = \delta r \cos\omega t - r_0 \delta\theta \sin\omega t, \quad \delta y = \delta r \sin\omega t + r_0 \delta\theta \cos\omega t. \tag{5.38}$$

Hence

$$\begin{aligned}
\frac{\partial \boldsymbol{x}_p}{\partial x_0} &= (1,0) \Rightarrow (\delta r, \delta\theta) = \left(\cos\omega t, -\frac{1}{r_0}\sin\omega t\right) \\
\frac{\partial \boldsymbol{x}_p}{\partial y_0} &= (0,1) \Rightarrow (\delta r, \delta\theta) = \left(\sin\omega t, \frac{1}{r_0}\cos\omega t\right) \\
\frac{\partial \boldsymbol{x}_p}{\partial T_0} &= (-r_0 \sin\omega t, r_0 \cos\omega t) \Rightarrow (\delta r, \delta\theta) = (0,1)\,, 
\end{aligned} \tag{5.39}$$

where all derivatives are evaluated at $x_0 = y_0 = T_0 = 0$. It follows that the zeros at $s = \pm \mathrm{i}\omega$ and $s = 0$ reflect the invariance of (5.9) under translation and rotation, respectively. The nontrivial eigenvalues of the linear stability problem (5.31) thus correspond to the roots of the function

$$F^*(s; r_0) \equiv \frac{F(s; r_0)}{s(s^2 + \omega^2)}, \tag{5.40}$$

which is analytic in the region $\Re(s) > -1$.

## 5.6 Stability properties of orbital solutions in various limiting cases

We proceed by assessing the stability of the orbital solutions in the various limiting cases of small radius, $r_0 \to 0$; large radius, $r_0 \to \infty$; and low memory, $\gamma \to {\gamma_W}^+$.

### 5.6.1 Orbital stability in the small radius limit

In this section, we prove the following theorem:

**Theorem 2** *For a fixed value of* $\gamma$, *there exists a value* $r_0^*$ *such that* $F^*(s; r_0)$ *has no roots in the region* $\Re(s) > 0$ *for* $0 < r_0 < r_0^*$.

This result suggests that the bouncing solution indeed destabilizes into a stable orbital solution at a critical rotation rate $\Omega = \Omega_0 \equiv \sqrt{\frac{\beta}{2} - 1}\,(1+\kappa)$, as suggested in §5.3.

Consider the regions $0 < r_0 < 1$ and $\Re(s) > -\sigma > -1$ for some fixed value of $\sigma$ (i.e. $\sigma = 1/2$). Note that $\beta$ and $\kappa$ are fixed through $\gamma$. The Laplace transforms in (5.34) decay as $|s| \to \infty$ for $\Re(s) > -\sigma$, which implies that $F(s; r_0) \sim \kappa^2 s^4$ as $|s| \to \infty$. It follows that the roots of $F^*$ in the right half-plane must satisfy $|s| < S$, where $S$ is independent of $r_0$.

We proceed by expanding (5.20) in the regime $r_0 \ll 1$ by writing $\omega = \omega_0 + r_0^2\omega_2$ and $\Omega = \Omega_0 + r_0^2\Omega_2$, where $\omega_0 = -\sqrt{\beta/2 - 1}$ and $\Omega_0 = -\omega_0(1+\kappa)$. At $O(r_0^2)$, we obtain

$$\begin{aligned} -r\Omega_2\omega_0 - r\left(\Omega_0 + 2\kappa\omega_0\right)\omega_2 &= -\frac{3\beta r^3\omega_0^4}{4\left(1+\omega_0^2\right)} + \frac{\beta r\omega_0\omega_2}{\left(1+\omega_0^2\right)^2} \\ r\omega_2 &= -\frac{\beta r\left(\omega_0^4 - 1\right)\omega_2}{2\left(1+\omega_0^2\right)^3} - \frac{3\beta r^3\omega_0^3}{8\left(1+\omega_0^2\right)\left(1+4\omega_0^2\right)}, \end{aligned} \tag{5.41}$$

which implies that

$$\omega_2 = \frac{3\omega_0^3}{4\left(\frac{4}{\beta} - 2\right)\left(1+4\omega_0^2\right)}, \quad \Omega_2 = \frac{3\omega_0\left(-4 + \beta(\kappa+3)\right)}{16(2\beta - 3)}. \tag{5.42}$$

We substitute these expansions into the definition of $F(s; r_0)$. After considerable algebra, we obtain

$$F^*(s; r_0) \quad = \quad G_0(s) + r_0^2 G_1(s) + O(r_0^4), \tag{5.43}$$

where

$$\begin{aligned} G_0(s) &= \frac{s\left[\left(\kappa(s+1)+1\right)^2 + \omega_0^2(\kappa-1)^2\right]}{(s+1)^2 + \omega_0^2}, \\ G_1(s) &= \frac{\omega_0^2 p(s)}{8(1+4\omega_0^2)(s+1)\left[(s+1)^2 + 4\omega_0^2\right]\left[(s+1)^2+\omega_0^2\right]^2}, \end{aligned} \tag{5.44}$$

and $p(s) = \sum_{k=1}^{6} p_k s^k$ is a sixth-degree polynomial with coefficients

$$\begin{aligned}
p_0 &= 3\beta(-3+2\beta)\left(-4+\beta(3+\kappa)\right) \\
p_1 &= 2\left(72+\beta^2(52+3\kappa)+2\beta^3(-1+6\kappa)-3\beta(41+12\kappa)\right) \\
p_2 &= 2\left(-48+\beta(13-162\kappa)+\beta^3(-3+5\kappa)+\beta^2(14+93\kappa)\right) \\
p_3 &= \beta(177-72\kappa)-12(13+24\kappa)+4\beta^2(-15+41\kappa) \\
p_4 &= 36-384\kappa+\beta^2(-21+37\kappa)+\beta(-9+196\kappa) \\
p_5 &= 60-168\kappa+\beta(-47+112\kappa) \\
p_6 &= 12-24\kappa+\beta(-9+16\kappa). \qquad (5.45)
\end{aligned}$$

Note that the error term in (5.43) is independent of $s$, since all instabilities are confined to the region $|s| < S$ in the right half-plane.

In the $r_0 \to 0$ limit, the only root of $F^*$ in the region $\Re(s) \geq 0$ is at $s = 0$, so we need to assess its behavior for small $r_0$. To this end, let $s = s(r_0)$ with $s(0) = 0$. Differentiating the equation $F^*(s(r_0); r_0) = 0$ twice with respect to $r_0$, we obtain

$$\begin{aligned}
s' F_s^* + F_{r_0}^* &= 0 \\
s'' F_s^* + 2s' F_{sr_0}^* + (s')^2 F_{ss}^* + F_{r_0 r_0}^* &= 0. \qquad (5.46)
\end{aligned}$$

Clearly $F_{r_0}^* = 0$ at $r_0 = 0$, which implies that $s'(0) = 0$. We thus obtain

$$s''(0) = -\frac{F_{r_0 r_0}^*(0;0)}{F_s^*(0;0)} = -\frac{2G_1(0)}{G_0'(0)}, \qquad (5.47)$$

where

$$G_1(0) = \frac{\omega_0^2 p_0}{8\left(1+4\omega_0^2\right)^2\left(1+\omega_0^2\right)^2} \quad \text{and} \quad G_0'(0) = \frac{(1+\kappa)^2+(\kappa-1)^2\omega_0^2}{1+\omega_0^2}. \qquad (5.48)$$

Since $p_0 > 0$ for $\beta > 2$ and $\kappa > 0$, we find that $s''(0) < 0$, so the root is in the left half-plane for sufficiently small values of $r_0$. This proves that orbits of sufficiently small radius are stable, as desired.

### 5.6.2 Orbital stability in the large radius limit

In this section, we prove the following theorem:

**Theorem 3** *For a fixed value of* $\gamma$*, there exists a value* $R_0$ *such that* $F^*(s; r_0)$ *has no roots in the region* $\Re(s) > 0$ *for* $r_0 > R_0$*.*

This result provides rationale for the experimental observation that orbits of sufficiently large radius are stable, as is evident from Figures 3-1 and 3-2 [32, 38]. We consider the region $r_0 > 1$ and $\Re(s) > -\sigma > -1$ for some fixed value of $\sigma$. We showed in §5.4 that $\omega \leq \beta c/r_0$, where $c \approx 0.6$ is the maximum value of the Bessel function $J_1(x)$. Using the argument in Appendix C, we may write (5.20) as

$$\begin{aligned} -\kappa u^2 &= \frac{\beta u}{2} \int_0^\infty J_1(uz) z \mathrm{e}^{-z} \, \mathrm{d}z + \Omega r_0 u + O(r_0^{-2}) \\ u &= \beta \int_0^\infty J_1(uz) \mathrm{e}^{-z} \, \mathrm{d}z + O(r_0^{-2}), \end{aligned} \tag{5.49}$$

where $r_0\omega = u$. The second equation may be solved to obtain

$$u = u_0 + O(r_0^{-2}), \quad \text{where} \quad u_0 = \frac{1}{\sqrt{2}} \left( -1 + 2\beta - \sqrt{1 + 4\beta} \right)^{-1/2}. \tag{5.50}$$

Note that $u_0$ corresponds to the formula (5.19) for the walking speed in a *non-rotating* system, suggesting that the Coriolis force is relatively weak in the regime $r_0 \gg 1$. Indeed, since $u_0$ is independent of $r_0$, the first equation in (5.49) implies that $\Omega = O(r_0^{-1})$.

We now expand the function $F^*(s; r_0)$ in the limit $r_0 \gg 1$. Using the argument in Appendix C, the Laplace transforms in (5.34) may be written as

$$\begin{aligned} \mathcal{L}\left[ g(t) \sin^2 \frac{\omega t}{2} - f(t) \cos^2 \frac{\omega t}{2} \right] &= \mathcal{L}\left[ \frac{J_1(u_0 t)}{u_0 t} \mathrm{e}^{-t} \right] + O(r_0^{-2}) \\ \mathcal{L}\left[ (f(t) + g(t)) \sin \omega t \right] &= O(r_0^{-1}) \\ \mathcal{L}\left[ f(t) \sin^2 \frac{\omega t}{2} - g(t) \cos^2 \frac{\omega t}{2} \right] &= \mathcal{L}\left[ -J_1'(u_0 t) \mathrm{e}^{-t} \right] + O(r_0^{-2}), \end{aligned} \tag{5.51}$$

where the error terms are independent of $s$. The integral term in $A(s)$ may be written as

$$\begin{aligned}\mathcal{I}\left[f(t)\cos^2\frac{\omega t}{2}+g(t)\sin^2\frac{\omega t}{2}\right] &= \mathcal{I}\left[\frac{J_1(u_0t)}{u_0t}\mathrm{e}^{-t}\right]+O(r_0^{-2}) \\ &= \frac{-1+\sqrt{1+u_0^2}}{u_0^2}+O(r_0^{-2}) \\ &= \frac{\sqrt{1+u_0^2}}{\beta}+O(r_0^{-2}), \qquad (5.52)\end{aligned}$$

using the definition of $u_0$ in (5.50). We thus deduce that

$$\begin{aligned}A(s) &= \kappa s^2+s-\sqrt{1+u_0^2}+\beta\mathcal{L}\left[\frac{J_1\left(u_0t\right)}{u_0t}\mathrm{e}^{-t}\right]+E_A, \\ B(s) &= sE_B, \quad C(s)=sE_C, \\ D(s) &= \kappa s^2+s-1+\beta\mathcal{L}\left[J_1'(u_0t)\mathrm{e}^{-t}\right]+E_D, \qquad (5.53)\end{aligned}$$

where the error terms are $O\left(r_0^{-2}\right)$ and independent of $s$. We may thus express the function $F(s;r_0)$ as

$$F(s;r_0) = P(s)Q(s)+\frac{R(s;r_0)}{r_0^2}, \qquad (5.54)$$

where

$$P(s)=\kappa s^2+s-1+\beta\mathcal{L}\left[J_1'(u_0t)\mathrm{e}^{-t}\right], \quad Q(s)=\kappa s^2+s-\sqrt{1+u_0^2}+\beta\mathcal{L}\left[\frac{J_1(u_0t)}{u_0t}\mathrm{e}^{-t}\right],$$

$R(s;r_0)$ is bounded in $r_0$ for $r_0>1$ and $R=O(|s|^2)$ as $|s|\to\infty$ for $\Re(s)>-\sigma$. The functions $P$, $Q$, and $F$ are analytic functions of $s$ in the region $\Re(s)>-\sigma$, so the same must be true for $R$. Since

$$\frac{1}{s^2+\omega^2}=\frac{1}{s^2}\left(1-\frac{\omega^2}{s^2+\omega^2}\right), \qquad (5.55)$$

we obtain

$$F^*(s;r_0) \;=\; \frac{P(s)Q(s)}{s^3} + \frac{\tilde{R}(s;r_0)}{r_0^2}, \tag{5.56}$$

where $\tilde{R}$ is also a bounded function of $r_0$ for $r_0 > 1$. As shown Chapter 2 [48], the functions $P(s)$ and $Q(s)$ appear when considering the stability of the solution $\boldsymbol{x}_p(t) = (u_0 t, 0)$ in a non-rotating container. It was shown that $P(s)Q(s)$ has a triple root at $s = 0$, and that all other roots are in the left half-plane. It follows that $\tilde{R}(s;r_0)$ is analytic for $\Re(s) > -\sigma$ and that $\tilde{R} = O(|s|^{-1})$ as $|s| \to \infty$ in this region. Since $P(s)Q(s) = O(|s|^4)$ as $|s| \to \infty$, it follows that we can choose $r_0$ to be sufficiently large that $F^*$ has no roots in the right half-plane, which proves the desired result.

We thus deduce that the stability problem for orbits of large radius $r_0 \gg 1$ in a rotating container is approximately equivalent to the stability problem for rectilinear walking in a non-rotating container. This is also apparent on physical grounds, as such orbits have small curvature and can be approximated locally by a straight line. Since the steady rectilinear walking solution is stable to perturbations, so are circular orbits of sufficiently large radius.

### 5.6.3 Orbital stability in the low-memory limit

In this section, we prove the following theorem:

**Theorem 4** *For every $r_0$, there exists a value $\beta^*$ such that $F^*(s;r_0)$ has no roots in the region $\Re(s) > 0$ for $2 < \beta < \beta^*$.*

This result provides rationale for the experimental observation that the observed orbital quantization only occurs at high memory, significantly above the walking threshold ($\beta = 2$), as is evident from Figures 3-1 and 3-2. We fix $r_0$ and let $\beta = 2+\alpha^2$, where $0 < \alpha < 1$. Note that $\omega = O(\alpha)$, since $\omega = \sqrt{\beta/2 - 1}$ at $r_0 = 0$ and decreases with $r_0$, as shown in §5.4. We thus expand the integrals in (5.20) in the small $\omega$ limit.

We begin with

$$\begin{aligned} J_1\left(2r_0\sin\frac{z}{2}\right)\sin\frac{z}{2} &= \frac{r_0z^2}{4}+O(z^4) \\ J_1\left(2r_0\sin\frac{z}{2}\right)\cos\frac{z}{2} &= \frac{r_0z}{2}-\frac{r_0\left(4+3r_0^2\right)}{48}z^3+O(z^5). \end{aligned} \tag{5.57}$$

Using the argument in Appendix C, we thus obtain the approximations

$$\begin{aligned} \frac{1}{\omega}\int_0^\infty J_1\left(2r_0\sin\frac{z}{2}\right)\sin\frac{z}{2}\mathrm{e}^{-z/\omega}\,\mathrm{d}z &= \frac{r_0\omega^2}{2}+O(\omega^4) \\ \frac{1}{\omega}\int_0^\infty J_1\left(2r_0\sin\frac{z}{2}\right)\cos\frac{z}{2}\mathrm{e}^{-z/\omega}\,\mathrm{d}z &= \frac{r_0\omega}{2}-\frac{r_0\omega^3\left(4+3r_0^2\right)}{4}+O(\omega^5). \end{aligned} \tag{5.58}$$

This yields the following expansion of (5.20) to $O(\alpha^2)$:

$$\begin{aligned} -\kappa r_0\omega^2-\Omega r_0\omega &= r_0\omega^2+O(\alpha^4) \\ r_0\omega &= r_0\omega-\frac{r_0\omega}{4}\left[-2\alpha^2+\left(4+3r_0^2\right)\omega^2\right]+O(\alpha^4), \end{aligned} \tag{5.59}$$

from which we obtain

$$\omega=\alpha\sqrt{\frac{2}{4+3r_0^2}}+O(\alpha^2), \quad \Omega=-\omega(1+\kappa)+O(\alpha^2). \tag{5.60}$$

As in the previous sections, we use (5.60) to expand $F(s;r_0)$ in the limit $\alpha \ll 1$. The integrands of the functions in (5.34) may be written as

$$\begin{aligned} f(t)\cos^2\frac{t}{2}+g(t)\sin^2\frac{t}{2} &= \frac{1}{2}-\frac{r_0^2t^2}{16}+O(t^4) \\ g(t)\sin^2\frac{t}{2}-f(t)\cos^2\frac{t}{2} &= -\frac{1}{2}+\frac{r_0^2+4}{16}t^2+O(t^4) \\ (f(t)+g(t))\sin t &= t-\left(\frac{r_0^2}{4}+\frac{1}{6}\right)t^3+O(t^5) \\ f(t)\sin^2\frac{t}{2}-g(t)\cos^2\frac{t}{2} &= -\frac{1}{2}+\frac{1}{4}\left(1+\frac{3r_0^2}{4}\right)t^2+O(t^4). \end{aligned} \tag{5.61}$$

It follows that

$$\begin{aligned}
\mathcal{I}\left[f(t)\cos^2\frac{t}{2}+g(t)\sin^2\frac{t}{2}\right] &= \frac{1}{2}-\frac{r_0^2\omega^2}{8}+O(\omega^4) \\
\mathcal{L}\left[g(t)\sin^2\frac{t}{2}-f(t)\cos^2\frac{t}{2}\right] &= -\frac{1}{2(s+1)}+\frac{(r_0^2+4)\,\omega^2}{8(s+1)^3}+O(\omega^4) \\
\mathcal{L}\left[(f(t)+g(t))\sin t\right] &= \frac{\omega}{(s+1)^2}-\left(\frac{3r_0^2}{2}+1\right)\frac{\omega^3}{(s+1)^4}+O(\omega^5) \\
\mathcal{L}\left[f(t)\sin^2\frac{t}{2}-g(t)\cos^2\frac{t}{2}\right] &= -\frac{1}{2(s+1)}+\frac{1}{2}\left(1+\frac{3r_0^2}{4}\right)\frac{\omega^2}{(s+1)^3}+O(\omega^4), \quad (5.62)
\end{aligned}$$

where the error terms are independent of $s$ in the region $\Re(s) > -\sigma > -1$. We thus obtain the expansion

$$F^*(s;r_0) = \frac{s(1+\kappa(s+1))^2}{(s+1)^2}+\frac{p(s;r_0)\alpha^2}{(s+1)^4(4+3r_0^2)}+O(\alpha^4), \quad (5.63)$$

where $p(s;r_0)=\sum_{k=0}^{3}p_k s^k$ is a third-degree polynomial with coefficients

$$\begin{aligned}
p_0 &= 3(1+\kappa)r_0^2, \quad p_1=\kappa(-8+3r_0^2), \\
p_2 &= 4-r_0^2-\kappa(12+r_0^2), \quad p_3=2-\kappa(4+r_0^2). \quad (5.64)
\end{aligned}$$

We write the expansion in the form $F^*(s;r_0)=G_0(s)+\alpha^2G_1(s;r_0)+O(\alpha^4)$, where the error term is bounded from above by a constant independent of $s$ in the region $\Re(s) > -\sigma > -1$. For $\alpha = 0$, $F^*$ has a single root in the right half-plane at $s = 0$. As in §5.6.1, we need to assess the behavior of this root for small values of $\alpha$, so we let $s = s(\alpha)$ with $s(0) = 0$. Adapting the argument in §5.6.1, we find that $s'(0) = 0$ and that

$$s''(0) = -\frac{2G_1(0)}{G_0'(0)}. \quad (5.65)$$

Since $G_1(0) = p_0/(4+3r_0^2) > 0$ and $G_0'(0) = (1+\kappa)^2$, it follows that $s''(0) < 0$. This implies that $F^*(s;r_0)$ has no roots in the right half-plane for sufficiently small values of $\alpha$, which proves the desired result.

## 5.7 Numerical method for assessing orbital stability

In §5.6, we established the stability of orbital solutions in various limiting cases, in which the function $F^*(s; r_0)$ could be approximated by simpler functions without roots in the region $\Re(s) \geq 0$. However, the stability of an arbitrary orbital solution must be assessed by finding the roots of $F^*(s; r_0)$ numerically. We proceed by developing and presenting the results of a numerical method for tracking these roots.

We first observe that $F(s; r_0)$ is not an entire function, as the region of convergence for the Laplace transforms in (5.34) is $\Re(s) > -1$. Recall that if $h(t)$ is periodic with period $T$, then

$$\mathcal{L}[h(t)\mathrm{e}^{-t}] = \frac{1}{1 - \mathrm{e}^{-(s+1)T}} \int_0^T h(t)\mathrm{e}^{-(s+1)t}\,\mathrm{d}t. \tag{5.66}$$

While the integral exists for all $s$, the Laplace transform may have poles at $s = -1 + 2\pi\mathrm{i}n/T$ for integer $n$. This could pose problems for our numerical method, since the poles and zeros of $F(s; r_0)$ may collide. For this reason, we instead track the zeros of $\tilde{F}(s; r_0) \equiv \left(1 - \mathrm{e}^{-(s+1)T}\right) F(s; r_0)$, where $T = 2\pi/|\omega|$. It is shown in Appendix E that $\tilde{F}$ is an entire function of $s$.

We proceed by rewriting the function $\tilde{F}(s; r_0)$ as follows. We first define the functions

$$\tilde{f}(t) = \frac{J_1\left(2r_0 \sin\frac{t}{2}\right)}{2r_0 \sin\frac{t}{2}}, \quad \tilde{g}(t) = J_1'\left(2r_0 \sin\frac{t}{2}\right). \tag{5.67}$$

The polynomial parts of the functions in (5.34) are

$$\begin{aligned} p_A(s) &= \kappa s^2 + s - \kappa\omega^2 - \Omega\omega - \beta c_A, \quad p_B(s) = (2\omega\kappa + \Omega)\,s - (\kappa\omega + \Omega) \\ p_C(s) &= (2\omega\kappa + \Omega)\,s + 2\omega + \kappa\omega + \Omega, \quad p_D(s) = \kappa s^2 + s - 1, \end{aligned} \tag{5.68}$$

where

$$c_A(r_0) = \frac{1}{|\omega|\left(1 - \mathrm{e}^{-2\pi/|\omega|}\right)} \tilde{\mathcal{I}}\left[\tilde{f}(t)\cos^2\frac{t}{2} + \tilde{g}(t)\sin^2\frac{t}{2}\right] \tag{5.69}$$

and

$$\tilde{\mathcal{I}}[h] = \int_0^{2\pi} h(t)\mathrm{e}^{-t/|\omega|}. \tag{5.70}$$

The Laplace transforms in (5.34) may be written as

$$\begin{aligned} A_2(s) &= \tilde{\mathcal{L}}\left[\tilde{g}(t)\sin^2\frac{t}{2} - \tilde{f}(t)\cos^2\frac{t}{2}\right], \quad B_2(s) = \tilde{\mathcal{L}}\left[\left(\tilde{f}(t) + \tilde{g}(t)\right)\sin t\right] \\ D_2(s) &= \tilde{\mathcal{L}}\left[\tilde{f}(t)\sin^2\frac{t}{2} - \tilde{g}(t)\cos^2\frac{t}{2}\right], \end{aligned} \tag{5.71}$$

where

$$\tilde{\mathcal{L}}[h] = \int_0^{2\pi} h(t)\mathrm{e}^{-(s+1)t/|\omega|}\,\mathrm{d}t. \tag{5.72}$$

The function $\tilde{F}(s; r_0)$ may thus be expressed in the form

$$\begin{aligned} \tilde{F}(s) &= \left(1 - \mathrm{e}^{-(s+1)T}\right)(p_A p_D + p_B p_C) - \beta\left(\frac{p_A D_2 + p_D A_2}{|\omega|} + \frac{(p_B + p_C)B_2}{2\omega}\right) \\ &\quad + \frac{\beta^2}{\omega^2\left(1 - \mathrm{e}^{-(s+1)T}\right)}\left(A_2 D_2 + \frac{B_2^2}{4}\right). \end{aligned} \tag{5.73}$$

As shown in §5.6.1, the function $\tilde{F}(s; r_0)$ assumes a particularly simple form in the $r_0 \to 0$ limit:

$$\lim_{r_0\to 0}\frac{\tilde{F}(s; r_0)}{s(s^2 + \omega^2)} = \frac{\left(1 - \mathrm{e}^{-(s+1)T_0}\right)s\left[(\kappa(s+1)+1)^2 + \omega_0^2(\kappa - 1)^2\right]}{(s+1)^2 + \omega_0^2}, \tag{5.74}$$

which has infinitely many roots at

$$s_z = 0, \quad s_b^{\pm} = -\left(1 + \frac{1}{\kappa}\right) \pm \mathrm{i}\omega_0\left|1 - \frac{1}{\kappa}\right|, \quad s_n = -1 + \mathrm{i}n|\omega_0|, \quad n \in \mathbb{Z}\backslash\{\pm 1\}. \tag{5.75}$$

Our numerical method tracks these roots as a function of $r_0$, starting at $r_0 = 0$. Theorem 3 guarantees that circular orbits are stable for sufficiently large values of $r_0$, $r_0 > R_0(\gamma)$. We thus track the roots of $\tilde{F}(s; r_0)$ for $0 \leq r_0 < R_0(\gamma)$, which allows us to identify all unstable orbital solutions. The method used to determine $R_0(\gamma)$ will be detailed in the following section.

### 5.7.1 Proof that only finitely many zeros of $\tilde{F}(s; r_0)$ need consideration

We now prove that, for a fixed value of $\gamma$, finitely many of the zeros of $\tilde{F}(s; r_0)$ could be in the right half-plane, $\Re(s) \geq 0$. This result ensures that our numerical method is tractable, and places an upper bound on the number of roots $s_n$ that could produce an instability.

Let $\tilde{s} = (s+1)/|\omega|$, and consider the regime $r_0 < R_0(\gamma)$. The orbital solution of radius $r_0$ is stable provided that $\Re(\tilde{s}) < 1/|\omega|$. We show in Appendix F that, for $\Re(\tilde{s}) > -\rho$ (with $\rho > 0$ to be determined), we may express the functions (5.71) as

$$\begin{aligned}
A_2(\tilde{s}) &= -\frac{1 - \mathrm{e}^{-2\pi\tilde{s}}}{2\tilde{s}} + \epsilon^{(A)}, \quad \left|\epsilon^{(A)}\right| \leq \frac{1}{|\tilde{s}|^3}\left(\epsilon_0^{(A)} + \frac{\epsilon_1^{(A)}}{|\tilde{s}|}\right) \\
B_2(\tilde{s}) &= \frac{1 - \mathrm{e}^{-2\pi\tilde{s}}}{\tilde{s}^2} + \epsilon^{(B)}, \quad \left|\epsilon^{(B)}\right| \leq \frac{\epsilon_0^{(B)}}{|\tilde{s}|^3} \\
D_2(\tilde{s}) &= -\frac{1 - \mathrm{e}^{-2\pi\tilde{s}}}{2\tilde{s}} + \epsilon^{(D)}, \quad \left|\epsilon^{(D)}\right| \leq \frac{1}{|\tilde{s}|^3}\left(\epsilon_0^{(D)} + \frac{\epsilon_1^{(D)}}{|\tilde{s}|}\right),
\end{aligned} \tag{5.76}$$

where the error terms $\epsilon_0$ and $\epsilon_1$ are bounded functions of $r_0$ in the region $r_0 < R_0$. We may thus write $\tilde{F}$ in the form

$$\tilde{F}(\tilde{s}) = \left(1 - \mathrm{e}^{-2\pi\tilde{s}}\right)\left[p_A p_D + p_B p_C + \frac{\beta}{|\omega|}\left(\kappa\omega^2\tilde{s} + |\omega|(1 - 2\kappa)\right)\right] + E(\tilde{s}), \tag{5.77}$$

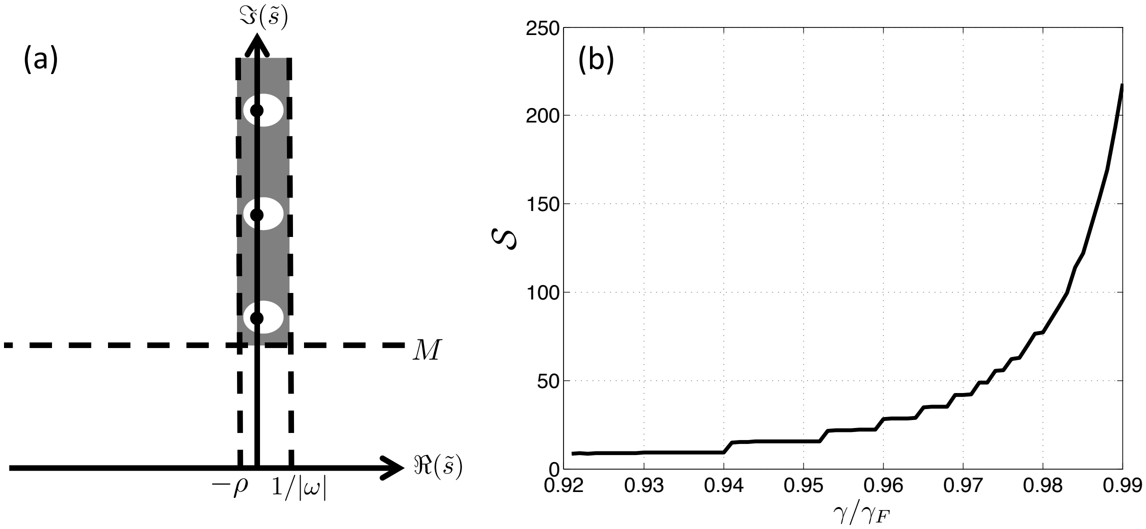

Figure 5-2: (a) Partition of the $\tilde{s}$-plane used in §5.7.1, where $\tilde{s} = (s+1)/|\omega|$. The black dots indicate the positions of the roots $\tilde{s} = \mathrm{i}n$ at $r_0 = 0$, where $n \in \mathbb{Z}$. The white regions surrounding these roots represent $C_n$, outside of which $\left|1 - \mathrm{e}^{-2\pi\tilde{s}}\right| > 1 - \mathrm{e}^{-2\pi/|\omega|}$. (b) Plot of $\mathcal{S}(\gamma)$ as a function of the forcing acceleration $\gamma/\gamma_F$, computed on the basis of (5.86). We show in §5.7.1 that the roots $s_n$ for $n > \lceil \mathcal{S} \rceil$ are confined within $C_n$ for all $r_0 < R_0(\gamma)$, which ensures that they do not generate an instability.

where

$$\begin{aligned} E(\tilde{s}) \;=\; & \left(1 - \mathrm{e}^{-2\pi\tilde{s}}\right)\left[\frac{\beta}{2|\omega|}\left(\frac{a_0 + d_0}{\tilde{s}} - \frac{(p_B + p_C)\,\mathrm{sgn}(\omega)}{\tilde{s}^2}\right) + \frac{\beta^2}{4\omega^2}\left(\frac{1}{\tilde{s}^2} + \frac{1}{\tilde{s}^4}\right)\right] \\ & - \frac{\beta}{|\omega|}\left(\epsilon^{(A)} p_D + \epsilon^{(D)} p_A + \frac{(p_B + p_C)\,\epsilon^{(B)}\mathrm{sgn}(\omega)}{2}\right) + \frac{\beta^2}{\omega^2}\left(-\frac{\epsilon^{(A)} + \epsilon^{(D)}}{2\tilde{s}} + \frac{\epsilon^{(B)}}{2\tilde{s}^2}\right) \\ & + \frac{\beta^2}{\omega^2\left(1 - \mathrm{e}^{-2\pi\tilde{s}}\right)}\left(\epsilon^{(A)}\epsilon^{(D)} + \frac{\epsilon^{(B)2}}{4}\right). \end{aligned} \tag{5.78}$$

Let $\mathcal{C}(r_0) = \{\tilde{s} : \left|1 - \mathrm{e}^{-2\pi\tilde{s}}\right| < c_E\}$, where $0 < c_E < 1$ is to be determined. One can see that $\mathcal{C}$ consists of a sequence of disjoint regions $C_n(r_0)$ containing $\tilde{s} = \mathrm{i}n, n \in \mathbb{Z}$, as depicted in Figure 5-2(a). Indeed, if $\tilde{s} = \lambda + \mathrm{i}\sigma$, the boundary of $C_n$ is defined by the equation $1 + \mathrm{e}^{-4\pi\lambda} - 2\mathrm{e}^{-2\pi\lambda}\cos 2\pi\sigma = c_E^2$, which has a solution provided that $n - 1/4 < \sigma < n + 1/4$. Solving this equation, we obtain $\mathrm{e}^{-2\pi\lambda} = \cos 2\pi\sigma \pm \sqrt{\cos^2 2\pi\sigma + (1 - c_E^2)}$. For $\sigma = n$, we have $\lambda_\mp = -\log(1 \pm c_E)/2\pi$, so it follows that $\lambda_- \le \lambda \le \lambda_+$ in $C_n$. We thus take $\rho > -\lambda_- = \log(1 + c_E)/2\pi$ and $c_E < 1 - \mathrm{e}^{-2\pi/|\omega|}$, so that $C_n$ is contained within the stability region, $\Re(\tilde{s}) < 1/|\omega|$.

Let $\mathcal{C}'$ be the complement of $\mathcal{C}$. In the region $\{\Re(\tilde{s}) > -\rho\} \cap \mathcal{C}'$, we have the following upper bound on $|E|$:

$$\begin{aligned}
|E(\tilde{s})| \;\; \leq \;\; & \left(1+\mathrm{e}^{2\pi\rho}\right)\left[\frac{\beta}{2|\omega|}\left(\frac{|a_0+d_0-(b_1+c_1)\operatorname{sgn}(\omega)|}{|\tilde{s}|}+\frac{|b_0+c_0|}{|\tilde{s}|^2}\right)+\frac{\beta^2}{4\omega^2}\left(\frac{1}{|\tilde{s}|^2}+\frac{1}{|\tilde{s}|^4}\right)\right] \\
& +\frac{\beta}{|\omega|}\left[\frac{1}{|\tilde{s}|}\left(\epsilon_0^{(A)}+\frac{\epsilon_1^{(A)}}{|\tilde{s}|}\right)\left(|d_2|+\frac{|d_1|}{|\tilde{s}|}+\frac{|d_0|}{|\tilde{s}|^2}\right)\right. \\
& \left.+\frac{1}{|\tilde{s}|}\left(\epsilon_0^{(D)}+\frac{\epsilon_1^{(D)}}{|\tilde{s}|}\right)\left(|a_2|+\frac{|a_1|}{|\tilde{s}|}+\frac{|a_0|}{|\tilde{s}|^2}\right)+\frac{\epsilon_0^{(B)}}{2|\tilde{s}|^2}\left(|b_1+c_1|+\frac{|b_0+c_0|}{|\tilde{s}|}\right)\right] \\
& +\frac{\beta^2}{2\omega^2|\tilde{s}|^4}\left[\epsilon_0^{(A)}+\frac{\epsilon_1^{(A)}}{|\tilde{s}|}+\epsilon_0^{(D)}+\frac{\epsilon_1^{(D)}}{|\tilde{s}|}+\frac{\epsilon_0^{(B)}}{|\tilde{s}|}\right] \\
& +\frac{\beta^2}{\omega^2 c_E|\tilde{s}|^6}\left[\epsilon_0^{(A)}\epsilon_0^{(D)}+\frac{\epsilon_0^{(A)}\epsilon_1^{(D)}+\epsilon_1^{(A)}\epsilon_0^{(D)}}{|\tilde{s}|}+\frac{\epsilon_1^{(A)}\epsilon_1^{(D)}}{|\tilde{s}|^2}+\frac{\epsilon_0^{(B)2}}{4}\right].
\end{aligned} \tag{5.79}$$

We may rewrite this in the form $|E(\tilde{s})| \leq \sum_{k=1}^{8} e_k/|\tilde{s}|^k$, where

$$\begin{aligned}
e_1 &= \frac{\beta}{2|\omega|}\left(2|d_2|\epsilon_0^{(A)}+2|a_2|\epsilon_0^{(D)}+\left(1+\mathrm{e}^{2\pi\rho}\right)|a_0+d_0-(b_1+c_1)\operatorname{sgn}(\omega)|\right) \\
e_2 &= \frac{\beta}{|\omega|}\left[|d_1|\epsilon_0^{(A)}+\frac{|b_1+c_1|\,\epsilon_0^{(B)}}{2}+|a_1|\epsilon_0^{(D)}+|d_2|\epsilon_1^{(A)}+|a_2|\epsilon_1^{(D)}\right. \\
&\qquad \left.+\frac{1+\mathrm{e}^{2\pi\rho}}{4}\left(\frac{\beta}{|\omega|}+2\beta\,|b_0+c_0|\right)\right] \\
e_3 &= \frac{\beta}{|\omega|}\left[|d_0|\epsilon_0^{(A)}+\frac{|b_0+c_0|\epsilon_0^{(B)}}{2}+|a_0|\epsilon_0^{(D)}+|d_1|\epsilon_1^{(A)}+|a_1|\epsilon_1^{(D)}\right] \\
e_4 &= \frac{\beta^2}{2\omega^2}\left(\frac{1+\mathrm{e}^{2\pi\rho}}{2}+\epsilon_0^{(A)}+\epsilon_0^{(D)}\right)+\frac{\beta}{|\omega|}\left(|d_0|\epsilon_1^{(A)}+|a_0|\epsilon_1^{(D)}\right) \\
e_5 &= \frac{\beta^2}{2\omega^2}\left(\epsilon_0^{(B)}+\epsilon_1^{(A)}+\epsilon_1^{(D)}\right), \quad e_6=\frac{\beta^2}{4c_E\omega^2}\left(\epsilon_0^{(B)2}+4\epsilon_0^{(A)}\epsilon_0^{(D)}\right) \\
e_7 &= \frac{\beta^2}{c_E\omega^2}\left(\epsilon_0^{(D)}\epsilon_1^{(A)}+\epsilon_0^{(A)}\epsilon_1^{(D)}\right), \quad e_8=\frac{\beta^2\epsilon_1^{(A)}\epsilon_1^{(D)}}{c_E\omega^2}.
\end{aligned} \tag{5.80}$$

We now establish a lower bound on the first term in (5.77). We consider the polynomial $P(\tilde{s}) = p_A p_D + p_B p_C$, and define $M$ to be the smallest number such that all of the roots $z_i$ of $P$ satisfy

$$|\tilde{s} - z_i| > \frac{|\tilde{s}|}{2} \quad \text{in the region} \quad \{\Im(\tilde{s}) > M\} \cap \left\{-\rho < \Re(\tilde{s}) < \frac{1}{|\omega|}\right\}. \tag{5.81}$$

This implies that

$$M - \frac{1}{2}\sqrt{\frac{1}{\max(\rho, 1/|\omega|)^2} + M^2} \geq I, \quad I = \max|\Im(z_i)|. \tag{5.82}$$

Solving for $M$, we obtain

$$M = \frac{1}{3}\left(4I + \sqrt{\frac{1}{\max(\rho, 1/|\omega|)^2} + 4I^2}\right), \tag{5.83}$$

from which it follows that

$$|P(\tilde{s})| \geq \frac{\left(\kappa\omega^2\right)^2}{16}|\tilde{s}|^4, \quad \{\Im(\tilde{s}) > M\} \cap \left\{-\rho < \Re(\tilde{s}) < \frac{1}{|\omega|}\right\}. \tag{5.84}$$

We have established the following three bounds:

- $\left|1 - \mathrm{e}^{-2\pi\tilde{s}}\right| \geq c_E$ for $\tilde{s} \in \mathcal{C}'$
- $|P(\tilde{s})| \geq \frac{\left(\kappa\omega^2\right)^2}{16}|\tilde{s}|^4$ in the region $\{\Im(\tilde{s}) > M\} \cap \left\{-\rho < \Re(\tilde{s}) < \frac{1}{|\omega|}\right\}$
- $|E(\tilde{s})| \leq \sum_{k=1}^{8} e_k/|\tilde{s}|^k$ in the region $\mathcal{C}' \cap \{\Re(\tilde{s}) > -\rho\}$.

Let $\mathcal{R}$ be the region in which these three bounds are simultaneously valid, indicated by the shaded region in Figure 5-2(a). We define $S = S(r_0; \gamma)$ as the solution to the equation

$$\frac{c_E\left(\kappa\omega^2\right)^2}{16}S^4 = \sum_{k=1}^{8}\frac{e_k}{S^k}. \tag{5.85}$$

We thus deduce that $\tilde{F}(\tilde{s}; r_0)$ has no roots in the region $\mathcal{R} \cap \{|\tilde{s}| > S\}$. Letting

$$\mathcal{S}(\gamma) = \sup_{r_0 \leq R_0} \max(S, M), \tag{5.86}$$

it follows that the roots originating at $\tilde{s} = \mathrm{i}n$ for $r_0 = 0$ must stay inside $C_n(r_0)$ for all $r_0 \leq R_0$, provided that $n \geq \lceil \mathcal{S} \rceil$. Since $C_n(r_0)$ is in the region $\Re(s) < 0$ by construction, only the (finitely many) roots $s_n$ satisfying $n < \lceil \mathcal{S} \rceil$ need to be tracked.

To compute $\mathcal{S}(\gamma)$, we make use of the following conjecture:

**Conjecture 1** *For a fixed value of* $\gamma$*, let* $R^*(\gamma)$ *be the largest value of* $r_0$ *for which* $\mathrm{d}\Omega/dr_0 = 0$*. Then the orbital solutions are stable for* $r_0 > R^*(\gamma)$*.*

We have verified this conjecture numerically for many values of $\gamma$, but were unable to prove it analytically. Based on this conjecture, we compute $\mathcal{S}$ using $R_0(\gamma) = R^*(\gamma)$. Figure 5-2(b) shows that $\mathcal{S}$ increases with $\gamma$, indicating that more roots need to be tracked as the forcing acceleration is increased progressively. In practice, we find that the computed values of $\mathcal{S}(\gamma)$ provide a significant overestimate for the number of unstable eigenvalues.

## 5.8 Results of stability analysis

Having constructed a methodology for assessing the stability of arbitrary orbital solutions, we now present the results of the stability analysis and compare them to both experimental data [38] and numerical simulations (Chapter 4 [51]). Following the experiments reported by Harris and Bush [38], we consider a walker of radius 0.4 mm and a silicone oil bath of viscosity 20 cS and forcing frequency $f = 80$ Hz, for which the dimensional parameters in (5.8) are $F = 1.1506 \times 10^{-2}$ g mm/s$^2$, $D = 1.997 \times 10^{-3}$ g/s, $m = 2.5441 \times 10^{-4}$ g, $k_F = 1.3224$ mm$^{-1}$ and $T_d = 1.8215 \times 10^{-2}$ s. The corresponding parameters $\kappa$ and $\beta$ are related to the forcing acceleration $\gamma$ through the formulae $\kappa = 6.994\,(1 - \gamma/\gamma_F)$ and $\beta = 0.10112/\,(1 - \gamma/\gamma_F)^2$. We perform the stability analysis for the parameter range $0 \leq r_0/\lambda_F \leq 5.5$ and $0.920 \leq \gamma/\gamma_F \leq 0.995$, in increments $\Delta r/\lambda_F = 0.016$ and $\Delta(\gamma/\gamma_F) = 0.001$.

Figure 5-3 shows selected roots of $\tilde{F}(s; r_0)$, plotted as a function of $r_0$ for various fixed values of $\gamma/\gamma_F$. As shown in Figure 5-3, the roots $s_0$ and $s_z$, as defined by (5.75), undergo cycles of merging and splitting on the real axis. We found the same

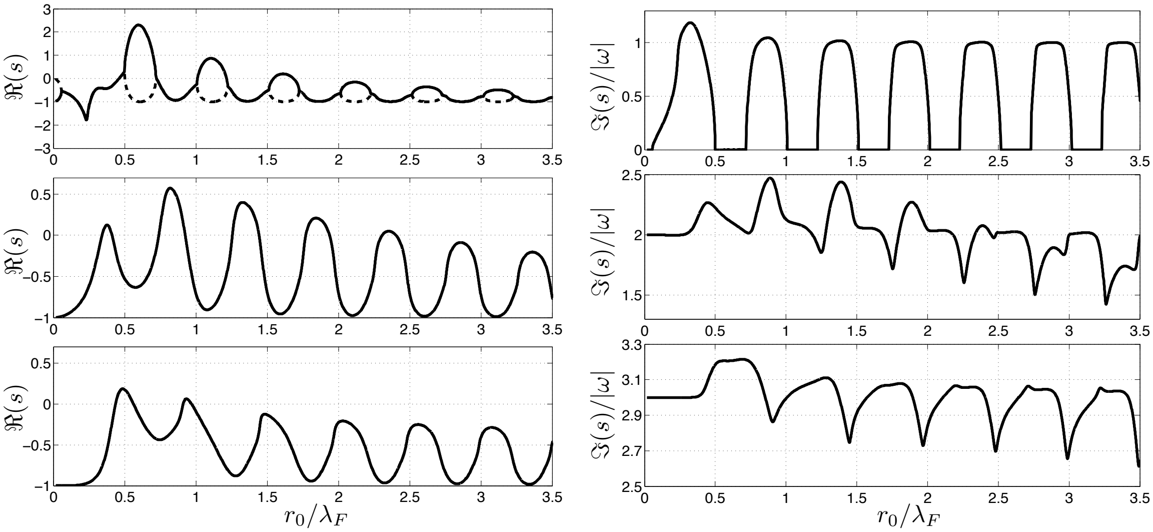

Figure 5-3: Plots of selected roots of $\tilde{F}(s; r_0)$ as a function of the orbital radius $r_0$, for fixed values of the forcing acceleration $\gamma/\gamma_F$. The left panels correspond to the real part of the roots, the right panel to the imaginary part. The first row shows the eigenvalue pair $s_0$ (solid) and $s_z$ (dashed) for $\gamma/\gamma_F = 0.956$. The second row shows $s_2(r_0)$ for $\gamma/\gamma_F = 0.970$, and the third $s_3(r_0)$ for $\gamma/\gamma_F = 0.975$.

to be true for the roots $s_b^+$ and $s_b^-$. For the parameter values used here, we find that all orbits are stable for $\gamma/\gamma_F \leq 0.920$. For $0.921 \leq \gamma/\gamma_F \leq 0.960$, the pair of roots $(s_0, s_z)$ generate instabilities in orbits for which $\mathrm{d}\Omega/\mathrm{d}r_0 > 0$, which were proven to be unstable in Theorem 1. For $0.961 \leq \gamma/\gamma_F \leq 0.995$, the pair $(s_b^+, s_b^-)$ generates these instabilities. We thus deduce that orbital quantization is generated by an instability corresponding to one of the eigenvalue pairs $(s_0, s_z)$ or $(s_b^+, s_b^-)$.

For the values of $\gamma/\gamma_F$ used, we found that the other eigenvalues $s_n$ for $n \neq 0$ did not merge with any of the other eigenvalues and thus always had a nonzero imaginary part, $\Im(s_n) \neq 0$. It follows that $s_n(r_0)$ and $s_{-n}(r_0)$ are complex conjugates for $n \neq 0$. The eigenvalues $s_n$ seem to generate instabilities sequentially as $\gamma/\gamma_F$ is increased progressively. Specifically, for a fixed value of $\gamma/\gamma_F$, we found that the stability of $s_n$ for all $r_0 < R_0$ ensured the stability of $s_m$ for $|m| > n$. Plots of $s_2(r_0)$ and $s_3(r_0)$ for specific values of $\gamma/\gamma_F$ are shown in Figure 5-3.

### 5.8.1 Stability diagram

Figure 5-4 shows the complete stability diagram for circular orbits. For a given value of $\gamma/\gamma_F$, the roots $s_0, s_z, s_b^{\pm}$, and $s_n$ for $n < \lceil \mathcal{S} \rceil$ were tracked as a function of $r_0$, where $\mathcal{S}(\gamma)$ was defined in §5.7.1. Due to Propositions 1 and 2, a single point on the diagram uniquely specifies the circular orbit. Points colored in blue denote stable orbits. We color the unstable orbits using the following color scheme. For a given orbit, let $s^*$ be the eigenvalue with the largest real part from the set $\{s_0, s_z, s_b^+, s_b^-\}$. We then order the eigenvalues $s^*$ and $s_n$ for $2 \leq n \leq \lceil \mathcal{S} \rceil$ by their imaginary parts, from which we obtain a list of eigenvalues, $q_1, q_2, \ldots$. From this list, we select the eigenvalue with the largest real part, and color the appropriate point on the stability diagram according to its index. The colors red, green, and yellow are used for the first three indices, the rest being listed in the caption of Figure 5-4.

It would appear easier to color the unstable orbits simply by the eigenvalue with the largest real part, without first ranking the eigenvalues by their imaginary parts. The reason for the complicated color scheme is evident from Figure 5-5, which shows the eigenvalues $s_2$ (solid) and $s_3$ (dashed) for $\gamma/\gamma_F = 0.981$. Note that the imaginary part of $s_2$ changes rapidly from $\Im(s_2) \approx 2|\omega|$ to $\Im(s_2) \approx 3|\omega|$, and vice versa for $s_3$. This suggests that the two instabilities generated by $s_2$ and $s_3$ in Figure 5-5 are actually similar Hopf bifurcations, as the imaginary parts of both eigenvalues are near $2|\omega|$ at the points of instability. The procedure described in the preceding paragraph allows us to distinguish between qualitatively different Hopf bifurcations.

### 5.8.2 Wobbling orbits

For $r_0/\lambda_F > 0.6$, we find that the boundaries of the green and yellow regions in Figure 5-4 correspond to supercritical Hopf bifurcations of the circular orbit, based on the numerical simulations presented in Chapter 4 [51]. Indeed, when the trajectory equation (5.9) is simulated near the instability boundary, the circular orbit solution destabilizes into a wobbling orbit. Near the boundaries of the green (yellow) regions, where the imaginary part of the unstable eigenvalue is approximately

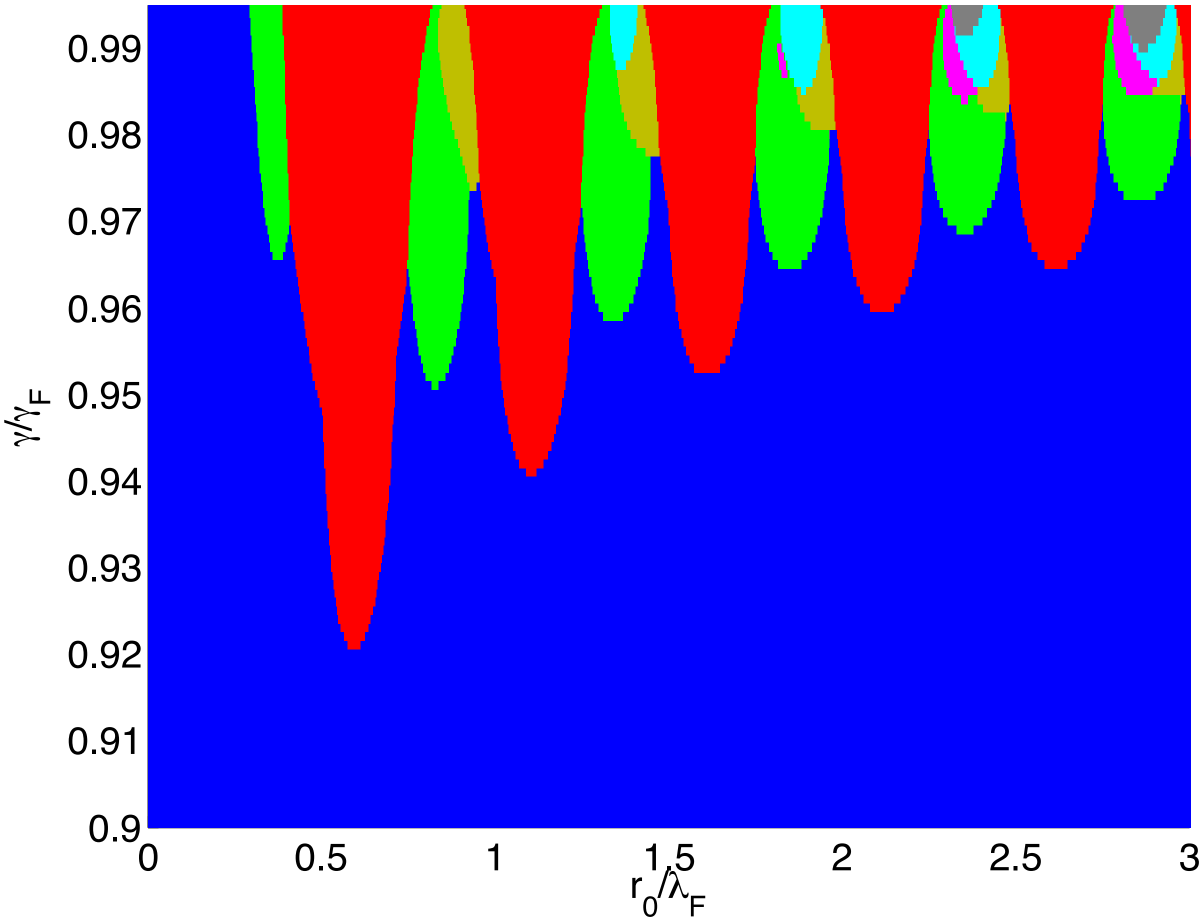

Figure 5-4: Orbital stability of circular orbit solutions to (5.9), plotted as a function of the dimensionless orbital radius $r_0/\lambda_F$ and forcing acceleration $\gamma/\gamma_F$. The results of §5.4 show that a point on this diagram uniquely specifies the circular orbit. For a given value of $r_0$ and $\gamma$, the roots of $\tilde{F}(s;r_0)$ are computed and ordered by their imaginary part, according to the scheme described in §5.8.1. We thus obtain a list of roots $q_1, q_2, \ldots$. We then select the root $q_i$ with the largest real part, and color the point on the stability diagram according to the index $i$. We use the color scheme $q_1$ = red, $q_2$ = light green, $q_3$ = yellow, $q_4$ = magenta, $q_5$ = cyan, $q_6$ = brown and $q_7$ = gray.

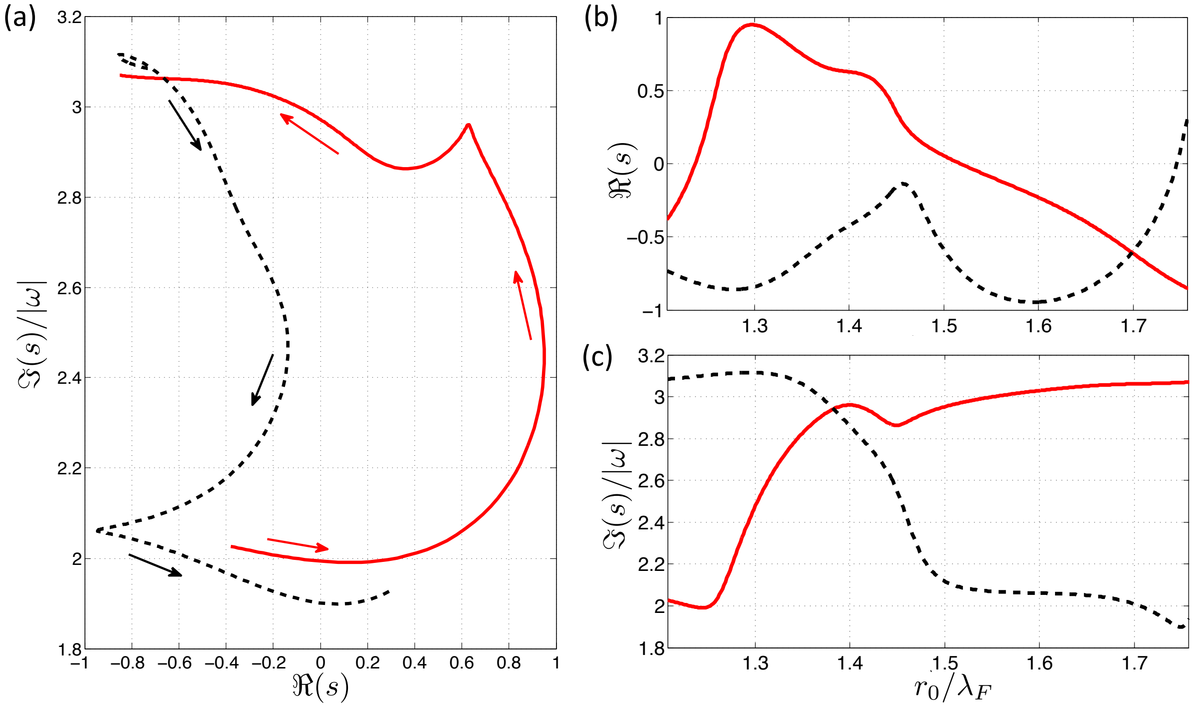

Figure 5-5: Plots of the eigenvalues $s_2(r_0)$ (solid) and $s_3(r_0)$ (dashed) for $\gamma/\gamma_F = 0.981$. Panel (a) shows the trajectory of the two eigenvalues in the complex plane as $r_0$ is varied. Panels (b) and (c) show, respectively, the real and imaginary parts of the two roots, plotted for the same values of $r_0$. The imaginary parts are normalized by the orbital frequency $|\omega|$. Note that the imaginary part of $s_2$, which starts at $\Im(s_2(0)) = 2|\omega|$, rapidly changes to $\Im(s_2) \approx 3|\omega|$, and vice versa for $s_3$.

$2|\omega|$ ($3|\omega|$), the wobbling orbits assume an elliptical (triangular) shape, their radii oscillating at roughly twice (thrice) the orbital frequency (Chapter 4 [51]). Wobbling orbits of higher frequencies were not found in the parameter range explored, as the corresponding instability regions in Figure 5-4 are contained entirely within the green or yellow tongues. The possibility of their presence for a different fluid or drop size is currently being explored. We note that the eigenvalue pairs $(s_0, s_z)$ and $(s_b^+, s_b^-)$ seem to only generate subcritical Hopf bifurcations when they cross the imaginary axis, as the corresponding wobbling orbits were not observed in numerical simulations (Chapter 4 [51]).

The $2\omega$-wobbling orbits in the green tongues for $r_0/\lambda_F > 0.6$ were predicted by the stability analysis presented herein, and subsequently observed in laboratory experiments [38]. Figure 5-6 shows the observed wobbling frequency as a function of the rotation rate $\Omega$. The theoretical curve plots the imaginary part of the unstable eigenvalues at the boundary of the second green region, between $0.7 \leq r_0/\lambda_F \leq 0.9$. The curve lies within the experimental error bars, indicating that the wobbling orbits predicted by the linear stability analysis correspond closely to those observed. Note that the theoretical curve only provides an approximation for the expected wobbling frequency, the complete analysis of which requires consideration of nonlinear corrections to (5.31). We note that $3\omega$-wobbling orbits have not been observed in laboratory experiments, presumably because the yellow tongues only arise in a relatively small parameter regime.

### 5.8.3 Chaotic dynamics at high memory

It was shown in Chapter 3 [50] that the orbital radii, as defined by (5.20), may be approximated by the zeros of $J_0(r)$ and $J_1(r)$ as $\gamma/\gamma_F \to 1$. Figure 5-4 suggests that virtually all of these circular orbits become unstable in this limit. This is confirmed by both numerical simulations (Chapter 4 [51]) and laboratory experiments [38], which demonstrate that the walker's trajectory is chaotic in this regime. In order to ascertain the underlying structure of the chaotic dynamics, we may compute the trajectory's loop radius $R(t)$ using the method detailed by Harris and Bush [38, Appendix B].

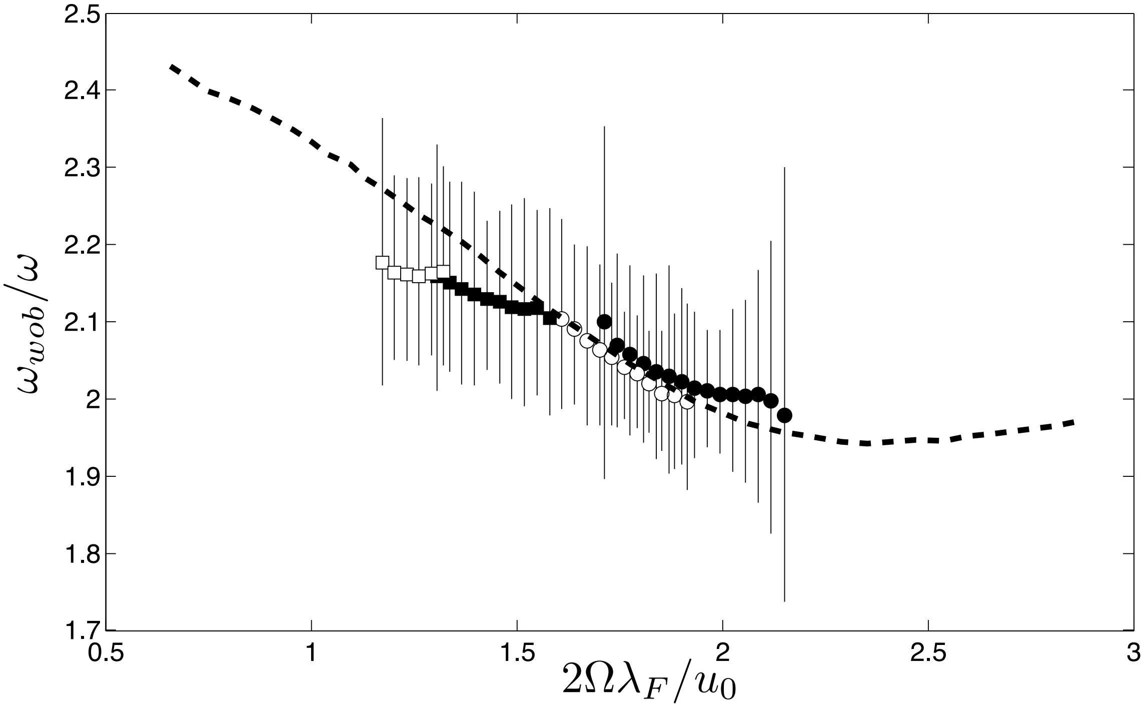

Figure 5-6: Plot of the wobbling frequency $\omega_{wob}$ normalized by the orbital frequency $\omega$ as a function of the dimensionless rotation rate $2\Omega\lambda_F/u_0$. The points indicate experimental data from Harris and Bush [38], corresponding to the four different values of the vibrational forcing $\gamma/\gamma_F$ and walking speed $u_0$: $\gamma/\gamma_F = 0.961 \pm 0.002$ and $u_0 = 12.0$ mm s$^{-1}$ (●); $\gamma/\gamma_F = 0.969 \pm 0.005$ and $u_0 = 12.3$ mm s$^{-1}$ (○); $\gamma/\gamma_F = 0.974 \pm 0.002$ and $u_0 = 12.3$ mm s$^{-1}$ (■); and $\gamma/\gamma_F = 0.978 \pm 0.003$ and $u_0 = 12.4$ mm s$^{-1}$ (□). The theoretical curve (dashed) plots the imaginary part of the unstable eigenvalue at the boundary of the green region in Figure 5-4, between $0.7 \leq r_0/\lambda_F \leq 0.9$.

The statistics of $R(t)$ exhibits a multimodal structure with peaks near the zeros of $J_0(r)$ ([38], Chapter 4 [51]). Figure 5-7(a) shows two such histograms, computed on the basis of numerical simulations of (5.9) for $\Omega = 0.70\ \mathrm{s}^{-1}$.

The red vertical lines in Figure 5-7(a) are located at the radii of the possible orbital solutions, as determined by (5.20). Their height is determined by $\tau \equiv 1/\Re(s_{max})$, $s_{max}$ being the eigenvalue of the appropriate orbital solution with the largest real part. The bars alternate in height, the taller ones being located near the zeros of $J_0(r)$ and the shorter near the zeros of $J_1(r)$. Note that $\tau$ provides an approximation for the time it takes for the circular orbit to destabilize. The strongly unstable orbital solutions, located near the roots of $J_1(r)$, are avoided by the walker, as the instability timescale $\tau$ of those orbits is relatively small. The chaotic dynamics of the walker may thus be understood as arising from its chaotic exploration of those circular orbits satisfying $J_0(r_0) \approx 0$, which take relatively long to destabilize. A similar conclusion may be drawn from Figure 5-7(b), in which the circular orbits are colored according to $\Re(s_{max})$. The red portions of the diagram, corresponding to large values of $\Re(s_{max})$, are concentrated around the zeros of $J_1(r)$, indicated by the dashed vertical lines.

We note that the relative amplitudes of the histogram's peaks in Figure 5-7(a) do not perfectly match those predicted by the eigenvalues. This is presumably because the peaks are determined by both the circular orbit's instability timescale $\tau$ and the basin of attraction, the characterization of the latter being beyond the scope of our linear stability analysis. Nevertheless, we note that a conceptually similar approach was taken by Gutzwiller [36], who considered the connection between the stability of classical periodic orbits and quantum mechanical statistics.

## 5.9 Discussion

We have analyzed the properties of solutions to the integro-differential trajectory equation (5.9), which models the pilot-wave dynamics of walking droplets in a rotating frame. We showed that, above a critical value of the forcing acceleration and below a critical value of the rotation rate, $\gamma > \gamma_W$ and $|\Omega| < \Omega_0$, the bouncing solution

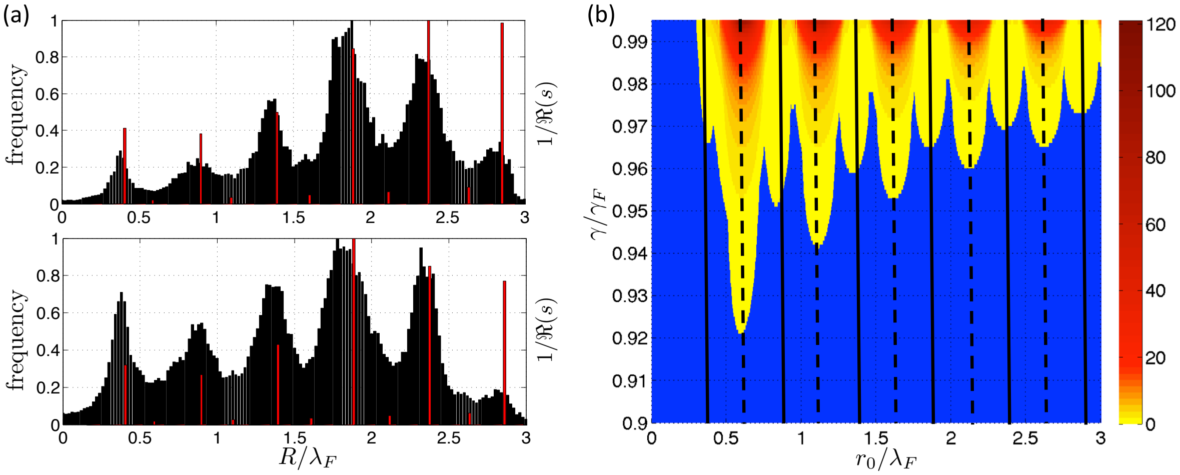

Figure 5-7: (a) Histogram of the walker's loop radius $R(t)$, computed on the basis of numerical simulations of (5.9) for $\Omega = 0.70$ s$^{-1}$ and $\gamma/\gamma_F = 0.983$ (top panel) and $\gamma/\gamma_F = 0.985$ (bottom panel) (Chapter 4 [51]). The red vertical bars are located at the radii of the possible orbital solutions, as determined by (5.20). Their height is determined by $\tau \equiv 1/\Re(s_{max})$, $s_{max}$ being the eigenvalue of the appropriate orbital solution with the largest real part. The vertical bars and histograms have been normalized so that their maximum height is 1. (b) Orbital stability diagram color coded according to the size of $\Re(s_{max})$. Blue denotes stable orbits, for which $\Re(s_{max}) < 0$. The solid lines are located at the roots of $J_0(2\pi r)$, and the dashed lines at the roots of $J_1(2\pi r)$. Note that the orbital radii satisfying $J_1(r_0/\lambda_F) \approx 0$ are more unstable than those satisfying $J_0(r_0/\lambda_F) \approx 0$, which explains why the latter are more prominent in panel (a).

$\boldsymbol{x}$ = constant may destabilize into a circular orbital solution with constant angular frequency, $\boldsymbol{x} = r_0(\cos\omega t, \sin\omega t)$. We derived formulae describing the dependence of $r_0$ and $\omega$ on $\Omega$ and $\gamma$, and showed that the governing equations define $\omega$ and $\Omega$ as single-valued functions of $r_0$.

We then analyzed the stability of these orbital solutions, and showed that the eigenvalues $s$ of the linear stability problem are the roots of a function $F(s)$. By expanding $F$ in various asymptotic limits, we showed that circular orbits are stable at low memory, $\gamma \gtrsim \gamma_W$, and at both small and large orbital radius, $r_0 \ll 1$ and $r_0 \gg 1$, which agrees with laboratory experiments [32, 38].

Outside of these asymptotic limits, the roots of $F$ must be found numerically. We showed that the roots can be computed explicitly in the limit $r_0 \to 0$. Our numerical method thus tracks the roots as a function of $r_0$, starting at $r_0 = 0$. While $F$ has infinitely many roots, we showed that, for a fixed value of $\gamma$, only finitely many of them can move into the right half-plane, $\Re(s) \geq 0$, and thus generate an instability. This result ensures that our numerical method is tractable. Our analysis culminated in a regime diagram delineating the dependence of the stability characteristics on the orbital radius $r_0$ and forcing acceleration $\gamma$. The mathematical methodology presented herein was used in Chapter 3 [50] to gain physical insight into the walker's orbital dynamics.

We then used the results of our stability analysis to rationalize some observations from laboratory experiments [38] and numerical simulations (Chapter 4 [51]). We showed that the frequencies of wobbling orbits, as predicted by the imaginary part $\Im(s_{max})$ of the dominant unstable eigenvalue, agree well with those observed in experiments [38]. We also deduced that orbits whose radii satisfy $J_1(r_0/\lambda_F) \approx 0$ are more unstable than those for which $J_0(r_0/\lambda_F) \approx 0$, by showing that $\Re(s_{max})$ is substantially larger for the former. This rationalized the laboratory experiments reported by Harris and Bush [38] and numerical simulations in Chapter 4 [51], which showed that the statistics of the walker's loop radius at high memory exhibits peaks near the zeros of $J_0(r)$. The walker's chaotic dynamics at high memory may thus be understood as arising from its chaotic exploration of preferred unstable orbital solutions.

We note that the mathematical framework presented herein can be easily extended to account for different external forces. In future work, we plan to assess the stability properties of orbital solutions in the presence of a central force, such as $\boldsymbol{F} = -k\boldsymbol{x}$, which has recently been explored in the laboratory [52].

# Chapter 6

# The wave-induced added mass of walking droplets

## 6.1 Introduction

Einstein [6] and de Broglie [21, 22] both sought to reconcile quantum mechanics and relativity through consideration of the wave nature of matter [13]. De Broglie's conception in his double-solution theory was of microscopic particles moving in resonance with and being guided by their own wave field. While neither the physical origins nor the detailed geometric form of the pilot-wave field was specified, it was posited that the resulting particle motion could give rise to a statistical behavior consistent with the predictions of standard quantum theory. Workers in stochastic electrodynamics [23] have suggested that an electromagnetic pilot-wave might arise through the resonant interaction between a microscopic particle's internal vibration and the electromagnetic vacuum field [7]. Some have further proposed that the interaction of moving particles with this vacuum field could give rise to a speed-dependent inertial mass, a feature of relativistic mechanics [37, 56]. We here explore the relevance of this

---

Chapter 5 appears as submitted: The wave-induced added mass of walking droplets, Bush, J. W. M., Oza, A. U. and Moláček, J., *Journal of Fluid Mechanics* [11].

perspective to the dynamics of walking droplets through inferring their wave-induced added mass.

The integro-differential trajectory equation (2.16) derived in Chapter 2 represents the starting point of the current study. Note that the hydrodynamic pilot-wave system is forced and dissipative. Nevertheless, it is interesting to imagine how the system might be described if one were unaware that it was either. Specifically, if one observes the system from above, and ignores the fact that it is a forced, dissipative pilot-wave system, how should one describe the dynamics? What is the effective mass of a walker? We demonstrate here that, in certain parameter regimes, the walker dynamics may be described in terms of the motion of a particle with a speed-dependent mass and a nonlinear drag force that drives it towards a fixed speed.

## 6.2 Pilot-wave hydrodynamics

In Chapter 2, we derived an integro-differential trajectory equation for the motion of a walker. In the presence of an external force $\boldsymbol{F}$, the equation takes the form

$$m\ddot{\boldsymbol{x}} + D\dot{\boldsymbol{x}} = \frac{W}{T_F}\int_{-\infty}^{t} J_1\left(k_F|\boldsymbol{x}(t)-\boldsymbol{x}(s)|\right)\,\frac{\boldsymbol{x}(t)-\boldsymbol{x}(s)}{|\boldsymbol{x}(t)-\boldsymbol{x}(s)|}\;e^{-(t-s)/T_M}\,\mathrm{d}s\;+\;\boldsymbol{F} \tag{6.1}$$

where $W = mgAk_F$. Introducing the dimensionless variables $\hat{\boldsymbol{x}} = k_F\boldsymbol{x}$ and $\hat{t} = t/T_M$, we obtain

$$\kappa\hat{\boldsymbol{x}}'' + \hat{\boldsymbol{x}}' = \beta\int_{0}^{\infty} J_1\left(\left|\hat{\boldsymbol{x}}(t)-\hat{\boldsymbol{x}}(\hat{t}-z)\right|\right)\frac{\hat{\boldsymbol{x}}(\hat{t})-\hat{\boldsymbol{x}}(\hat{t}-z)}{\left|\hat{\boldsymbol{x}}(\hat{t})-\hat{\boldsymbol{x}}(\hat{t}-z)\right|}\mathrm{e}^{-z}\,\mathrm{d}z + \hat{\boldsymbol{F}}, \tag{6.2}$$

where $\kappa = m/DT_M$ and $\beta = Wk_FT_M^2/DT_F$ are the nondimensional mass and the memory force coefficient, $\hat{\boldsymbol{F}} = \boldsymbol{F}k_FT_M/D$ is the dimensionless applied force, and primes denote differentiation with respect to $\hat{t}$.

### 6.2.1 The weak-acceleration limit

We now consider the simplified dynamics that arise when the walker accelerates in response to a force that varies slowly relative to the memory time $T_M$, $\hat{\boldsymbol{F}} = \hat{\boldsymbol{F}}\left(\epsilon t/T_M\right)$, where $0 < \epsilon \ll 1$. In this weak-acceleration limit, the walker velocity varies slowly relative to the timescale $T_M$, so we may write $\hat{\boldsymbol{x}}' = \boldsymbol{v}(\epsilon t/T_M)$.

We proceed by expanding the integral (6.2) in powers of $\epsilon$. Since

$$\hat{\boldsymbol{x}}(\hat{t}) - \hat{\boldsymbol{x}}(\hat{t}-z) = \boldsymbol{v}(\epsilon\hat{t})z - \frac{\epsilon}{2}\boldsymbol{v}'(\epsilon\hat{t})z^2 + O(\epsilon^2), \tag{6.3}$$

we obtain

$$\begin{aligned} &J_1\left(\left|\hat{\boldsymbol{x}}(\hat{t}) - \hat{\boldsymbol{x}}(\hat{t}-z)\right|\right)\frac{\hat{\boldsymbol{x}}(\hat{t}) - \hat{\boldsymbol{x}}(\hat{t}-z)}{\left|\hat{\boldsymbol{x}}(\hat{t}) - \hat{\boldsymbol{x}}(\hat{t}-z)\right|} = \frac{\boldsymbol{v}}{|\boldsymbol{v}|}J_1\left(|\boldsymbol{v}|\,z\right) \\ &+\frac{\epsilon}{2\,|\boldsymbol{v}|}\left\{\left[\frac{\boldsymbol{v}\left(\boldsymbol{v}\cdot\boldsymbol{v}'\right)}{|\boldsymbol{v}|^2} - \boldsymbol{v}'\right]J_1\left(|\boldsymbol{v}|\,z\right)z - \frac{\boldsymbol{v}\left(\boldsymbol{v}\cdot\boldsymbol{v}'\right)}{|\boldsymbol{v}|}J_1'\left(|\boldsymbol{v}|\,z\right)z^2\right\} + O(\epsilon^2), \end{aligned} \tag{6.4}$$

which yields

$$\begin{aligned} &\int_0^\infty J_1\left(\left|\hat{\boldsymbol{x}}(\hat{t}) - \hat{\boldsymbol{x}}(\hat{t}-z)\right|\right)\frac{\hat{\boldsymbol{x}}(\hat{t}) - \hat{\boldsymbol{x}}(\hat{t}-z)}{\left|\hat{\boldsymbol{x}}(\hat{t}) - \hat{\boldsymbol{x}}(\hat{t}-z)\right|}\mathrm{e}^{-z}\,\mathrm{d}z = \frac{\boldsymbol{v}}{|\boldsymbol{v}|^2}\left(1 - \frac{1}{\sqrt{1+|\boldsymbol{v}|^2}}\right) \\ &+\frac{\epsilon}{2\,|\boldsymbol{v}|}\left\{\left[\frac{\boldsymbol{v}\left(\boldsymbol{v}\cdot\boldsymbol{v}'\right)}{|\boldsymbol{v}|^2} - \boldsymbol{v}'\right]\frac{\boldsymbol{v}}{\left(1+|\boldsymbol{v}|^2\right)^{3/2}} - \frac{\boldsymbol{v}\left(\boldsymbol{v}\cdot\boldsymbol{v}'\right)}{|\boldsymbol{v}|}\frac{1-2\,|\boldsymbol{v}|^2}{\left(1+|\boldsymbol{v}|^2\right)^{5/2}}\right\} + O(\epsilon^2). \end{aligned} \tag{6.5}$$

The trajectory equation (6.2) thus takes the form

$$\begin{aligned} \kappa\hat{\boldsymbol{x}}'' + \hat{\boldsymbol{x}}' \quad = \quad & \frac{\beta\hat{\boldsymbol{x}}'}{\left|\hat{\boldsymbol{x}}'\right|^2}\left(1 - \frac{1}{\sqrt{1+\left|\hat{\boldsymbol{x}}'\right|^2}}\right) + \frac{\beta}{2}\left[\frac{3\left(\hat{\boldsymbol{x}}'\cdot\hat{\boldsymbol{x}}''\right)\hat{\boldsymbol{x}}'}{\left(1+\left|\hat{\boldsymbol{x}}'\right|^2\right)^{5/2}} - \frac{\hat{\boldsymbol{x}}''}{\left(1+\left|\hat{\boldsymbol{x}}'\right|^2\right)^{3/2}}\right] \\ & +\hat{\boldsymbol{F}} + O(\epsilon^2), \end{aligned} \tag{6.6}$$

which may be expressed as

$$\frac{\mathrm{d}}{\mathrm{d}\hat{t}}\left(\kappa\gamma_B\hat{\boldsymbol{x}}'\right) + \hat{\boldsymbol{x}}'\left[1 - \frac{\beta}{\left|\hat{\boldsymbol{x}}'\right|^2}\left(1 - \frac{1}{\sqrt{1+\left|\hat{\boldsymbol{x}}'\right|^2}}\right)\right] = \hat{\boldsymbol{F}} + O(\epsilon^2), \tag{6.7}$$

where the hydrodynamic boost factor is defined as

$$\gamma_B = \gamma_B\left(|\boldsymbol{x}'|\right) = 1 + \frac{\beta}{2\kappa\left(1+\left|\hat{\boldsymbol{x}}'\right|^2\right)^{3/2}}. \tag{6.8}$$

We note that, in the absence of an applied force ($\hat{\boldsymbol{F}} = 0$), (6.7) has a solution:

$$\left|\hat{\boldsymbol{x}}'\right| = \hat{u}_0 \equiv \frac{1}{\sqrt{2}}\left(-1+2\beta-\sqrt{1+4\beta}\right)^{1/2}. \tag{6.9}$$

This corresponds precisely to the formula for the free rectilinear walking speed of a droplet, which was found to adequately rationalize the observed dependence of $u_0$ on the forcing acceleration $\gamma$ (Chapter 2 [48]).

In terms of dimensional variables, we may write the trajectory equation (6.7) as

$$\frac{\mathrm{d}}{\mathrm{d}t}\left(m\gamma_B\dot{\boldsymbol{x}}\right) + D_w\dot{\boldsymbol{x}} = \boldsymbol{F}, \tag{6.10}$$

$$\text{where} \qquad D_w = D_w(|\dot{\boldsymbol{x}}|) = D\left[1 - \frac{mgA}{DT_F\,|\dot{\boldsymbol{x}}|^2}\left(1 - \frac{1}{\sqrt{1+\left(k_F T_M\,|\dot{\boldsymbol{x}}|\right)^2}}\right)\right]$$

$$\text{and} \qquad \gamma_B = 1 + \frac{gAk_F^2T_M^3}{2T_F\left(1+\left(k_FT_M\,|\dot{\boldsymbol{x}}|\right)^2\right)^{3/2}}. \tag{6.11}$$

We may rewrite the trajectory equation (6.10) in the form

$$\frac{\mathrm{d}\boldsymbol{p}_w}{\mathrm{d}t} + D_w\dot{\boldsymbol{x}} = \boldsymbol{F}, \tag{6.12}$$

so both the mass $m_w$ and momentum $\boldsymbol{p}_w$ of the walker may now be expressed in terms of the hydrodynamic boost factor; specifically

$$\boldsymbol{p}_w = m_w\dot{\boldsymbol{x}}, \quad \text{where} \quad m_w = m\gamma_B. \tag{6.13}$$

In the weak-acceleration limit under consideration, the effect of the wave force on the walker dynamics is twofold. First, it augments the walker's effective mass by a factor $\gamma_B$, which depends on its speed $|\dot{\boldsymbol{x}}|$. The dependence of $\gamma_B$ on the walker

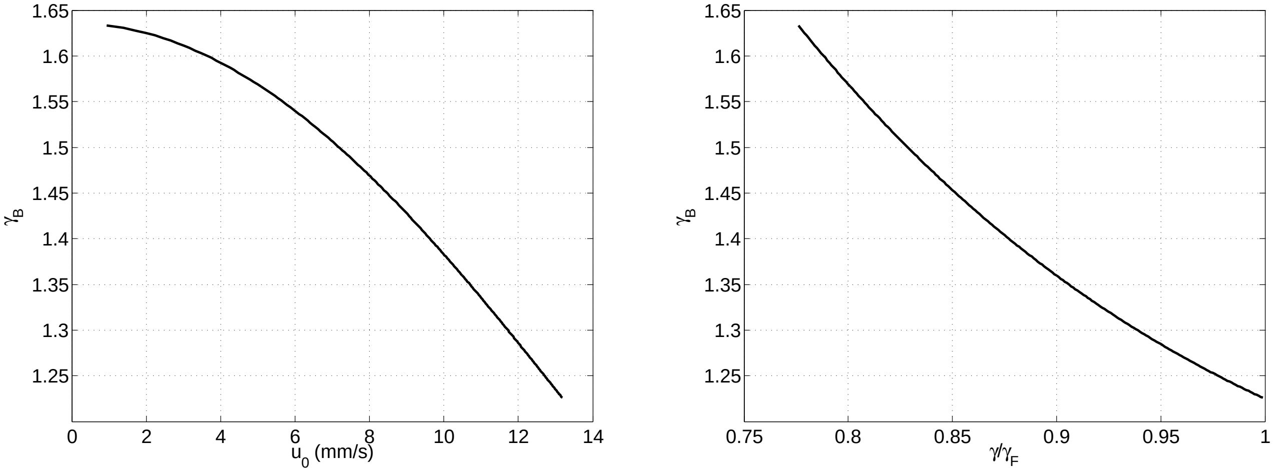

Figure 6-1: Dependence of the hydrodynamic boost factor $\gamma_B$ on the walker speed $u_0$ and forcing acceleration $\gamma/\gamma_F$.

speed $u_0$ and the forcing acceleration $\gamma/\gamma_F$ is illustrated in Figure 6-1. We note that $\gamma_B$ decreases monotonically with speed through the entire walking regime, for $\gamma_w < \gamma < \gamma_F$. Second, it generates a nonlinear drag coefficient $D_w$, where $D_w > 0$ if $|\dot{\boldsymbol{x}}| > u_0$ and $D_w < 0$ otherwise. The wave-induced drag thus acts as a restoring force that drives the walker towards its free walking speed $u_0$.

## 6.3 Response to a weak unidirectional force

We first consider the special case in which the slowly-varying applied force is also weak and unidirectional. Specifically, we assume that the applied force is small relative to the drag, so that $|\boldsymbol{F}|k_F T_M/D = O(\epsilon)$. We thus write $\hat{\boldsymbol{F}} = \epsilon \hat{f}(\epsilon t/T_M)\boldsymbol{s}$, where $\boldsymbol{s}$ is a constant unit vector.

For the remainder of this section, we assume all variables to be dimensionless and drop all hats. In the Cartesian coordinate system in which $\boldsymbol{s} = [1, 0]$, we write $\dot{\boldsymbol{x}} = v(T)\,[\cos\theta(T), \sin\theta(T)]$, where $T = \epsilon t$. The equations of motion (6.7) take the form

$$
\begin{aligned}
m_w(v)v\theta' &= -f(T)\sin\theta + O(\epsilon) \\
\epsilon\frac{\mathrm{d}}{\mathrm{d}T}\left(m_w(v)v\right) + D_w(v)v &= \epsilon f(T)\cos\theta + O(\epsilon^2),
\end{aligned}
\tag{6.14}
$$

$$
\text{where} \quad m_w(v) = \kappa\gamma_B(v) \quad \text{and} \quad D_w(v) = 1 - \frac{\beta}{v^2}\left(1 - \frac{1}{\sqrt{1+v^2}}\right) \tag{6.15}
$$

are the dimensionless wave-induced mass and drag, as introduced in §6.2.1, and primes denote differentiation with respect to the slow timescale $T$.

To leading order in $\epsilon$, the walker will move at its free walking speed $u_0$. To examine the perturbation from the steady walking solution, we substitute $v = u_0 + \epsilon u_1(\epsilon t)$ into (6.14) and deduce

$$
\begin{aligned}
m_w(u_0)u_0\theta' &= -f\sin\theta + O(\epsilon) \\
\tilde{D}_w(u_0)u_1 &= f\cos\theta + O(\epsilon),
\end{aligned}
\tag{6.16}
$$

$$
\text{where} \quad \tilde{D}_w(u_0) = \frac{\mathrm{d}}{\mathrm{d}v}\left(D_w(v)v\right)\bigg|_{v=u_0}. \tag{6.17}
$$

Equations (6.16) may readily be solved to obtain

$$
\left|\cot\frac{\theta(T)}{2}\right| = \left|\cot\frac{\theta(0)}{2}\right| \exp\left(\frac{F(T)}{m_w(u_0)u_0}\right), \quad v(T) = u_0 + \frac{\epsilon f(T)\cos\theta(T)}{\tilde{D}_w(u_0)} + O(\epsilon^2), \tag{6.18}
$$

where $F'(T) = f(T)$ and $F(0) = 0$. These expressions uniquely determine the evolution of the walking speed $v(T)$ and direction $\theta(T)$.

To gain insight into (6.18), we consider the special case in which the applied force $f$ is constant. The solution (6.18) implies that the walker's direction $\theta$ approaches that of the force over the timescale $T_\theta$, where

$$
T_\theta = \frac{m_w(u_0)u_0}{|f|}. \tag{6.19}
$$

Thus, the turning timescale $T_\theta$ is prescribed by the ratio of the walker's modified momentum $p_w(u_0)$ to the applied force, and is independent of the drag. A plot of the

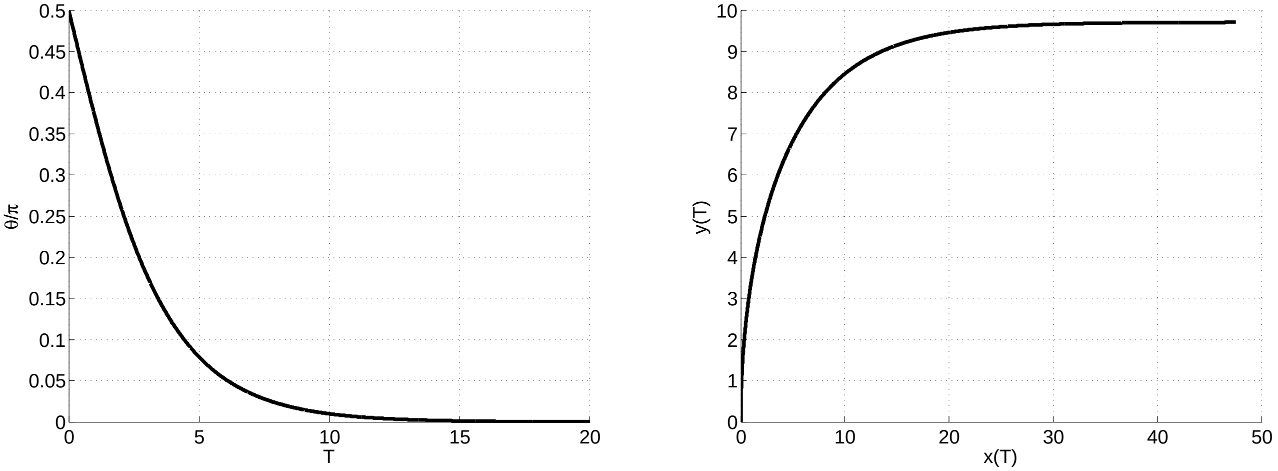

Figure 6-2: Walker's trajectory under the influence of a weak unidirectional force, computed on the basis of (6.18). The left panel shows the evolution of the walking direction $\theta(T)$. The right panel shows the walker's trajectory $(x(T), y(T))$. Calculations were based on values of $\gamma/\gamma_F = 0.9$, $\epsilon = 0.1$ and $f(T) = 1$, for which the timescale of turning $T_\theta \approx 2.4$. The walker starts with $\theta(0) = \pi/2$ and rapidly turns toward the direction of the applied force, $\theta = 0$, over the timescale $T_\theta$.

walker's trajectory for $f(T) = 1$, computed using (6.18), is shown in Figure 6-2.

## 6.4 Orbital motion

We now consider the case of circular motion of the form $\boldsymbol{x}(t) = (r_0 \cos\omega t, r_0 \sin\omega t)$. Defining $\boldsymbol{t} = (-\sin\omega t, \cos\omega t)$ and $\boldsymbol{n} = (\cos\omega t, \sin\omega t)$ as the unit tangent and outward normal allows us to write the normal and tangential components of (6.10) in the form:

$$-m\gamma_B r_0\omega^2 = \boldsymbol{F}\cdot\boldsymbol{n} \tag{6.20}$$

$$r_0\omega\left[D - \frac{mgA}{T_F(r_0\omega)^2}\left(1 - \frac{1}{\sqrt{1+(k_F T_M r_0\omega)^2}}\right)\right] = \boldsymbol{F}\cdot\boldsymbol{t} \tag{6.21}$$

where $\gamma_B$ is defined in (6.11) with $|\dot{\boldsymbol{x}}| = r_0\omega$. The weak-acceleration approximation of §6.2.1 holds provided the velocity $\dot{\boldsymbol{x}}$ varies slowly relative to the memory time, or equivalently, the orbital period is much larger than the decay time of the wave field, $T_M \ll T_{orb} \equiv 2\pi r_0/u_0$. In this case the walker does not interact with its own wake, specifically, the wave field generated by its previous orbit. This limit thus corresponds to the weak-orbital-memory limit defined in Chapter 3 [50], in which orbital quantization does not arise. We consider in turn inertial orbits arising in a rotating frame, and circular orbits arising in the presence of a central force arising from a harmonic potential.

### 6.4.1 Walking in a rotating frame

When an object of mass $m$ translates in a horizontal plane at a constant speed $u$ in a frame rotating about a vertical axis with constant angular speed $\Omega$, it will in general move along a circular orbit. The radius $R_c$ and frequency $\omega_c = -u/R_c$ of such an inertial orbit are prescribed by the balance between the outwards inertial force $mu^2/R_c$ and the inwards Coriolis force, $2mu\Omega$; thus, $R_c = u/2\Omega$ and $\omega_c = -2\Omega$. In their examination of droplets walking in a rotating frame, Fort et al. [32] demonstrated that at high memory, the influence of the wave force leads to orbital quantization on the Faraday wavelength, and that such quantized orbits are analogous to the Landau levels that arise for electric charges moving in the presence of a uniform magnetic field. In the low-memory limit, they report that the inertial orbits vary continuously with rotation rate, but that the orbits are typically 20-50% larger than would be expected from the classical balance. This orbital offset, as further detailed in Harris and Bush [38] and Chapter 3 [50], may be readily understood on the basis of the foregoing developments.

For circular motion in the presence of a Coriolis force $\boldsymbol{F} = -2m\boldsymbol{\Omega}\times\dot{\boldsymbol{x}}$, the tangential component of the force vanishes, $\boldsymbol{F}\cdot\boldsymbol{t} = 0$, so the tangential force balance (6.21) requires that the orbital speed correspond to the free walking speed $u_0 \equiv r_0|\omega|$. The radial force balance (6.20) then indicates the dependence of the orbital frequency and radius on the boost factor:

$$\omega = -\frac{2\Omega}{\gamma_B} \quad , \quad r_0 = \gamma_B\frac{u_0}{2\Omega}. \tag{6.22}$$

The net effect of the wave field is thus to decrease the orbital frequency and increase

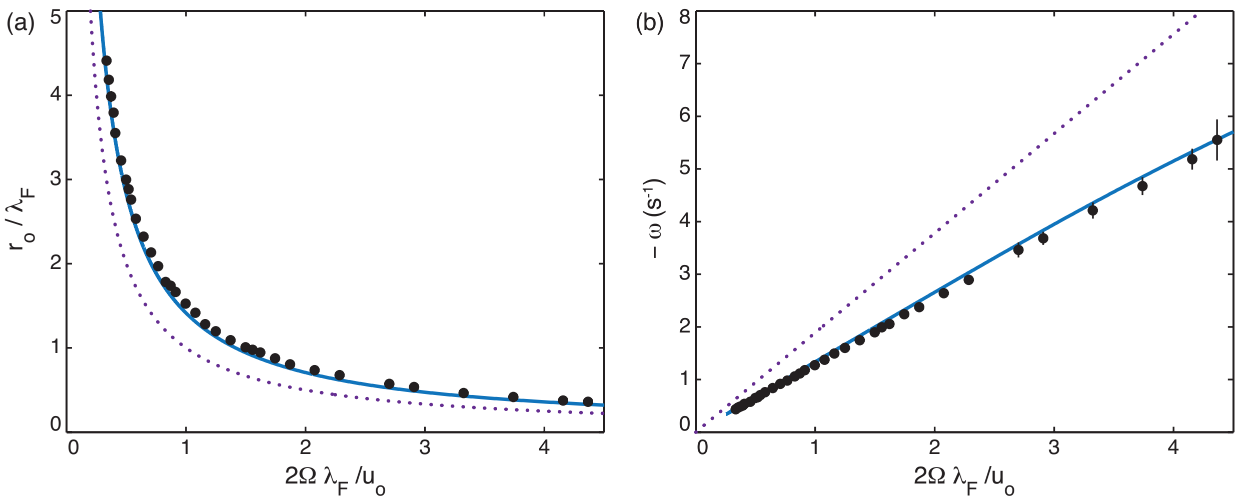

Figure 6-3: The observed dependence of the orbital radius $r_0$ and frequency $\omega$ on the rotation rate $\Omega$ for a droplet walking at speed $u_0$ in a rotating frame in the low-memory regime ($u_0 = 9.0$ mm s$^{-1}$, $\gamma/\gamma_F = 0.82$). The experimental data are those reported by Harris and Bush [38]. The dashed lines indicate the standard solutions for inertial orbits, $r_0 = R_c \equiv u_0/2\Omega$ and $\omega = \omega_c \equiv -2\Omega$. The solid lines correspond to the predictions of (6.22), which incorporate the walker's wave-induced added mass.

the orbital radius relative to the familiar results, $\omega_c$ and $R_c$. Figure 6-3 indicates the observed dependence of the orbital radius and orbital frequency on the rotation rate at low memory reported by Harris and Bush [38]. The dashed line indicates the standard results, $R_c = u_0/2\Omega$ and $\omega_c = -2\Omega$, while the solid lines correspond to our predictions (6.22) that incorporate the boost factor.

### 6.4.2 Walking in a central force

Perrard et al. [52] report the results of a study of walker motion in the presence of a central force. By encapsulating ferrofluid within a walker, and applying a vertical magnetic field with a radial gradient, they were able to produce a force field that increased linearly with radius, $\boldsymbol{F} = -k\boldsymbol{x}$. In certain regimes, orbital motions were observed; in others, more complex periodic and aperiodic motions arose. We focus here on the circular orbits reported. From the classical balance of the applied force $kR$ and inertial force $mu_0^2/R$, one expects circular orbits with radius $R_h = u_0\sqrt{m/k}$ and frequency $\omega_h = \sqrt{k/m}$. Like their counterparts arising in the rotating frame, the observed orbits exhibited a radial offset, being typically 10% larger than $R_c$, an observation we can now readily rationalize.

For circular motion in the presence of a central force $\boldsymbol{F} = -k\boldsymbol{x}$, once again $\boldsymbol{F} \cdot \boldsymbol{t} = 0$, so the tangential force balance equation (6.21) requires that the orbital speed correspond to the free walking speed $u_0 \equiv r_0|\omega|$. The radial force balance (6.20) then indicates the dependence of the orbital frequency and radius on the boost factor:

$$\omega = \sqrt{\frac{k}{m\gamma_B}} \qquad , \qquad r_0 = \sqrt{\gamma_B}\frac{u_0}{\sqrt{k/m}} \tag{6.23}$$

Once again, the net effect of the wave field is thus to decrease the orbital frequency, and to increase the orbital radius relative to the familiar results, $\omega_h$ and $R_h$. Figure 6-4 indicates the observed dependence of the orbital radius and orbital frequency on the rotation rate at low memory reported by Perrard et al. [52]. The dashed line indicates the standard results, $R_h = u_0\sqrt{m/k}$ and $\omega_h = \sqrt{k/m}$, while the solid lines correspond to our predictions (6.23) that incorporate the boost factor.

For the case of orbital dynamics, we can thus rationalize the increase of the orbital radius relative to that expected in the absence of the wave force. In the low memory limit, the drop is influenced primarily by the wave generated by its most recent impact. As the drop is turning in a circular orbit, the wave force generated during impact necessarily has a radial component, the result being an increase in the orbital radius and rationalized above.

We note that Labousse and Perrard [42] proposed the following equation to describe the dynamics of a walker under a central force in the low-memory regime:

$$m\ddot{\boldsymbol{x}} + D_w\dot{\boldsymbol{x}} = -k\boldsymbol{x}, \quad D_w = D\left(\frac{|\dot{\boldsymbol{x}}|^2}{u_0^2} - 1\right). \tag{6.24}$$

This trajectory equation captures certain features of (6.10); in particular, the nonlinear drag coefficient $D_w$ acts as a restoring force that drives the walker towards its free walking speed $u_0$. However, in neglecting the contribution of the walker's wave-induced added mass, it cannot account for the anomalously large orbital radii

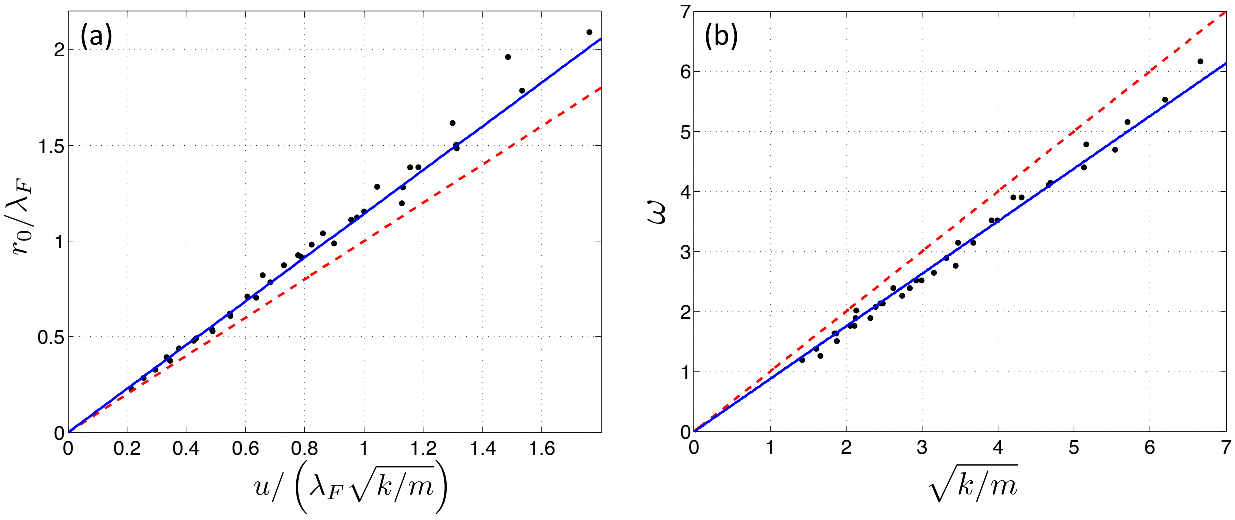

Figure 6-4: The observed dependence of the orbital radius $r_0$ and frequency $\omega$ on the spring constant $k$ for a droplet walking at speed $u_0$ under a spring force $\boldsymbol{F} = -k\boldsymbol{x}$ in the low-memory regime ($u_0 = 12.2$ mm s$^{-1}$, $\gamma/\gamma_F = 0.9$). The experimental data are from Perrard et al. [52]. The dashed lines indicate the standard solutions $r_0 = R_h \equiv u_0/\sqrt{k/m}$ and $\omega = \omega_h \equiv \sqrt{k/m}$. The solid lines correspond to the predictions of (6.23), which incorporate the walker's wave-induced added mass.

reported in laboratory experiments.

## 6.5 Discussion

A droplet walking in resonance with its own monochromatic wave field represents a rich dynamical system, the first realization of a double-wave pilot-wave system of the form envisaged by de Broglie [21, 22]. While Couder and coworkers have highlighted their quantum mechanical aspects as emerge in the high-path-memory limit [15, 32, 39], we have here explored their first tenuous connections to relativistic mechanics. The leading order force balance on the walker is between a propulsive wave force and a viscous drag term. The steady walking state is sustained by vibrational forcing: the mechanical work done by the vibration balances the viscous dissipation. In the weak-acceleration limit, the walker's motion may be described in terms of the mechanics of a particle with a speed-dependent mass subject to a nonlinear restoring force that drives it towards a fixed speed. The relative magnitude of inertial mass of the walker and the droplet mass is prescribed by the hydrodynamic boost factor, whose dependence on the system parameters has been deduced. This boost factor is always greater than 1, and decreases with increasing speed in the weak-acceleration limit examined.

For the case of orbital dynamics, if the system were observed from above with no knowledge of either the vibrational forcing or the wave field, the walker's motion may be described in terms of the inviscid dynamics of a particle whose mass depends on its speed. Doing so has allowed us to rationalize the offset in the radius of the walkers' inertial orbits in terms of their wave-induced added mass; moreover, it has provided a more general framework for understanding and describing the walker dynamics.

# Chapter 7

# Concluding remarks

In this thesis, we have developed and studied the integro-differential trajectory equation

$$m\ddot{\boldsymbol{x}} + D\dot{\boldsymbol{x}} = \frac{F}{T_F}\int_{-\infty}^{t} J_1\left(k_F \left|\boldsymbol{x}_p(t) - \boldsymbol{x}_p(s)\right|\right) \frac{\boldsymbol{x}_p(t) - \boldsymbol{x}_p(s)}{\left|\boldsymbol{x}_p(t) - \boldsymbol{x}_p(s)\right|} \mathrm{e}^{-(t-s)/T_M}\, \mathrm{d}s + \boldsymbol{F}, \quad (7.1)$$

with a view to describing the subtle pilot-wave dynamics of droplets walking on the surface of a vibrating fluid bath. Our model differs from its predecessors in that it can be treated analytically and contains no free parameters, thus allowing quantitative and testable predictions to be made. Indeed, many of the phenomena reported in this thesis were predicted through analyzing (7.1) and subsequently observed in laboratory experiments. Our model has given valuable insight into the emergence of both quantization and multimodal statistics, the two primary quantum-like features of the walker system.

In Chapter 2, we studied the dynamics of walkers in the absence of an external force, $\boldsymbol{F} = 0$. We showed that the bouncing state $\boldsymbol{x} = \text{constant}$ may destabilize into a steady rectilinear walking solution $\boldsymbol{x} = (u_0 t, 0)$, provided that the vibrational forcing exceeds a critical value. The walking speed $u_0$ deduced on the basis of (7.1) agrees well with experimental data [46]. We then analyzed the stability of this walking solution, and showed that it is stable to perturbations in the direction of motion and neutrally stable to lateral perturbations. This result lends insight into the emergence of chaotic dynamics when droplets walk in confined geometries [39].

In Chapter 3, we studied the walker dynamics in a rotating frame, in which $\boldsymbol{F} = -2m\Omega\hat{\boldsymbol{z}} \times \dot{\boldsymbol{x}}$. We showed that (7.1) admits orbital solutions of the form $\boldsymbol{x} = r_0(\cos\omega t, \sin\omega t)$, in which the walker traverses a circle of radius $r_0$ with constant angular frequency $\omega$. The predicted dependence of $r_0$ and $\omega$ on the rotation rate $\Omega$ and the vibrational forcing agrees well with experimental data [38]. We showed that, in the high-memory limit, $\gamma \to \gamma_F$, the orbital radii may be approximated by the zeros of the Bessel functions $J_0(r)$ and $J_1(r)$. We then demonstrated that the observed orbital quantization may be understood in terms of a linear stability analysis of the orbital solutions. In particular, we showed that orbital solutions for which $\mathrm{d}\Omega/\mathrm{d}r_0 > 0$ are unstable and thus cannot be observed in laboratory experiments.

In Chapter 4, we presented a numerical investigation of the walker dynamics in a rotating frame, which culminated in a regime diagram delineating the dependence of the dynamics on the initial orbital radius $r_0$ and vibrational forcing $\gamma$. We showed that, as the vibrational forcing is progressively increased, circular orbits may destabilize into wobbling orbits, which exhibit periodic fluctuations in their radius. For higher values of memory, the wobbling orbits destabilize into drifting orbits and wobble-and-leap trajectories, both of which arise due to instabilities of the orbital center. In the high-memory limit, $\gamma \to \gamma_F$, the walker's trajectory is chaotic, but the statistics of its loop radius exhibits a multimodal structure with peaks near the roots of $J_0(r)$. The simulations agree well with the experimental results of Harris and Bush [38].

In Chapter 5, we presented a detailed mathematical treatment of the stability of circular orbits in a rotating frame. We recast (7.1) as an initial value problem, and showed that the eigenvalues of the linear stability problem are the zeros of a function $F(s)$. We analyzed these roots in various asymptotic limits, and established the stability of circular orbits with sufficiently small radius, large radius, and at low memory. Outside of these asymptotic regimes, the roots of $F(s)$ must be found numerically, and we presented a tractable numerical procedure for finding them. We showed that the frequencies of wobbling orbits, as predicted by the stability analysis, agree well with experimental data from Harris and Bush [38]. We also showed that the circular orbits for which $J_1(r) \approx 0$ are more unstable than those for which $J_0(r) \approx 0$, thus rationalizing the absence of the former when the walker dynamics is chaotic.

In Chapter 6, we performed an asymptotic expansion of (7.1) in the limit of weak acceleration, in which the walker accelerates over a timescale long relative to the memory time $T_M$. In this limit, the contribution of the wave force to the walker dynamics is twofold. First, the walker responds to a nonlinear drag force, which drives it at the free walking speed $u_0$. Second, the walker's effective mass changes with its speed, so we may draw an analogy with relativistic mechanics and define the walker's hydrodynamic boost factor. This result allows us to rationalize the anomalously large orbital radii reported in recent experiments [38, 52].

While our model has provided rationale for a number of experimental phenomena, it is worth discussing its shortcomings. Note that (7.1) only describes the walker's horizontal motion and neglects consideration of its vertical dynamics, assuming it to be perfectly periodic. Recent experiments have shown this assumption to be false in certain parameter regimes, as the walker's vertical motion can be aperiodic or even chaotic [65]. Indeed, recent experiments suggest that the original single-slit diffraction experiments [15] were performed with chaotically bouncing walkers. We have also assumed the bouncing phase to be independent of the forcing acceleration $\gamma$, whereas it is known to exhibit weak dependence on both $\gamma$ and the fluid viscosity [46]. Incorporating this effect would make the coefficient $F$ in (7.1) depend on $\gamma$, which would significantly complicate the analysis presented herein.

## 7.1 Future directions

We have recently begun to explore the following dimensionless formulation of the trajectory equation (7.1):

$$\begin{aligned}\kappa_0(1-\Gamma)\ddot{\boldsymbol{x}}+\dot{\boldsymbol{x}} &= \frac{2}{(1-\Gamma)^2}\int_{-\infty}^{t} J_1\left(|\boldsymbol{x}_p(t)-\boldsymbol{x}_p(s)|\right)\frac{\boldsymbol{x}_p(t)-\boldsymbol{x}_p(s)}{|\boldsymbol{x}_p(t)-\boldsymbol{x}_p(s)|}\mathrm{e}^{-(t-s)}\,\mathrm{d}s+\boldsymbol{F},\\ \text{where}\quad \Gamma &= \frac{\gamma-\gamma_W}{\gamma_F-\gamma_W}\quad\text{and}\quad \kappa_0=\frac{m}{D}\sqrt{\frac{Fk_F}{2DT_F}}. \end{aligned}\tag{7.2}$$

In this equation, $\Gamma$ increases with the forcing acceleration $\gamma$, $\Gamma=0$ corresponding to the walking threshold $\gamma=\gamma_W$ and $\Gamma=1$ to the Faraday threshold $\gamma=\gamma_F$. The advantage of this reformulation is that all of the fluid parameters appear in the coefficient $\kappa_0$, the value $\kappa_0\approx 1$ corresponding to the fluid typically used in experiments. We have recently demonstrated that, for $\kappa_0\leq 0.18$, the trajectory equation (7.2) admits stable self-orbiting solutions, in which the walker executes a circular orbit in the absence of an external force, $\boldsymbol{F}=0$. Such solutions bear resemblance to the Kerr-Newman model of the electron, in which the electron is modeled as a charged particle orbiting in its own wave field [8]. When subjected to rotation, these hydrodynamic "spin states" exhibit an analogue of Zeeman splitting, as solutions that co-rotate with the bath have slightly larger radii than counter-rotating counterparts. We note that such solutions are also present for larger values of $\kappa_0$, but are unstable and thus cannot be observed.

Having benchmarked the trajectory equation (7.1) against the laboratory experiments of Harris and Bush [38], we may now use it to analyze the walker's dynamics under different external forces $\boldsymbol{F}$. A pilot-wave analogue of the quantum harmonic oscillator, in which $\boldsymbol{F}=-k\boldsymbol{x}$, has been explored in the laboratory of Yves Couder [52], and is currently being studied theoretically using (7.1). It is our hope that we may now apply our model to pilot-wave systems that are not necessarily accessible in the laboratory.

In future work, we would like to extend our model to account for the influence of boundaries or other nearby walkers, as the walker dynamics is significantly influenced by both in the single-slit diffraction [15], tunneling [27], corral [39] and Zeeman splitting [30] experiments. Our trajectory equation (7.1) only models the standing waves generated by the walker, neglecting the traveling wave that propagates away from the walker after each impact. While we do not expect this transient to significantly affect a single walker's dynamics in free space, it could interact with boundaries or other walkers. This research direction is currently being explored by Milewski et al. [44].

Our pilot-wave trajectory equation (7.1) provides the basis for rationalizing the observed dynamics of walking droplets and predicting new phenomena. We expect that future research will reveal the extent to which this pilot-wave system can be viewed as a macroscopic analog of a quantum system. It is our hope that the theoretical developments presented in this thesis might ultimately provide insight into the plausibility of a rational pilot-wave theory of quantum mechanics.

# Appendix A

# Evaluation of integral terms in $F_1(s), F_2(s), G_1(s), G_2(s)$

We evaluate some of the integrals appearing in the definition (3.35) of the functions $F_1(s), F_2(s), G_1(s)$, and $G_2(s)$, by repeatedly employing the fact that $r_0$ and $\omega$ are defined as the solution to (3.9):

$$\begin{aligned}\mathcal{I}[f(t)\sin\omega t] &= \int_0^\infty \frac{J_1\left(2r_0\sin\frac{\omega z}{2}\right)}{2r_0\sin\frac{\omega z}{2}}\sin\omega z\mathrm{e}^{-z}\,\mathrm{d}z\\ &= \int_0^\infty \frac{J_1\left(2r_0\sin\frac{\omega z}{2}\right)}{r_0}\cos\frac{\omega z}{2}\mathrm{e}^{-z}\,\mathrm{d}z = \frac{\omega}{\beta}. \end{aligned}\tag{A.1}$$

$$\begin{aligned}\mathcal{I}[g(t)\sin\omega t] &= \int_0^\infty J_1'\left(2r_0\sin\frac{\omega z}{2}\right)\sin\omega z\mathrm{e}^{-z}\,\mathrm{d}z\\ &= 2\int_0^\infty J_1'\left(2r_0\sin\frac{\omega z}{2}\right)\cos\frac{\omega z}{2}\sin\frac{\omega z}{2}\mathrm{e}^{-z}\,\mathrm{d}z\\ &= \frac{2}{r_0\omega}\int_0^\infty \left[J_1\left(2r_0\sin\frac{\omega z}{2}\right)\sin\frac{\omega z}{2} - \frac{\omega}{2}J_1\left(2r_0\sin\frac{\omega z}{2}\right)\cos\frac{\omega z}{2}\right]\mathrm{e}^{-z}\,\mathrm{d}z\\ &= -\frac{2}{\beta}\left[\kappa\omega+\Omega+\frac{\omega}{2}\right], \end{aligned}\tag{A.2}$$

where we integrate by parts in the third line. Combining (A.1) and (A.2), we obtain

$$\begin{aligned}\frac{1}{2}\left(\mathcal{I}[f(t)\sin\omega t]+\mathcal{I}[g(t)\sin\omega t]\right) &= -\frac{\kappa\omega+\Omega}{\beta},\\ \frac{1}{2}\left(\mathcal{I}[g(t)\sin\omega t]-\mathcal{I}[f(t)\sin\omega t]\right) &= -\frac{\kappa\omega+\omega+\Omega}{\beta},\end{aligned}\tag{A.3}$$

which appear in $F_2(s)$ and $G_1(s)$, respectively. Similarly:

$$\mathcal{I}\left[f(t)\sin^2\frac{\omega t}{2}\right]=\int_0^\infty \frac{J_1\left(2r_0\sin\frac{\omega z}{2}\right)}{2r_0}\sin\frac{\omega z}{2}\mathrm{e}^{-z}\,\mathrm{d}z=-\frac{\kappa\omega^2+\Omega\omega}{2\beta}\tag{A.4}$$

$$\begin{aligned}\mathcal{I}\left[g(t)\cos^2\frac{\omega t}{2}\right] &= \int_0^\infty J_1'\left(2r_0\sin\frac{\omega z}{2}\right)\cos\frac{\omega z}{2}\cos\frac{\omega z}{2}\mathrm{e}^{-z}\,\mathrm{d}z\\ &= \frac{1}{r_0\omega}\int_0^\infty\left[\frac{\omega}{2}J_1\left(2r_0\sin\frac{\omega z}{2}\right)\sin\frac{\omega z}{2}\mathrm{e}^{-z}+J_1\left(2r_0\sin\frac{\omega z}{2}\right)\cos\frac{\omega z}{2}\mathrm{e}^{-z}\right]\mathrm{d}z\\ &= \frac{1}{\beta}\left[-\frac{1}{2}(\kappa\omega^2+\Omega\omega)+1\right],\end{aligned}\tag{A.5}$$

where we integrate by parts in the second line. Combining (A.4) and (A.5), we obtain

$$\mathcal{I}\left[g(t)\cos^2\frac{\omega t}{2}\right]-\mathcal{I}\left[f(t)\sin^2\frac{\omega t}{2}\right]=\frac{1}{\beta},\tag{A.6}$$

which appears in $G_2(s)$.

There do not appear to be simple expressions for the terms $\mathcal{I}\left[f(t)\cos^2\frac{\omega t}{2}\right]$ and $\mathcal{I}\left[g(t)\sin^2\frac{\omega t}{2}\right]$ that appear in $F_1(s)$.

# Appendix B

# Proof that $F_0(r_0) = r_0\omega d_1\frac{\mathrm{d}\Omega}{\mathrm{d}r_0}$

We first expand the functions (3.37) around $s = 0$ and obtain $A(s) = a_0 + O(s)$, $B(s) = b_1 s + O(s^2)$, $C(s) = c_0 + O(s)$, and $D(s) = d_1 s + O(s^2)$, where

$$\begin{aligned} a_0 &= -\left(\kappa\omega^2 + \Omega\omega + 2\beta\mathcal{I}\left[g(t)\sin^2\frac{\omega t}{2}\right]\right), \quad b_1 = 2\omega\kappa + \Omega + \frac{\beta}{2}\mathcal{I}\left[\left(f(t)+g(t)\right)t\sin\omega t\right] \\ c_0 &= 2\left[\omega\left(1+\kappa\right)+\Omega\right], \quad d_1 = 1 + \beta\mathcal{I}\left[\left(f(t)\sin^2\frac{\omega t}{2} - g(t)\cos^2\frac{\omega t}{2}\right)t\right]. \end{aligned} \tag{B.1}$$

Thus $F_0(r_0) = a_0 d_1 + b_1 c_0$.

We now deduce an equation for $\frac{\mathrm{d}\Omega}{\mathrm{d}r_0}$ by first differentiating the governing equations (3.9) with respect to $r_0$:

$$\begin{aligned} 2\omega\kappa\frac{\mathrm{d}\omega}{\mathrm{d}r_0} + \omega\frac{\mathrm{d}\Omega}{\mathrm{d}r_0} + \Omega\frac{\mathrm{d}\omega}{\mathrm{d}r_0} &= -2\beta\mathcal{I}\left[\left(\frac{\partial f}{\partial r_0} + \frac{\partial f}{\partial\omega}\frac{\mathrm{d}\omega}{\mathrm{d}r_0}\right)\sin^2\frac{\omega t}{2} + \frac{\mathrm{d}\omega}{\mathrm{d}r_0}\frac{t}{2}f(t)\sin\omega t\right] \\ \frac{\mathrm{d}\omega}{\mathrm{d}r_0} &= \beta\mathcal{I}\left[\frac{\mathrm{d}\omega}{\mathrm{d}r_0}tf(t)\cos\omega t + \left(\frac{\partial f}{\partial r_0} + \frac{\partial f}{\partial\omega}\frac{\mathrm{d}\omega}{\mathrm{d}r_0}\right)\sin\omega t\right]. \end{aligned} \tag{B.2}$$

Since

$$\frac{\partial f}{\partial r_0} = \frac{1}{r_0}\left(g(t) - f(t)\right), \quad \frac{\partial f}{\partial\omega} = \frac{t}{2}\cot\frac{\omega t}{2}\left(g(t) - f(t)\right), \tag{B.3}$$

we deduce that

$$\begin{aligned}
\frac{\mathrm{d}\omega}{\mathrm{d}r_0}\left(2\omega\kappa+\Omega\right)+\omega\frac{\mathrm{d}\Omega}{\mathrm{d}r_0} &= \frac{2\beta}{r_0}\mathcal{I}\left[\left(f(t)-g(t)\right)\sin^2\frac{\omega t}{2}\right]-\frac{\beta}{2}\mathcal{I}\left[\left(f(t)+g(t)\right)t\sin\omega t\right]\frac{\mathrm{d}\omega}{\mathrm{d}r_0} \\
\frac{\beta}{r_0}\mathcal{I}\left[\left(g(t)-f(t)\right)\sin\omega t\right] &= \frac{\mathrm{d}\omega}{\mathrm{d}r_0}\left(1-\beta\mathcal{I}\left[\left(g(t)\cos^2\frac{\omega t}{2}-f(t)\sin^2\frac{\omega t}{2}\right)t\right]\right). \qquad \text{(B.4)}
\end{aligned}$$

Some of the integrals can be simplified using the results in Appendix A, yielding

$$\begin{aligned}
-\omega\frac{\mathrm{d}\Omega}{\mathrm{d}r_0} &= \frac{\mathrm{d}\omega}{\mathrm{d}r_0}\left(2\omega\kappa+\Omega+\frac{\beta}{2}\mathcal{I}\left[\left(f(t)+g(t)\right)t\sin\omega t\right]\right) \\
&\quad+\frac{2\beta}{r_0}\mathcal{I}\left[g(t)\sin^2\frac{\omega t}{2}\right]+\frac{1}{r_0}\left(\kappa\omega^2+\Omega\omega\right) \\
-\frac{2}{r_0}\left(\omega\left(1+\kappa\right)+\Omega\right) &= \frac{\mathrm{d}\omega}{\mathrm{d}r_0}\left(1-\beta\mathcal{I}\left[\left(g(t)\cos^2\frac{\omega t}{2}-f(t)\sin^2\frac{\omega t}{2}\right)t\right]\right). \qquad \text{(B.5)}
\end{aligned}$$

Using (B.1), these equations can be written as

$$a_0-r_0b_1\frac{\mathrm{d}\omega}{\mathrm{d}r_0}=r_0\omega\frac{\mathrm{d}\Omega}{\mathrm{d}r_0},\quad c_0+r_0d_1\frac{\mathrm{d}\omega}{\mathrm{d}r_0}=0. \qquad \text{(B.6)}$$

We eliminate $\frac{\mathrm{d}\omega}{\mathrm{d}r_0}$, yielding an equation for $\frac{\mathrm{d}\Omega}{\mathrm{d}r_0}$:

$$a_0+\frac{b_1c_0}{d_1} = r_0\omega\frac{\mathrm{d}\Omega}{\mathrm{d}r_0}, \qquad \text{(B.7)}$$

which is valid since $d_1 > 0$ (see Proposition 2 in Chapter 5). We thus obtain the desired result

$$F_0(r_0)=r_0\omega d_1\frac{\mathrm{d}\Omega}{\mathrm{d}r_0}. \qquad \text{(B.8)}$$

# Appendix C

# Asymptotic limit $\omega \ll 1$

The integrals in (5.20) and (5.34) have the form

$$I(r_0) \equiv \frac{1}{\omega}\int_0^\infty \Phi\left(2r_0 \sin\frac{z}{2}\right) P(z) \mathrm{e}^{-\eta z/\omega}\,\mathrm{d}z, \quad \Re(\eta) > \sigma > 0, \tag{C.1}$$

where all derivatives of $\Phi$ and $P$ are bounded. As shown in §5.4, orbital solutions exist in the regime $\omega \le \beta c/r_0$, $c \approx 0.6$ being the maximum value of $J_1(x)$. We thus write (C.1) as

$$I(r_0) = \frac{r_0}{\tilde{\omega}}\int_0^\infty \Phi\left(2r_0 \sin\frac{z}{2}\right) P(z) \mathrm{e}^{-r_0\eta z/\tilde{\omega}}\,\mathrm{d}z, \tag{C.2}$$

where $\tilde{\omega} = O(1)$. We proceed by analyzing the behavior of $I(r_0)$ for $r_0 \gg 1$.

We first consider the case where $P$ is an even function with $P(0) \neq 0$. Note that

$$\left|2r_0 \sin\frac{z}{2} - r_0 z\right| \le \frac{r_0 z^3}{24}, \tag{C.3}$$

so

$$\begin{aligned}\left|\Phi\left(2r_0\sin\frac{z}{2}\right)P(z) - \Phi(r_0 z)P(0)\right| &= \left|\left(\Phi\left(2r_0\sin\frac{z}{2}\right) - \Phi(r_0 z)\right)P(0)\right.\\ &\quad \left.+\Phi\left(2r_0\sin\frac{z}{2}\right)(P(z) - P(0))\right|\\ &\le \frac{P(0)\|\Phi'\|_\infty r_0 z^3}{24} + \frac{\|\Phi\|_\infty\|P''\|z^2}{2},\end{aligned} \tag{C.4}$$

where both inequalities follow from Taylor's remainder theorem. We thus obtain the upper bound

$$\left|\int_0^\infty \left[\Phi\left(2r_0\sin\frac{z}{2}\right)P(z)-\Phi(r_0z)P(0)\right]\mathrm{e}^{-r_0\eta z/\tilde{\omega}}\,\mathrm{d}z\right| \le \frac{\tilde{\omega}^3}{r_0^3\Re(\eta)^3}\left(\frac{\|\Phi'\|_\infty\tilde{\omega}}{4\Re(\eta)}+\|\Phi\|_\infty\|P''\|_\infty\right).$$

Since $\Re(\eta)>\sigma>0$, we may write

$$I(r_0)=\frac{P(0)}{\omega}\int_0^\infty \Phi(r_0z)\mathrm{e}^{-\eta z/\omega}\,\mathrm{d}z+E, \quad \text{where} \quad |E|\le\frac{k}{r_0^2} \tag{C.5}$$

and $k$ is independent of both $r_0$ and $\eta$.

We obtain a similar result if $P$ is an odd function with $P'(0)\neq 0$. Using the same argument as that above, we obtain

$$I(r_0)=\frac{P'(0)}{\omega}\int_0^\infty \Phi(r_0z)z\mathrm{e}^{-\eta z/\omega}\,\mathrm{d}z+E, \quad \text{where} \quad |E|\le\frac{k}{r_0^3} \tag{C.6}$$

and the constant $k$ is also independent of both $r_0$ and $\eta$.

# Appendix D

# Asymptotic limit $\omega \gg 1$

We expand the integrals in (5.20) in the limit $\omega \gg 1$. Note that the second equation in (5.20) may be written as

$$r_0\omega = \frac{\beta}{r_0\omega}\left[1 - \int_0^\infty J_0\left(2r_0 \sin\frac{\omega z}{2}\right) \mathrm{e}^{-z}\,\mathrm{d}z\right]. \tag{D.1}$$

Both integrals in (5.20) thus have the form

$$I(\epsilon) = \epsilon \int_0^\infty f(z)\mathrm{e}^{-\epsilon z}\,\mathrm{d}z, \tag{D.2}$$

where $0 < \epsilon \ll 1$ and $f$ is a $2\pi$-periodic even function. We approximate $I$ for small $\epsilon$, obtaining

$$\begin{aligned} I(\epsilon) &= \frac{\epsilon}{1-\mathrm{e}^{-2\pi\epsilon}} \int_0^{2\pi} f(z)\mathrm{e}^{-\epsilon z}\mathrm{d}z \\ &= \frac{1}{2\pi}\left(1 + \epsilon\pi + O(\epsilon^2)\right) \int_0^{2\pi} f(z)\left(1 - \epsilon z + \epsilon^2 R(z)\right)\mathrm{d}z, \end{aligned} \tag{D.3}$$

where $|R| \leq z^2/2$ by Taylor's remainder theorem. Since $f$ is bounded, we may write

$$I(\epsilon) = \frac{1}{2\pi}\int_0^{2\pi} f(z)\,\mathrm{d}z + \frac{\epsilon}{2\pi}\int_0^{2\pi} f(z)(\pi - z)\,\mathrm{d}z + O(\epsilon^2). \tag{D.4}$$

We note that $f(\pi - z)$ must be an even function of $z$, since $f$ is even and $2\pi$-periodic, which implies that

$$\int_0^{2\pi} f(z)(\pi - z)\,\mathrm{d}z = \int_{-\pi}^{\pi} f(\pi - u)u\,\mathrm{d}u = 0. \tag{D.5}$$

It follows that

$$I(\epsilon) = \frac{1}{2\pi}\int_0^{2\pi} f(z)\,\mathrm{d}z + O(\epsilon^2). \tag{D.6}$$

# Appendix E

# Proof that $\tilde{F}(s;r_0)$ is an entire function of $s$

We show that $\tilde{F}(s;r_0)$ is an entire function of $s$, where $\tilde{F}(s;r_0)$ is defined in (5.73). This is equivalent to showing that

$$\left(A_2D_2+\frac{B_2^2}{4}\right)\bigg|_{s=-1+\mathrm{i}n|\omega|}=0, \tag{E.1}$$

where

$$\begin{aligned}
A_2(-1+\mathrm{i}n|\omega|) &= \int_0^{2\pi}\left[-\frac{J_1\left(2r_0\sin\frac{t}{2}\right)}{2r_0\sin\frac{t}{2}}\cos^2\frac{t}{2}+J_1'\left(2r_0\sin\frac{t}{2}\right)\sin^2\frac{t}{2}\right]\cos nt\,\mathrm{d}t,\\
B_2\left(-1+\mathrm{i}n|\omega|\right) &= \mathrm{i}\int_0^{2\pi}\left[\frac{J_1\left(2r_0\sin\frac{t}{2}\right)}{2r_0\sin\frac{t}{2}}+J_1'\left(2r_0\sin\frac{t}{2}\right)\right]\sin t\sin nt\,\mathrm{d}t,\\
D_2\left(-1+\mathrm{i}n|\omega|\right) &= \int_0^{2\pi}\left[\frac{J_1\left(2r_0\sin\frac{t}{2}\right)}{2r_0\sin\frac{t}{2}}\sin^2\frac{t}{2}-J_1'\left(2r_0\sin\frac{t}{2}\right)\cos^2\frac{t}{2}\right]\cos nt\,\mathrm{d}t.
\end{aligned}$$

This is equivalent to proving that

$$\begin{aligned}
&\left(\int_0^\pi \left[\frac{J_1\left(2r_0\sin t\right)}{2r_0\sin t} + J_1'(2r_0\sin t)\right]\cos 2(n+1)t\,\mathrm{d}t\right)\\
&\times\left(\int_0^\pi \left[\frac{J_1\left(2r_0\sin t\right)}{2r_0\sin t} + J_1'(2r_0\sin t)\right]\cos 2(n-1)t\,\mathrm{d}t\right)\\
= \;&\left(\int_0^\pi \left[\frac{J_1\left(2r_0\sin t\right)}{2r_0\sin t} - J_1'(2r_0\sin t)\right]\cos 2nt\,\mathrm{d}t\right)^2.
\end{aligned}$$

Since $\frac{J_1(x)}{x} = \frac{1}{2}\left(J_0(x) + J_2(x)\right)$ and $J_1'(x) = \frac{1}{2}\left(J_0(x) - J_2(x)\right)$, this is equivalent to

$$\begin{aligned}
&\left(\int_0^\pi J_0(2r_0\sin t)\cos 2(n+1)t\,\mathrm{d}t\right)\left(\int_0^\pi J_0(2r_0\sin t)\cos 2(n-1)t\,\mathrm{d}t\right)\\
= \;&\left(\int_0^\pi J_2(2r_0\sin t)\cos 2nt\,\mathrm{d}t\right)^2. \qquad \text{(E.2)}
\end{aligned}$$

Using the identities in Watson [63, p. 151], we obtain

$$\begin{aligned}
\int_0^{\pi/2} J_0\left(2r_0\cos t\right)\cos 2nt\,\mathrm{d}t &= \frac{\pi}{2}(-1)^n J_n^2(r_0),\\
\int_0^{\pi/2} J_2\left(2r_0\cos t\right)\cos 2nt\,\mathrm{d}t &= \frac{\pi}{2}(-1)^{n-1} J_{n-1}(r_0)J_{n+1}(r_0). \qquad \text{(E.3)}
\end{aligned}$$

Since $J_0(x)$ and $J_2(x)$ are even functions, it follows that

$$\begin{aligned}
\int_0^{\pi} J_0\left(2r_0\sin t\right)\cos 2nt\,\mathrm{d}t &= \pi J_n^2(r_0),\\
\int_0^{\pi} J_2\left(2r_0\sin t\right)\cos 2nt\,\mathrm{d}t &= -\pi J_{n-1}(r_0)J_{n+1}(r_0), \qquad \text{(E.4)}
\end{aligned}$$

which proves (E.2).

# Appendix F

# Computation of the error terms in (5.76)

We here prove the formulae given in (5.76). The Laplace transforms in (5.71) have the form $A_2 = \hat{\mathcal{L}}[F_A(t)]$, $B_2 = \hat{\mathcal{L}}[F_B(t)]$ and $D_2 = \hat{\mathcal{L}}[F_D(t)]$, where

$$\begin{aligned} F_A(t) &= \tilde{g}(t)\sin^2\frac{t}{2} - \tilde{f}(t)\cos^2\frac{t}{2}, \\ F_B(t) &= \Big(\tilde{f}(t) + \tilde{g}(t)\Big)\sin t, \\ F_D(t) &= \tilde{f}(t)\sin^2\frac{t}{2} - \tilde{g}(t)\cos^2\frac{t}{2}, \end{aligned} \tag{F.1}$$

the functions $\tilde{f}(t)$ and $\tilde{g}(t)$ are defined in (5.67), and the modified Laplace transform operator $\hat{\mathcal{L}}$ is defined as in (5.72):

$$\hat{\mathcal{L}}\left[h(t)\right] = \int_0^{2\pi} h(t)\mathrm{e}^{-\tilde{s}t}\,\mathrm{d}t, \quad \tilde{s} = \frac{s+1}{|\omega|}. \tag{F.2}$$

We use integration by parts to deduce that, if $F(t)$ is a $2\pi$-periodic function with $(N+1)$ derivatives, then

$$\begin{aligned} \hat{\mathcal{L}}[F(t)] &= \sum_{n=0}^{N} \frac{(1-\mathrm{e}^{-2\pi\tilde{s}})F^{(n)}(0)}{\tilde{s}^{n+1}} + \frac{1}{(N+1)!}\int_0^{2\pi} \frac{F^{(N+1)}(t)\mathrm{e}^{-\tilde{s}t}}{s^{N+1}}\,\mathrm{d}t \\ &= \sum_{n=0}^{N} \frac{(1-\mathrm{e}^{-2\pi\tilde{s}})F^{(n)}(0)}{\tilde{s}^{n+1}} + \epsilon_{N+1}, \quad |\epsilon_{N+1}| \leq \frac{\|F^{(N+1)}\|_\infty\left(1-\mathrm{e}^{-2\pi\Re(\tilde{s})}\right)}{\Re(\tilde{s})|\tilde{s}|^{N+1}(N+1)!}, \end{aligned} \tag{F.3}$$

where $\|F\|_\infty$ denotes the maximum value of $F(t)$. In the region of interest, $\Re(\tilde{s}) > -\rho$, we have the upper bounds

$$\left|1-\mathrm{e}^{-2\pi s}\right| < 1+\mathrm{e}^{2\pi\rho}, \qquad \frac{1-\mathrm{e}^{-2\pi\Re(\tilde{s})}}{\Re(\tilde{s})} < \frac{\mathrm{e}^{2\pi\rho}-1}{\rho}. \tag{F.4}$$

We will also require the following derivatives of the functions in (F.1):

$$\begin{aligned}
F_A(0) &= -\frac{1}{2}, \quad F_A''(0) = \frac{4+r_0^2}{8}, \quad F_A^{(4)}(0) = \frac{r_0^4+26r_0^2+8}{16}, \\
F_B'(0) &= 1, \quad F_B^{(3)}(0) = -\frac{2+3r_0^2}{2}, \\
F_D(0) &= -\frac{1}{2}, \quad F_D''(0) = \frac{4+3r_0^2}{8}, \quad F_D^{(4)}(0) = \frac{5r_0^4+30r_0^2+8}{16},
\end{aligned} \tag{F.5}$$

where the odd derivatives of $F_A$ and $F_D$ and the even derivatives of $F_B$ are zero.

A number of numerical experiments convinced us that

$$\|F_A^{(4)}\|_\infty \leq F_A^{(4)}(0), \quad \|F_B^{(3)}\|_\infty \leq 2F_B^{(3)}(0), \quad \|F_D^{(4)}\|_\infty \leq F_D^{(4)}(0). \tag{F.6}$$

Using (F.3), combined with (F.4) and (F.5), we thus obtain

$$\begin{aligned}
A_2(\tilde{s}) &= -\frac{1-e^{-2\pi\tilde{s}}}{2\tilde{s}} + \epsilon^{(A)}, \quad |\epsilon^{(A)}| \leq \frac{(1+e^{2\pi\rho})(4+r_0^2)}{8|\tilde{s}|^3} + \frac{e^{2\pi\rho}-1}{16\cdot 4!\cdot\rho}\cdot\frac{r_0^4+26r_0^2+8}{|\tilde{s}|^4}, \\
B_2(\tilde{s}) &= \frac{1-e^{-2\pi\tilde{s}}}{\tilde{s}^2} + \epsilon^{(B)}, \quad |\epsilon^{(B)}| \leq \frac{e^{2\pi\rho}-1}{\rho}\cdot\frac{2+3r_0^2}{6|\tilde{s}|^3}, \\
D_2(\tilde{s}) &= -\frac{1-e^{-2\pi\tilde{s}}}{2\tilde{s}} + \epsilon^{(D)}, \quad |\epsilon^{(D)}| \leq \frac{(1+e^{2\pi\rho})(4+3r_0^2)}{8|\tilde{s}|^3} + \frac{e^{2\pi\rho}-1}{16\cdot 4!\cdot\rho}\cdot\frac{5r_0^4+30r_0^2+8}{|\tilde{s}|^4},
\end{aligned}$$

which proves the formulae in (5.76).

# Bibliography

[1] G. Bacciagaluppi and A. Valentini. *Quantum Theory at the Crossroads: Reconsidering the 1927 Solvay Conference.* Cambridge University Press, 2009.

[2] J. S. Bell. *Speakable and unspeakable in quantum mechanics.* Cambridge University Press, 1988.

[3] T. B. Benjamin and F. Ursell. The stability of the plane free surface of a liquid in vertical periodic motion. *Proceedings of the Royal Society A*, 225:505–515, 1954.

[4] D. Bohm. A suggested interpretation of the quantum theory in terms of hidden variables, I. *Physical Review*, 85:166–179, 1952.

[5] D. Bohm. A suggested interpretation of the quantum theory in terms of hidden variables, II. *Physical Review*, 85:180–193, 1952.

[6] D. J. Bohm and B. J. Hiley. The de Broglie pilot wave theory and the further development of new insights arising out of it. *Foundations of Physics*, 12(10): 1001–1016, 1982.

[7] T. H. Boyer. Any classical description of nature requires classical electromagnetic zero-point radiation. *American Journal of Physics*, 79:1163–1167, 2011.

[8] A. Burinskii. The Dirac-Kerr-Newman electron. *Gravitation and Cosmology*, 40 (2):109–122, 2008.

[9] J. W. M. Bush. Quantum mechanics writ large. *PNAS*, 107(41):17455–17456, 2010.

[10] J. W. M. Bush. Pilot-wave hydrodynamics. *Annual Review of Fluid Mechanics (under review)*, 2015.

[11] J. W. M. Bush, A. U. Oza, and J. Moláček. The wave-induced added mass of walking droplets. *Journal of Fluid Mechanics (submitted)*, 2014.

[12] J. C. Butcher. *Numerical methods for ordinary differential equations.* John Wiley & Sons, 2nd edition, 2008.

[13] L. Chebotarev. Introduction: The de Broglie-Bohm-Vigier approach in quantum mechanics. In Stanley Jeffers, Bo Lehnert, Nils Abramson, and Lev Chebotarev,

editors, *Jean-Pierre Vigier and the stochastic interpretation of quantum mechanics.* Berkeley Press, 2000.

[14] C. Cohen-Tannoudji, B. Diu, and F. Laloë. *Quantum mechanics.* John Wiley & Sons, 1977.

[15] Y. Couder and E. Fort. Single-particle diffraction and interference at a macroscopic scale. *Physical Review Letters*, 97(154101), 2006.

[16] Y. Couder and E. Fort. Probabilities and trajectories in a classical wave-particle duality. *Journal of Physics: Conference Series (Emergent Quantum Mechanics 2011)*, 361(012001):343–358, 2012.

[17] Y. Couder, C.-H. Gautier, and A. Boudaoud. From bouncing to floating: non-coalescence of drops on a fluid bath. *Physical Review Letters*, 94(177801), 2005.

[18] Y. Couder, S. Protière, E. Fort, and A. Boudaoud. Walking and orbiting droplets. *Nature*, 437(208), 2005.

[19] M. Crommie, C. Lutz, and D. Eigler. Confinement of electrons to quantum corrals on a metal surface. *Science*, 262(5131), 1993.

[20] C. Davisson and L. H. Germer. Diffraction of electrons by a crystal of nickel. *Physical Review*, 30:705–740, 1927.

[21] L. de Broglie. *Ondes et mouvements.* Gauthier-Villars, 1926.

[22] L. de Broglie. Interpretation of quantum mechanics by the double solution theory. *Annales de la Fondation Louis de Broglie*, 12(4), 1987.

[23] L. de la Peña and A. M. Cetto. *The quantum dice: an introduction to stochastic electrodynamics.* Kluwer Academic, 1996.

[24] S. Douady. Experimental study of the Faraday instability. *Journal of Fluid Mechanics*, 221:383–409, 1990.

[25] A. Eddi, D. Terwagne, E. Fort, and Y. Couder. Wave propelled ratchets and drifting rafts. *Europhysics Letters*, 82(44001), 2008.

[26] A. Eddi, A. Decelle, E. Fort, and Y. Couder. Archimedean lattices in the bound states of wave interacting particles. *EPL*, 87(56002), 2009.

[27] A. Eddi, E. Fort, F. Moisy, and Y. Couder. Unpredictable tunneling of a classical wave-particle association. *Physical Review Letters*, 102(240401), 2009.

[28] A. Eddi, A. Boudaoud, and Y. Couder. Oscillating instability in bouncing droplet crystals. *EPL*, 94(20004), 2011.

[29] A. Eddi, E. Sultan, J. Moukhtar, E. Fort, M. Rossi, and Y. Couder. Information stored in Faraday waves: the origin of path memory. *Journal of Fluid Mechanics*, 675:433–463, 2011.

[30] A. Eddi, J. Moukhtar, S. Perrard, E. Fort, and Y. Couder. Level splitting at macroscopic scale. *Physical Review Letters*, 108(264503), 2012.

[31] M. Faraday. On a peculiar class of acoustical figures, and on certain forms assumed by groups of particles upon vibrating elastic surfaces. *Philosophical Transactions of the Royal Society of London*, 121:299–340, 1831.

[32] E. Fort, A. Eddi, A. Boudaoud, J. Moukhtar, and Y. Couder. Path-memory induced quantization of classical orbits. *PNAS*, 107(41):17515–17520, 2010.

[33] T. Gilet, N. Vanderwalle, and S. Dorbolo. Controlling the partial coalescence of a droplet on a vertically vibrated bath. *Physical Review E*, 76(35302), 2007.

[34] T. Gilet, D. Terwagne, N. Vanderwalle, and S. Dorbolo. Dynamics of a bouncing droplet onto a vertically vibrated surface. *Physical Review Letters*, 100(167802), 2008.

[35] G. Grössing, S. Fussy, J. Mesa Pascasio, and H. Schwabl. An explanation of interference effects in the double slit experiment: classical trajectories plus ballistic diffusion caused by zero-point fluctuations. *Ann. Phys.*, 327:421–427.

[36] M. C. Gutzwiller. Periodic orbits and classical quantization conditions. *Journal of Mathematical Physics*, 12(3):343–358, 1971.

[37] B. Haisch and A. Rueda. On the relation between a zero-point-field-induced inertial effect and the Einstein-de Broglie formula. *Physical Review A*, 268:421–427, 2000.

[38] D. M. Harris and J. W. M. Bush. Droplets walking in a rotating frame: from quantized orbits to multimodal statistics. *Journal of Fluid Mechanics*, 739:444–464, 2014.

[39] D. M. Harris, J. Moukhtar, E. Fort, Y. Couder, and J. W. M. Bush. Wavelike statistics from pilot-wave dynamics in a circular corral. *Physical Review E*, 88 (011001), 2013.

[40] D. L. Hu, B. Chan, and J. W. M. Bush. The hydrodynamics of water-strider locomotion. *Nature*, 424:663–666, 2003.

[41] K. Kumar. Linear theory of Faraday instability in viscous fluids. *Proceedings of the Royal Society A*, 452:1113–1126, 1996.

[42] M. Labousse and S. Perrard. Non Hamiltonian features of a classical pilot-wave dynamics. *Physical Review E (under review)*, 2014.

[43] J. Miles and D. Henderson. Parametrically forced surface waves. *Annual Review of Fluid Mechanics*, 22:143–165, 1990.

[44] P. Milewski, C. Galeano-Rios, A. Nachbin, and J. W. M. Bush. A numerical model of pilot-wave hydrodynamics. *Journal of Fluid Mechanics, in preparation.*

[45] J. Moláček and J. W. M. Bush. Drops bouncing on a vibrating bath. *Journal of Fluid Mechanics*, 727:582–611, 2013.

[46] J. Moláček and J. W. M. Bush. Drops walking on a vibrating bath: towards a hydrodynamic pilot-wave theory. *Journal of Fluid Mechanics*, 727:612–647, 2013.

[47] H.W. Müller, R. Friedrich, and D. Papathanassiou. Theoretical and experimental investigations of the Faraday instability. In F. Busse and S. C. Müller, editors, *Evolution of Spontaneous Structures in Dissipative Continuous Systems*, volume 55 of *Lecture Notes in Physics*, pages 231–265. Springer, 1998.

[48] A. U. Oza, R. R. Rosales, and J. W. M. Bush. A trajectory equation for walking droplets: hydrodynamic pilot-wave theory. *Journal of Fluid Mechanics*, 737: 552–570, 2013.

[49] A. U. Oza, J. W. M. Bush, and R. R. Rosales. Orbital stability in hydrodynamic pilot-wave theory. *SIAM Journal on Applied Mathematics, in preparation*, 2014.

[50] A. U. Oza, D. M. Harris, R. R. Rosales, and J. W. M. Bush. Pilot-wave dynamics in a rotating frame: on the emergence of orbital quantization. *Journal of Fluid Mechanics*, 744:404–429, 2014.

[51] A. U. Oza, Ø. Wind-Willassen, D. M. Harris, R. R. Rosales, and J. W. M. Bush. Exotic orbits in hydrodynamic pilot-wave theory. *Submitted to Physics of Fluids*, 2014.

[52] S. Perrard, M. Labousse, M. Miskin, E. Fort, and Y. Couder. Self-organization into quantized eigenstates of a classical wave-driven particle. *Nature Communications*, 5(3219), 2014.

[53] A. Prosperetti. Viscous effects on small-amplitude surface waves. *Physics of Fluids*, 19(2), 1976.

[54] S. Protière, A. Boudaoud, and Y. Couder. Particle-wave association on a fluid interface. *Journal of Fluid Mechanics*, 554:85–108, 2006.

[55] S. Protière, S. Bohn, and Y. Couder. Exotic orbits of two interacting wave sources. *Physical Review E*, 78(036204), 2008.

[56] A. Rueda and B. Haisch. Gravity and the quantum vacuum inertia hypothesis. *Ann. Phys. (Leipzig)*, 14(8):479–498, 2005.

[57] M. J. Shelley and J. Zhang. Flapping and bending bodies interacting with fluid flows. *Annual Review of Fluid Mechanics*, 33:449–465, 2011.

[58] D. Shirokoff. Bouncing droplets on a billiard table. *Chaos*, 23(013115), 2013.

[59] J. T. Stuart. On the non-linear mechanics of hydrodynamic stability. *Journal of Fluid Mechanics*, 4:1–21, 1958.

[60] G. I. Taylor. Interference fringes with feeble light. *Proceedings of the Cambridge Philosophical Society*, 15:114–115, 1909.

[61] D. Terwagne, T. Gilet, N. Vanderwalle, and S. Dorbolo. Metastable bouncing droplets. *Physics of Fluids*, 21(054103), 2009.

[62] J. Walker. Drops of liquid can be made to float on the liquid. What enables them to do so? *Scientific American*, 238-6:151–158, 1978.

[63] G. N. Watson. *A treatise on the theory of Bessel functions*. Cambridge University Press, 2nd edition, 1966.

[64] A. Weinstein and J. R. Pounder. An electromagnetic analogy in mechanics. *The American Mathematical Monthly*, 52(8):432–438, 1945.

[65] Ø. Wind-Willassen, J. Moláček, D. M. Harris, and J. W. M. Bush. Exotic states of bouncing and walking droplets. *Physics of Fluids*, 25(082002), 2013.